Forschungsbericht 2020-45

Aeroelastic Stability of Flat Rectangular Shell Structures in High Subsonic and Low Supersonic Flow

Jannis Lübker

Deutsches Zentrum für Luft- und Raumfahrt
Institut für Aeroelastik
Göttingen

ISSN 1434-8454

ISRN DLR-FB--2020-45

ISRN DLR-FB--2020-45

J. Lübker

Deutsches Zentrum
DLR für Luft- und Raumfahrt

Herausgeber
Deutsches Zentrum
für Luft- und Raumfahrt e. V.
Bibliotheks- und
Informationswesen
D-51170 Köln
Porz-Wahnheide
Linder Höhe
D-51147 Köln

Telefon (0 22 03) 6 01 - 44 44
Telefax (0 22 03) 6 01 - 47 47

ISSN 1434-8454

Forschungsbericht 2020-45

Aeroelastic Stability of Flat Rectangular Shell Structures in High Subsonic and Low Supersonic Flow

Jannis Lübker

Deutsches Zentrum für Luft- und Raumfahrt
Institut für Aeroelastik
Göttingen

226 Seiten
210 Bilder
24 Tabellen
104 Literaturstellen

DLR Deutsches Zentrum für Luft- und Raumfahrt

Aeroelastic Stability of Flat Rectangular Shell Structures in High Subsonic and Low Supersonic Flow.

Von der Fakultät für Maschinenbau

der Technischen Universität Carolo-Wilhelmina zu Braunschweig

zur Erlangung der Würde

eines Doktor-Ingenieurs (Dr.-Ing.)

genehmigte Dissertation

von: Jannis Lübker
aus: Braunschweig

eingereicht am: 23.04.2020
mündliche Prüfung am: 10.11.2020

Gutachter:
Prof. Dr.-Ing. Lorenz Tichy
Prof. Dr.-Ing. Peter Horst

2020

Abstract

In the years preceding the first manned moon landing within the Apollo 11 mission, extensive engineering was carried out on the Saturn V rocket that was chosen to send the first humans to the moon. This work included, among others, thorough studies on an aeroelastic instability known as panel flutter. Under certain flow conditions, the damping of the aeroelastic system of a flow exposed plate or shell structure disappears and self-excited oscillations arise. As a result of the structure's nonlinear characteristics, those oscillations are usually of a limit cycle type and can lead to structural failure.
Theoretical models developed in the 1960s and 70s provide satisfactory results for subsonic and high supersonic flows, but are inaccurate in predicting the aeroelastic behavior of those structures exposed to transonic flows. In the recent years, new fluid-structure interaction (FSI) methods by means of coupled computational fluid dynamics (CFD) and finite element method (FEM) computations have shown an increased accuracy in this Mach number range. Extensive new wind tunnel activities are required though to gain a deeper understanding of the underlying fluidic mechanisms and to allow for the validation of numerical approaches.
The thesis at hand fills this gap and presents the necessary experimental data on the aeroelastic stability of plate and shell structures exposed to high subsonic and low supersonic flows. The performed tests comprise the measurement of structural deformation and the associated aerodynamic response by means of unsteady pressure data. In advance, a new test environment was developed, whose first test campaigns are presented here. The test setup allows the investigation of numerous parameters that strongly affect the aeroelastic behavior of plate and shell structures. The described tests are performed in the Transonic Wind Tunnel Göttingen (DNW-TWG) within a Mach number range of $0.7 < M_\infty < 1.2$ and with a variation of the Reynolds number in a range of $2.5 \cdot 10^6 < Re < 7.5 \cdot 10^6$. The main aim of the activity is the determination of the aerodynamic response evoked by the structural deformation of the used rectangular and flat plate model. The experiments are based on a forced motion conception, which focuses on the first two streamwise bending eigenmode shapes of the structure. Hydraulic actuators are used in order to ensure harmonically oscillating deformations of the plate, which are measured by a stereo pattern recognition system, over a wide range of amplitudes and frequencies. The induced aerodynamic response is measured by highly sensitive and unsteady miniature pressure transducers that are arranged in both streamwise and spanwise sections. The boundary layer thickness, which was found to be of strong influence on the aeroelastic stability, is identified by means of a Pitot tube equipped wake rake. The measured data is validated with theoretical approaches based on potential flow theory. Based on the measurement of pressure and deformation, the influence of the various fluidic and structural parameters is identified and the general-

ized aerodynamic forces are calculated in order to obtain information on the system's stability. The obtained generalized aerodynamic forces indicate an aerodynamic damping, which increases with increasing excitation frequency of the structural deformation, in both the high subsonic and the low supersonic domain. This damping decreases for the latter with further increasing Mach number, whereas for the subsonic domain a decrease is obtained with decreasing Mach number. The measured boundary layer velocity profiles agree with the analytical comparison data, whereas a significant impact of the fluid's boundary layer on the aerodynamic damping cannot be proven with the current possibilities of the test setup. Therefore, a conception is presented which enhance the setup and allows an extensive adjustment of the boundary layer in future experiments.

Kurzfassung

In den Jahren vor der ersten bemannten Mondlandung wurde unter Hochdruck an der Fertigstellung und der Optimierung der Saturn V Rakete gearbeitet, welche die ersten Menschen im Apollo 11 Projekt zum Mond bringen sollte. In diesen Arbeiten wurde unter anderem auch die als Panel Flutter bekannte dynamische aeroelastische Instabilität von Platten- und Schalenstrukturen, welche einer Strömung ausgesetzt sind, untersucht. Unter bestimmten Strömungsbedingungen kann die Dämpfung eines solchen aeroelastischen Systems aufgehoben werden, wodurch selbsterregte Schwingungen der Struktur auftreten können. Aufgrund von Nichtlinearitäten in der Struktur handelt es sich bei diesen üblicherweise um Grenzzyklusschwingungen, welche letztendlich das Versagen der betroffenen Struktur zur Folge haben können.
Die während der 1960er und 70er entwickelten Theorien bieten zufriedenstellende Ergebnisse sowohl für subsonische als auch für hohe supersonische Anwendungen, zeigen aber deutliche Schwächen bei der Vorhersage des aeroelastischen Verhaltens dieser Strukturen bei Strömungen nahe der Schallgeschwindigkeit. Mit fortschreitender Rechenleistung wurde mit numerischen gekoppelten Fluid-Struktur-Ansätzen die Übereinstimmung von theoretischen und experimentellen Daten deutlich erhöht. Neue und umfangreiche Windkanalversuche sind erforderlich geworden, welche einerseits ein detaillierteres Verständnis der auftretenden strömungsmechanischen Phänomene und andererseits die Validierung numerischer Ergebnisse ermöglichen sollen.
Die vorliegende Dissertation knüpft an diese Forderung an und präsentiert die nötigen experimentellen Ergebnisse zum aeroelastischen Verhalten von Plattenstrukturen unter hohen subsonischen und niedrigen supersonischen Strömungsbedingungen. Der Fokus der Datenerfassung und -auswertung liegt auf den Verformungen der untersuchten Strukturen und den aerodynamischen Lasten, welche auf diesen wirken. Zuvor wird der Auslegungs- und Konstruktionsprozess der neuen Versuchsumgebung beschrieben, welche die angestrebten Experimente am Institut für Aeroelastik des DLR Göttingen erlaubt.
Der Versuchsaufbau bietet die Möglichkeit zur Untersuchung einer Vielzahl von strömungsmechanischen und strukturellen Einflussparametern. Die ersten mit dem neu entwickelten Versuchsaufbau durchgeführten Versuche wurden am Transsonischen Windkanal Göttingen (DNW-TWG) in einem Machzahlbereich von $0,7 < Ma_\infty < 1,2$ und bei Reynolds-Zahlen von $2,5 \cdot 10^6 < Re < 7,5 \cdot 10^6$ vorgenommen. Ziel ist die Bestimmung der aerodynamischen Antwort, welche durch die Auslenkung der Teststruktur hervorgerufen wird. Basierend auf vorangegangenen Untersuchungen wurden die ersten beiden Eigenformen einer flachen und allseitig fest eingespannten, rechteckigen Platte als dominierende Formen während einer solchen Instabilität identifiziert. Das auf zwangserregten harmonischen Bewegungen beruhende Versuchskonzept sieht vor, diese beiden Formen in zwei separaten Versuchen durch den Einsatz hydraulischer Linearzylinder zu

simulieren, wobei die Auslenkungsamplitude sowie die Anregungsfrequenz im Experiment variiert werden. Ein Stereo-Kamera-Markertracking-System, welches eine flächige Auflösung der Strukturverformung zulässt, wird genutzt um die realisierten Verformungen und Bewegungen zu vermessen und zu bewerten. Die instationäre Aerodynamik wird durch instationäre Referenzdrucksensoren bestimmt, die in mehreren Schnitten in Strömungsrichtung und in Spannweitenrichtung angeordnet sind. Die Strömungsgrenzschicht, ebenfalls ein wichtiger Einflussparameter, wird mit einem mit Staudrucksonden ausgerüsteten Nachlaufrechen vermessen. Die Messdaten werden anschließend mit analytischen auf der Potentialtheorie beruhenden Daten validiert.
Es werden die Ergebnisse von Deformations- und Druckmessungen hinsichtlich ihrer Abhängigkeit voneinander und dem Einfluss der genannten strukturellen und aerodynamischen Einflussparameter ausgewertet. Darauf basierend werden die generalisierten aerodynamischen Kräfte bestimmt, welche Auskunft über kritische Bereiche der aerodynamischen Dämpfung geben.
Die Ergebnisse nahe der Schallgeschwindigkeit zeigen eine erhöhte aerodynamische Dämpfung, welche mit steigender Anregungsfrequenz zunimmt. Somit nimmt diese Dämpfung im subsonischen Bereich mit sinkender Machzahl und im supersonischen Bereich mit steigender Machzahl ab. Eine negative Dämpfung wird nicht festgestellt. Trotz der erheblichen Variation der Strömungsbedingungen in der Versuchsanlage können die Grenzschichteigenschaften nicht derart verändert werden, dass ihr Einfluss belastbar untersucht werden kann. Allerdings zeigen sich die gemessenen Geschwindigkeitsprofile konform mit den analytischen Vergleichsprofilen und es kann ein Konzept vorgestellt werden, welches die umfassende Anpassung der Grenzschichtdicke in zukünftigen Versuchen erlaubt.

Preface

"With the first link, the chain is forged.
The first speech censored, the first thought forbidden, the first freedom denied,
chains us all irrevocably."

[*Jean Luc Picard*]

The work shown in the present thesis was carried out at the DLR Institute of Aeroelasticity between 2012 and 2020 in the department Aeroelastic Experiments. During the different project phases, I needed and, fortunately, received support on a variety of levels. I would like to use this preface to thank those who willingly offered this support:
Especially in the first period of the project, many meetings took place to find a suitable experimental concept. Since the project was founded as a sponsorship between DLR and Airbus, I would like to thank Dr. Bernhard Kotzias, Peter Nöding und Dr. Martin Konopka for supporting this small project.
After a concept was found, the setup was designed and manufactured at DLR-SHT, so my thanks goes to all colleagues involved. In particular, I would like to thank Helena Fink, who designed the Setup and provided all construction drawings. Furthermore, I want to express my gratitude to Norbert Kassler and the entire DLR locksmith's shop for the installation of the test setup and to Martin Brinsa from the SHT work-scheduling department. I would like to thank Marko Alder, then employed at DLR-AS, for the good cooperation during the entire project and the common development of the panel flutter topic. The tests were finally carried out in the Transonic Wind Tunnel operated by DNW. My thanks go to all colleagues involved, but especially to my project managers Dr. Markus Jacobs and Dr. Andreas Benkel for the joint planning of the test procedures and problems solved together.
With regard to my doctoral thesis resulting from these experiments, I would like to thank Professor Lorenz Tichy, my doctoral supervisor, Professor Peter Horst, second supervisor, Professor Cord Rossow, chairman of the examination committee, and Dr. Holger Mai, who gave me all the freedom I needed to complete my work. My gratitude for the support during the test campaigns goes to Christian Stieg, Thommy Büte, Holger Ernst and Heiko Böhlken.
But above all I thank those with whom I have worked most closely: Anne Hebler, for her extensive support and for the order she has brought to my measurement protocols, Johannes Nuhn, for the wisdom passed on, the most hilarious moments in my time at DLR and for never calling it a day before the job is done, and Nils van Hinsberg, for the support and advice given. Last but not least my thanks go to Christoph Kaiser, Goran Jelicic, Jörn Biedermann and Matthias Schuff for lots of discussions, Palak Paneer and refreshing beverages. I thank you all for your support and your friendship!

Nomenclature

Latin Symbols

A	Area	m^2
$\hat{A}$	Amplitude	mm
a	Speed of Sound	m/s
a_G	Material Constant	$-$
$a_{R,\sigma}$	Material Constant	$-$
B_1	Empirical Parameter	$-$
B_2	Empirical Parameter	K
b	Arc Length of a Curved Panel	m
b_G	Material Constant	$-$
c	Specific Heat Capacity	$-$
c_p	Pressure Coefficient	$-$
D	Plate Bending Stiffness	Nm
Div	Divergence	mm/m
d	Time Depending z Deflection	mm
$\hat{d}$	Amplitude of z Deflection	mm
$\hat{d}_n$	Parameter of Equation of Motion	mm
E	Young's Modulus	N/m^2
E_p	Error (Pressure)	kPa
E_{c_p}	Error (Pressure Coeff.)	$-$
F	Force	N
$\mathcal{F}$	Fast Fourier Transformation	$-$
f	Frequency	Hz
$f(\cdot)$	Function	$-$
$\hat{f}(\cdot)$	Fourier Transformed Function	$-$
$f_{W,\sigma}$	Fatigue Strength Factor	Hz
G_σ	Stress Gradient	$1/mm$
g	WT Wall Distance	mm
h	Panel Thickness	mm
$\Im(\cdot)$	Imaginary Part of a Complex Number	$-$
i	Half-Wavelength in x-direction	$-$
j	Half-Wavelength in y-direction	$-$
$K_{R,\sigma}$	Roughness Factor	$-$
k	Red. Frequency	$-$
L	Reference Length	mm
l	Panel Length	mm

l_{ref}	Reference length	mm
M	Mach Number	$-$
M_n	Generalized Mass (n-th mode)	kg
$M_{x,y,z}$	x,y,z-axis Moment	Nm
m, n	Counter Variables $\in \mathbb{N}$	$-$
n_σ	Fatigue Parameter	$-$
p	Pressure	Pa
Q	Generalized Aerodynamic Force	N
$\overline{Q}$	Complex GAF	N
q	Dynamic Pressure	Pa
q_n	Generalized Coordinate (n-th mode)	$-$
$\overline{q}_n$	Complex Generalized Coordinate (n-th mode)	$-$
R	Radius	m
R_m	Tensile Strength	MPa
$R_{m,N,min}$	Material Constant	MPa
$R_{p0.2}$	Yield Point	MPa
R_s	Specific Gas Constant of Air	Nm/KgK
R_Z	Surface Roughness	μm
$\Re(\cdot)$	Real Part of a Complex Number	$-$
r	Radius	mm
s	Actuator Stroke	mm
T	Temperature	K
T_d	Total Measurement Time	s
t	Time	s
U_∞	Free Stream Velocity	m/s
u	Local Stream Velocity	m/s
$\dot{V}$	Volume Flow	m^3/s
v	Eigenfunction Factor	$1/m$
W	Work	Nm
w	Panel Width	mm
x	x-Coordinate	mm
y	y-Coordinate	mm
z	z-Coordinate	mm

Greek Symbols

α	Panel Mounting Angle	$^\circ$
β	SPR Camera Orientation Angle	$^\circ$
γ	Isentropic Exponent	$-$
δ	Boundary Layer Thickness	mm
$\delta^\star$	Displacement Thickness	mm
η	Dynamic Viscosity	Ns/m^2
λ	Nondimensional Dyn. Pressure	$-$
λ	Wave Length	m

μ	Mass Ratio	$-$
ν	Poisson Number	$-$
ν	Kinematic Viscosity	m^2/s
ρ	Density	kg/m^3
ρ_A	Density/Area	kg/m^2
σ	Stress	Pa
τ	Eigenfunction Factor Clamped BCs	$-$
φ	Phase Angle	mm
Ψ	Eigenfunction	$-$
ω	Angular Frequency	$1/s$

Subscripts and Indices

0	Total Value
A	Aerodynamic
∞	Static Value
$crit$	Critical Value
$\ominus$	Downstream
E	Elastic
exc	Excitation
F	Force
I	Inertial
i	Inner
LE	Leading Edge
o	Outer
p	Pressure
per	Period
$\oplus$	Upstream
s	Structure
$samp$	Sampling
$Turb$	Turbulent
TE	Trailing Edge
W, b	Fatigue for Bending
W, zd	Fatigue for Tension-Compression

Abbreviations

A4	Aggregat 4
ACC	Accelerometer
AMIS	Anlage zur Messung Instationärer Daten
AVA	Aerodynamische Versuchsanstalt
BL	Boundary Layer
BNC	Bayonet Neill Concelman

CFD	Computational Fluid Dynamics
CMOS	Complementary Metal Oxide Semiconductor
CUST	Cryogenic Upper Stage Technologies
DAQ	Data Acquisition
DeAs	Datenerfassungs- und Anlagensteuerungssoftware
DLR	Deutsches Zentrum für Luft- und Raumfahrt (German Aerospace Center)
DNW	German Dutch Wind Tunnels
DOF	Degree Of Freedom
ELM	Element
ESA	European Space Agency
FEM	Finite Element Method
FFT	Fast Fourier Transformation
FLPP	Future Launcher Preparatory Program
fps	Frames Per Second
FSI	Fluid Structure Interaction
FSO	Full Scale Output
GP	Grid Points
LCO	Limit Cycle Oscillation
LED	Light Emitting Diode
LSB	Least Significant Bits
LDV	Laser Doppler Vibrometry
MAC	Modal Assurance Criterion
MBC	Mechanical Boundary Condition
MP	Measurement Point
MR	Mid-Range
MS	Measurement Series
NAA	North America Aviation
DNW-TWG	Transsonischer Windkanal Göttingen
PLC	Programmable Logic Controller
PSD	Position Sensitive Device
RANS	Reynolds-Avaraged Navier-Stokes
SF	Factor of Safety
SMR	Start of Measurement Range
SPR	Stereo Pattern Recognition
TS	Test Section
TPS	Thermal Protection System
TTL	Transistor-Transistor Logic
TWG	Transsonischer Windkanal Göttingen
VD	Variable Diffuser
VTI	Versatile Thermal Insulation
VZLU	Czech Aerospace Research Center
WT	Wind Tunnel

Contents

1. Introduction

The field of aeroelasticity addresses the interaction of fluid flows with elastic structures, which can cause numerous phenomena. The aeroelastic system can be described by means of the acting forces, which are the elastic forces F_E, the aerodynamic forces F_A and the inertia forces F_I, as illustrated in Figure 1.1. Static phenomena involve the first two mentioned forces, while the dynamic phenomena additionally involve inertia forces. One particular type of dynamic phenomena is the so-called flutter instability. Critical flow conditions cause self-excited oscillations of the structure, which eventually lead to catastrophic material failure [1]. Those oscillations' origins are initially marginal structural movements causing motion induced aerodynamic forces, which again increase the structure's motion.

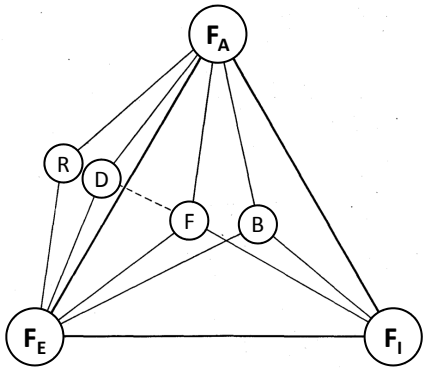

Figure 1.1.: Triangle of aeroelasticity by Collar [2]; In this Figure: reversal of control R, divergence D, flutter F, buffeting B.

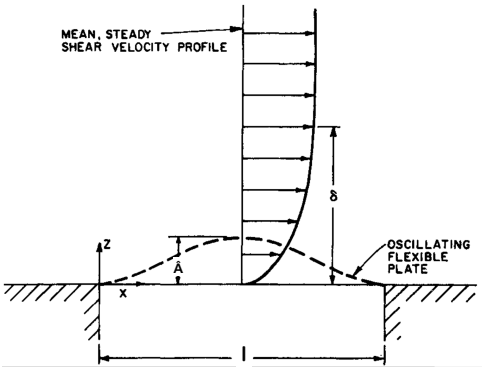

Figure 1.2.: Panel flutter model by Dowell [3]; In this Figure: Amplitude $\hat{A}$, panel length l, boundary layer thickness δ.

Panel flutter is one particular flutter mechanism that affects shell and plate structures. A common illustration of that phenomenon is given in Figure 1.2. A flat plate, which is supported at its leading edge ($x_{LE} = 0$) and its trailing edge ($x_{TE} = l$), has one side exposed to a fluid flow. The plate's back is facing a cavity with a static volume inside [4]. The interaction between plate and flow, which has a boundary layer with a thickness δ, causes an oscillation of the plate in z-direction with an amplitude $\hat{A}$. Due to the nonlinear characteristics of the structure, a limit cycle oscillation results, which eventually leads to a structural failure of the plate.
Since panel flutter was observed for the first time in 1944, it has been subjected to numerous theoretical and experimental investigations, from which the motivation of the

thesis at hand is directly derived and described in the following section of this chapter (Section 1.1). The studies point out a gap of knowledge for high subsonic and low supersonic flow conditions, where classic analytic methods cannot provide reliable predictions on the aeroelastic stability. It has become evident that structures exposed to those flows are on the one hand particularly prone to flutter. On the other hand, the flow's boundary layer has shown a stabilizing impact on flutter. With regard to high performance aircraft and launch vehicles, which are subject to those flow conditions, understanding and controlling that aeroelastic instability is of high relevance [5, 6]. Numerical fluid-structure-interaction methods are very promising to close this gap, which is why a comprehensive experimental data base is needed.
Section 1.2 describes the objectives, which are derived from the above mentioned motivation. A forced motion experiment, which enables the separate assessment of the structure's motion and the induced aerodynamic response, is carried out under the mentioned flow conditions. In addition to providing a suitable data base for subsequent numerical studies, a deeper insight in the aeroelastic mechanism is aspired. Further, the newly designed test setup shall allow various future experiments on shell and plate structures. The necessary work steps illustrated in the thesis at hand are summarized in Section 1.3. The last section of this chapter (Section 1.4) gives an overview of the hitherto conducted experimental studies on panel flutter, which is needed to define fluidic and structural parameters of importance and to obtain indications on how such kind of experiments can be designed and carried out. The last section of this chapter (Section 1.4) gives an overview of the experimental studies on panel flutter, which have been conducted and published so far. From these, fluidic and structural parameters of importance are defined and indications on how such kind of experiments can be designed and carried out are obtained. In addition to wind tunnel test campaigns on generic structures and specific components of spacecraft and aircraft, in-flight tests are also illustrated to complete the survey of experimental activities, which have been done over the last eight decades.

1.1. Motivation

Extensive theoretical and experimental investigation on the aeroelastic stability of plates and shells has been carried out since panel flutter was observed for the first time. In this section, only very few studies are illustrated, by which the gap in knowledge can be pointed out:
Very early, panel flutter was found to be a supersonic phenomenon [7], but only a couple of studies were performed at low supersonic flow conditions. An experimental setup, which essentially corresponds to the scheme shown in Figure 1.2, was used in 1969 by Muhlstein and Gaspers [8, 9] for investigation at low supersonic Mach numbers and involving the impact of the flow's boundary layer. The resulting flutter boundaries, which depend on the Mach number and on the boundary layer thickness, are represented in Figure 1.3 by means of the critical dynamic pressure. Here, the parameter of the depicted set of curves is the boundary layer thickness. Each curve shows the most critical domain at about $M_\infty = 1.15$, which indicates a highly increased susceptibility to flut-

ter. The successive rise of the boundary layer thickness from zero to about one inch (2.54 cm) shows clearly an accompanying increase of the flutter boundary. This effect is especially pronounced where the maximum susceptibility to flutter occurs. Consequently, the accurate prediction for low supersonic Mach numbers is crucial, since the most critical conditions occur here. This prediction must consider the stabilizing effect of the boundary layer, which can lead to significant structural savings during the design process of aerospace structures.

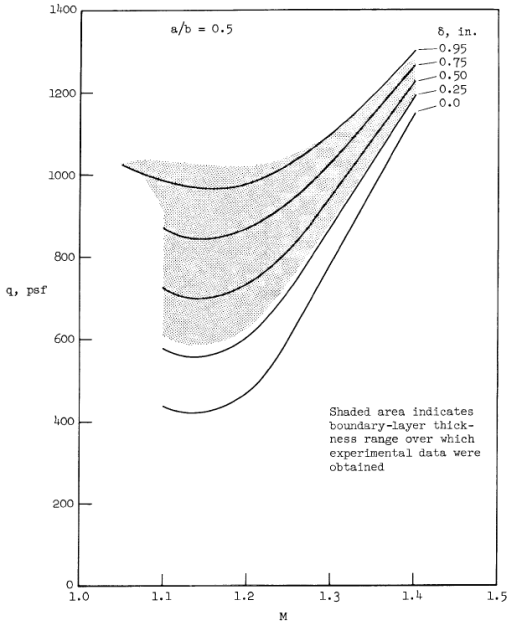

Figure 1.3.: Experimentally determined influence of Mach number and boundary layer thickness on critical dynamic pressure [8].

Several theoretical approaches have been carried out to meet the experimentally obtained results. One theory to estimate aerodynamic forces acting on a plate structure has been published in 1956 by Ashley [10], which uses a mathematical formulation of a piston that is moving in a one-dimensional tube. The induced pressure results from the velocity, which is calculated on the one hand by the piston's motion and on the other hand by the streamwise inclination of the structure. The scope of this so-called piston theory is restricted to high speed applications or high reduced frequencies of the oscillating structure and can only be used for plane or very slightly inclined surfaces. Reasonable results can be obtained for $M_\infty > 2$, but erroneous data results at $M_\infty < \sqrt{2}$ [11,12]. A further limitation is the applicability to small length-width ratios [13], since three-dimensional effects become dominant at high ratios [14, 15]. Dowell [7, 15, 16] evolved another approach based on unsteady linearized potential flow theory. This approach considers the influence of the neighboring structural coordinates on the aerodynamics, as well as the influence of the previously calculated time steps. More advanced approaches consider the boundary layer by use of a predefined non-uniform mean flow or a one-seventh power

law velocity profile. Although a stabilizing influence can be demonstrated, there is still disagreement with the experimental data [17]. Either way, all three presented approaches show unsatisfactory results in the Mach number domain which has been proven to be important.

In recent years, fluid-structure interaction computations have been used to investigate the panel flutter phenomenon. Hashimoto [17] solved Reynolds-averaged Navier-Stokes (RANS) equations by using computational fluid dynamics (CFD), which were coupled with the von Kármán plate equation. The von Kármán plate equation takes into account in-plane stresses, which reduce the resulting panel deflections. A comparison of his results with different approaches is depicted in Figure 1.4. Figure 1.4 (a) compares Euler computations with Dowell's transonic potential flow theory [3,18] and with extrapolated experimental data by Muhlstein [8]. A fair agreement between both theoretical approaches and the experimental data is evident. In Figure 1.4 (b), a comparison of approaches is shown that take the boundary layer into account. Two different RANS computations by Hashimoto [17] and results of Dowell's shear flow theory [3,18] are compared with experimental data again by Muhlstein [8] and Gaspers [9]. Results obtained with the Spalart-Allmaras (RANS-SA) and the Baldwin-Lomax (RANS-BL) turbulence model are in good agreement with the experimental data, whereas the shear flow theory shows a significantly reduced agreement.

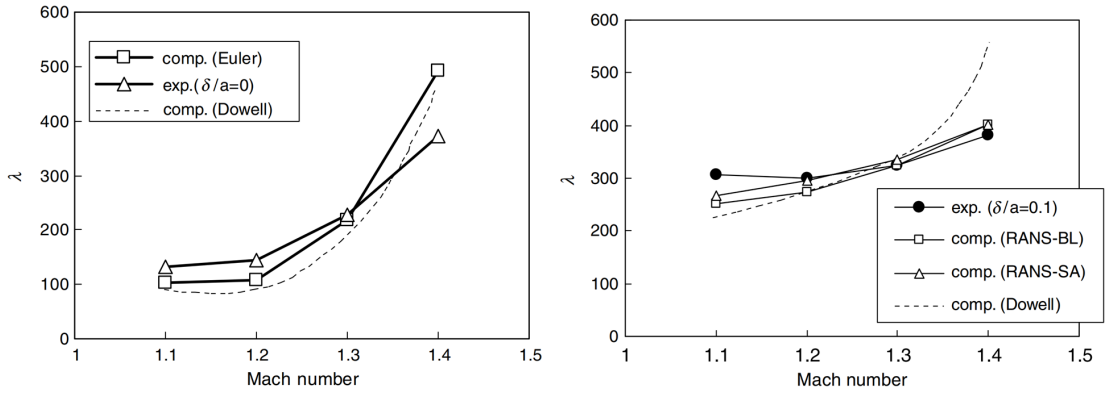

(a) Inviscid results with non-dimensional boundary layer thickness $\delta/l = 0.0$.

(b) Viscous results with non-dimensional boundary layer thickness $\delta/l = 0.1$.

Figure 1.4.: Flutter boundary by means of non-dimensional dynamic pressure λ for inviscid flow (a) and for viscous flow (b) for supersonic Mach numbers [17].

This section has shown that an accurate prediction of the aeroelastic stability of plate and shells including the consideration of the boundary layer is crucial for a proper design of aircraft and spacecraft components, which are exposed to low supersonic flows. The classic and analytic methods are not able to meet these requirements, whereas the new numerical fluid-structure interaction (FSI) methods have proved promising. Experiments focusing on the key aspects Mach number influence and impact of the boundary layer on the aeroelastic stability of plates and shells are needed and will give a deeper

insight in the arising aeroelastic mechanisms. Thus, a data base needed for validation activities will be provided.

1.2. Objectives

From the stated motivation the major goals of this thesis can directly be derived:

- A shell structure which is subject to low supersonic flow is to be investigated regarding its aeroelastic stability. This includes the determination of the boundary layer's influence on the aeroelastic system.
  In contrast to the experiments performed so far, the applied forced-motion approach allows for the separation of unsteady aerodynamics from aeroelasticity and thus to disregard the nonlinear structural dynamics. The aerodynamics are identified by numerous unsteady pressure transducers which ensure detailed information on the local and global flow phenomena occurring over the test structure. This will provide comprehensive data for the validation of unsteady aerodynamic models of CFD methods.

A detailed breakdown of this key objective, which is extended due to demands concerning the chosen wind tunnel, the measurement technique and the general conception of the upcoming experiment, is described below:

1. In advance to the upcoming experiments, a test setup is to be designed. In addition to the key parameters regarding the Mach number and the boundary layer, further parameters have to be identified. The parameters are to be prioritized with regard to their influence on the above-mentioned main objectives and their feasibility and implemented into the test setup design. Founded on the expertise of the institute, the experiment is to be carried out according to a forced motion approach, which allows a direct measurement of the aerodynamic forces induced by the structure's motion. For comparison of the arising phenomena, high subsonic flow conditions are to be considered too. Since the test setup is meant to allow further studies on the aeroelastic stability of plate and shell structures in future test campaigns, a most versatile design approach is aspired.

2. The outcome of the experiments shall provide an extensive data base for validation activities, which includes the data on several fluidic and structural parameters. The key aspects of the experiment are the induced aerodynamic loads in the low supersonic Mach number range and the consideration of the boundary layer's properties.

3. The local mechanisms, which occur on the test structure, are to be observed and described with regard to all identified parameters. A proper spatial discretization of the sensors, used for the measurement of structural displacement and the induced aerodynamic forces, shall give thorough insight.

4. Information on the state of the entire aeroelastic system gives an integration of the obtained local data sets. The generalized aerodynamic forces, which can be considered as a measure for the system's damping, are to be calculated based on the aerodynamic response and the corresponding deformations.

1.3. Outline of the Present Thesis

After the motivation of this work and the resulting objective has been identified, this section states the steps taken to meet the given requirements. The obtained outline of the thesis at hand contains a brief summary of each step from the experiment's conceptual phase to the data acquisition including a description of where detailed information can be found in this document.

Test Setup Design

- **Conception:** A summary of previously done wind tunnel experiments on panel flutter over the last eight decades including a description of the applied measurement techniques and test methods is given in Section 1.4. Ideas for the design of a new test set-up are to be drawn from this. Information on some main parameters is given in Chapter 2 providing the theoretical background, which shall also help to understand the main mechanisms of panel flutter.
  A literature review is presented in Chapter 3 to identify fluidic and structural parameters in addition to the key parameters stated in the beginning of this chapter. The design must take a multitude of further parameters into account for future test campaigns that focus on other key parameters. Furthermore, the chapter contains a description of the principle of forced motion [19, 20], according to which the experiment is employed. A defined structural deformation, which is driven by an actuator mechanism, induces an aerodynamic response that allows the investigation of the aeroelastic stability without touching any stability boundaries. Concerning the required investigation of the boundary layer's impact, a proper way to control and measure the boundary layer's characteristics is to be found.
  A suitable test facility was to be found that allows test campaigns to be carried out in the defined range of Mach numbers. For this purpose, the Transonic Wind Tunnel Göttingen (DNW-TWG) was selected, which is described in detail in Section 5.1. The test setup must be tailored to the wind tunnel's design features, which means another set of boundary conditions.

- **Final Setup:** One outcome of the conceptual phase is a modular test setup design, which allows an adaptation to different test structures, measurement techniques and experimental concepts. The final design for the experiments presented in this document is divided into several subassemblies, which are discussed separately in Chapter 4. The chapter also contains descriptions of how the parameters, which are found to be important, but are neglected for the present activities, can be applied for future activities.

- **Testing Technology:** Chapter 5 comprises on the one hand a description of the used test facility including its measurement techniques for the wind tunnel's quantities and the associated data acquisition system. On the other hand, the unsteady measurement techniques embedded in the actual test setup are presented with the corresponding data acquisition system and the used actuating system, which is needed for realizing the forced motion approach. The main components of the measurement technique, which acquires data over the entire structure's surface, are focused on the structure's deformation and the induced pressure. A wake rake is placed downstream behind the model to determine the boundary layer's properties based on pressure measurement. The chapter also contains information on how the sensor signals are processed preparing the results' analysis.

Experimental Procedure

In preparation for the tests, a test matrix is created, which contains the variation of the structural and fluidic parameters of the three test campaigns presented in this thesis. The included parameters related to the structure are the deflection amplitude, which is equal to the actuator's stroke, and the excitation frequency, which is the actuators oscillation frequency. With regard to the flow, the Mach number is varied in a range from high subsonic to low supersonic conditions to cover the range around a Mach number of one. The second fluidic parameter is the Reynolds number, which is varied by adapting the wind tunnel's total pressure and aims at a change in the flow's boundary layer. The resulting test matrices are shown in Section 5.3. The three conducted test campaigns differ in the structure's forced deformation shape and in the investigated influencing parameters. The first test campaign focused on the first forced motion shape in consideration of the forced motion's excitation frequency, its amplitude and the Mach number. In the second test campaign on the first shape, the Reynolds number was considered instead of the deflection amplitude. The third test campaign corresponds to the latter, whereby the second forced motion shape was investigated.

Data Analysis

After the measurements are performed and the raw data is processed, the analyses start with showing the reliability of the data. This is done in each introducing part of the results' presentation of the measured unsteady deformation and unsteady pressure by using statistical considerations based on the standard deviation. The analysis of pressure and deflection allow insight into the local physical mechanisms of the aeroelastic system. Accordingly, Chapter 6 contains the outcome of the three main measurement techniques, which give information on the boundary layer, the structural deformation and the induced pressure (which is the aerodynamic response):

- The boundary layer's thickness and velocity profile is measured by means of a wake rake equipped with 64 Pitot tubes (Section 6.1). A comparison with a one-seventh power law approach is carried out in order to verify the presented results.

- The deformation of the panel is measured by a stereo pattern recognition (SPR) system, which allows the three-dimensional tracking of markers that are arranged in a specific pattern over the panel's surface (Section 6.2). The results are compared with the design shapes, which have been defined in Chapter 2 with regard to the plate's eigenfunctions.
- Highly sensitive unsteady pressure transducers are used to measure the aerodynamic response, which is induced by the structural forced motion, by means of the pressure difference between the flow faced side and the rear side of the test structure (Section 6.3). In this section, the impact of the defined structural and fluidic parameters is described extensively. In order to verify the pressure measurements, the theories introduced in Chapter 2, which are based on potential flow theory, are used for comparison.

A final section of this chapter leads from the so far discussed local mechanisms connected with the motion induced aerodynamic forces to the integrated global quantities, which give information on the state of the aeroelastic system. The generalized aerodynamic forces, which are the integrated pressure weighted with the underlying structure's shape, indicate whether a negative or a positive system's damping is present (Section 6.4).

1.4. Once Upon a Time ... the History of Experimental Panel Flutter Investigation

The first time (known to the author) the aeroelastic instability called panel flutter came onto the scene of history was by the end of World War II in 1944. The German ground-to-ground missile Aggregat 4 (A4) showed burst metal skin panels of its outer ribs-and-stringers-design fairing [21]. The testing of the missile was done at the research site of the "Heeresversuchsanstalt" in Peenemünde. The Institute for Unsteady Processes, which was part of the Aerodynamische Versuchsanstalt (AVA) in Göttingen (whose successor is the today's DLR), was instructed to investigate the newly observed phenomenon initially referred to as "Beplankungsflattern". Engineer in charge was P. J. Jordan, who was also responsible for flutter investigations on back-swept wings [21] that were invented here several years before. Subsonic experiments at velocities of $U_\infty \leq 70$ m/s were carried out with flat models supported at the leading edge and weighted at the trailing edge for creating in-plane stresses [22]. Further, Jordan used flat and curved all-edge supported models (Figure 1.5), which were made of fabric, with weights at the trailing edge and the longitudinal edges. Depending on the used mechanical boundary conditions (MBCs), the gained data showed moderate agreement with the prior done theoretical work. Besides the subsonic tests, further experiments under supersonic conditions at $M_\infty = 3.0$ were carried out with models made of paper and plywood. No flutter was observed, though it was remarked that in case of very small amplitudes, which were caused by high flow velocities, the model oscillations were not detectable by the used stroboscope-light measurement technique. The resulting recommendation for preventing flutter was to increase the stiffness of the used structures, which could be realized

by applying in-plane pre-stresses [22]. After the war, a significant part of the German aviation research staff moved to USA and USSR to continue the interrupted work. In 1956, Jordan was employed at Martin Company, where he published further results of his work comprising additional data of tested panels made of metal. Again, panel flutter was not observed. Besides the assumption of too low amplitudes it was supposed that the flow velocities needed for the high Young's Modulus of structures made of metal could not be established [23]. At the same time, additional experimental activities were

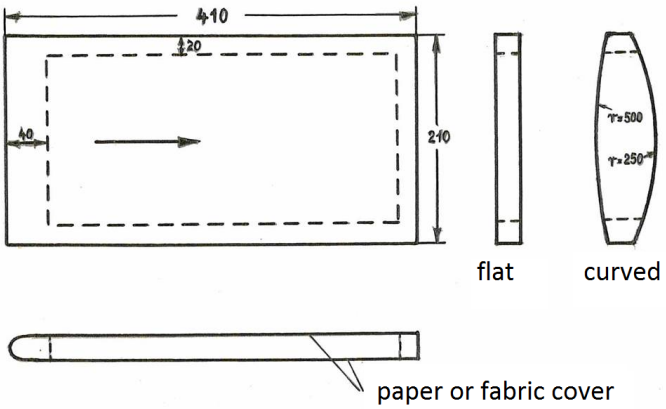

Figure 1.5.: Curved and flat all-edge-supported panel types used by Jordan [22]. The panels were made of paper or fabric and show in the case at hand no additional loads to induce pre-stresses.

carried out at NACA Langley Aeronautical Laboratory, which is today's NASA Langley Research Center, by Sylvester et al. [24–26]. The extensive activities at $1.2 \leq M_\infty \leq 3.0$ comprised investigations on numerous parameters, which would remain on the agenda of experimental studies for the next decades to come. Just as that, the whole test setup design was leading the way for following investigations. The structures used in the tests were flat as well as buckled, curved and lengthwise stiffened rectangular plates, which were made of different isotropic materials (steel, aluminum, magnesium and brass) and showed a wide variety of the dimensions thickness, length and width. The panel MBCs were either clamped at leading and trailing edge or all-edge clamped with some samples being equipped with streamwise stiffeners. The test specimen was placed in the wind tunnel test section's side-wall. A vented and sealed chamber (cavity), which was used for releasing pressure as well as for applying pressure differentials between the two panel surfaces, was located at the panel's rear side. A turntable offered the possibility to investigate streamwise and spanwise curved structures. Clamps with tension screws and compression screws allowed the adjustment of in-plane stresses and initial buckling. Another possibility to establish buckling was heating the panel and thus taking advantage of the resulting material elongation. The test setup was equipped with inductive transducers located along the streamwise panel center line in order to measure the panel deflections. The measurement of the static pressure in the cavity and the tunnel was realized by quick-response strain gauge pressure cells. During some of the test campaigns,

one strain gauge was applied on the panel to indicate the magnitude of the arising flutter stresses. The panel temperature was measured by thermocouples at the panel rear side. During the tests, the pressure in the cavity was adjusted for examining the pressure differential's impact on the flutter boundary. For buckled panels, it was found that an increase of the pressure differential can stop panel flutter. The flutter tendency was found being strongly dependent on the generated buckling shape and the structure's width-to-length ratio. Flat panels clamped front and rear and with applied in-plane stresses were prevented from flutter by increasing the tensile load, decreasing the length or increasing the bending stiffness. Increasing the latter included an increase of the plate thickness. The observed oscillation of a panel while fluttering was of a limited cycle type (Figure 1.6), which was proven generally valid in following tests. Consequently and in contrast to wing flutter, panel flutter was rated to be a fatigue problem, since occurring panel flutter does not mean an inevitable and immediate destruction of the panel [24].

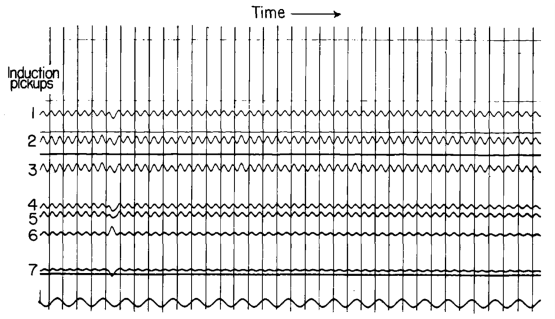

Figure 1.6.: Deflection measurements of aligned pickups showing established limited amplitude oscillation during flutter [24].

At the turn of the decade, the North American Aviation company (NAA) was assigned to build a rocket propelled experimental aircraft, which should provide the US space flight project with data collected in hypersonic flight [27]. The first of the three manufactured X-15 aircraft accomplished its first flight in 1959 and after altogether 199 flights the last one was performed in 1968 [28]. The objects of investigation were the large-length-to-width ratio unstiffened panels, which were used in the vertical tail, and corrugation stiffened panels applied at the side fairing (Figure 1.7 (a)) [29]. Accompanying flight tests showed panel flutter of the long narrow rectangular panels of the vertical tail of the X-15 [5]. Based on prior wind tunnel tests, a flutter boundary was established depending on the length-to-width ratio, which revealed an increasing flutter tendency with increasing ratio. In the end, full scale WT tests for tail and fairing panels confirmed the in-flight test results of flutter being present in the X-15 operating range. Likewise, full scale wind tunnel tests of corrugation stiffened and unstiffened panels of the vertical tail and the side fairing indicated panel flutter in the X-15 flight trajectory [29]. In-flight test and WT test results were in agreement with each other and proved the flutter suppressing impact of increased structural bending stiffness. It appeared that the corrugation of a panel should be directed in flow direction to cause the strongest effect on flutter

margin. Further, it was found that changes in the flow-direction angle (swept panels) affect the determined flutter boundary strongly. Additional full scale wind tunnel tests on the X-15 lower vertical stabilizer, which had different narrow high length-to-width ratio skin panels, were carried out in the 9- by 6- foot Thermal Structures Tunnel at Langley Research Center [30]. The flow conditions were varied within a total pressure range of 414 kPa$\leq p_0 \leq$ 1379 kPa, a dynamic pressure range of 72 kPa$\leq q \leq$ 240 kPa and temperatures within a range of 420 K$\leq T_0 \leq$ 530 K. The tested samples, which had shown to be prone to panel flutter in the studies mentioned before, were applied to rib and spar constructions. Iron-constantan thermocouples were used for measuring the skin panel temperature and inductive-type deflectometers were used to determine the panel deformation behavior by measuring changes in its distance to the panel rear surface. Attached strain gauges were used to double-check those measurements. The static pressure at the stabilizer's outer surface was determined by quick response strain gauge-type pressure transducers. In general, the results of the prior investigations could be confirmed. The critical un-stiffened and corrugation-stiffened panels, which were subject to flutter, were improved by stiffening.

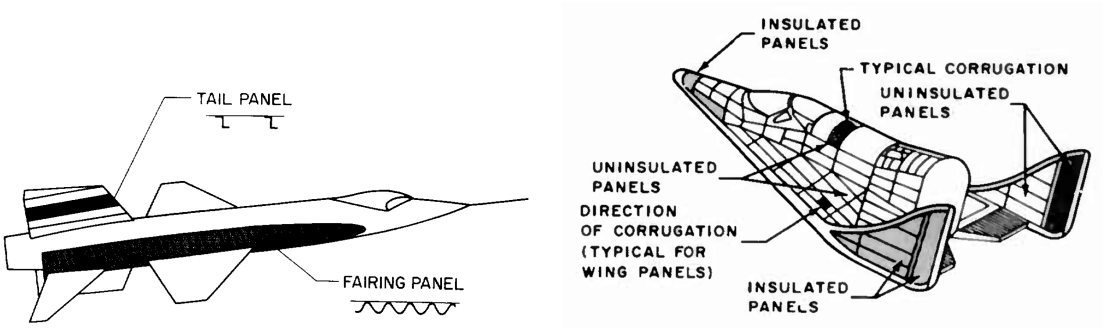

(a) Regions of X-15 research aircraft affected by panel flutter [29] with unstiffened tail panels and corrugation stiffened fairing panels.

(b) Upper locations of insulated and uninsulated panels of X-20 Dyna-Soar [31].

Figure 1.7.: Experimental aircraft X-15 and X-20.

Further test campaigns carried out from 1961 onwards at $M_\infty = 3.0$ by Dixon [32–35] focused further extensive investigations on the panel length-to-width ratio, which was already rated having a strong impact on panel flutter behavior, as well as on in-plane stresses due to thermal loads. Those in-plane stresses were considered important, because of the compression stresses occurring in supersonic flight. The same test facility was used as done for the investigations summarized above. The test samples were made of aluminum alloy and steel with numerous width-to-length ratios ranging from 0.96 to 10 and with various numbers of bays. The panel edges were riveted to a frame construction. The all-edge supported panels were mounted to a support, which was applied in a vertical manner in the test section's center from the ceiling to the bottom. This support had an airfoil profile shaped leading edge and flat sides where the test structure was placed. Pneumatically operated sliding doors protected the panel against heating and buffeting

during the start procedure of the tunnel. Those effects were caused by the intermittent supersonic blowdown operation principle of the wind tunnel, which allowed maintaining the necessary flow conditions for about one minute [36]. Another safety measure was the application of aerodynamic fences that protected the panel during the test run by preventing shock waves over the panel. A venting device located at the rear side of the panel support allowed the adjustment of the panel rear side pressure. The fixture was designed with clearances at all edges to allow thermal stress lengthening. Inductive-type deflectometers (for some test campaigns reluctance-type deflectometers were used instead) were used to measure the panel deflection during the test runs, whereas iron-constantan thermocouples and strain-gauge-type pressure transducers recorded the static pressure at several positions on the support and in the cavity on the panel rear side. Footage was recorded with high frame rates of about 2600 frames per second, which gave additional data on the panel's behavior. The analyses showed that the flat panels became more susceptible to panel flutter with increasing temperature, which was driven upwards by aerodynamic heating. Once buckling appeared, the increased temperature led to increased buckling depth and thus to an increased stiffness, which led to less susceptibility to flutter. The most critical conditions were reached at the transition point, which occurs shortly before buckling. Depending on the pressure difference between the two panel surfaces, two types of flutter were observed. A standing wave characteristic occurred at low differential pressures, whereas flutter with traveling wave characteristics was observed at high differential pressures. The test setup was further used for studies focusing on the influence of thermal stresses on corrugation stiffened panels [37].
Experiments done in the same period on titanium low aspect ratio flat and curved panels were carried out at NASA Langley Research Center Unitary Plan Wind Tunnel at $1.72 \leq M_\infty \leq 2.62$ by Presnell [38]. The effect of the differential pressure between the panel surfaces was observed for the all-edge riveted test panels. The results showed a fair agreement with previously mentioned publications [29]. A need for investigations on the effect of the cavity behind the panels was noted. Done in the same facility and compared to the same reference results, the flutter behavior of unstiffened and corrugation stiffened simply supported panels was studied at $1.57 < M_\infty < 2.87$ and 6 kPa $< q_\infty <$ 124 kPa by Weidmann [39]. The setup provided a splitter-plate type leading edge, whose purpose is to control and/or to adjust the fluid's boundary layer independently from the wind tunnel conditions, and a pressurizable cavity beneath the panel. An offset between plate and tunnel wall establishes either a new origin of boundary layer for the following structure or cuts off only a part of the approaching wind tunnel boundary layer.
In case of another X-Series aircraft, the X-20 Dyna-Soar, more wind tunnel panel flutter tests were carried out [40]. The project, which was started in 1957, was canceled in 1963 even though its research findings strongly influenced the Space Shuttle project that started in the early 70s [41]. Based on the foregone investigations, panel flutter was identified for being one of the limiting factors of the aircraft flight during the boost phase and the reentry phase at low altitude [42]. The panel was designed to allow high thermal stresses during reentry that led, among other requirements, to orthotropic characteristics, for which almost no database was available until then. Objective of the conducted tests was the investigation of the parameters length-to-width-ratio, thickness, corruga-

tion stiffening, edge constraints and the reduced stiffness due to reentry temperatures (Figure 1.7 (b)) [31].
From 1962, the Atlas Space Launch Vehicle, which was derived from the originally Atlas intercontinental ballistic missile, was equipped with the Centaur upper stage to carry up to $m = 5200$ kg of payload into earth orbit [43]. The so-called Interstage Adapter was the structural connection between the Atlas rocket and its upper stage [6]. This component, with a diameter of 10 foot, was composed of circumferential ring stiffeners, which were located on the inner side of the cylindrically shaped structure. Stringers were applied in direction of flow on the outer surface (Figure 1.8 (a)). This way, a checkerboard-alike pattern of rectangular aluminum skin panels was established. Wind tunnel tests were first carried out at NASA Langley Research Center at $M_\infty = 1.63$ and $M_\infty = 1.84$ on flat individual panels (aluminum) in the Unitary Plan Wind Tunnel [6] and later at $M_\infty = 3.0$ on full scale quarter segments (aluminum) in the 9- by 6- foot Thermal Structures Tunnel [44]. In case of the latter, data concerning the influence of the curvature and concerning the cascading effect were collected. Besides a flutter model, a rigid model was tested in advance to obtain the pressure distribution over the test structure. Compressive loads were not applied by thermal lengthening, but by hydraulic jacks attached to the stringers downstream end, whereas the test specimen was fixed at its upstream edge. The loads were recorded by strain gauges, which were only attached to stringer elements to avoid influences on the test structure's aeroelastic behavior. Previous observations on in-plane compressive loads could be confirmed. The flutter tests were performed at dynamic pressures, increased by 50% compared to flight condition pressures. No cascading effect was observed and the curvature showed a stabilizing effect on panel flutter behavior. The flutter test results were compared to in-flight measurements, whose instrumentation comprised high response accelerometers in one panel's center, high-frequency pressure fluctuation transducers to measure the pressure excitation on the panel surface and longitudinal strain gauges to identify the compression forces. Although vibrations and oscillations were observed, no panel flutter was detected. The observed oscillations were attributed to sound and boundary layer noise. Flight data showed the strongest vibrations occurring close to sonic conditions, which was impossible to repeat during the wind tunnel test campaign and thus resulted in the demand for transonic data. The comparison of wind tunnel test results and in-flight data indicated that in-flight conditions were always within a safety margin with regard to the flutter boundary except for a very short period of time at conditions close to $M_\infty = 1.0$. According to that report, the Interstage Adapter was found to be adequate to withstand the loads occurring in flight.
In contrast to previous experiments, which investigated the characteristics of isotropic materials, further wind tunnel tests on the more complex structure of the insulation panels of the Centaur stage were performed in 1967 at Lewis Research Center (Glenn Research Center) 10- by 10-foot Supersonic Wind Tunnel (Figure 1.8 (b)). Full-scale quarter segments, which consisted of polystyrene-foam filled fiber-glass honeycombs sandwiched between fiberglass skins, of the Centaur upper stage insulation were tested at $2.0 < M_\infty < 3.5$ and at about 9.5 kPa $< q_\infty <$ 33.5 kPa. The objective was to simulate the environmental conditions during flight regarding aerodynamic and structural bound-

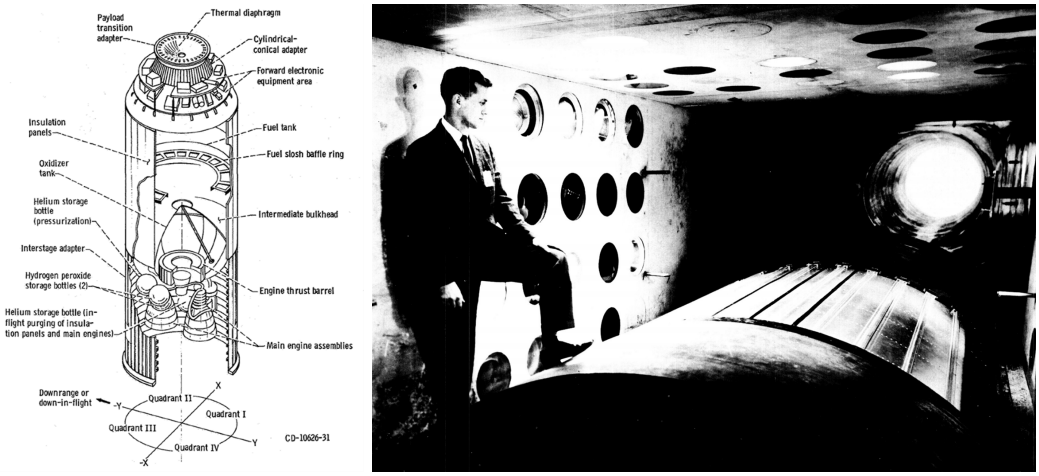

(a) General arrangement of Centaur vehicle, AC-17 [45].

(b) Mounting device in tunnel test section with model installed as viewed from upstream. Protective cover in retracted position [44].

Figure 1.8.: Panel flutter investigations on Atlas Centaur launch vehicle.

ary conditions. The main parameters were the Mach number, the dynamic pressure and the in-plane tension of the panel structures. Liquid nitrogen was used to establish flight conditions and in order to get real structural conditions, circumferential pre-stress was applied introduced by gearboxes located on the panels' longitudinal sides. A differential pressure of zero between the two panel surfaces was set to maintain conservative conditions. The instrumentation consisted of strain gauges and thermocouples, which were located at different positions of the setup. Although several operational problems emerged, the results verified the absence of flutter for the insulation panels [46].
A new approach to establish flutter boundaries was introduced in 1966 at NASA Ames Research Center at Moffett Field by Muhlstein [47]. The underlying principle based on the mechanical impedance, the measurement of which allows the determination of the aeroelastic system's damping. For this purpose, a Mach number range of $1.1 \leq M_\infty \leq 1.4$ was established in the Ames 2- by 2-Foot Transonic Wind Tunnel. The all-edge clamped magnesium test panels, which had a cavity on the rear side, were mounted to the tunnel side wall. The so-called forced-vibration method (which is not the forced-motion method applied in the experiments presented in the thesis at hand) requires a known sinusoidal excitation force, which was applied to the panel rear side by a shaker, and the measurement of the panel response. A piezoelectric mechanical impedance head recorded the response force and the acceleration. A phase meter was used for the measurement of the phase angle between force and acceleration signal. The mechanical impedance, the real part of which corresponds to the damping, was calculated by dividing the complex amplitudes of force and resulting velocity. By approaching the flutter boundary, the damping decreased successively and finally became zero at flutter onset. For the first time the flutter boundary could be determined, without actually reaching it, by that

non-destructive method. An advantage of the method is the possibility to monitor the aeroelastic system during the ongoing test. Occurring mode coalescence as well as single mode flutter and coupled mode flutter were determined (Figure 1.9).

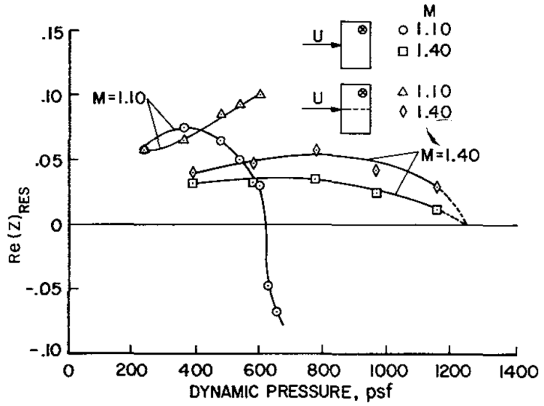

Figure 1.9.: Real component of panel mechanical impedance at resonance [47].

Further experiments concentrated, besides already mentioned parameters as the impact of the pressure differential, thermal loads and the air density, on the influence of the cavity depth on the eigenfrequencies of the test specimen. By studying also the influence of the flow boundary layer on panel flutter at $1.05 \leq M_\infty \leq 1.4$, Muhlstein et al. [8, 9] dedicated their work to a previously ignored experimental parameter. It was motivated by the fact that large boundary layer thicknesses occur for large launch vehicles and supersonic aircraft. The results obtained are still used for comparison with theory today. The test structures were made of magnesium alloy or invar and were milled from a single block of material. The resulting design was a panel with a surrounding integrated and stiff frame, which was attached to another frame that increased the frame stiffness and ensured high-quality mechanical boundary conditions. The sharp wedge shaped leading edge (splitter plate) of the panel support provided the adjustment of the boundary layer thickness by the variation of the distance between the leading edge and the wind tunnel wall. Retractable pressure probes were used for the measurement of the boundary layer properties. Since this experiment was a free flutter experiment, pneumatic flutter breaks were applied in the sealed panel cavity. Another possibility of stopping flutter, which was already done in prior activities, is the pressurization of the cavity. For the variation of the length-to-width ratio, the panel support was mounted onto a turntable, which could change the ratio to its reciprocal value. The test setup was equipped with capacitance-type displacement transducers, which produced an output voltage linear to the panel displacement, strain gauge differential pressure transducers for static pressure measurements for boundary layer thickness and panel surface, piezoresistive pressure transducers for dynamic pressure measurements and iron-constantan thermocouples for the determination of panel and frame temperatures. The flutter boundaries were established by increasing the dynamic pressure while the Mach number was kept constant. The results showed that the turbulent boundary layer has a considerable stabilizing

influence on the aeroelastic stability in the low supersonic Mach number range. That influence had its maximum at about $M_\infty = 1.2$ and was decreasing with further increasing Mach number. Results were compared to 3D unsteady potential flow theory [13, 48] with good agreements with experimental results extrapolated for a zero boundary layer thickness.

During the Apollo project, which was started in 1961, the Saturn V launcher brought twelve astronauts to the moon between 1968 and 1972 [43]. As done before for the Atlas Centaur launcher, panel flutter investigations were conducted e.g. on full-scale thirty degree segment models of the Saturn D-IVB stage Forward Skirt (Figure 1.10), which was the Saturn V third stage. The tests were performed at Arnold Engineering Development Center's Propulsion Wind Tunnel at low supersonic Mach numbers ($1.1 \leq M_\infty \leq 1.6$) [49–51]. The transonic continuous flow test facility provided a perforated wall test section. The test setup was floor-mounted and had a leading edge section which was borne by two struts along its longitudinal sides. The leading edge (boundary layer splitter plate), which was in some cases equipped with a boundary layer tripping device, was followed by a support that contained a cavity to which the test panel was attached.

In a first step, a rigid steel model with several rows of static pressure orifices was used to identify the static pressure distribution over the test panel and to measure the boundary layer characteristics. The boundary layer was identified by means of a rake with 26 total-pressure-lines. The flutter models, which were made of aluminum, were used for the determination of the flutter behavior for different axial compression loads and pressure differentials caused by the variation of the cavity pressure by injecting nitrogen. The panels were riveted to internal ring stiffeners and external stiffeners for longitudinal stiffness. The axial loads were applied by means of hydraulic jacks attached at the down-stream end of the model. Strain gauges were attached to the panels. Accelerometers and microphones, which were attached to the test specimen and the bottom of the cavity, recorded information about panel frequencies, noise levels in the boundary layer and in the cavity and the structure's acceleration. During the measurements, the flow conditions were kept constant, while load sweeps were done. Flutter conditions were found during most of the sweeps, whereas no flutter was found at zero axial loads. No structural failures due to flutter were detected. The measurements of boundary layer thickness and boundary layer displacement thickness showed almost no dependency on the Mach number and on the Reynolds number. Since the wind tunnel tests showed more severe conditions than the flight trajectory, failure during flight was excluded.

In 1972 the Space Shuttle project was started and along with that further activities on panel flutter investigation, which benefitted from afore-mentioned fundamental studies [9]. Continuative panel flutter studies on the thermal protection system (TPS) of the Space Shuttle were published, which emphasized once again the importance of stiffened panels and the correct alignment of the maximum bending stiffness in flow direction [53, 54]. The studies included wind tunnel tests at NASA Langley Research Center Unitary Plan Wind Tunnel at $M_\infty = 1.6$ with $p_0 = 70.6$ kPa and at $M_\infty = 2.0$ with $p_0 = 85.1$ kPa [55]. All-edge bolted aluminum panels (orthotropic due to different wavy surface stiffening-types) of different stiffness were installed on a turntable, which allowed

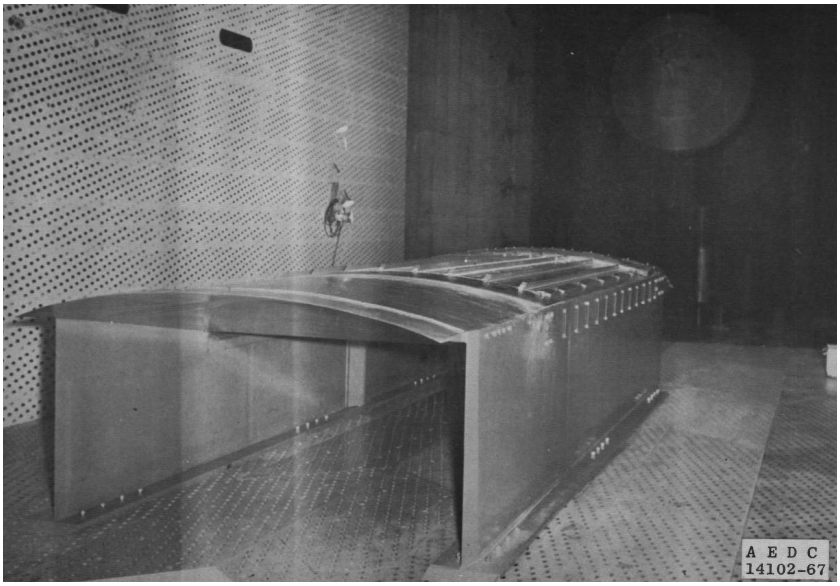

(a) Photograph of fixture with flutter panel installed in tunnel 16T [50].

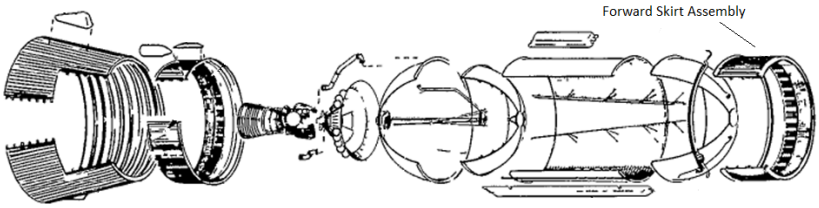

(b) Exploded view of S-IVB Stage for Saturn V [52]. Wind tunnel tests were conducted to qualify the Forward Skirt [51].

Figure 1.10.: Saturn V S-IVB stage experimental setup and exploded view.

the variation of the yaw angle. As seen before, a splitter plate leading edge ensured a boundary layer, which was free of wind tunnel wall influences and a pressurizable cavity was present at the panel's rear side. The instrumentation consisted of iron-constantan strain gauges to detect flutter onset and flutter frequency. During the flutter tests, uncertainties due to temperature-caused buckling were detected. Nevertheless, the establishment of the flutter boundary as a function of the yaw angle revealed a considerable influence of the angle on flutter behavior. The results showed the same behavior as seen before in case of flat unstiffened panels [5]. A panel corrugation aligned with the flow direction was recommended [56], since an increase of the flow component directed perpendicular to the corrugation increases flutter proneness.
Beginning at the start of the new millennium, studies were carried out dealing with the phenomenon of the so-called single-mode-flutter [57–60]. As afore-stated, panel flutter can emerge with either one aeroelastic mode's damping is decreasing or with a coalescence of two modes' damping is decreasing and finally vanishing. The wind tunnel

studies, performed in the perforated test section of the A-7 supersonic wind tunnel at the Institute of Mechanics of Lomonosov Moscow State University, were done in the transonic Mach number range at $0.85 \leq M_\infty \leq 1.3$ and at $M_\infty = 3.0$ (112 kPa $\leq p_0 \leq$ 142 kPa). The all-edge clamped plate model, which was a flat steel made plate welded on a rigid frame at all four edges, was designed for undergoing only single mode flutter. The support was fixed to the wind tunnel test section wall. Venting holes in a cavity beneath the plate were to equalize the pressure difference between the panel's rear side and the test section. The panel motion was measured by strain gauges on the rear surface of the structure, whereas pressure was measured by pressure gauges. The tunnel vibration was monitored to break down the different sources of vibration. Single mode flutter was detected at $1.2 \leq M_\infty \leq 1.3$.

In the recent past, investigations on aeroelastic stability of shell structures were published connected to the so-called Cryogenic Upper Stage Technologies (CUST) program, part of the Future Launcher Preparatory Program (FLPP) of the European Space Agency (ESA). The studied Versatile Thermal Insulation (VTI) panel's purpose was the insulation of the cryogenic tanks of the launcher's upper stage. Wind tunnel activities were carried out at the Czech Aerospace Research Center (VZLU) at $M_\infty = 0.776$ and $M_\infty = 1.729$ [61, 62]. Different 1/60 scale models, made of sandwich material, (180 and 45 degree cylinder segments), which had pinched mechanical boundary conditions, were tested. Rigid models were used to investigate the flow field conditions around the model by means of pressure transducers, whereas another active model with an actuator placed beneath was used for the evaluation of FSI methods. Afterwards, an aeroelastic model was used for flutter tests. It was found that accelerometers mounted to the thin skin panel seemed to influence the aeroelastic behavior. Since a high scaling of the test structures was necessary, the experimental results served mainly for the comparison with the simultaneously done theoretical activities rather than for the simulation of real flight conditions. Nevertheless, the analysis of the results suggested that the tested panel base line configuration had its stability boundary close to flight conditions at transonic Mach numbers.

During the last decades, several comprehensive survey reports were published to recap and summarize the done experimental and theoretical work on aeroelastic stability and in particular on panel flutter [11, 14, 16, 63, 64]. Several documents focus in particular on resulting criteria for aircraft and space vehicle design [12, 65, 66].

Obviously, a lot of experimental research has been carried out so far. Most of it focused on the measurement of the flutter boundaries for a multitude of different test structures. Flow conditions were set and the structure's behavior was measured. The experiment presented in this thesis shall allow a separate observation of the structure's motion and the arising pressure distribution by employing a forced motion experiment, which is described later. It allows the determination of the aeroelastic system's state during all subcritical, critical and supercritical conditions. Another advantage is aspired by spatial high resolution measurements, which shall give insight into the local fluidic phenomena occurring on the test structure. Besides, only few experiments were performed in the aimed Mach number range.

2. Theory

This chapter focuses on three main points: First, getting insight into the basic panel flutter mechanism, second, an introduction to the eigenfunctions of plates and third, an overview of the different approaches to calculate the aerodynamic loads for subsonic and supersonic flow conditions. Regarding the first, a theoretical approach is presented, which can be applied to supersonic flows and is based on the potential flow theory. The theory includes some of the parameters already introduced in the previous chapter. Those parameters' role in the aeroelastic system becomes clearer by knowing the corresponding equations. In addition, especially in the second part of this chapter about the eigenfunctions of plates, some important information on the design of the experimental setup is gained. The considerations carried out in the following section on the aeroelastic system is based on the work of Dowell [7], while the contemplations of the structure's characteristics in the second section are based on the work of Irretier [67]. The theoretical approaches presented in the third section are the potential theory for subsonic flows, the piston theory for supersonic flows and the traveling wave theory, which combines these two approaches.

The aeroelastic system is described in Equation 2.1 with terms referring to the structural forces on its left side, and a term for external pressure on its right side. The applied structural model describes the flat rectangular plate shown in Figure 1.2. This simple design of a plate or shell structure has one side exposed to the flow, whereas its back is facing a cavity. The structural model is expressed by the equation of the plate theory by Kirchhoff [68], which is a continuous system that does not consider shear deformations and rotational inertia and has a constant bending stiffness. In contrast to the illustrated case in Figure 1.2, the mathematical model shown here extends in x- and y-direction. The deflection d in z-direction depends on the time t and the coordinates x and y.

$$\underbrace{\overbrace{D\left(\frac{\partial^4 d}{\partial x^4}+2\frac{\partial^4 d}{\partial x^2\partial y^2}+\frac{\partial^4 d}{\partial y^4}\right)}^{\text{Elastic forces}}+\overbrace{\rho_s h\frac{\partial^2 d}{\partial t^2}}^{\text{Inertia forces}}}_{\text{Structural forces}}=\underbrace{-\Delta p(x,y,t)}_{\text{Aerodynamic forces}} \tag{2.1}$$

The external forces are expressed by the time- and location- dependent pressure Δp, which acts on the structure's surface. The terms of the equation's left side show on the one hand the inertia forces, which are depending on the structure's density ρ_s, the plate's thickness h and its time depending deflection. On the other hand, the elastic

forces are shown, which are caused by the structure's deflection and are multiplied by the plate's bending stiffness:

$$D = \frac{Eh^3}{12 \cdot (1 - \nu^2)} \tag{2.2}$$

For calculating the bending stiffness, the plate's Young's Modulus E and its material parameter ν, which is the Poisson's ratio, is required. The Kirchhoff theory plate exhibits strongly linear characteristics with regard to the deflections in z- direction and can be only applied for low ratios of the plate's thickness to its width and to its length. Both boundary conditions seem to be suitable here with regard to the experimental implementation.

2.1. The Aeroelastic System

The equilibrium of motion shown in Equation 2.1 can be written in its one dimensional form, which is sufficient for the considerations in this section:

$$D\frac{\partial^4 d}{\partial x^4} + \rho_{s,A}\frac{\partial^2 d}{\partial t^2} = -\Delta p(x,t) \tag{2.3}$$

The density $\rho_{s,A}$ of the second term on the equation's left side has the dimension mass per area. Using generalized coordinates q_n, where n denotes the system's n-th degree of freedom, the equation can also be written as follows:

$$M_n \left[\omega_n^2 q_n + \frac{d^2 q_n}{dt^2}\right] + Q_n = 0 \tag{2.4}$$

The generalized mass is denoted by M_n and the corresponding angular eigenfrequency is denoted by ω_n. The aerodynamic loads are included in the generalized aerodynamic forces Q_n:

$$Q_n = \int_0^l \Delta p \Psi_n dx \tag{2.5}$$

The eigenfunction of the plate's n-th mode is denoted by Ψ_n, which will be discussed in detail in the next section. The external loads Δp, which need to be integrated over the plate's length l, are defined as the pressure difference between the panel's top and its rear side. The so-called piston theory, which applies to supersonic flow $M_\infty > \sqrt{2}$ and is based on a linear theory by Lighthill [69] and Ashley [10], allows the exemplary

approximation of this pressure difference:

$$\Delta p = \frac{\rho_\infty U_\infty^2}{M_\infty} \left[\frac{\partial d}{\partial x} + \frac{1}{U_\infty} \frac{\partial d}{\partial t} \right] \tag{2.6}$$

The equation applied on a one dimensional plate shows a steady part, which takes into account the streamwise inclination $\frac{\partial d}{\partial x}$ of the structure, and an unsteady term that is containing the time depending structural deformation $\frac{\partial d}{\partial t}$ in z-direction. With increasing flow velocity U_∞, the second term is growing smaller and is eventually negligible so that only the steady term remains. However, with decreasing velocity the time depending term's influence is increased. By using generalized coordinates, the z-wise deflection d can be expressed as $q_n \Psi_n$. Inserting Equation 2.6 into Equation 2.5 leads to:

$$Q_n = \sum_m Q_{mn} = \sum_m \frac{\rho_\infty U_\infty^2}{M_\infty} \left[q_m \int_0^l \frac{\psi_m}{dx} \Psi_n dx + \frac{\dot{q}_m}{U_\infty} \int_0^l \Psi_m \Psi_n dx \right] \tag{2.7}$$

The resulting load for a modal degree of freedom (DOF) n of a system, which has multiple DOFs, shows shares of all considered degrees of freedom, which is indicated only in this section by the counter variable m. With $q_n = \bar{q}_n(x) e^{j\omega t}$ and $\bar{Q}_{mn} = \bar{q}_m \bar{\bar{Q}}_{mn}$, Equations 2.4 and Equations 2.5 result in

$$M_n \bar{q}_n \left[\omega_n^2 - \omega^2 \right] + \bar{Q}_n = 0 \tag{2.8}$$

and

$$\bar{\bar{Q}}_n = \sum_m \frac{\rho_\infty U_\infty^2}{M_\infty} \left[\int_0^l \frac{\Psi_m}{dx} \Psi_n dx + \frac{j\omega}{U_\infty} \int_0^l \Psi_m \Psi_n dx \right] \tag{2.9}$$

Due to the orthogonality of eigenfunctions, the dot products

$$\Psi_n \cdot \Psi_m = 0 \tag{2.10}$$

for $n \neq m$, and

$$\frac{\Psi_n}{dx} \cdot \Psi_m = 0 \tag{2.11}$$

for $n = m$ must be zero. The latter reflects the sinusoidal and thus symmetrical characteristic of the eigenfunctions of beams and plates, which are discussed in detail and

derived in Section 2.2. The generalized aerodynamic forces are simplified to:

$$\bar{\bar{Q}}_{11} = \frac{\rho_\infty U_\infty^2}{M_\infty} \frac{j\omega}{U_\infty} \int_0^l \Psi_1 \Psi_1 dx \tag{2.12}$$

$$\bar{\bar{Q}}_{22} = \frac{\rho_\infty U_\infty^2}{M_\infty} \frac{j\omega}{U_\infty} \int_0^l \Psi_2 \Psi_2 dx \tag{2.13}$$

$$\bar{\bar{Q}}_{21} = \frac{\rho_\infty U_\infty^2}{M_\infty} \int_0^l \frac{\Psi_2}{dx} \Psi_1 dx \tag{2.14}$$

$$\bar{\bar{Q}}_{12} = \frac{\rho_\infty U_\infty^2}{M_\infty} \int_0^l \frac{\Psi_1}{dx} \Psi_2 dx \tag{2.15}$$

The unsteady terms depend on only one of the respected eigenfunctions, whereas the steady terms couple the regarded degrees of freedom. The equation of motion (Equation 2.4) can be rewritten as:

$$\begin{bmatrix} M_1 \left[\omega_1^2 - \omega^2\right] + \bar{\bar{Q}}_{11} & \bar{\bar{Q}}_{21} \\ \bar{\bar{Q}}_{12} & M_2 \left[\omega_2^2 - \omega^2\right] + \bar{\bar{Q}}_{22} \end{bmatrix} \begin{bmatrix} \bar{q}_1 \\ \bar{q}_2 \end{bmatrix} = \begin{bmatrix} 0 \\ 0 \end{bmatrix} \tag{2.16}$$

This equation, which mathematically outlines main influencing variables and dependencies, shows the whole aeroelastic system depends strongly on the structure's eigenfreqencies and the generalized forces that are defined by the structure's eigenfunctions and the flow conditions. The two types of dynamic instability already introduced in the first chapter as Single Mode flutter and Coupled Mode flutter are now to be clarified by the equation at hand.
With increasing flow velocity, the generalized forces with $m = n$ grow small compared to those with $m \neq n$, which is why they can finally be neglected. In consideration of $\bar{\bar{Q}}_{21} = -\bar{\bar{Q}}_{12}$ (see Dowell [7]), the matrix can be solved for ω:

$$\omega^2 = \frac{\omega_1^2 + \omega_2^2}{2} \pm \sqrt{\left(\frac{\omega_1^2 - \omega_2^2}{2}\right)^2 - \frac{\bar{\bar{Q}}_{21}^2}{M_1 M_2}} \tag{2.17}$$

With increasing dynamic pressure $q_\infty = \frac{\rho_\infty U_\infty^2}{2}$, the second term of the square root is increasing. Finally, the entire root term becomes zero, once the critical dynamic pressure $q_{\infty,crit}$ is reached. At this point, the two resulting eigenfrequencies have the same value, which is purely real in the described case. By increasing the dynamic pressure further, the root term becomes negative leading to complex eigenfrequencies. One of the

eigenfrequencies has a negative imaginary part, which indicates Coupled Mode flutter. In order to deal with the second type of instability, the simple one degree of freedom system is applied as described in Equation 2.8. With view on the low supersonic domain, the forces with $n = m$, which are neglected in the first example, now have a considerable influence on the aeroelastic system. In contrast to the forces' coupling terms, these forces are purely imaginary complex numbers, which depend on the frequency ω:

$$\omega^2 = \omega_1^2 + \frac{\bar{\bar{Q}}_{11}(\omega)}{M_1} \tag{2.18}$$

Since $\bar{\bar{Q}}_{11} = \Im(\bar{\bar{Q}}_1)$, a negative aerodynamic force induces Single Mode flutter. According to the piston theory, which is used here for the calculation of the aerodynamic loads, only positive aerodynamic forces are allowed. The result is a damping of the single mode approach shown here. Further theories, which are based on the linearized potential flow theory, apply here and allow also negative aerodynamic forces [7].

2.2. Plate Theory

2.2.1. Equation of Motion

The previous section has shown that the arising aerodynamic forces strongly depend on the structure's mode shapes and their derivatives with respect to time and spatial coordinates. To continue the theoretical considerations, this section presents the derivation of the eigenmode shapes of a flat rectangular plate, as shown in Figure 2.1.

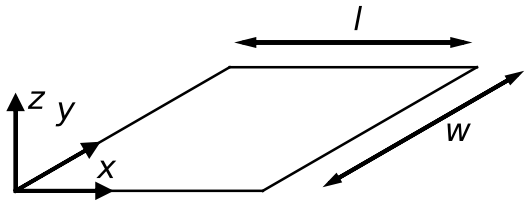

Figure 2.1.: Flat rectangular plate of length l and width w.

The information is decisive in order to design the experimental setup, as will be shown in the next chapter. By discarding the external loads $p(x, y, t)$ and choosing a harmonic approach for the z-wise deformation $d(x, y, t) = \hat{d}(x, y)sin(\omega t)$, the homogeneous plate equation based on Equation 2.1 can be expressed as:

$$\frac{\partial^4 \hat{d}}{\partial x^4} + 2\frac{\partial^4 \hat{d}}{\partial x^2 \partial y^2} + \frac{\partial^4 \hat{d}}{\partial y^4} - \omega^2 \frac{\rho_s h}{D}\hat{d} = 0 \tag{2.19}$$

By separating the differential equation into its time depending part and its position function, a solution of the latter for the coordinate x is

$$\hat{d}(x) = \hat{d}_A cos(vx) + \hat{d}_B sin(vx) + \hat{d}_C cosh(vx) + \hat{d}_D sinh(vx) \tag{2.20}$$

whose parameters $\hat{d}_n$ are to be determined by the application of the particular mechanical boundary conditions from which the eigenfunctions can be derived. The derivation of this function, which is also used for the y-coordinate, can be looked up in [67].

2.2.2. Eigenfunctions

As already mentioned, the full position function of the plate's equation of motion can be expressed as $\hat{d}(x, y) = \hat{d}(x)\hat{d}(y)$, where both functions depend on only one of the spatial variables and are of the same type that is shown in Equation 2.20. In order to simplify the next steps, it is therefore sufficient to consider only one of the functions in the following. Structures that were of particular interest in mentioned past experiments are plates with clamped MBCs at their four edges. An advantage of those structures is that the boundary conditions can be implemented well in the manufacturing processes. In order to determine the eigenfunctions, which describe the structure's eigenmode shapes, a consideration of the MBCs is to be carried out. In the first step no translation is permitted at the leading and the trailing edges, as shown in Equation 2.21 and Equation 2.22:

$$\hat{d}(x = 0, y) = 0 \tag{2.21}$$

$$\hat{d}(x = l, y) = 0 \tag{2.22}$$

Further, the clamped conditions do not allow rotation around the y-axis and admit thus a bending of the structure. Consequently, an inclination of zero occurs at the structure's edges, which is shown in Equation 2.23 and Equation 2.24:

$$\frac{\partial \hat{d}}{\partial x}(x = 0, y) = 0 \tag{2.23}$$

$$\frac{\partial \hat{d}}{\partial x}(x = l, y) = 0 \tag{2.24}$$

In order to implement those conditions, the first derivative of the equation of motion's solution with respect to x is required:

$$\frac{\partial \hat{d}(x)}{\partial x} = -v\hat{d}_A sin(vx) + v\hat{d}_B cos(vx) + v\hat{d}_C sinh(vx) + v\hat{d}_D cosh(vx) \tag{2.25}$$

The stated boundary conditions lead to four equations

$$\hat{d}_A + \hat{d}_C = 0 \tag{2.26}$$

$$\hat{d}_A cos(vl) + \hat{d}_B sin(vl) + \hat{d}_C cosh(vl) + \hat{d}_D sinh(vl) = 0 \tag{2.27}$$

$$v\hat{d}_B + v\hat{d}_D = 0 \tag{2.28}$$

$$-v\hat{d}_A sin(vl) + v\hat{d}_B cos(vl) + v\hat{d}_C sinh(vl) + v\hat{d}_D cosh(vl) = 0 \tag{2.29}$$

that result in a matrix

$$\begin{bmatrix} 1 & 0 & 1 & 0 \\ cos(vl) & sin(vl) & cosh(vl) & sinh(vl) \\ 0 & 1 & 0 & 1 \\ -sin(vl) & cos(vl) & sinh(vl) & cosh(vl) \end{bmatrix} \begin{bmatrix} \hat{d}_A \\ \hat{d}_B \\ \hat{d}_C \\ \hat{d}_D \end{bmatrix} = \begin{bmatrix} 0 \\ 0 \\ 0 \\ 0 \end{bmatrix} \tag{2.30}$$

whose determinant is to be calculated. The resulting eigenvalues $v_i l$ cannot directly be calculated, but must be determined numerically:

$$v_1 l = 4.7300 \tag{2.31}$$

$$v_2 l = 7.8532 \tag{2.32}$$

$$v_3 l = 10.9956 \tag{2.33}$$

Three of the four parameters $\hat{d}_A$ to $\hat{d}_D$ can now be expressed as a function of the forth one. By normalizing the resulting equation with the remaining parameter the solution, where i is the number of eigenvalue, is:

$$\hat{d}_i^*(x) = cos(v_i x) - cosh(v_i x) - \tau_i(sin(v_i x) - sinh(v_i x)) \tag{2.34}$$

with

$$\tau_i = \frac{cos(v_i l) - cosh(v_i l)}{sin(v_i l) - sinh(v_i l)} \tag{2.35}$$

The shown procedure is also performed for $\hat{d}(y)$ which allows to complete the plate's eigenfunctions, which describe the plate's eigenmode shapes. Following, the eigenmodes $\Psi_{ij} = \hat{d}_i^*(x) \cdot \hat{d}_j^*(y)$ for the three calculated eigenvalues are presented, which are also

shown in Figure 2.2. In order to shorten the terms it applies $c = cos$ and $s = sin$.

$$\Psi_{11} = \left[c(4.73\frac{x}{l}) - ch(4.73\frac{x}{l}) - 0.9825\left(s(4.73\frac{x}{l}) - sh(4.73\frac{x}{l})\right)\right] \left[c(4.73\frac{y}{w}) - ch(4.73\frac{y}{w}) - 0.9825\left(s(4.73\frac{y}{w}) - sh(4.73\frac{y}{w})\right)\right] \tag{2.36}$$

$$\Psi_{21} = \left[c(7.8532\frac{x}{l}) - ch(7.8532\frac{x}{l}) - 1.0008\left(s(7.8532\frac{x}{l}) - sh(7.8532\frac{x}{l})\right)\right] \left[c(4.73\frac{y}{w}) - ch(4.73\frac{y}{w}) - 0.9825\left(s(4.73\frac{y}{w}) - sh(4.73\frac{y}{w})\right)\right] \tag{2.37}$$

$$\Psi_{31} = \left[c(10.996\frac{x}{l}) - ch(10.996\frac{x}{l}) - 0.9999\left(s(10.996\frac{x}{l}) - sh(10.996\frac{x}{l})\right)\right] \left[c(4.73\frac{y}{w}) - ch(4.73\frac{y}{w}) - 0.9825\left(s(4.73\frac{y}{w}) - sh(4.73\frac{y}{w})\right)\right] \tag{2.38}$$

It should be noted that another and simply cosine approach is an adequate approximation to describe the first clamped mode:

$$\Psi_{11} = \frac{1}{4}\left(1 - cos\left(\frac{2\pi x}{l}\right)\right)\left(1 - cos\left(\frac{2\pi y}{w}\right)\right) \tag{2.39}$$

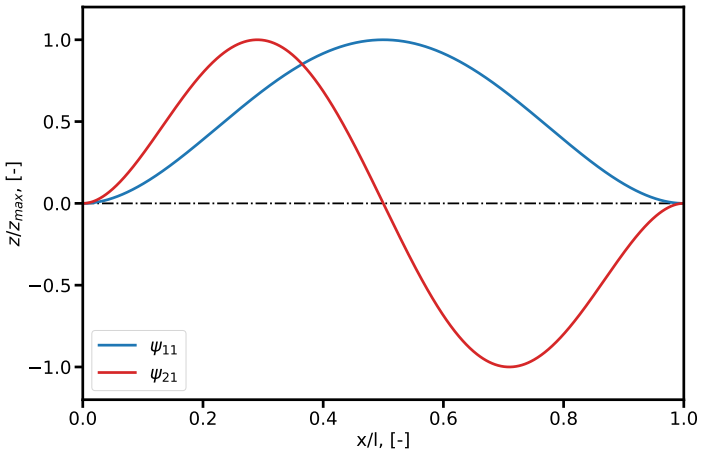

Figure 2.2.: First three 1D mode shapes of a flat plate with clamped MBCs.

2.3. Unsteady Aerodynamics

In the first section of this chapter the generalized aerodynamic forces were introduced, calculated based on the pressure according to the piston theory. The anticipation of that supersonic theory was necessary to present the aeroelastic system and its basic characteristics. The following section deals in more detail with the calculation of the resulting pressure. First, a method based on potential flow theory covering the subsonic domain is presented, which is followed by additional information on the piston theory for supersonic conditions. Based on the findings of these approaches, another theory, based on the superposition on two traveling waves, is described that improves the previous theories and brings the theoretical considerations of the present thesis to an end.

2.3.1. Subsonic Potential Flow Theory

Corresponding to the already presented piston theory, which allows the calculation of the aerodynamic loads in the supersonic Mach number range, this approach is applied to the subsonic range $M_\infty < 1$. The potential flow theory is based on the assumption of a flow free of rotation and friction, with the Bernoulli equation to determine the pressure. The method, which is based on this theory and used in the present work to validate the subsonic flow measurements, follows Dowell's "plates and shells" as also done for the calculations at supersonic conditions [7]:

$$\Delta p_{sub,i}(x,t) = \rho_\infty U_\infty^2 \frac{\hat{A}l}{2\pi}\left[\frac{\partial^2\Psi_i(x)}{\partial x^2} + j\omega\frac{2}{U_\infty}\frac{\partial\Psi_i(x)}{\partial x} - \omega^2\frac{\Psi_i(x)}{U_\infty^2}\right] \tag{2.40}$$

First of all, a division of the pressure by the dynamic pressure q_∞ results in the non-dimensional pressure coefficient:

$$c_{p,sub,i}(x,t) = \frac{\hat{A}l}{\pi}\left[\overbrace{\frac{\partial^2\Psi_i(x)}{\partial x^2}}^{\Re} + \overbrace{j\omega\frac{2}{U_\infty}\frac{\partial\Psi_i(x)}{\partial x}}^{\Im} - \overbrace{\omega^2\frac{\Psi_i(x)}{U_\infty^2}}^{\Re}\right] \tag{2.41}$$

The first and the third term of the equation correspond to the real part of the complex pressure, whereby the latter indicates the inertia forces of the moving structure that strongly decrease with increasing flow velocity. Consequently, the dominant part at high Mach numbers is the first term, which is based on the second derivative of the structure's eigenfunction with respect to x representing its curvature. Assuming a sinusoidal structural deformation, the resulting dominant real and imaginary parts must have characteristics as described below:

$$\Re(c_{p,sub,i}) \sim \frac{\partial^2\psi_i(x)}{\partial x^2} \sim -sin(i\pi\frac{x}{l}) \tag{2.42}$$

In the same way, the following applies to the imaginary part:

$$\Im(c_{p,sub,i}) \sim \frac{\partial \Psi_i(x)}{\partial x} \sim cos(i\pi \frac{x}{l}) = sin(\frac{\pi}{2} + i\pi \frac{x}{l}) \tag{2.43}$$

Since the assumption of a sinusoidal structural deformation is not completely correct with respect to the eigenfunctions presented in the Equations 2.36 to 2.38, the resulting real part presented in Figure 2.3 differs from that at the LE and the TE. Neglecting this, the pressure's real part is shifted $\Delta\varphi_x = \pi$ compared with the structural deformation as it is assumed in Equation 2.42. As expected in Equation 2.43, the imaginary part is a pure sine function.

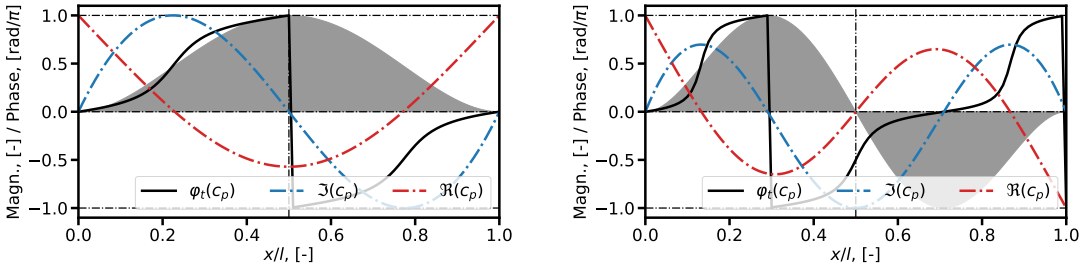

(a) First streamwise mode shape; Ψ_{11}.

(b) Second streamwise mode shape; Ψ_{21}.

Figure 2.3.: Analytic approach of induced aerodynamic response due to structural eigenfunctions with potential flow theory equation for subsonic flow with $\frac{\omega}{2\pi} = 22.5$ Hz.

By using the Prandtl-Glauert Transformation for the subsonic flow [70, 71]

$$\beta_{sub} = \sqrt{1 - M_\infty^2} \tag{2.44}$$

the pressure coefficient can be determined as follows:

$$c_{p,sub,i}(x,t) = \frac{\hat{A}l}{\pi\beta_{sub}} \left[\frac{\partial^2 \Psi_i(x)}{\partial x^2} + j\omega \frac{2}{U_\infty} \frac{\partial \Psi_i(x)}{\partial x} - \omega^2 \frac{\Psi_i(x)}{U_\infty^2} \right] \tag{2.45}$$

This way, a correct calculation is possible beyond $M_\infty = 0.3$, but loses its validity for $M_\infty \geq 0.7$, which is the lowest Mach number set in the coming experiments. The equation shows a singularity at $M_\infty = 1.0$ (Prandtl-Glauert singularity), which proves its inadequacy for this particular Mach number [70] and is depicted in Figure 2.5. The figure shows the resulting real and imaginary parts with and without Prandtl-Glauert transformation. Without the transformation, the real part quickly approaches the limit

value defined by the structure's curvature after the inertia forces' influence at very low Mach numbers has decreased. The imaginary part decreases due to the division by U_∞^2, while the second relevant factor, the frequency, is kept constant in this figure. The transformation by β_{sub} leads to an increase of both real and imaginary part with increasing Mach number that eventually leads to the singularity at $M_\infty = 1.0$.

2.3.2. Piston Theory

The piston theory has already been introduced in the first section of this chapter presenting the general aeroelastic system. Equation 2.6, which describes the calculation of the pressure difference between the panel's back and its flow faced surface, can be rewritten as:

$$c_{p,sup.i} = 2\frac{\hat{A}}{M_\infty}\left[\frac{\partial \Psi_i}{\partial x} + \frac{j\omega}{U_\infty}\Psi_i\right] \tag{2.46}$$

By dividing the equation by the dynamic pressure, the non-dimensional pressure coefficient $c_{p,sup,i}$ related to the particular panel's deflection shape Ψ_i (which is an eigenfunction, which is an eigenmode shape) results. Using a harmonic deformation approach, the equation's real part, which is described by its first term, corresponds to the equation of Ackeret that is formulated for flows over wavy walls [70]. By assuming a sinusoidal shape, the resulting real part of the complex pressure coefficient is *cos*-shaped, due to its derivative with respect to x. This means a spatial phase shift between the structural deformation and the induced pressure of $\Delta\varphi_x = \pi/2$.

$$\Re(c_{p,sup,i}) \sim \frac{\partial \Psi_i(x)}{\partial x} \sim cos(i\pi\frac{x}{l}) \tag{2.47}$$

The equation's second term describes the pressure's imaginary part, whose temporal phase shift of $\Delta\varphi_t = -\pi/2$ is caused by the derivation with respect to time. The resulting characteristic over the panel's length has the same shape as the underlying eigenfunction of the structure:

$$\Im(c_{p,sup,i}) \sim \Psi_i(x) \sim sin(i\pi\frac{x}{l}) \tag{2.48}$$

Being aware of these simple facts will later help to understand and compare the measured results. Figure 2.4 illustrates the imaginary and the real pressure parts over panel deflections in the first and the second streamwise mode shape with clamped conditions. The imaginary part's characteristic is equal to that of the structure's shape, whereas the real part has sinusoidal properties that are positive at the positive slope of the deformation and becomes negative when that slope becomes negative. The depicted phase angle $\varphi_t(c_p)$ represents the difference between the pressure's temporal phase angle and that of the structure's motion. Due to the known limitation of Mach number validity

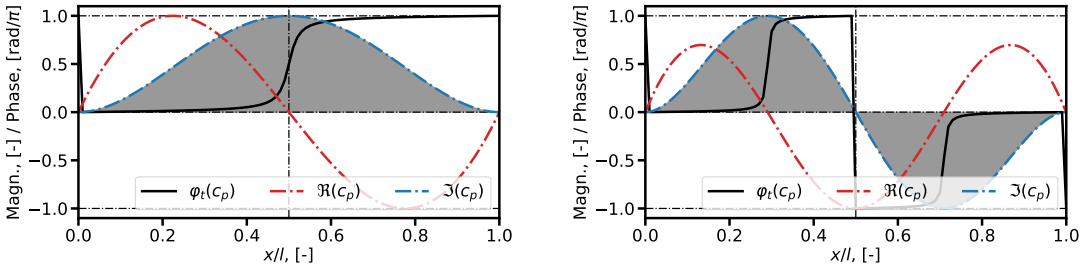

(a) First streamwise mode shape; Ψ_{11}.

(b) Second streamwise mode shape; Ψ_{21}.

Figure 2.4.: Analytic approach of aerodynamic response due to induced mode shapes with piston theory equation for supersonic flow with $\frac{\omega}{2\pi} = 22.5$ Hz.

range of the theory, this approach can also be extended by a transformation term for supersonic flows:

$$\beta_{sup} = \sqrt{M_\infty^2 - 1} \tag{2.49}$$

The resulting equation has an advanced validity for low supersonic flow conditions:

$$\Delta c_{p,sup,i}(x,t) = \frac{2\hat{A}}{\sqrt{M_\infty^2 - 1}} \left(\frac{\partial \Psi_i}{\partial x} + \frac{M_\infty^2 - 2}{M_\infty^2 - 1} \frac{1}{U_\infty} \frac{\partial \Psi_i}{\partial t} \right) \tag{2.50}$$

For supersonic Mach numbers, Figure 2.5 shows the results of the piston theory with and without the Prandtl-Glauert correction for one exemplary excitation frequency. The illustrated pressure coefficient $\bar{c}_p$ is the pressure coefficient multiplied by the factor $l/\hat{A}$, where $\hat{A}$ is the eigenfunction's amplitude.
The uncorrected real part results are equal to those resulting from the potential flow theory, whereas the corrected results start at $M_\infty = 1.0$ in the singularity and decrease with increasing Mach number. The imaginary part, which depends on the excitation frequency, is strongly decreasing in its uncorrected form and in its corrected form with increasing Mach number. The decreasing characteristic is intensified by the Prandtl-Glauert transformation.

2.3.3. Traveling Wave Theory

The third theoretical approach is based on the assumption that standing waves, as the oscillating panel is, can be described by one upstream traveling wave and another downstream traveling wave of the same magnitude and propagation speed [7, 11, 72]. With this approach, the structural deformations and the induced aerodynamic responses can be calculated for both subsonic and supersonic flow conditions. This approach requires both a harmonic oscillating time dependency as well as a harmonic oscillation

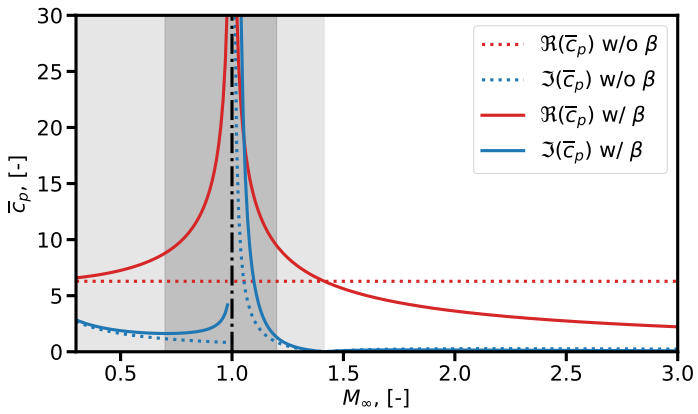

Figure 2.5.: Pressure coefficient versus (normalized) Mach number; Potential flow theory for subsonic Mach numbers and piston theory for supersonic Mach numbers; $\frac{\omega}{2\pi} = 45.0$ Hz.

with respect to the spatial coordinate x. Thus, the first eigenfunction of the clamped panel, which is used in this example, is considered being:

$$\Psi_1(x,t) = \frac{sin(-\frac{\pi}{2} + 2\pi\frac{x}{l}) - sin(-\frac{\pi}{2})}{2} sin(\omega t) \tag{2.51}$$

This shape that has a harmonic time dependency can be described by two traveling waves $\Psi_{1,\oplus}(x,t)$ and $\Psi_{1,\ominus}(x,t)$:

$$\Psi_{1,\oplus}(x,t) = \frac{1}{4} sin(\omega t + 2\pi\frac{x}{l}) - \frac{1}{4} sin(\omega t) \tag{2.52}$$

$$\Psi_{1,\ominus}(x,t) = \frac{1}{4} sin(-\omega t + \pi + 2\pi\frac{x}{l}) - \frac{1}{4} sin(-\omega t + \pi) \tag{2.53}$$

The following descriptions focus on the first sine functions of the two equations, whereas the second functions are required only for fulfilling the clamped MBCs. The direction of travel is given by the algebraic sign of the time depending terms, while the opposing spatial phase angles are denoted by the second terms of Equation 2.52 and Equation 2.53. The resulting pressure can be described in the same way. The estimation of the pressure's characteristics under subsonic and supersonic flow conditions and the determination of the respective magnitude are based on the findings of the previous sections. Consequently, the two traveling waves, whose superposition results in the arising pressure

coefficient c_{p1}, can be written as follows:

$$c_{p1,\oplus}(x,t) = |c_{p\oplus}|sin(\omega t + \pi + d\varphi_x + 2\pi\frac{x}{l}) \tag{2.54}$$

$$c_{p1,\ominus}(x,t) = |c_{p\ominus}|sin(-\omega t + d\varphi_x + 2\pi\frac{x}{l}) \tag{2.55}$$

The spatial phase shift $d\varphi_x$ depends on whether supersonic or subsonic flow conditions are present:

$$d\varphi_{x,sub} = -\pi \tag{2.56}$$

$$d\varphi_{x,sup} = \pi/2 \tag{2.57}$$

For equal magnitudes $|c_{p,1,\oplus}| = |c_{p,1,\ominus}|$ another standing wave results, which is spatially shifted relative to the standing wave describing the structural deformation. These amplitudes are based on the theory by Ackeret [70], which considers no time depending terms of the pressure. Depending on excitation frequency, a propagation velocity of the traveling waves results. By considering that, effective Mach numbers M_{eff} are to be calculated that differ from M_∞:

$$M_{eff,\oplus} = M_\infty + \frac{f_{exc}l}{i\sqrt{\gamma RT}} \tag{2.58}$$

$$M_{eff,\ominus} = M_\infty - \frac{f_{exc}l}{i\sqrt{\gamma RT}} \tag{2.59}$$

Figure 2.5 illustrates clearly that by using the Prandtl-Glauert transformation the resulting pressure amplitude is a function of the Mach number. Thus, an increasing frequency means that the initial properties of the superposed standing wave give way to those of a traveling wave. The direction of travel is determined by that traveling wave showing the dominant amplitude. Due to the different effective velocities, each wave has its singularity at another free stream Mach number as described in Equation 2.60 and Equation 2.61:

$$M_{crit,\oplus} = 1. - \frac{f_{exc}l}{i\sqrt{\gamma RT}} \tag{2.60}$$

$$M_{crit,\ominus} = 1. + \frac{f_{exc}l}{i\sqrt{\gamma RT}} \tag{2.61}$$

This means on the one hand that an upstream traveling wave reaches $M = 1.0$ with the free stream conditions still being subsonic. On the other hand, a downstream traveling wave still shows subsonic conditions, although the free stream conditions are supersonic. With regard to the discussed spatial phase shift $d\varphi_x$, the waves show the change from subsonic to supersonic phase characteristics at different free stream Mach numbers depending on the excitation frequency. The example in Figure 2.6 (a) shows the superposed waves at an excitation frequency of $f_{exc} = 45.0$ Hz. The domain to the left of the critical Mach number of the upstream traveling wave shows completely subsonic characteristics for each of the traveling waves and the superposed wave. However, the domain to the right of the downstream traveling wave's critical Mach number shows purely supersonic characteristics for both the traveling waves and the resulting wave. In addition, a domain close to $M_\infty = 1.0$ is present, where the upstream part already has passed the sound barrier, while the downstream wave still has subsonic conditions.
Figure 2.6 (b) shows the corresponding partition of the pressure in its real and its imaginary parts. For the Mach numbers that show the strongest differences between the magnitudes of the two traveling waves and thus the most significant resulting traveling wave characteristics, the imaginary parts have a maximum. Apart from the two occurring peaks, the real part and the imaginary part correspond to the results obtained in the previous sections for subsonic and supersonic Mach numbers.

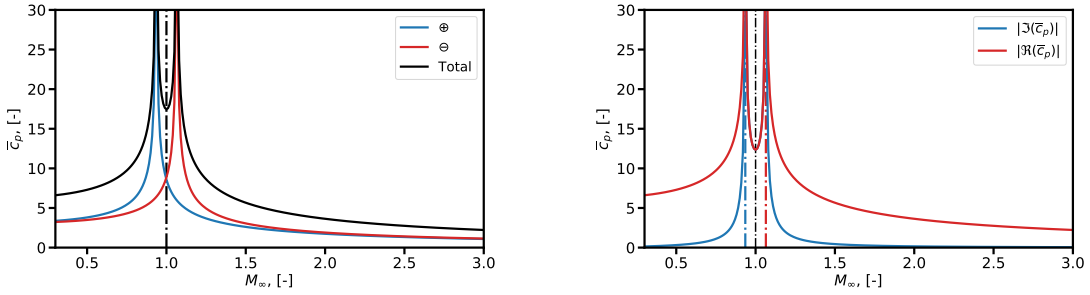

(a) Superposed amplitudes of upstream and downstream traveling waves.

(b) Real and imaginary parts of the resulting amplitudes.

Figure 2.6.: Amplitudes of two counteracting traveling waves at $\frac{\omega}{2\pi} = 45.0$ Hz.

Following the discussion on the global pressure characteristics resulting from the traveling waves approach, a look is taken at the local pressure distribution over the moving structure for the four different Mach number domains obtained. For comparison with the above presented results for the first streamwise mode shape in Figure 2.3 (a) and Figure 2.4 (a), Figure 2.7 shows results of the purely subsonic Mach number domain ($M_\infty < 0.85$) and the purely supersonic Mach number domain ($M_\infty > 1.15$). The subsonic case in the left picture corresponds almost completely with the results of the potential flow theory, although the real part at the LE and the TE deviate due to the slightly different assumed structural deformation (Equation 2.38 and Equation 2.39). The comparison of the supersonic case with that resulting from the piston theory shows

an agreement of the real parts, whereas differences in the imaginary parts are obvious. In addition to the differences close to the TE and the LE, the imaginary part shows a change in the sign, which is noticed and will be of importance for the presentation of the results at the end of this thesis.

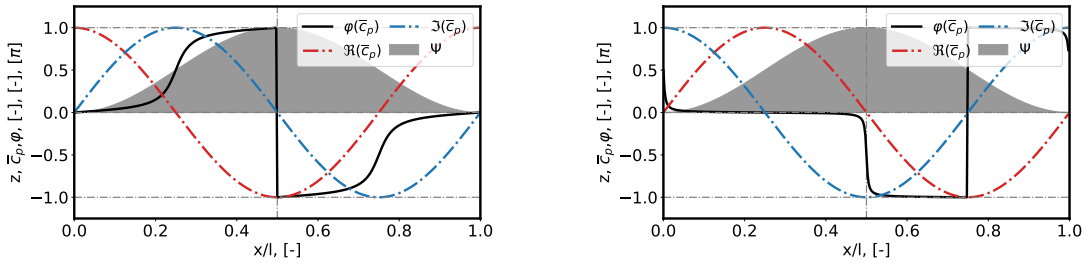

(a) Ψ_{11}; Subsonic.

(b) Ψ_{11}; Supersonic.

Figure 2.7.: Analytic approach with traveling wave equations.

The results shown so far are calculated for domains with both waves showing either subsonic or supersonic characteristics. Figure 2.8 shows the state in between, which is limited by the two critical Mach numbers. Each of the two depicted cases shows the imaginary part and the real part of the pressure. The depicted spatial phases differ from all the cases previously presented. Figure 2.8 (a) shows the pressure distribution occurring for flow properties between the critical Mach number of the upstream traveling wave and sonic free stream conditions. An oscillating structure induces a pressure with a dominant magnitude of the upstream directed wave, whereas the downstream fraction remains small. The depicted local temporal phase angle φ_t between the structure's oscillation and the pressure maintains its positive slope, which is also observed for low subsonic conditions. In contrast, Figure 2.8 (b) shows a negative slope of the local

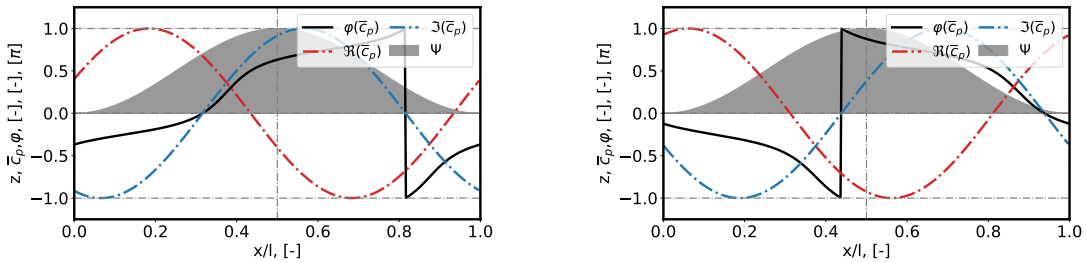

(a) Ψ_{11}; High subsonic.

(b) Ψ_{11}; Low supersonic.

Figure 2.8.: Analytic approach with traveling wave equations.

phase angle, which also occurs under high supersonic conditions. The spatial phase angles φ_x of the two traveling waves remain almost constant, only the ratio between their magnitudes is reversed.

3. Experimental Conception

On the one hand, the upcoming test setup must be suited to the objectives defined in Section 1.2, which include the variation of the mentioned fluidic and structural parameters and the forced motion based experimental principle. On the other hand, the facility should allow studies to be carried out with a focus on further structural and fluidic parameters. Parameters are therefore to be figured out and anticipated to design a setup that is suitable also for future activities. As the literature review of the introducing chapter has shown, extensive experimental research on the present topic is published hitherto. The references on experimental studies as well as to publications on theoretical considerations are used in this section to define further important parameters and to work out the setup design. The conceptual study at hand comprises the following points:

- Specification of aerodynamic parameters, which are based on the demand to conduct an experiment in the high subsonic and low supersonic Mach number range in consideration of the boundary layer's influence.
- Specification of structural parameters on the basis of a comprehensive literature study and under consideration of manufacturing aspects and the feasibility concerning the available test facility.
- Based on advantages and disadvantages of previous test setup conceptions and with respect to the objective at hand, a new design approach is derived.

3.1. Fluid Mechanical Parameters

As already introduced in Section 1.4 and Section 1.2, it is common use to establish the flutter boundary by the variation of the dynamic pressure

$$q_\infty = \frac{\rho_\infty U_\infty^2}{2} \tag{3.1}$$

that is a measure for the aerodynamic loads, calculated with the fluid density ρ_∞ and the fluid velocity U_∞. Often, the non-dimensional expression of the dynamic pressure

$$\lambda = \frac{\rho_\infty {U_\infty}^2 l^3}{D} \tag{3.2}$$

is used, which includes the structural parameters bending stiffness D and panel length l. Once a certain magnitude of dynamic pressure $q_{\infty,crit}$ is reached, a strong increase in the panel's deflection amplitude $\hat{A}$, which clearly stands out from the noise induced deflections, arises that indicates the flutter onset. Figure A.1 in the appendix depicts that phenomenon by showing the panel deflection normalized by the panel thickness h, as a function of the dynamic pressure. Examples for the usage of the non-dimensional dynamic pressure are illustrated in Figure 1.3 and Figure 1.4. One way to rise the dynamic pressure in an experimental facility is to increase the test section's total pressure p_0, which induces an increased density of the fluid. Another way is to increase directly the free stream velocity in the test section. In case the particular test facility has no velocity control, the Mach number is to be adjusted. The Mach number

$$M_\infty = \frac{U_\infty}{a} = \frac{U_\infty}{\sqrt{\gamma R_s T_0}} \tag{3.3}$$

is defined as the ratio of the free stream velocity to the speed of sound a. γ denotes the heat capacity ratio and R_s denotes the specific gas constant of air. Assuming a constant fluid total temperature T_0, this ratio only depends on the free stream velocity. Another dimensionless quantity is the Reynolds number

$$Re = \frac{U_\infty L}{\nu} = \frac{U_\infty L \rho_\infty}{\eta} \tag{3.4}$$

with L being the characteristic length, η the dynamic viscosity of the fluid and ν the fluid's kinematic viscosity. Consequently, the Reynolds number, which is the ratio of the fluid's inertia forces to its viscous forces, can be adjusted by changing either the Mach number

$$Re(M_\infty) = \frac{a M_\infty L \rho_\infty}{\eta} \tag{3.5}$$

or the total pressure:

$$Re(p_0) = \frac{U_\infty L p_0}{\eta T_\infty R_s} \left(1 + \frac{\gamma - 1}{2} M_\infty^2\right)^{\frac{-\gamma}{\gamma - 1}} \tag{3.6}$$

Its meaning in connection with the fluid's boundary layer will be of interest later in this thesis in Section 3.3.

3.2. Forced Motion Approach

Most experiments performed hitherto were based on the determination of the critical dynamic pressure for a wide range of Mach numbers and dynamic pressures. Panels showing numerous structural parameters concerning geometry and material were subject to those parameter studies. By the variation of pressure and velocity, as described in the previous section, the focus was on establishing a flutter boundary based on the aeroelastic system's conditions "flutter" and "no flutter". Different characteristics and phenomena, such as Single Mode Flutter and Coupled Mode Flutter, are distinguishable after flutter starts. However, changes in the conditions of the still stable aeroelastic system, which occurred while the parameters were adjusted, remained unrecognized. From this point of view, a more sophisticated approach was done by Muhlstein's forced vibration method [47], which is based on the determination of the change in the system's damping during the pre-flutter phase.
Another approach working without exceeding the critical stability conditions, which is called forced-motion method, is used in the present experimental activities. This method offers the possibility to investigate the unsteady aerodynamics of an aeroelastic system without considering the structural dynamics. The latter is completely defined by an actuator mechanism which deforms the test structure and thus ignoring its actual material properties. The approach is based on the determination of aerodynamic forces, derived from the measured pressure, which is induced by the actuator driven structural deformations. Based on those deformations and the aerodynamic loads, the transfer of energy between the structure and the fluid can be studied. This can be done by the determination of the generalized aerodynamic forces, which were introduced in Chapter 2. Here, the force's dependence on the excitation frequency, the structure's shape and the flow conditions are described.
Referring to Dowell [73], a flow field in the low supersonic Mach number domain gives rise to phase shifts between aerodynamic force and panel deformation, which cause a negative aerodynamic damping of one specific panel mode. This phenomenon is referred to as Single Mode Flutter. It is further mentioned that the region of this single-degree-of-freedom instability is limited to $M_\infty < 1.5$ [13]. However, this does not mean no Coupled Mode Flutter, which is observed at high supersonic speeds, can arise here [73]. Muhlstein [8, 47] and Hashimoto [17] showed experimental and theoretical results that prove that statement. Muhlstein showed arising flutter, which includes only the plate's first bending mode, at low supersonic flow, at $M_\infty = 1.1$. For increased Mach numbers, at $M_\infty = 1.4$, a coalescence of the first two modes was extrapolated. Referring to Hashimoto, panel flutter occurs mainly in the first structural eigenmode shape in the low supersonic flow region ($1.0 \leq M_\infty \leq 1.4$) [17]. At higher Mach numbers, a coalescence of the first and the second streamwise bending mode was observed. According to Vedeneev [60], Single Mode Flutter of the first bending mode typically emerges in the low supersonic domain at $1.0 \leq M_\infty \leq \sqrt{2}$, although Coupled Mode Flutter is not impossible in that domain. Alder [74] showed the transition from Single Mode Flutter at low supersonic speeds to Coupled Mode Flutter by increasing the Mach number.
Regarding the flow conditions, a wind tunnel is chosen in the present activities that

provides the needed low supersonic Mach number range. Since this test facility already provides a control of the flow parameters, this no longer needs to be considered in the design of the actual test setup. Based on the mentioned investigations, it is concluded that the mode shapes to be considered for the experimental activities are the first two streamwise-directed bending modes. Section 2.1 comprehensively describes the eigenfunctions of plates Ψ_{ij}, which correspond to the mode shapes, with different sets of mechanical boundary conditions. Taking into account the results of previous measurements (Figure 1.6) stated in Chapter 1 and the theoretical considerations of Chapter 2, harmonic oscillations seem to be appropriate for handling the issue. A resulting objective is to cover a wide range of structural excitation frequencies at appropriate deflection amplitudes.

3.3. Boundary Layer Thickness Control

The stabilizing influence of the turbulent boundary layer on the aeroelastic system illustrated by Muhlstein and Gaspers [8, 9] reaches its maximum at low supersonic Mach numbers, as is indicated in Figure 1.3. In order to investigate that influence an adjustment of the boundary layer's thickness on the panel's surface is inevitable. Various approaches are known from the literature. On the one hand, the wind tunnel flow conditions have a strong influence on the resulting thickness of a turbulent boundary layer

$$\delta_{Turb}(x) = 0.37x \left(\frac{U_\infty \; x \; \rho_\infty}{\eta} \right)^{-\frac{1}{5}} \tag{3.7}$$

that depends on the run length x, the free stream velocity and the dynamic viscosity [75]. Since the dynamic viscosity depends only on the temperature, the two remaining quantities are adjustable by the total pressure and the Mach number, respectively. According to Equation 3.7, an exemplary change in the velocity or the density by a factor of ten would lead to a change in the boundary layer thickness of $\delta_{max}/\delta_{min} \approx 1.6$. Consequently, to achieve significant changes in the boundary layer's thickness at a constant velocity, the test facility must be capable of adjusting the pressures in a wide range. Experiments presented the Reynolds number's influence on the boundary layer thickness and the associated boundary layer displacement thickness (Figure A.2). The variation of the Reynolds number by a factor of two and the increase in the Mach number from $M_\infty = 1.1$ to $M_\infty = 1.35$ showed hardly any influence on the measured boundary layer characteristics.
Another option already introduced is to use a splitter plate. A plate-like structure featuring a sharp leading edge is placed close to the wind tunnel wall. The boundary layer, which originally was formed along the wind tunnel wall, is cut off by that leading edge at the height of the splitter plates distance to the WT wall. By increasing the plates distance to the wall, a new boundary layer originates at the plate's leading edge. A

disadvantage of this approach is the potentially occurring blockage of the test section's cross section. In accordance to another concept, the injection of fluid through the WT wall allows a thickening (due to the increased wall-near flow velocity) of the wall-near boundary layer velocity profile, which results in a reduction of its thickness [76, 77]. A similar effect can be achieved by drawing fluid through the test section's perforated wall, which shifts the velocity profile in wall direction and thus also decreases the thickness [76]. A mixed solution including the splitter plate and the suction device approach is illustrated in Figure 3.1 [78], which shows results of a 2D CFD calculation at a reference Mach number of $M_\infty = 0.7$.

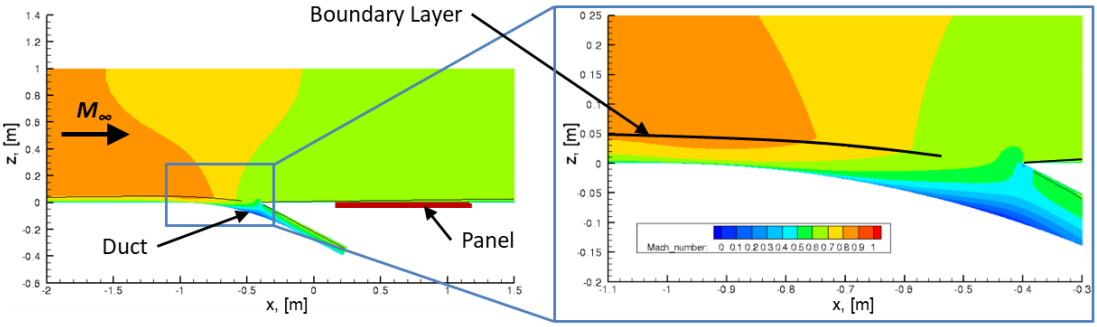

Figure 3.1.: Boundary layer control conception [78].

The depicted part of the test section in the left figure has a height of $h_{TS,CFD} = 1.0$ m and a length of $l_{TS,CFD} = 3.5$ m. A fluid mass extraction is realized by a duct, which is diverging from the main flow at the test section's lower wall. The extraction is driven by both low pressure at the duct's outlet and the dynamic pressure of the fluid. At the x_{CFD}-coordinates of the beginning enlargement of the test section's cross section geometry, as a consequence of the branching suction duct and due to the extracted mass flow, a change in the Mach number occurs. In that part of the test section where the panel is located, which is depicted by a red line from $x_{CFD} = 0.2$ m to $x_{CFD} = 1.2$ m, the Mach number remains constant. The detailed illustration in the right figure shows the flow conditions more closely in the vicinity of the suction duct. The flow is separating from the lower wall, which fills a large part of the duct's inlet. An advanced design of the inlet might ensure a flow following the wall's geometry. Nevertheless, the fluid extracted by the presented design is about 5% of the entire tunnel mass flow. This is roughly the same proportion as the boundary layer has. The boundary layer thickness is indicated by the thin black line that starts at about $z_{CFD} = 0.05$ m. In order to realize a new boundary layer origin, the parameters are chosen in a way that allows for a complete extraction of the wall's boundary layer. At $x_{CFD} = -0.4$ m, the flow is divided and a new boundary layer originates, which confirms the previous and complete removal. Based on these preliminary simulations, the shown principle of boundary layer suction is considered suitable. Related to the example, it is noted that optimization work is still required to finalize a design, which is suitable for all operation points in the subsonic and the supersonic Mach number range. In particular, arising shocks possibly

reflected can lead to strong in-homogeneous Mach numbers over the test structure. The perforated test section walls, which are not taken into account in the calculations, may give some remedy here. Another challenge is the design of a proper geometry, which depends strongly on the flow conditions. Subsonic flow and supersonic flow can benefit from different geometric approaches regarding the changeover from the test section to the suction duct's inlet. A continuous variation of the boundary layer thickness can be achieved by a variation of the suction duct angle, which is also a measure of the wall-to-splitter-plate distance.
In the presented example, identical pressures are set at the outlet of the test section and at the outlet of the suction duct. In order to improve that design, a decrease in the suction's outlet pressure should lead to an increased extracted mass flow. Pressure measurements performed in preparation to the present test campaigns [79] have shown a significant pressure differential between the test section and the variable diffuser, which is located downstream of the test section. This component of the wind tunnel is used in order to control the test section's free stream Mach number by a variation of the diffuser's cross-section. Depending on the test facility's operation point, static pressures far below the test section's pressure were measured, which may help to extract boundary layer mass flow from the test section by means of a bypass line between the domains of different pressure levels. Examples for four operation points, mainly defined by the Mach number and the total pressure, are depicted in Figure 3.2 and Figure 3.3.

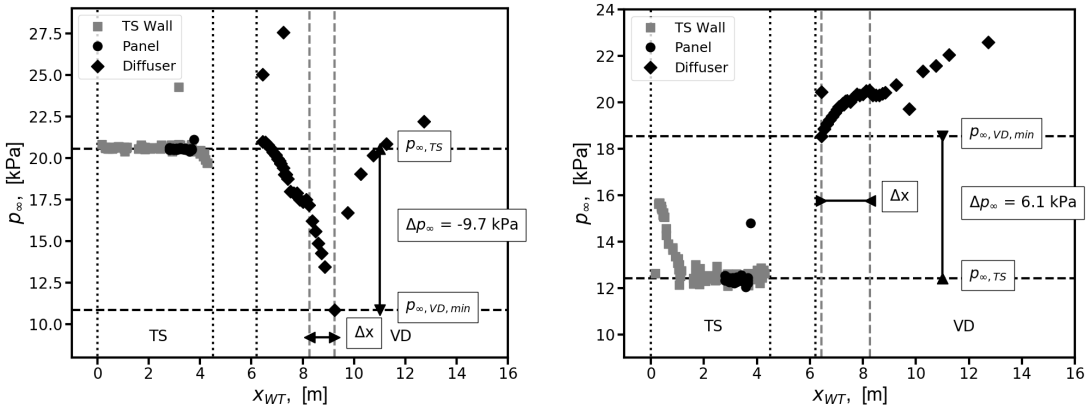

(a) $M_\infty = 0.75$; $p_0 = 30.0$ kPa.

(b) $M_\infty = 1.2$; $p_0 = 30.0$ kPa.

Figure 3.2.: WT static pressure and static pressure gradient Δp_∞ between the test section (TS) and the variable diffuser (VD) with the distance Δx_{WT} between the measured pressure minimum and available access hatches; (I).

The x-axis is divided into different sections, which are associated to the wind tunnel's components. The pressure in the test section is illustrated at 0.0 m $< x_{WT} <$ 4.25 m, while the pressure in the variable diffuser is presented at 6.0 m $< x_{WT} <$ 13.0 m. The pressure in the test section remains constant throughout its entire length, whereas the measured data in the diffuser is strongly alternating caused by the massive change in

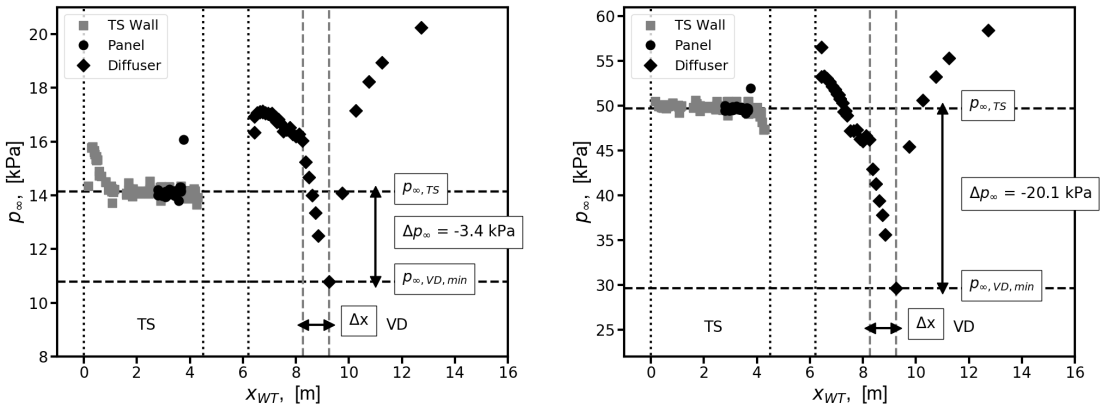

(a) $M_{\infty} = 1.1$; $p_0 = 30.0$ kPa.

(b) $M_{\infty} = 0.85$; $p_0 = 80.0$ kPa.

Figure 3.3.: WT static pressure and static pressure gradient Δp_{∞} between the test section (TS) and the variable diffuser (VD) with the distance Δx_{WT} between the measured pressure minimum and available access hatches; (II).

the tunnel's geometry here. The challenge in using this pressure gradient is to find a location of low pressure that is available for all required operational points. This is easier said than done, as this location is unfortunately changing its position with the change of the wind tunnel's flow conditions. Additional parameters, which influence the pressure's minimum and its location, are the compressor's revolution speed and the diffuser's opening angle. The first of the four examples (Figure 3.2 (a)) shows a strong pressure gradient Δp_{∞}, which is well suited to establish a mass flow between the two WT components. The next example illustrated in Figure 3.2 (b) for supersonic flow shows a reversed pressure gradient, whereas the third example presented in Figure 3.3 (a), also at supersonic flow, has again a promising gradient. Besides a slight change in the Mach number, the main difference between the two examples is the compressor speed. That parameter strongly affects the characteristics of the diffuser's pressure, which is to be adapted to the changes in the compressor's operation. By maintaining the flow conditions, the simultaneous adjustment of the compressor speed and the diffuser's opening angle may lead to promising pressure gradients for a wide range of flow conditions. The influence of the total pressure of the wind tunnel on the usability of that approach is small, since the arising gradients depend approximately linear on the set pressure, which is shown in Figure 3.2 (a) and Figure 3.3 (b). To settle the outcome of this point right away, the approach done in the first experiments of the presented test activities is to control the boundary layer by adjusting the flow conditions, as suggested at the beginning of this section. A conception of an additional device to bypass a part of the test section's flow has been created, but no detailed design-engineering has been performed so far.

3.4. Structural Parameters

The following section contains a description of the structural parameters, which are considered important for the present activities. Structural parameters are quantities that are inherent to the test structure's body. Most of those parameters are related to the structure's geometry, such as length, width and curvature. Examples for other quantities are the structure's material parameters and stresses, which are generated by heat or applied forces.

1. **Mechanical Boundary Conditions (MBCs):** The support conditions of the panel's edges have a significant influence on the flutter behavior, which is subject of numerous publications. Clamped conditions (constraints of all six DOFs), only at the leading edge and the trailing edge and at all four edges [8, 9, 57, 63], and simply supported conditions (no constraints of the rotation around the edge-axis), only at the leading edge and the trailing edge and at all four edges, are the most common types that are investigated. Investigations have proven that simply supported panels are more prone to panel flutter in the low supersonic Mach number range [80]. For more detailed information, Figure A.3 (a) presents a comparison of experimental and theoretical flutter boundaries and a comparison of theoretical results of clamped flat panels and simply supported flat panels [80]. The difficulty with regard to the upcoming experiment is the implementation of those different MBCs into a real structure in order to carry out experiments meeting the ideal conditions. The manufacture of clamped condition panels is shown in literature several times, whereas simply supported type panels cannot be found at all in experimental publications. A more exotic type of boundary conditions, which plays a minor role in panel flutter investigations so far, but is to be mentioned here for the sake of completeness, has all four corners pinned. The final experimental setup should be able to retain panels with different MBCs.

2. **Aspect Ratio:** A change in the structure's length-to-width ratio is significantly affecting the critical dynamic pressure. Theoretical investigations by Dowell show the dependence of the flutter boundary and the flutter frequency on the aspect ratio [63]. An increase from zero to an aspect ratio of one results in an increase of the flutter boundary. Figure A.4 shows results by Kordes [29], which prove those findings. Experimental results by Muhlstein and Gaspers [8, 9, 47] show an additional impact of the boundary layer thickness, which can result in a reversal of the aforestated dependence. For a low boundary layer thickness, a low aspect ratio panel is more susceptible to flutter, whereas for an increased thickness, the low aspect ratio panel exhibits a dropped susceptibility (Figure A.5). A way to investigate two aspect ratios with the same panel is to use a rotational frame that allows the change of the ratio of a flat rectangular panel to its reciprocal value.

3. **Cavity Effects:** A fluid volume, which is enclosed in a chamber on the rear side of the panel, strongly affects the structural eigenmodes and eigenfrequencies and must be considered as a part of the aeroelastic system [13]. A pressurization of a

sealed chamber leads to an increase in panel stiffness caused by the enclosed gas volume and leads to an increased critical dynamic pressure (Figure A.6) [73]. A venting device can ensure an equalization of the static pressure difference applied between the flow faced side of the panel and its rear side to diminish the mentioned effect. A change in the static pressure differential is accompanied by changes in the frequency and the amplitude at flutter conditions. This can be used to stop flutter when the cavity's static pressure is controlled (Figure A.7).
A parameter of importance connected with the cavity is its depth. Its change influences in particular the low panel eigenfrequencies [9, 81]. The influence is going toward a limit value with increasing depth (Figure A.8). Depending on the ratio of cavity depth and cavity pressure, one of the two mentioned effects becomes dominant. The compressed fluid enclosed by the cavity acts like a mechanical spring, which can increase the lower eigenfrequencies on the one hand. On the other hand, the enclosed fluid also acts like a mass, which is able to lower the eigenfrequencies of the panel. A challenge within the design of this feature might be to realize a suitable sealing of the cavity, which becomes even more difficult in case of panels with free edges.

4. **Pre-Stresses:** Different sources of pre-stresses have been studied hitherto. Aforementioned experiments used heated panels to investigate the resulting buckled panel state. The temperature leads to material expansion, which causes stresses due to the structure's edge fixation. Knowledge about how thermal loads affect the aeroelastic behavior may be important with regard to the heat generating friction between fluid and test structure during the experiment. Another conception for applying pre-stresses, which leads in principle to the same result, is the application of forces at the test structure edges' in-plane-directions.
Different states can be detected when comparing the dynamic pressure and the applied pre-stresses: For a flat plate and a low dynamic pressure, a stable area appears in case of low loads, in which the panel remains flat. The panel becomes buckled, yet remains dynamically stable, with increasing loads. An increase in the dynamic pressure beyond the critical dynamic pressure results in a dynamic instability in terms of a limit cycle oscillation for both panel states. Here, the buckled panel shows a reduced critical dynamic pressure. With regard to the upcoming experiment, it is assumed that the application of a homogeneous and controlled heating will be more ambitious than the application of in-plane loads caused by forces that act at the panel edges. Figure A.9 shows the different domains of stability and instability in terms of the dynamic pressure as a function of non-dimensional in-plane loads in x-direction.

5. **Material:** Panels investigated hitherto can be divided into two groups. The first group contains structures made of isotropic materials applying to metals as aluminum, magnesium and steel, which were subject to numerous experimental activities [8, 9]. Another isotropic material means another Young's Modulus and thus a changed stiffness, disregarding the small changes in the Poisson number.

Imperfections in the test specimen due to the manufacturing process can strongly affect the test results and can cause problems when comparing the experimental setup and the associated numerical model.
Structures of the second group show an orthotropic characteristic, which means by definition a flexural stiffness that depends on the structure's orientation. On the one hand, orthotropic properties can be established by stiffening a panel with additional stringers that can be made of isotropic material [82]. On the other hand, composite materials, such as sandwich structures or carbon fibre re-enforced polymers (CFRP), have orthotropic properties depending on the number and orientation of the used plies [83]. Due to the complex manufacturing process of those materials, the probability of occurring imperfections is high. The wide range of different orthotropic materials, the resulting number of parameters and the probability of imperfections suggest that studies on these materials should not be prioritized for the upcoming activities.

6. **Thickness:** Besides the material characteristics Young's Modulus E and Poisson ratio ν, which are available with high accuracy in literature for common isotropic materials, the flexural stiffness or bending stiffness of a plate depends on its thickness h. Its increase is accompanied by an increase of the stiffness and thus with a decrease of flutter proneness. The integration of the stiffness in the non-dimensional dynamic pressure λ is already described at the beginning of this section. For an accurate interpretation of experimental flutter results, the panel thickness must be as homogeneous as possible throughout the test structure or the inaccuracies must be known exactly, which is important for an accurate FEM-modeling of the structure. In the case of desired aeroelastic instabilities in a certain range of flow conditions, detailed knowledge of the system's aeroelastic characteristics must be available to determine a suitable thickness. Any inaccuracies occurring are of particular interest as they can decide between a stable and an unstable state of the system.

7. **Curvature:** Generally, there are two different types of curved panels. The first shows a curvature directed in streamwise direction, whereas the other shows a spanwise curvature. Panels used in aircraft and spacecraft applications, e.g. in launcher systems, are usually designed spanwise curved. Those panels were investigated by Ganapathi and Varadan [84], whose findings are presented in Figure A.10. The critical dynamic pressure is plotted over the radius-to-arc-length ratio R/b for isotropic panels with a thickness-to-arc-length ratio of $h/b = 100$. The flutter boundary in the low ratio range is very sensitive to this parameter, whereas the results strive toward those of a flat plate with increasing ratio. In the shown case, the curvature has a stabilizing effect on the aeroelastic behavior. Since this parameter has not yet been investigated extensively, the creation of a data base for the validation of numerical results for launcher applied structures appears to be reasonable.

3.5. Attachment to the Test Facility

The experiments performed so far have shown a large number of test setup designs, which can be condensed into two basic design concepts with regard to their application in the test facility's test section. The first one consists of an airfoil-like or wedge shaped body, which extends from the test section's ceiling to its bottom. Applied to this fixture is the test specimen [32–34, 85], as is exemplary illustrated in Figure 3.4 (a). Depending on the particular design, the panel is mounted to one side of that central body, whereas the other side can provide access or venting holes. Disadvantages are the little space inside that central body that is available for measurement technique, flutter breaks or actuators. A significant advantage is the absence of wind tunnel wall effects. The second setup type is applied to a wind tunnel's wall, as is depicted in Figure 3.4 (b). All necessary equipment can be placed outside the test section where probably sufficient space is available.

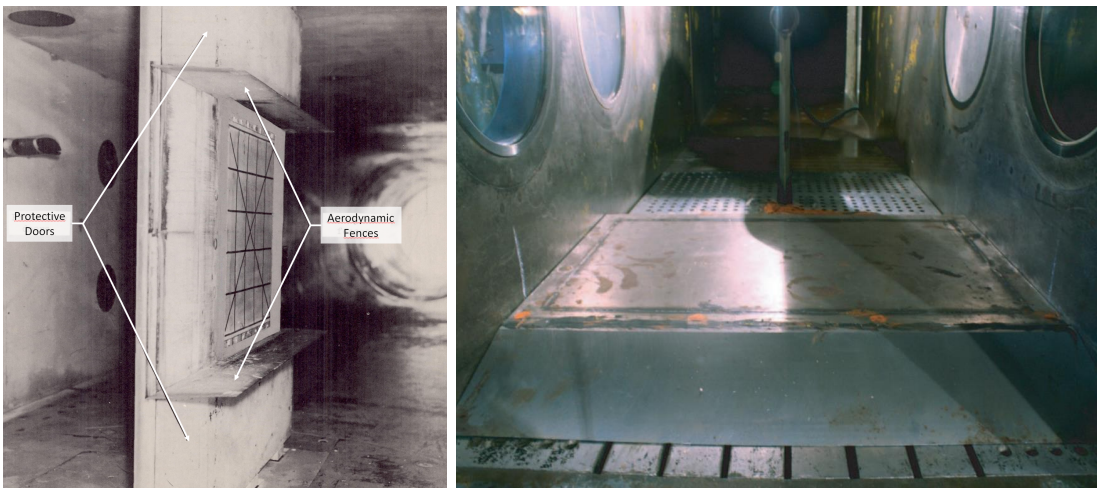

(a) Test structure mounted in a central body by Dixon [33].

(b) Wall mounted test setup by Vedeneev [57].

Figure 3.4.: Mounting conceptions; Streamwise directed view.

The setup of Muhlstein and Gaspers showed a combination of such a flush-to-the-wall design and an adjustable splitter plate, which is shown in Figure A.11. Since no blockage of the test section occurs, no shocks or other significant changes of the flow conditions (e. g. Mach number) are expected in the vicinity of the panel. With regard to the numerical modeling, a flow, which passes a constant geometry, is considered to be another advantage of this design.

4. Setup

This chapter presents the final test setup design, which is derived from the previous section's findings. In the experiments carried out with the new experimental setup for studies on the aeroelasticity of shells and plates, not all of the parameters shown can be taken into account. The number of parameters is kept low, which shall allow a clear allocation of the obtained phenomena to the particular influencing parameter. In addition, an extensive investigation of all presented parameters would go beyond the scope of the activities published in this thesis. That is why a modular design of the setup is chosen, which gives the possibility to add missing features and devices in future experiments. Following, the test setup is described and the implementation of the discussed features and parameters is pointed out. The description of the test setup is subdivided into the main components of the final test setup with the focus on the design of the test structure and its deflection mechanism. A rudimentary sketch of the test setup is illustrated in Figure 4.1, which shows an all-edge clamped panel attached flush to the wind tunnel wall. An actuator located at mid-length of the panel deflects the panel, whose upper side is facing the flow of the wind tunnel's test section. The sketch shows one of two used experimental configurations that differ in the number and the position of attached actuators.

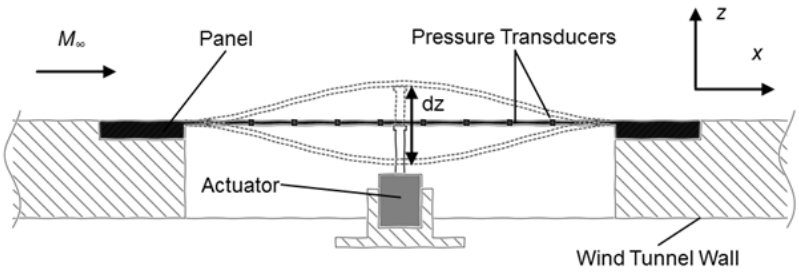

Figure 4.1.: Test setup sketch.

Figure 4.2 illustrates different views of the setup, which is attached to one of the two vertical test section walls. The left figure shows a view from the inside of the wind tunnel test section in the direction of flow, where the test structure within its fixture is attached flush to the right tunnel wall. The structure's surface is covered with a pattern of white dots, which are part of a deformation measurement technique described in detail in Chapter 5. Directly behind the panel, applied half way up the wall, a wake rake is located that enables the measurement of the flow's boundary layer. A view from outside the test section on the setup's rear side is depicted in the right figure,

which reveals the tripartite frame assembly, measurement technique and the hydraulic actuating mechanism. The actuating mechanism is carried by a rack located at the back of the panel. The rack and the test structure are mounted to an inner frame, which is finally attached to an outer frame that connects the entire test setup to the wall of the wind tunnel's test section. The following description of the setup is divided in the different setup main components support, panel and actuating system, which is concluded by a brief illustration of the calculated test section's eigenfrequencies.

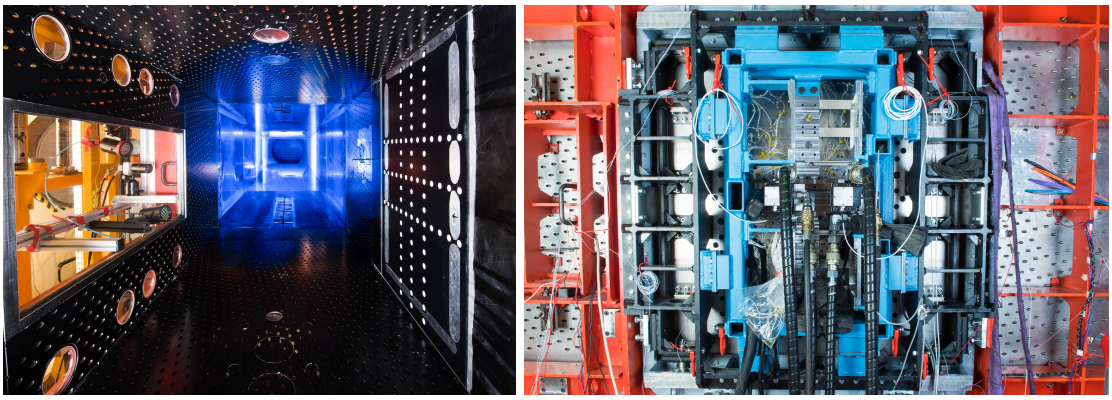

(a) View in flow direction with the test setup mounted to the right sidewall.

(b) View from outside the test section with the actuator rack (blue), the inner frame (black), the outer frame (gray) and the test section wall (red).

Figure 4.2.: Test setup.

4.1. Support

The support assembly allows the installation of the actual test structure in the test facility by connecting the test setup, including the belonging equipment, to the facility's test section. As shown in Figure 4.3, the support consists of two different frame assemblies, each equipped with a pair of wall plates which serve as additional wind tunnel walls. The inner frame carries the panel assembly fixture, which consists of the panel and another massive steel frame, to which the panel is attached. This frame is attached to the outer frame, which represents the actual connection to the test facility. To align the frames with each other and also to adjust the whole setup in the wind tunnel wall slot, ejector screws at the outer frame allow an adjustment in x- and y-direction, which are the panel's in-plane directions. An adjustment with regard to the z-direction is realized by additional forcing screws at the wall plates and the panel assembly. A feature that takes into account the investigation on the structure's aspect ratio is the possibility of turning the inner frame, which results in a reversal of the panel's aspect ratio. To take into account numerous parameters, which are directly related to the panel, any other future test structure with appropriate external dimensions can be connected to the inner frame component.

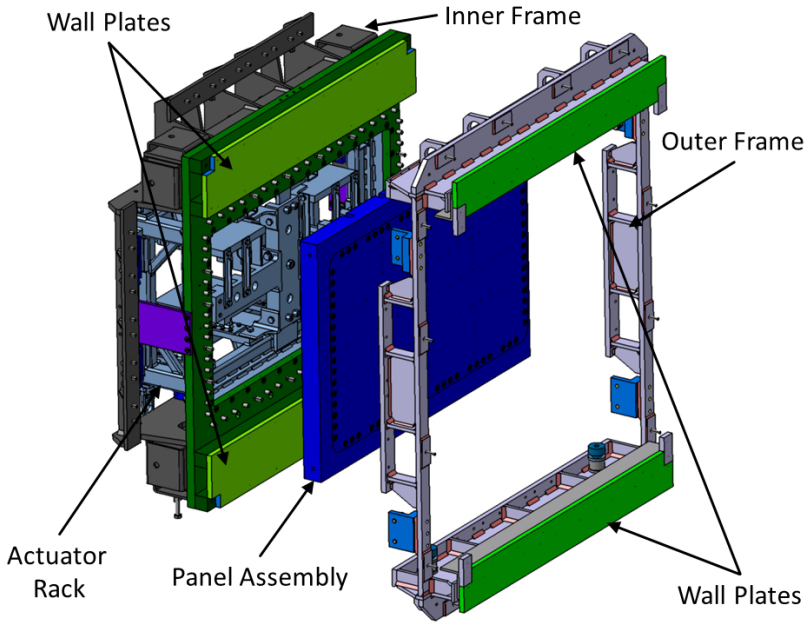

Figure 4.3.: Test Setup divided in its outer frame, the panel assembly and the inner frame with applied actuator rack.

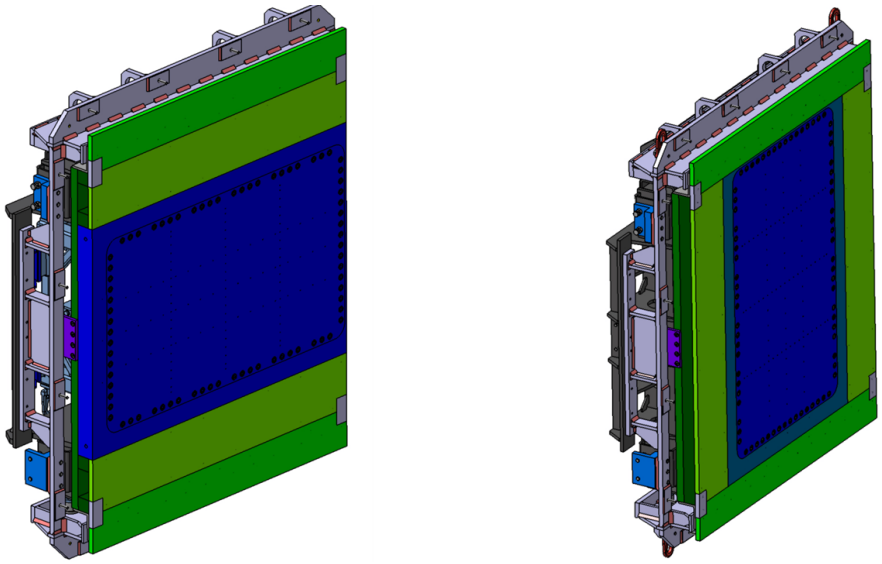

(a) $\alpha = 90°$.

(b) $\alpha = 0°$.

Figure 4.4.: Different configurations of the test setup with revolvable inner frame.

4.2. Panel

In this thesis, the actual test structure is also referred to as panel or panel model. A broad variation of panel structures in terms of its geometry and the used material is worth being subject to tests, which requires a simple interchangeability of the different test structures. The variation of the test structures is limited by the dimensions of the frame illustrated in Figure 4.5, to which present and future test structures must be mounted by means of a bolt connection. The frame ensures a solid and rigid connection between panel and test setup, which shall ensure a proper implementation of the chosen mechanical boundary conditions of the panel edges. The frame also exhibits several features designed forward-looking to future tests, which may focus on a pressurized cavity on the test structure's back. The structure has a circumferential notch for the application of a sealing chord, which enables a sealing of the cavity against the surrounding pressure. In the same context, holes are drilled for the application of a venting and pressurization system and for the passage of cables and tubes of measurement technique.

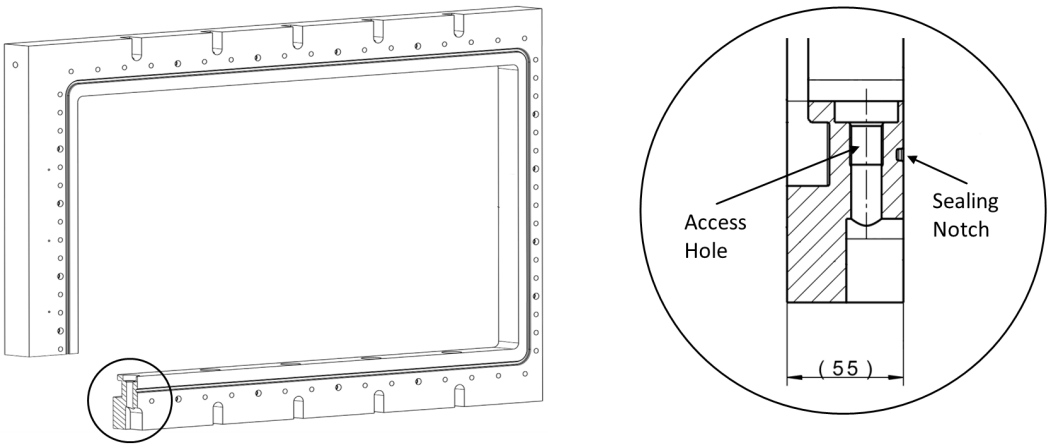

(a) Frame design with circumferential sealing notch and accesses for measurement equipment.

(b) Sectional detail drawing shows cavity access and sealing notch.

Figure 4.5.: General panel frame features.

4.2.1. Sizing

The test structures invented for the experiments presented in this thesis are designed as simple as possible. This allows the assignment of occurring phenomena to specific parameters on the one hand. On the other hand, the exact implementation of the design in the manufacturing process must be assured. The result are flat plates with clamped mechanical boundary conditions at all four edges, whose general properties are given in Table 4.1.

Dimension	**Value**
Length, l_i $[mm]$	500.0
Width, w_i $[mm]$	875.0
Thickness, h_i $[mm]$	3.0
Young's Modulus, E $[GPa]$	210.0
Tensile Point, R_m $[MPa]$	1080.0
Yield Point, $R_{p0.2}$ $[MPa]$	950.0

Table 4.1.: Panel properties.

In order to meet the desired clamped MBCs (see Section 2.2.2), two measures are taken in the manufacturing process: The first is to manufacture the panels from a single piece of steel with an overall length of $l_o = 550.0$ mm, an overall width of $w_o = 925.0$ mm and an overall thickness of $h_o = 20.0$ mm. In its center, an area of $l_i = 500.0$ mm by $w_i = 875.0$ mm is milled to a thickness of $h_i = 3.0$ mm, which represents the actual panel model. Width and length of the structure are chosen as large as possible, limited only by the geometric conditions of the WT test section. The panel thickness h_i is defined on the one hand by a strength analysis based on the actuator forces. On the other hand it is based on a risk assessment regarding emerging aeroelastic instabilities under test conditions. Both analyses are content of Section 4.2.2. By manufacturing the panel from a single piece, an integrated circumferential rigid frame results, which has a frame-to-panel-stiffness ratio of $D_o/D_i \approx 300$. Due to the manufacturing processes and the safety margin for unacceptable stresses, radii are applied at the edges of the thickness transition from h_i to h_o and at the four corners, which lead to minor deviations from the intended ideal rectangular geometry, as shown in Figure 4.6.

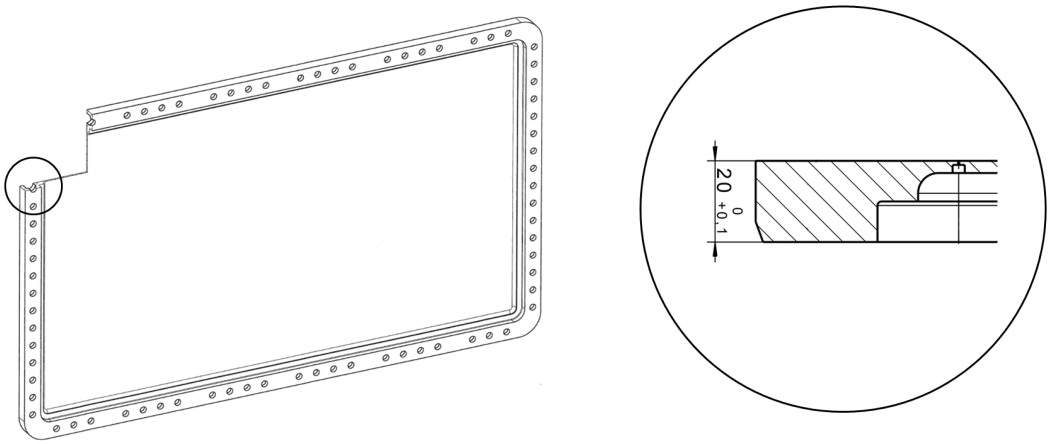

(a) Basic panel design with integrated circumferential frame and drilling holes.

(b) Sectional drawing shows integrated frame design and radius for stress prevention.

Figure 4.6.: General panel design features.

The second measure to implement the MBCs is mounting the panel on the mentioned steel framework shown in Figure 4.5, which leads to an increased stiffness ratio of $D_{Frame}/D_i \approx 6200$. Since the panel is forced to undergo oscillating motions with different amplitudes, a steel with a high toughness is chosen (Toolox 33). The used coordinate system's origin is located at the panel's leading edge, as depicted in Figure 5.11. The x_{Panel}-coordinate is directed in the direction of flow, the y_{Panel}-coordinate points in spanwise-direction and the z_{Panel}-coordinate is oriented toward the test section's interior. Unless otherwise stated those coordinates are referred to as x, y and z.

4.2.2. Forced Motion Approach

The description of the forced motion approach connects the literature review's findings on observed panel flutter phenomena in Section 1.1, the corresponding theoretical outcome with regard to the eigenfunctions in Section 2.2 and the design of the panel and its support frame assembly, which was presented in this section so far. The dominating shapes detected during panel flutter are the first and the second structural bending eigenmode shapes in the direction of flow. Thus, those shapes, which correspond to the already introduced eigenfunctions Ψ_{11} and Ψ_{21}, are to be simulated during the upcoming experiments. The plate theory by Kirchhoff gives the required information on those corresponding shapes. A simple FEM model validates the results and gives some additional information in order to realize an appropriate test design. The model of a flat rectangular plate with constraints of all six DOFs at the grid points along each of the four edges is set up with MSC Nastran. It consists of 100 by 100 CQUAD4 shell elements with a density of $\rho_{FEM} = 7850.0$ kg/m^3 and the same geometric dimensions l_i, w_i and h_i as shown in Table 4.1. Figure 4.7 shows the results of a modal analysis for the first four eigenmodes with the belonging eigenfrequencies.

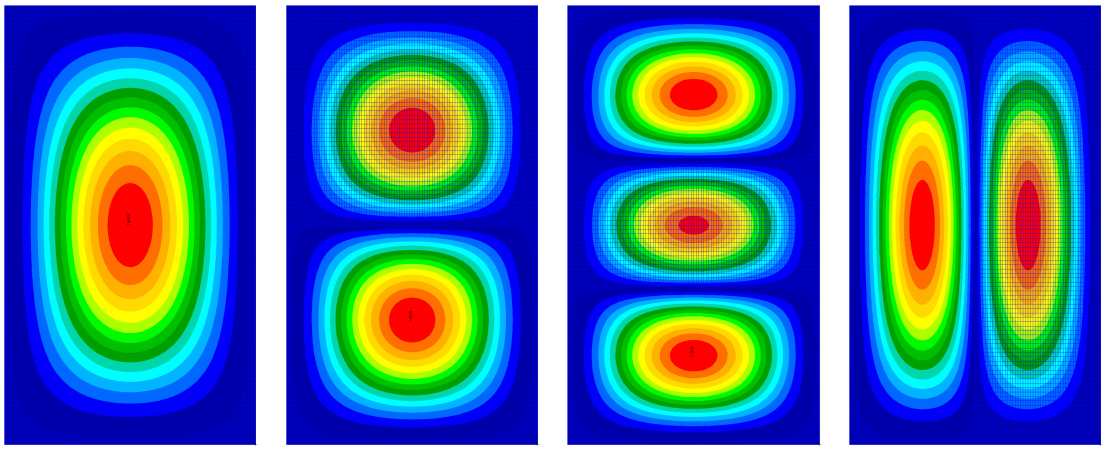

(a) First eigenmode Ψ_{11}; $f_{\Psi 11} = 76.3$ Hz. (b) Second eigenmode Ψ_{12}; $f_{\Psi 12} = 106.5$ Hz. (c) Third eigenmode Ψ_{13}; $f_{\Psi 13} = 159.1$ Hz. (d) Fourth eigenmode Ψ_{21}; $f_{\Psi 21} = 194.0$ Hz.

Figure 4.7.: Mode shapes and frequencies of the FEM model.

The modes of interest are the first and the fourth at $f_{\Psi 11} = 76.3$ Hz and $f_{\Psi 21} = 194.0$ Hz, respectively. Figure 4.8 (a) shows the resulting shapes of both the FEM modal analyses (at mid-span) and the analytic results of Chapter 2 of the two eigenfunctions Ψ_{11} and Ψ_{21}. A good match between the different approaches can be seen for both eigenfunctions.

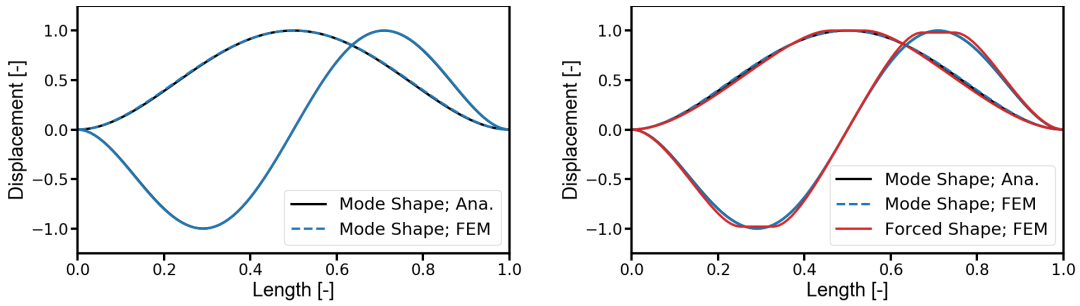

(a) Kirchhoff plate theory vs. FEM modal analysis. (b) Kirchhoff plate theory vs. FEM modal analysis vs. FEM forced deflection.

Figure 4.8.: Comparison of shapes Ψ_{11} and Ψ_{21}.

The next step is to estimate how well those ideal shapes can be simulated by using an actuator driven mechanism. The basic idea is the application of one or two actuator forces respectively in order to simulate the shapes, as can be seen in Figure 4.9 and Figure 4.10. At $y_F = 0.5w_i$, loads are applied at $x_{F,\Psi 11} = 0.5l_i$ to simulate the first mode shape and at $x_{F,\Psi 21,1} = 0.29l_i$ and $x_{F,\Psi 21,2} = 0.71l_i$ in order to simulate the fourth mode. A comparison of the resulting deformations for the half-span cross section is illustrated in Figure 4.8 (b). A satisfying agreement with the structure's eigenfunctions can be identified. Following, the FEM model characteristics in terms of its material properties and its geometry must be matched with the hydraulic actuator's specifications. On the one hand, the resulting panel deflections are determined, which are caused by the applied actuator forces. On the other hand, the structure's resistance to fracture and its fatigue resistance are estimated by means of a strength analysis. The magnitude of the applied forces corresponds to the specifications of the hydraulic actuators, which are available at the Institute of Aeroelasticity, and thus actually represents an additional boundary condition for the structure's design. The nominal actuator force $F_N = 7.0$ kN causes static deflections of about $dz_{\Psi 11} = 7.5$ mm and $dz_{\Psi 21} = 4.0$ mm, which lead to maximum stresses of $\sigma_{\Psi 11} = 380.0$ MPa and $\sigma_{\Psi 21} = 700.0$ MPa. Figure 4.9 and Figure 4.10 show the static deflection and the associated stresses (Von Mises) that result from the actuating forces for the two configurations Ψ_{11} and Ψ_{21}.
The most critical domains in terms of stresses are located in the area of the actuator connection and at the panels' edges at half-span. The emerging stress magnitudes are significantly below the material's yield point $R_{p0,2} = 950.0$ MPa (Figure B.1) and can

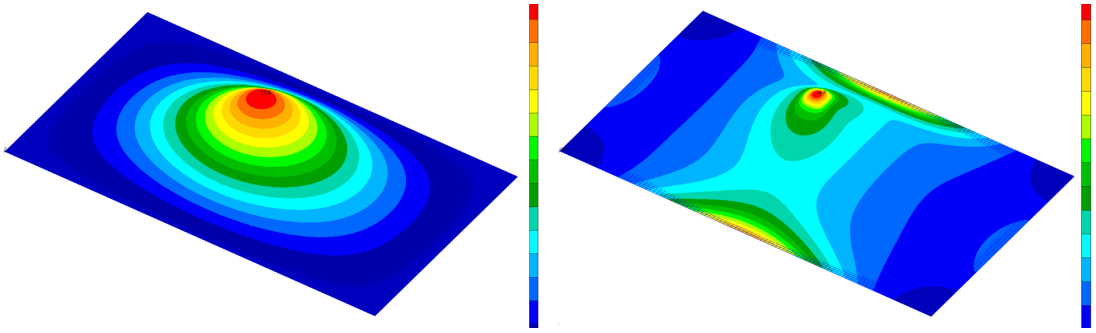

(a) Qualitative illustration of displacements. (b) Qualitative illustration of stresses.

Figure 4.9.: Simulation of the panel's first eigenfunction Ψ_{11} by applying a force $F_N = 7.0$ kN at $x_{F,\Psi 11}$ and y_F.

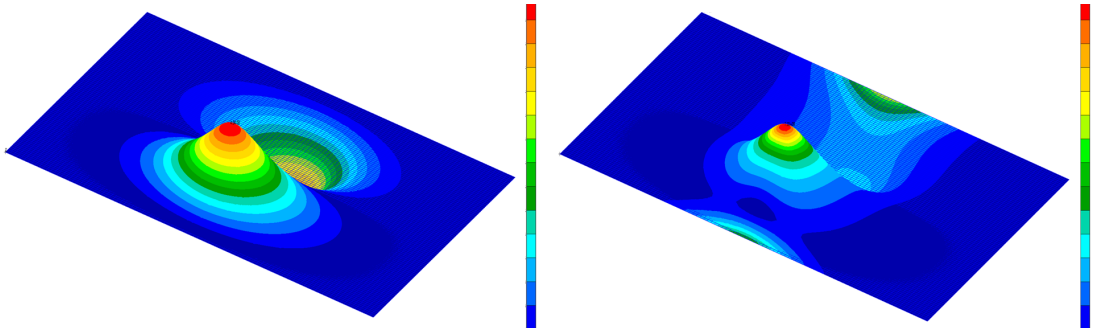

(a) Qualitative illustration of displacements. (b) Qualitative illustration of stresses.

Figure 4.10.: Simulation of the panel's fourth eigenfunction Ψ_{21} by applying forces $F_N = 7.0$ kN at $x_{F,\Psi 21,1}$ and y_F and $x_{F,\Psi 21,2}$ and y_F.

be expressed by a factor of safety:

$$SF_{N,\Psi ij} = \frac{R_{p0,2}}{\sigma_{N,n}} \tag{4.1}$$

The result is a factor of $SF_{N,\Psi 11} = 2.5$ for Ψ_{11} and a factor of $SF_{N,\Psi 21} = 1.36$ for the Ψ_{21} simulation. In the case that the actuator's maximum force is acting on the panel, the structure's integrity is still maintained. This applies for static loads and short-time loads, whereas a verification for dynamic loads is still pending. The mentioned critical domains of high stress levels are subject to another more detailed analysis that is based on the FKM guideline [86]. Based on the static results, dynamic limits are derived. First, the fatigue strengths for tension-compression loads

$$\sigma_{W,zd} = f_{W,\sigma} \cdot R_m = 0.4 \cdot 1080.0 \text{ MPa} = 432.0 \text{ MPa} \tag{4.2}$$

and for bending loads

$$\sigma_{W,b} = n_\sigma(d_0) \cdot \sigma_{W,zd} \tag{4.3}$$

are calculated. The tension-compression fatigue strength factor $f_{W,\sigma} = 0.4$ and the constants $a_G = 0.4$ and $b_G = 2400.0$ are material characteristics, which are necessary to calculate the Stuetzzahl:

$$n_\sigma = 1 + \sqrt{G_\sigma \cdot \text{mm}} \cdot 10^{-\left(a_G + \frac{R_m}{b_G \cdot \text{MPa}}\right)} \tag{4.4}$$

The stress gradient

$$G_\sigma = \frac{d_\sigma}{\sigma_{max} \cdot dz} = \frac{2}{h} = 0.67/\text{mm} \tag{4.5}$$

describes the gradient due to bending. In consideration of the roughness factor

$$K_{R,\sigma} = 1 - a_{R,\sigma} \cdot \log\left(\frac{R_Z}{\mu m}\right) \cdot \log\left(\frac{2 \cdot R_m}{R_{m,N,min}}\right) \tag{4.6}$$

with the model surface roughness $R_Z = 100.0 \cdot 10^{-6}$ m and the material constants $R_{m,N,min} = 400.0$ MPa and $a_{R,\sigma} = 0.22$, the permissible fatigue strength can be estimated:

$$\sigma_{perm} = K_{R,\sigma} \cdot \sigma_{W,b} = 324.0 \text{ MPa} \tag{4.7}$$

Since the calculated static stresses exceed that boundary, the dynamic structural deformation must be limited: Another FEM model shall give more detailed data about the structure's most critical stress domains. The second model shown in Figure 4.11 is a partial half-span 2D cutout of the panel at $y = 0.5w_i$ that extends from the clamped edge to the panel's center at $x = 0.5l_i$ in x-direction, where the maximum stress magnitude arises.
Due to its elongated geometry, which is difficult to illustrate, only the two domains of interest of the full FEM model are shown. Corresponding to Figure 4.6 (b), Figure 4.11 (a) depicts the panel edge domain with the applied MBCs. Figure 4.11 (b) shows a simplification of the actuator connection domain in the panel's center. Here, the actuator forces are applied, which act in z-direction. The full MSC-Nastran model is composed of altogether $n_{el} = 14043$ CQUAD4 and CTRIA 2D Solid elements. Several scenarios for negative and positive deflections in z-direction (-5.0 mm $\leq dz \leq 5.0$ mm) and for different pressure gradients Δp between the panel surfaces are simulated. The maximum pressure difference is $\Delta p_{max} = 10.0$ kPa, which was, according to the test facility's operator, the threshold valued used for the original wind tunnel design. The yield strength and the Young's Modulus are conform to the values of the manufactured model again

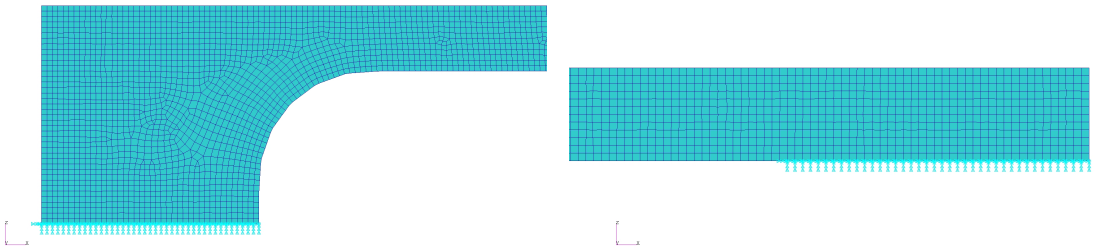

(a) Panel edge domain; The cyan colored arrows at the depicted part of the integrated frame indicate the constraints of all six DOFs.

(b) Panel actuator connection domain. The cyan colored arrows indicate the applied force in z-direction with DOF constraints in x-direction.

Figure 4.11.: FEM Model 2.

with the structure's density $\rho_{FE} = 7850.0$ kg/m^3. The two different deformation cases with a deflection amplitude of $\hat{A} = 2.0$ mm are illustrated in Figure 4.12, where the Ψ_{21} model has additionally constraints for all translation DOFs in the panel center. The arising stresses are indicated by the illustrated color bars.

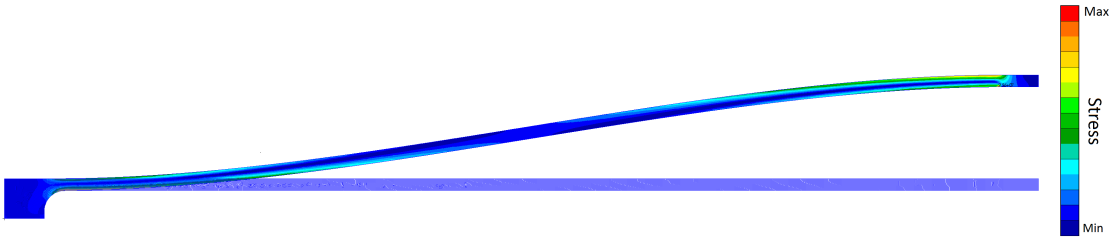

(a) Ψ_{11} simulation.

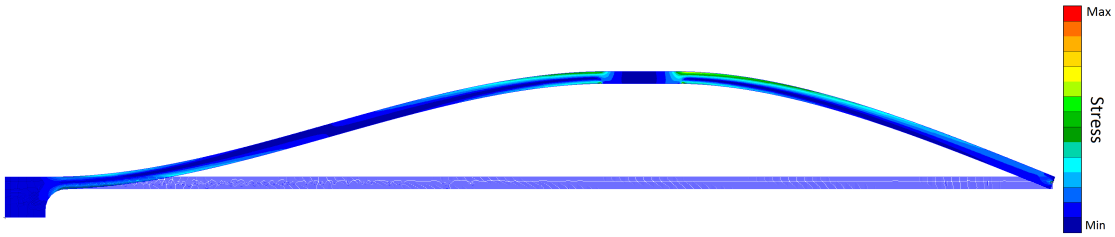

(b) Ψ_{21} simulation.

Figure 4.12.: FEM model 2; Half-span deformations and stresses ($\hat{A} = 2.0$ mm).

The depicted stresses prove that the most critical conditions occur in the vicinity of the actuator connection and at the $R = 5.0$ mm edge radius, which is the thickness transition area between the panel and its integrated frame. Magnifications of the critical design details are shown in Figure 4.13 and Figure 4.14, where the maximum stresses in both cases are located at the actuator connection ($\sigma_{\Psi 11,max} = 95.6$ MPa and $\sigma_{\Psi 21,max} = 432.0$ MPa).

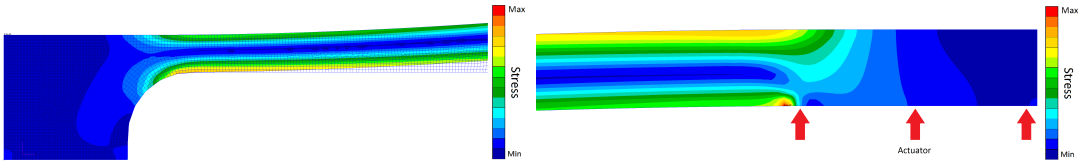

(a) Detail 1; Edge domain. (b) Detail 2; Actuator connection domain.

Figure 4.13.: FEM model 2; Ψ_{11}; Details; $\hat{A} = 2.0$ mm.

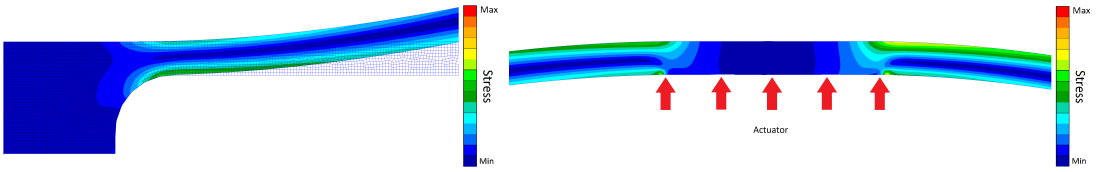

(a) Detail 1; Edge domain. (b) Detail 2; Actuator connection domain.

Figure 4.14.: FEM model 2; Ψ_{21}; Details; $\hat{A} = 2.0$ mm.

For the Ψ_{11} simulation, a deflection of $\hat{A} = 4.0$ mm is within the safety margin given by σ_{perm}, whereas the Ψ_{21} results exceed the determined limit. Consequently, the Ψ_{21} configuration requires a restriction for the maximum deflection. An analysis of the most critical model elements (ELM 496, ELM 2506, ELM 1021, ELM 1890, ELM 1971) is shown in Figure 4.15, where the element stress is a function of the actuator stroke, which is the amplitude $\hat{A}$.

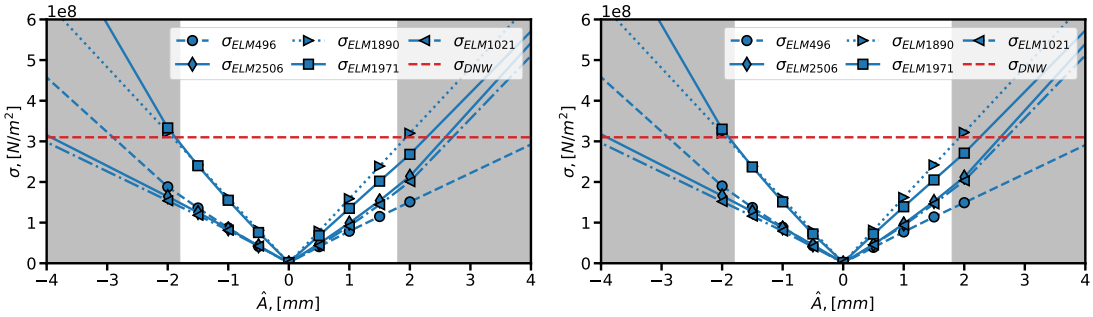

(a) $\Delta p = 10.0$ kPa. (b) $\Delta p = -10.0$ kPa.

Figure 4.15.: FEM model 2; Ψ_{21}; Critical elements; Actuator deflection vs. stress.

The two presented scenarios, which show the most critical stress magnitudes, include the mentioned additional positive and negative pressure gradients between the panel surfaces. The drawn dashed red line denotes the set strength limit, which is equal to σ_{perm}. The results show a permissible deflection amplitude that is slightly below $\hat{A} = 2.0$ mm for both load cases. Based on these results, a maximum deflection amplitude of $\hat{A}_{\psi 11,max} = \hat{A}_{\psi 21,max} = 1.8$ mm is defined for the present experimental activities.

It is not claimed that the presented FEM based estimations have a high degree of precision. Therefore the data is proved in the following section by experimental data, which was achieved in preparation of the experiments on the aeroelastic stability of plates and shells.
The general theoretical considerations on the forced motion approach are now complete, which can now be implemented in the design of the panel. The actuator mechanism, which is described in the following section, needs to be connected to the test structure's rear side. The exact position depends on the respective eigenfunction that is to be simulated. Due to the high acting static and dynamic loads, a solid bolted connection is chosen, which comprises a panel-integrated threaded pin. Since such a pin means an additional mass and a local change in stiffness, one test structure is designed for each configuration, which is depicted in Figure 4.16. Besides the added pins, the illustrated panels already show patterns belonging to the pressure measurements, which are subject of Chapter 5.

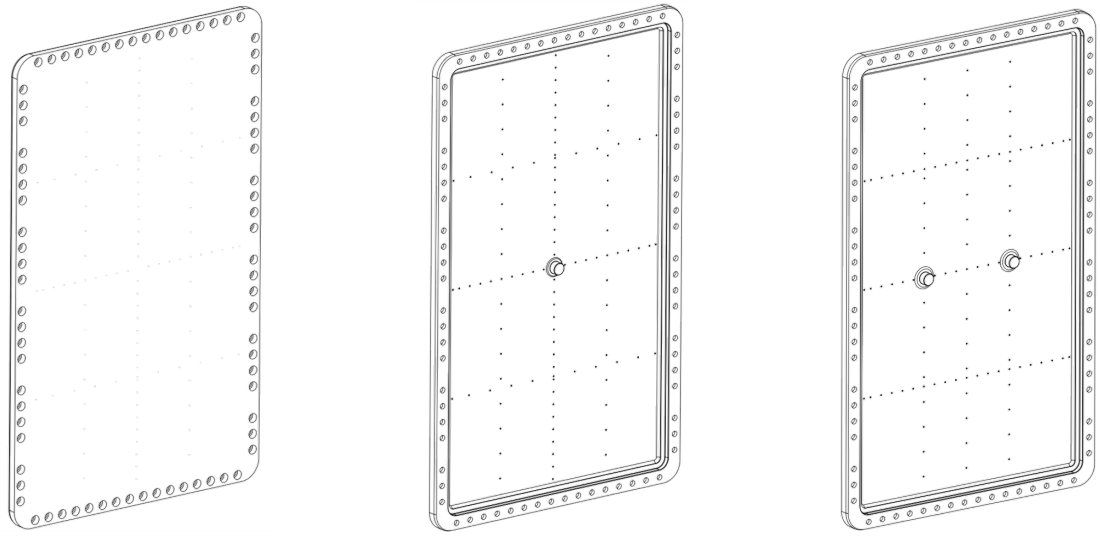

(a) Ψ_{11} panel; Front. (b) Ψ_{11} panel; Back. (c) Ψ_{21} panel; Back.

Figure 4.16.: Final panel designs.

In addition to the presented requirements regarding the mechanical strength, the aeroelastic stability during the tests is to be ensured in order to avoid flutter. The stability can be increased by increasing the structure's bending stiffness. Since the panel's length and width are restricted by the dimensions of the test facility's test section, the simplest way is to adjust the panel thickness. Experimental data by Muhlstein [8] and Gaspers [9] permit conclusions for the present test setup. For this purpose, the mass ratio parameter

$$\mu = \frac{\rho_\infty l}{\rho_s h} \tag{4.8}$$

is introduced, which contains, besides the panel's length and thickness, the ratio of the fluid's density ρ_∞ and the structural density ρ_s. Figure 4.17 depicts the non-dimensional dynamic pressure as a function of the mass ratio parameter. Critical values λ_{crit}, above which flutter starts, are determined for two tested structures at $M_\infty = 1.2$ with an aspect ratio of $l/w = 0.5$. One of the tested structures was made of Invar (red solid line), whereas the second was made of magnesium (blue dotted line). The magnesium panel was additionally investigated at an aspect ratio of $l/w = 2.0$ (blue dash-dotted line) and a Mach number of $M_\infty = 1.1$ (blue dashed line). The four measured and extrapolated flutter boundaries show a strong and linear dependence of the critical dynamic pressure on the mass ratio. The variation of the mass ratio parameter was achieved by the variation of the static pressure within the test section, which was required to determine the flutter boundary at a constant Mach number.

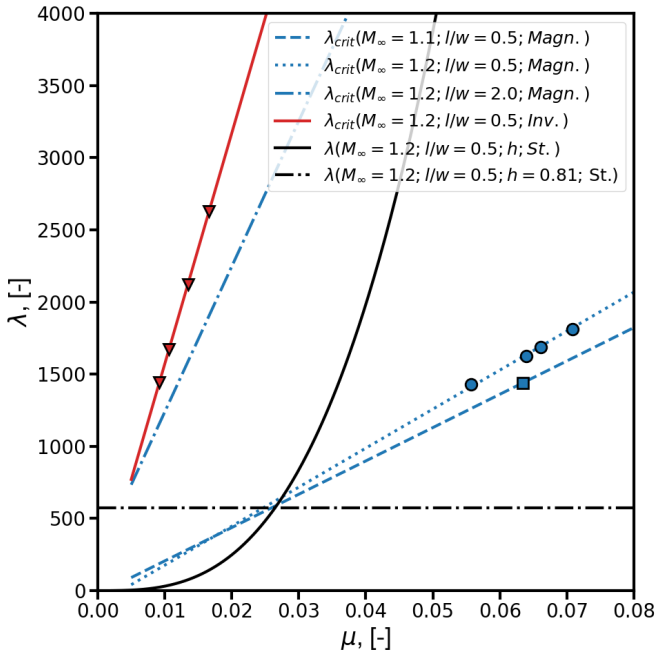

Figure 4.17.: Non-dimensional dynamic pressure λ vs. mass ratio μ; Experimental data by Muhlstein [8] and Gaspers [9].

The results show that the Mach number's impact is low, which becomes clear when the magnesium panel's results with $l/w = 0.5$ at $M_\infty = 1.1$ and $M_\infty = 1.2$ are compared. In contrast, the impacts of the change in the material properties and the aspect ratio are dominant. The increased Young's Modulus of the Invar panel and the increase in the aspect ratio of the magnesium panel show similar stabilizing effects on the aeroelastic system. Since the ratio of $l/w = 0.5$ resembles the ratio of the structures designed for the present activities (which is $l/w = 0.57$) and the material properties of Invar are similar to those of steel, the Invar panel's stability boundary is considered as a reference for the upcoming WT tests. Nevertheless, it should be noted that the Young's Modulus

of Invar ($E \approx 145$ GPa) is lower than that of steel.
In addition to the four sets of measured and extrapolated flutter boundaries, calculated non-dimensional pressure data $\lambda(h, \mu(h))$, which are not the critical values, are shown for a steel panel at a Mach number of $M_\infty = 1.2$ (solid black line). The structure's properties are those presented in Table 4.1 with a variation in thickness from $h = 5.0 \cdot 10^{-4}$ mm to $h = 1.0 \cdot 10^{-2}$ mm. The fluid density results from the specifications of the DNW-TWG (Figure 5.28). An increase in the structure's thickness leads to a reduction in both the mass ratio and the non-dimensional dynamic pressure. With regard to the reference used, the aeroelastic system remains stable over the whole range considered, since they are below the reference flutter boundary. Even when the more critical data sets of the magnesium plate are considered, a panel thickness of $h_{min} > 0.81$ mm ensures stable conditions. This limit is shown by the dash-dotted black line. Consequently, the thickness of $h = 3.0$ mm of the final panel design, which results from the strength analysis, is also considered appropriate under aeroelastic considerations. In addition, the first eigenfrequency is that high, that a large margin to the intended excitation frequencies of the forced motion activities is achieved.

4.3. Actuating System

So far, the actuating system has been considered only as a force causing the intended structural deflection needed for the panel design. The hardware realizing this deformation in the experiments consists mainly of a hydraulic pump connected to one or two hydraulic linear cylinders, which depends on the particular eigenfunction of the structure that is simulated. The used Hydropuls PLF 7 type hydraulic linear cylinder has a nominal stroke of $s_N = \pm 10.0$ mm and a nominal force of $F_N = 7$ kN (Figure 4.18).

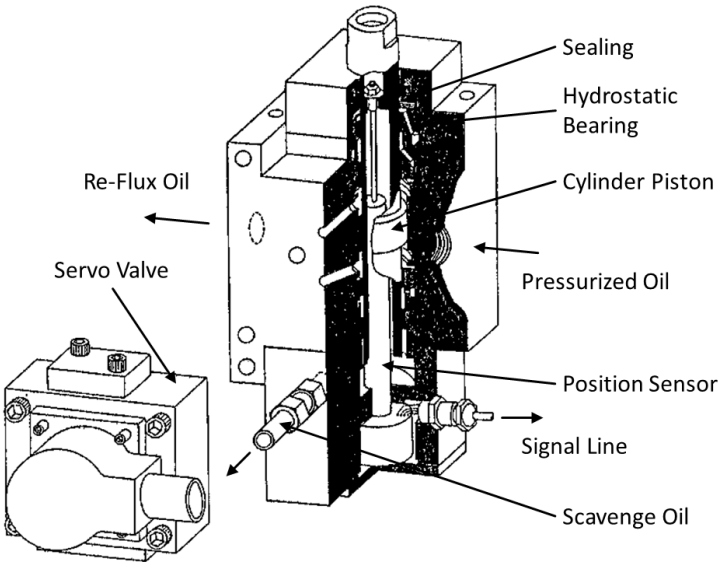

Figure 4.18.: Hydraulic actuator Hydropuls PLF 7 [87].

In order to control the hydraulic system, the cylinder piston's position is measured by an inductive travel sensor Messotron WLH 20 C, which is located at the actuator's rear behind the piston. A MOOG D 760-232 A High-Response servo valve controls the motion of the actuator with a pressurized oil flow of $\dot{V} = 19$ l/min. The valve is fed by a Schenck PP 40 B hydraulic pump providing maximum oil flows of $\dot{V}_{max} = 40$ l/min at a maximum oil pressure of $p_{max} = 21.0$ MPa. The pump provides two connection devices. A Schenck LPL scavenge oil pump ensures the re-flux of the oil, which is necessary for the operation of the piston's hydrostatic plain bearing. For connecting the actuator to the panel, an extension rod is screw-mounted to the piston top's internal thread. The other end of the extension is also threaded and is to be connected to the threaded pin of the panel as illustrated in Figure 4.19.

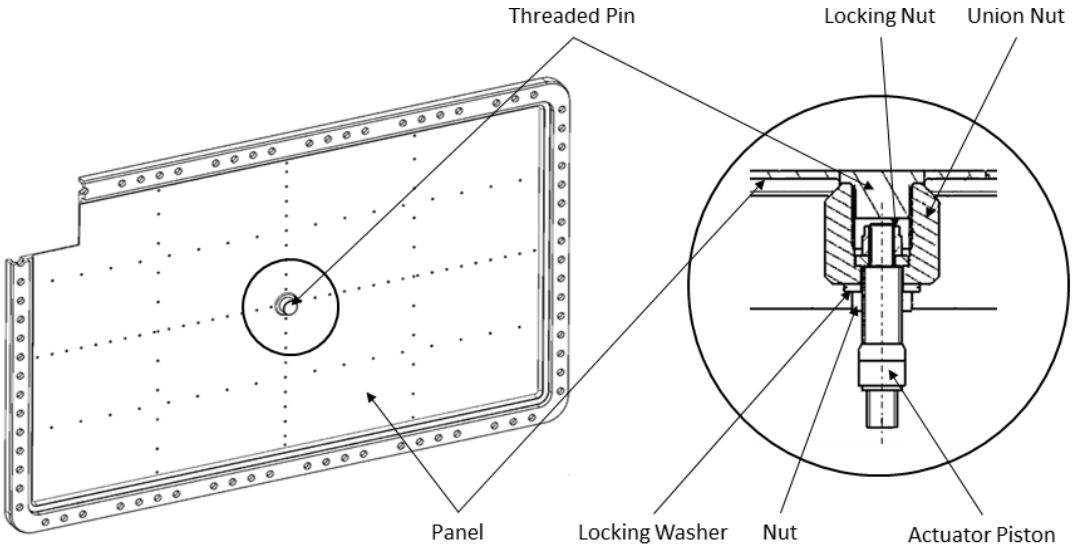

Figure 4.19.: Hydraulic system; Connection to test structure Ψ_{11}.

The key component of the connection mechanism is a union nut connecting the actuator's piston to the threaded pin of the panel. Its z-wise position is determined by two locking washer-nut combinations. Besides the need of this connection to deflect the panel, another safety mechanism to avoid free flutter or other unwanted structural motions is established. Most important for an actuator driven dynamic experiment is to get the information about the performance of the system based on the dependence of the amplitude on the frequency. Since a wide range of frequencies exciting the panel is planned, adequate amplitudes and sound harmonic motions must be ensured even at high frequencies. This characteristic strongly depends on the provided oil pressure and the applied mechanical loads, which are in this case the inertia forces and the elastic forces of the panel. In order to achieve the information, a pretest was carried out, consisting of a steel plate, which has the same characteristics as the final panel structure. The plate was mounted on a solid table made of welded steel. The hydraulic cylinders were located beneath the plate as shown for the Ψ_{11} configuration in Figure 4.20.

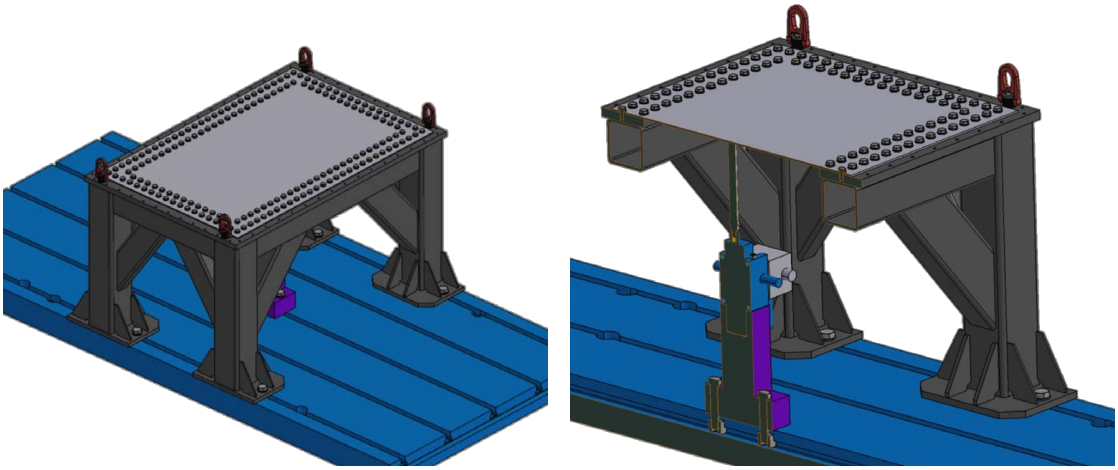

Figure 4.20.: Pretest; Ψ_{11} configuration.

Laser triangulators, which are described in Chapter 5, were used to double-check the position sensor's data about the plate's deformation. They were mounted on a frame surrounding the whole pretest setup and pointed on the actuator-plate connection from above. Tests were performed with zero loads, which means with removed plate, with Ψ_{11} configuration and with Ψ_{21} configuration. Figure 4.21 shows a comparison of the data with the manufacturer's specifications by illustrating the maximum stroke over the frequency.

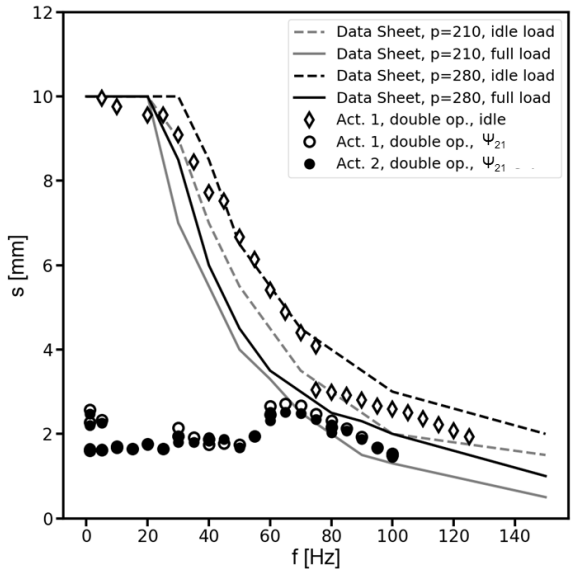

Figure 4.21.: Pretest; Actuator performance check; Idle load and Ψ_{21} configuration.

The data sheet gives information on the idle load and the full load configurations. The

latter means a load of eighty percent of the nominal actuator force. Besides the data for an oil pressure of $p = 280.0$ bar, data for $p = 210.0$ bar is illustrated, which is justified by the fact that the pressure of the pump is restricted during the WT experiment. Since the actuator piston carries components of the connection fixture, an exact agreement with the manufacturer's idle load data is not expected. The measured data shows clearly that the mean actuator performance is above the manufacturer's data for idle load performance at reduced oil pressure. Fluctuations in the slope of the actuator stroke with increasing frequency are caused by the additional adjustment of several control parameters during the tests. The quality of the resulting oscillation's sinusoidal shape was checked only with the bare eye, which may lead to more inaccuracies. Since the performance of the hydraulics lies in the range of the manufacturer's specifications, this rough approach is considered sufficient for the evaluation of the hydraulic system's operability. The left sets of experimental data are about the performance of two actuators operating simultaneous subject to Ψ_{21}-load conditions. Here, the most critical load conditions occur. For a frequency range from static conditions to dynamic conditions at $f = 100.0$ Hz, an actuator stroke of about $s = 2.0$ mm was maintained with satisfactory sinusoidal quality. In the final WT test setup, the hydraulic cylinders are mounted on a rack located behind the panel's rear, which is connected to the test setup's inner frame. In order to realize different deflection, the rack provides mounting slots for numerous actuator configurations, which is depicted in Figure 4.22 (a).

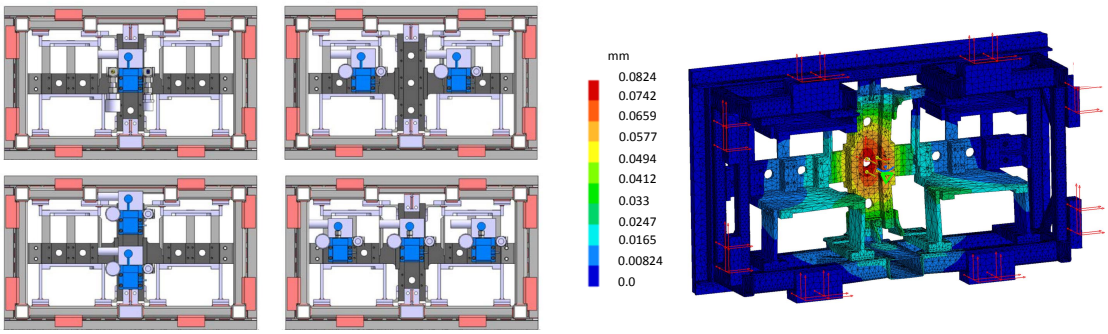

(a) Hydraulic actuator rack configurations. (b) Deformation due to maximum actuator force.

Figure 4.22.: Actuator rack

Depending on the rotational position of the panel (Figure 4.4), four different eigenfunctions can be simulated. The deflection of the panel is controlled by the actuator piston's stroke directly detected by the integrated displacement sensor. The force induced by the piston's stroke is naturally directed in both directions, which causes deformations of the panel and of the mounting rack. The mounting rack's deformation must be known in order to correctly indicate the deformation of the panel. Either the resulting deformation of the fixture must be included in the determination of the panel deformation, or the rack's deformations must be small enough to be neglectable. Results of a FEM calculation are presented in Figure 4.22 (b), which shows the rack's static deformation

of the ψ_{11} configuration at the nominal actuator force, which is by about $dz = 0.08$ mm. More information on the hydraulics' performance can be found in Chapter 6, which is about the measured motions in the WT experiment. A scheme of the complete hydraulic system is shown in Figure 4.23.

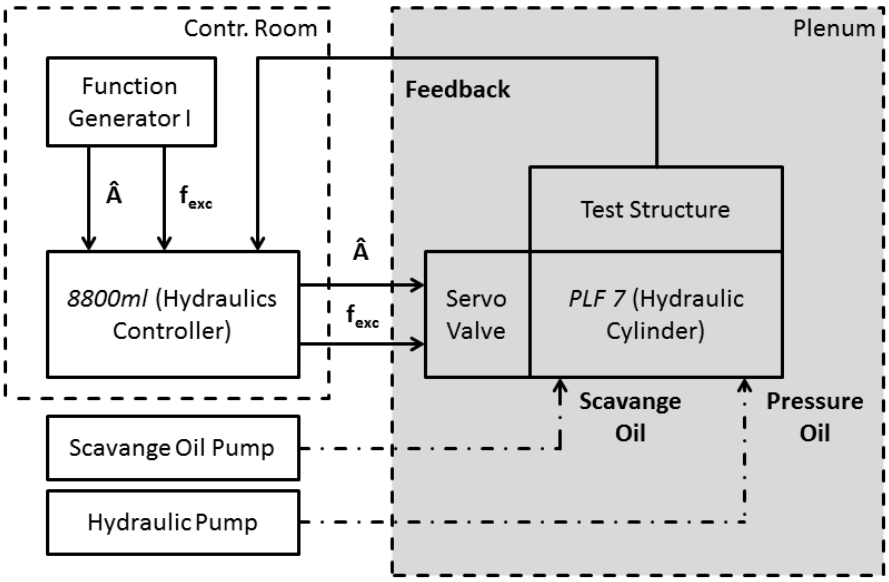

Figure 4.23.: Hydraulic system.

The operation of the hydraulics is controlled from the test facility's control room, where the oscillation of a cylinder (defined by frequency and amplitude) is set by an IST 8800ml Control Electronics hydraulic control unit. Its integrated Processor Control Module (PCM) allows the use of two channels, each of them is connected to one hydraulic actuator. The control signal defined by the excitation frequency and the actuator's stroke is generated and committed by a Yokogawa FG300 function generator. The adjustment of its output signal's voltage defines the magnitude of the actuator stroke. The data of the actuator's position sensor used for the control system's input is fed back to the 8800ml. Before a measurement point is recorded, the adjustment of frequency and amplitude is done manually.
Regarding the definition of parameters in Chapter 3, for future activities the possibility is given to exchange the actuator rack for a sealed and thus pressurizable cavity. During operation, the panel shall oscillate only with the intended excitation frequency and the required amplitude, which is given by the function generator. Thus, any overlap of the excitation frequency range and the natural frequencies of the test setup must be avoided. Based on the CAD model, FEM calculations on the eigenvalues of the setup were performed. Due to the outcome of those calculations, necessary refinement steps in the design (e. g. the adding of strutting structures) were done until a sufficient safety margin was reached. The results illustrated in Figure 4.24 and Table 4.2 come from the

CATIA CAD software included FEM solver.

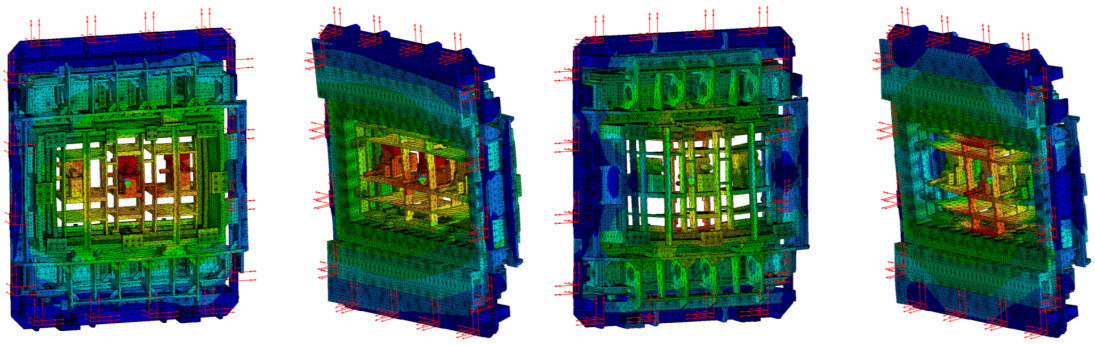

(a) First eigenfrequency at $f = 180.7$ Hz. (b) Second eigenfrequency at $f = 213.5$ Hz.

Figure 4.24.: Test setup eigenfrequencies ($\alpha = 90°$ configuration).

The model consists of 456911 tetrahedron elements (CTETRA) with 810623 grid points. The material has a Young's Modulus of $E = 200.0$ GPa, a density of $\rho = 7.86$ g/cm^3 and a Poisson number of $\nu = 0.226$. The connection points of the test setup's outer frame show constraints of all DOFs to simulate the connection to the wind tunnel wall. The design shown here is not the design finally manufactured and used in the wind tunnel tests and the test structure is not applied yet. An actuator configuration with three connected hydraulic cylinders is chosen, which should assure the lowest eigenfrequencies due to the additional mass. Since no additional major changes are implemented in the course of the design process, the performed calculations of the structure's eigenfrequencies are sufficiently accurate. The first and the second eigenfrequency are found at $f = 180.7$ Hz and $f = 213.5$ Hz, which is far away from the planned maximum excitation frequency. Illustrations of three more mode shapes mentioned in Tabular 4.2 can be found in the appendix of this document in Figure B.2 and Figure B.3.

Mode No.	**Frequency [Hz]**
1	180.7
2	213.5
3	232.4
4	276.8
5	289.2

Table 4.2.: Calculated test setup eigenfrequencies.

5. Testing Technology

After the introducing the test setup directly connected with the test structure to be investigated, this chapter contains the description of the remaining hardware required to perform the WT tests. The first section focuses on the description of the chosen test facility, whereas the second section's focus is on the presentation of the measurement technique applied to the test structure. The third and last section provides an overview of the various test campaigns carried out and shows which parameters and which parameter ranges were taken into account.

5.1. Wind Tunnel

The wind tunnel chosen for the present investigations is the Transonic Wind Tunnel Göttingen (DNW-TWG), illustrated in Figure 5.1. The closed return type wind tunnel allows experiments in a wide range of subsonic and supersonic Mach numbers. Constructional properties and design features are presented below to complete the presentation of the experimental setup. Subsequently, the test facility's measurement technique is described, which is used to control the wind tunnel on the one hand. On the other hand, the data on the flow conditions is recorded for the data analysis carried out later.

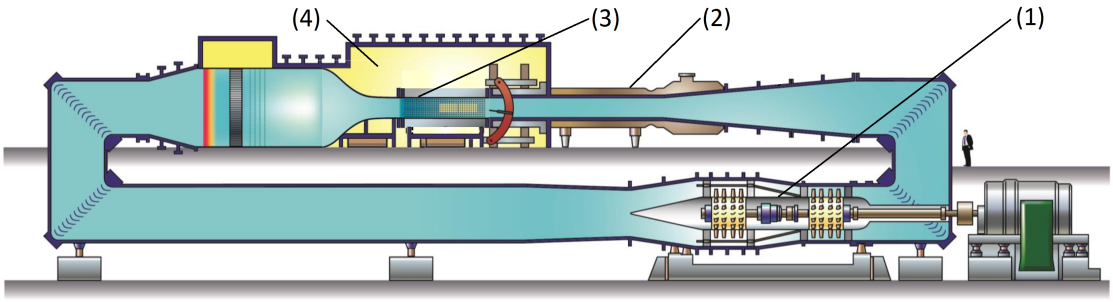

Figure 5.1.: Transonic Wind Tunnel Göttingen (DNW-TWG, source: DNW).

5.1.1. Design Parameters

Three interchangeable test sections are available: The Adaptive Test Section for experiments under subsonic flow conditions, the Laval Test Section providing supersonic Mach numbers and the Perforated Test Section enabling investigations in the required high subsonic and low supersonic flow at $0.7 < M_\infty < 1.2$. The Mach number is controlled

by a gradual increase of the compressor (1) rotation speed and a continuous adjustment of the Variable Diffuser (2), which is located downstream the test section. The diffuser's cross section, where a Mach number of $M_\infty = 1.0$ is established during operation, is adjustable by four lateral mounted electric motors in order to control the tunnel fluid mass flow. The Perforated Test Section (3) illustrated in Figure 5.2 has a cross section of one meter squared and is surrounded by a pressure chamber (4), which allows a variation of the wind tunnel's total pressure in a range of 35.0 kPa $< p_0 <$ 135.0 kPa. For the shown dimensions in direction of flow applies $x = x_{WT} - 2960$ mm. A constant Mach number throughout the entire test section's length is ensured through a slight divergence of the upper and the lower walls by $Div_{TWG} = 2.8$ mm/m. This assures a compensation for the increasing displacement thickness of the increasing boundary layer in flow direction. The established constant effective cross section of the test section leads to a constant Mach number in the test section, whose cross section. Another mechanism, which is necessary to cover the needed Mach number range, is assured by the wall perforation combined with a suction system, which allows an exceeding of the speed of sound in the test section. Fluid is let out through the perforated walls, which reduces the displacement thickness. The result is a displacement thickness that is De Laval Nozzle shaped in stream wise direction. A Mach number of $M_\infty = 1.0$ is established in its narrowest part, followed by supersonic flow conditions.

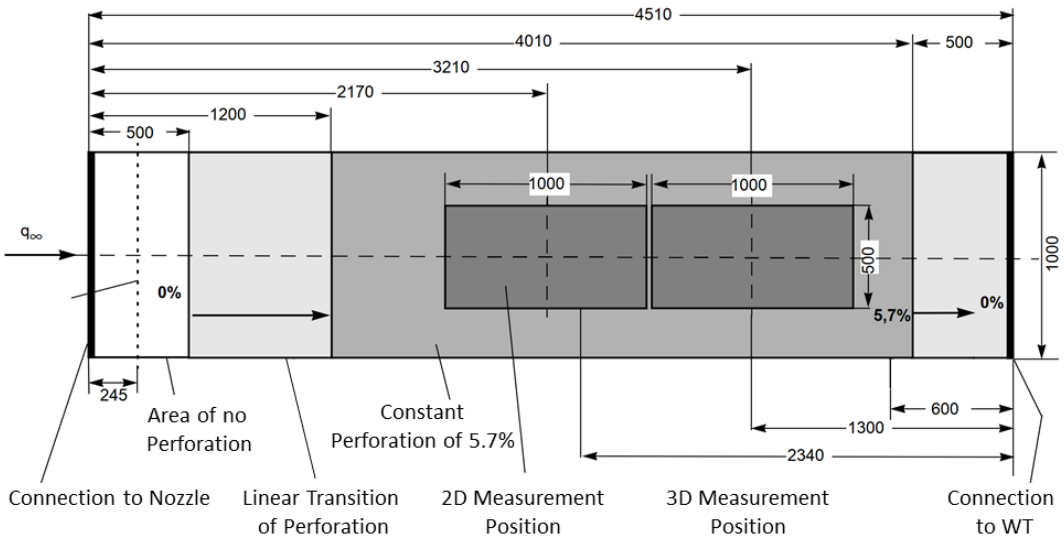

Figure 5.2.: TWG Perforated Test Section (Source: DNW).

At the test section's inlet, the walls show a perforation ratio of zero that gradually reaches a ratio of $A_{perf}/A_{wall} = 5.8\%$, as depicted in Figure 5.2. Referring to the shown Cartesian coordinates of the wind tunnel's test section, which extends from 0.0 mm $\leq x_{WT} \leq$ 4510 mm, two different locations for placing test setups are available. The 2D Measurement Position extends from $x_{WT} = 1670$ mm to $x_{WT} = 2670$ mm and is followed by the 3D Measurement Position that extends from $x_{WT} = 2710$ mm to

$x_{WT} = 3710$ mm. Figure 5.3 shows a more detailed view of the two test setup locations with each having an exchangeable square wall segment with an edge length of one meter.

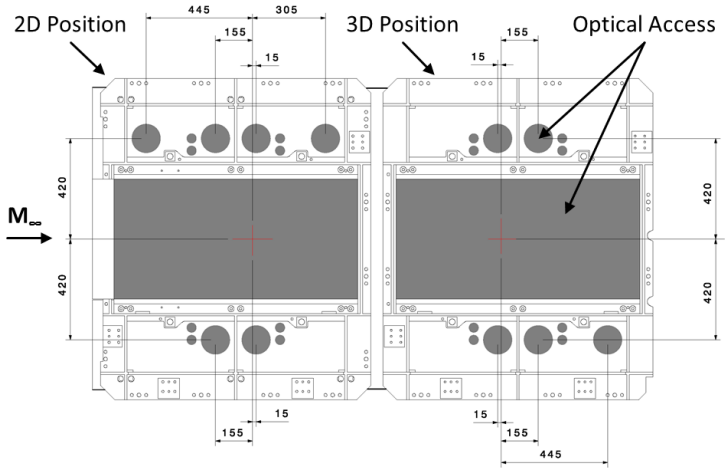

Figure 5.3.: DNW-TWG Measurement Positions.

Both measurement positions have several optical accesses for various measurement techniques. The accesses of the 2D Position located upstream are exchanged for purely perforated wall segments for the present experiments. For future activities, this position is considered to be suitable to apply a boundary layer control device, since its position is directly upstream of the test structure. The 3D-Position wall segment shown in Figure 5.3 is entirely exchanged for the test setup shown in Figure 4.4 (b). Analogue to the carried out FEM modal analyses of the test setup, extended calculations are carried out on the wind tunnel wall including the test setup, as is depicted in Figure 5.4 and Figure 5.5.

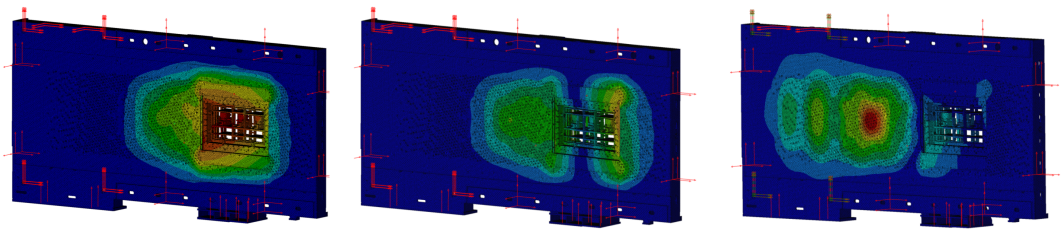

(a) Mode 1 at $f_1 = 102.5$Hz. (b) Mode 2 at $f_2 = 120.7$Hz. (c) Mode 3 at $f_3 = 152.9$Hz.

Figure 5.4.: Wind tunnel wall eigenmodes; Front view.

In order to take the remaining wind tunnel components into account, constraints of all DOFs are applied at the connection areas. The applied test setup, without the actual test structure, is considered to be a single component. The FEM model, including

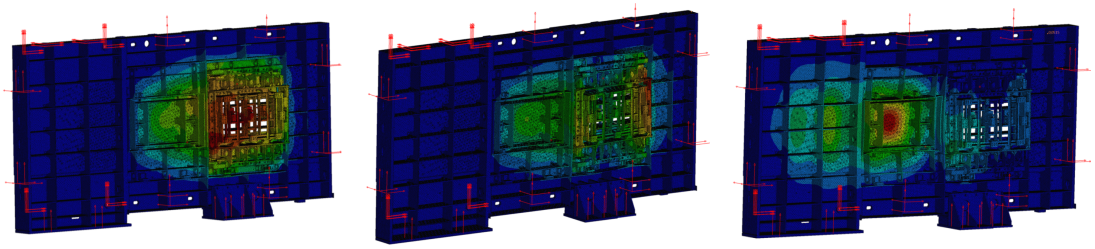

(a) Mode 1 at $f_1 = 102.5$Hz. (b) Mode 2 at $f_2 = 120.7$Hz. (c) Mode 3 at $f_3 = 152.9$Hz.

Figure 5.5.: Wind tunnel wall eigenmodes; Rear view.

the wall and the test setup, comprises $n_{El} = 1375909$ tetrahedron elements (TET10) with $n_{GP} = 2556862$ grid points. The results show eigenfrequencies of $f_1 = 102.5$ Hz, $f_2 = 120.7$ Hz and $f_3 = 152.9$ Hz, which means a decrease of the lowest eigenfrequencies in comparison with the test-section-only results presented in the previous section. Table 5.1 shows additional results of the same model obtained by using MSC Nastran, which prove the CATIA based values on the whole.

Mode No.	**Frequency [Hz], NASTRAN**	**Frequency [Hz], CATIA**
1	102.50	100.37
2	120.70	118.04
3	152.87	149.75
4	171.79	168.05
5	184.77	179.83

Table 5.1.: Wind tunnel wall eigenfrequencies; Comparison of CATIA and MSC Nastran.

5.1.2. Instrumentation and Data Acquisition

The wind tunnel components are controlled and monitored by a PLC (Programmable Logic Controller) based system combined with the data acquisition and controlling software DeAs. Once the test section's inlet geometry is reduced to constant effective cross section of one by one meter, steady pressure probes applied to the test section's wall measure the fluid's static pressure p_∞. The tunnel's total pressure p_0 is measured in the wind tunnel's settling chamber upstream of the test section, where also the total temperature T_0 is measured at four circumferential positions. The pressure p_k is measured in the plenum, which is the pressurizable chamber surrounding the test section. The global WT flow properties p_0, p_k and T_0, which are measured to operate the facility by DNW, are also recorded by the DLR-AE AMIS measurement system, which is described in detail later in this chapter. The error in pressure measurement is 0.01% of the sensor's full scale output (FSO), which is $p_{FSO} = 1.5$ bar. The error in measurement of the PT100 temperature probes is ± 0.5 K. The resulting errors in measurement are illustrated in

Table 5.2.

Quantity	p_0	T_0	p_∞	p_k
Error	$\pm$15 Pa	$\pm$0.5 K	$\pm$15 Pa	$\pm -$ 15 Pa

Table 5.2.: WT measurement errors (Source: DNW).

Based on those steady measurements done with an integration time of $t_{Int} = 1.0$ s and a maximum sampling frequency of $f_{DeAs,max} = 300.0$ Hz, additional quantities are calculated. The equations of isentropic gas kinetics lead to a preliminary Mach number

$$M^\star = \sqrt{\frac{2}{\gamma - 1}\left[\left(\frac{p_0}{p_k}\right)^{\frac{\gamma-1}{\gamma}} - 1\right]} \tag{5.1}$$

by using the total pressure, the plenum pressure and the heat capacity ratio γ. Following, based on characteristic parameters of the Perforated Test Section of the wind tunnel, a corrected Mach number M_∞ is calculated. The static temperature

$$T_\infty = \frac{T_0}{1 + \frac{\gamma-1}{2} M_\infty^2} \tag{5.2}$$

can be determined with the measured total temperature and the previously calculated corrected Mach number. For the determination of the Reynolds number Re, the dynamic viscosity

$$\eta = \frac{B_1 \cdot T_\infty^{\frac{1+\gamma}{4(\gamma-1)}}}{T_\infty + B_2} \tag{5.3}$$

is calculated with the parameters $B_1 = 1.4605 \cdot 10^{-6}$ and $B_2 = 110.4$. The fluid density

$$\rho_\infty = \frac{p_0}{R_s \cdot T_0} \cdot \left(1 + \frac{\gamma - 1}{2} \cdot M_\infty^2\right)^{\frac{1}{1-\gamma}} \tag{5.4}$$

is calculated following the ideal gas flow law and the laws of gas kinetics with the specific gas constant of air R_s. Finally, the free stream Reynolds number

$$Re = \frac{U_\infty \cdot l_{ref} \cdot \rho_\infty}{\eta} = \frac{U_\infty \cdot l_{ref}}{\nu} \tag{5.5}$$

is determined by using the free stream velocity

$$U_\infty = M_\infty \sqrt{\gamma R_s T_0} \tag{5.6}$$

, the reference length l_{ref} and the kinematic viscosity ν, the last resulting from the ratio of the dynamic viscosity and the fluid density. The free stream dynamic pressure is given as

$$q_\infty = \frac{\rho_\infty}{2} U_\infty^2 \tag{5.7}$$

is obtained by multiplying the fluid density by the square of the free stream velocity. The related propagation of measurement errors as a function of the Mach number is illustrated in Figure 5.6.

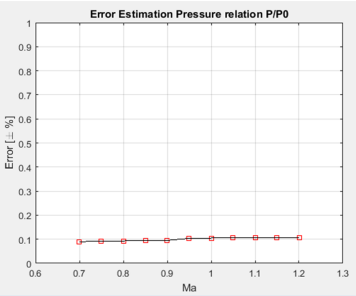

(a) Free stream static pressure maximum error versus experimental Mach numbers, for given total pressures.

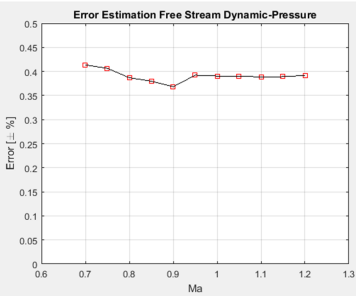

(b) Free stream dynamic pressure maximum error versus experimental Mach numbers, for given total pressures.

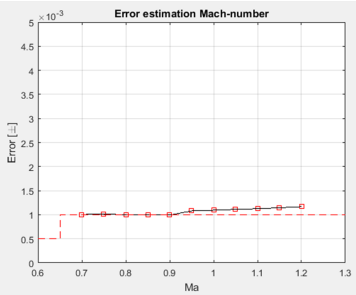

(c) Mach-Number maximum error versus experimental Mach numbers, for given total pressures.

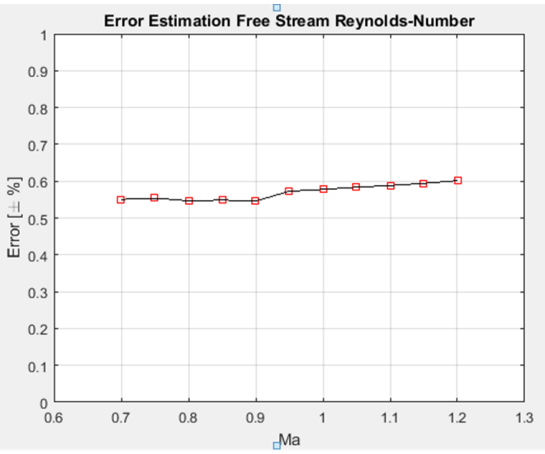

(d) Reynolds number maximum error versus experimental Mach numbers, for given total pressures.

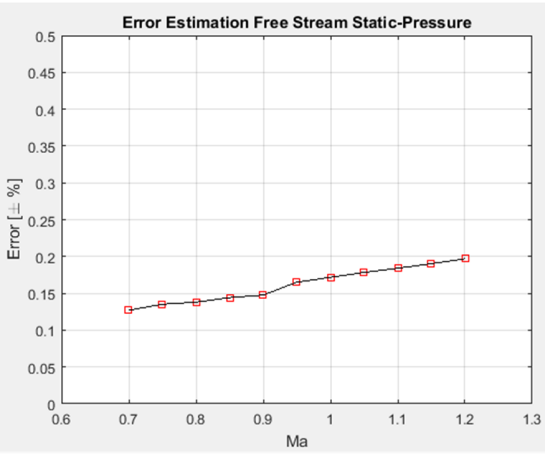

(e) Free stream static pressure maximum error versus exp. Mach numbers, for given total pressures.

Figure 5.6.: DNW-TWG measurement error estimation (Source: DNW).

5.1.3. Mach Number Accuracy

In preparation of the test campaigns several pretests were carried out to support the design process and to estimate the Perforated Test Section's characteristics under the new test setup's boundary conditions. One test focused on the resulting wind tunnel performance, when a large area of the perforated tunnel wall is covered with a plate corresponding to the final test setup dimensions. A negative impact was feared, since the perforated walls are essential components of the entire fluidic principle that enables the establishment of subsonic and supersonic flows. The used test setup mock-up was an aluminum plate of one meter by one meter, equipped with lines of steady pressure orifices in streamwise direction. The plate was adhered to that part of the wall to which the final test setup with the panel model is connected later as shown in Figure 5.7 (a). Based on the steady pressure measurements at different free stream Mach numbers and total pressures from $p_0 = 30.0$ kPa to $p_0 = 80.0$ kPa, the local Mach numbers throughout the test setup's length were calculated (Figure 5.8). Additional pressure orifices are distributed over the test section walls including the wall opposing the mock-up, which gave further pressure data.

(a) Test setup mock-up for pretest with three streamwise sections with pressure orifices.

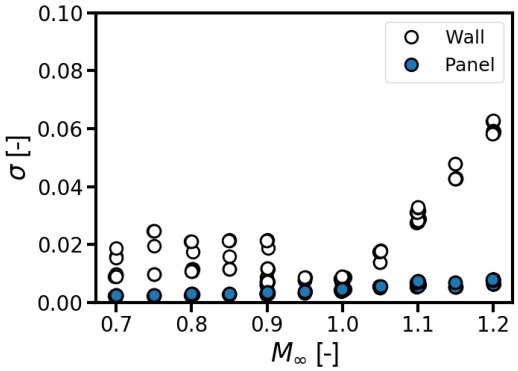

(b) Standard deviation of measured Mach numbers.

Figure 5.7.: Pretest II; Setup and measurement results.

The most important required information was whether it is possible to reach supersonic flow conditions in a test section that is crippled that way. Once the aspired Mach number was reached, its constancy throughout the covered length was examined to ensure that later in the test phase the entire panel will be exhibited to constant flow conditions. Figure 5.8 shows the Mach number calculated based on the measured static pressure probes of the WT walls throughout the whole test section. Examples for different nominal Mach numbers and different total pressures are shown, with the 2D Position and the 3D Position indicated by the vertical dashed lines. In contrast to the other parts of the test section that show only results of the WT wall, data of the test structure and the opposing WT wall are available at the 3D Position. In the subsonic domain, the nominal Mach number is maintained throughout the entire test section from the inlet

at $x_{TWG} = 0.0$ m to the end of the 3D position at $x_{TWG} = 3.71$ m with a deviation of less than one percent of the nominal Mach number (Figure 5.8 (a)) for almost all of the measured local Mach numbers. In contrast, a significant change in the Mach number characteristic can be observed in the supersonic domain. In the first part of the test section the subsonic flow of the wind tunnel's settling chamber is still accelerating until the nominal value is reached, which occurs shortly before the 2D Position. Comparative data without the applied mock-up are not available. For the remaining length of the test section, the deviation of the local Mach numbers slightly increases, though no significant deviations are obtained at the 3D Position, which is where the final setup will be located.

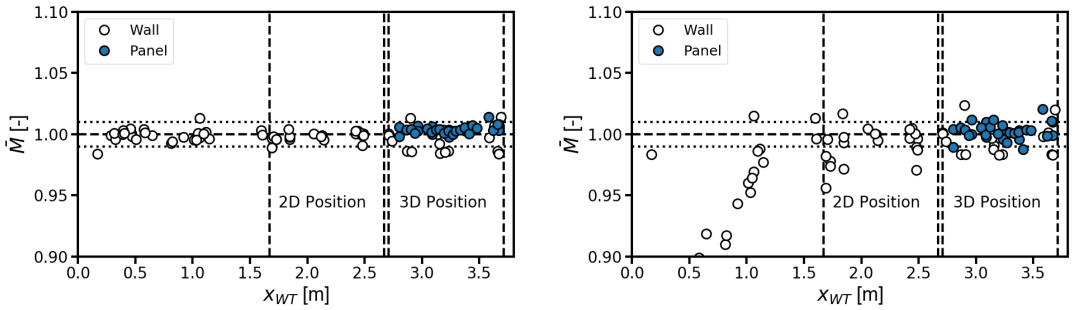

(a) $M_\infty = 0.7$; $p_0 = 30.0$ kPa.

(b) $M_\infty = 1.2$; $p_0 = 80.0$ kPa.

Figure 5.8.: Local Mach number in the TS normalized by the nominal Mach number.

The standard deviation σ, presented in Figure 5.7 (b), is calculated based on the local Mach numbers measured by pressure probes attached to the wall and the panel mock-up. An increase of the deviation is depicted for increasing Mach numbers, whereby the measurements by the pressure probes on the panel show considerably better results ($\sigma_{panel} < 0.1$) than those obtained directly at the wall. The deviation increases in particular for $M_\infty > 1.0$ and is caused by the impact of the data measured at the test section's inlet where the nominal Mach number is not yet established.
It has been shown that a panel structure applied to the test section, which is intended for the upcoming WT tests, does not interfere with the fluid mechanical functionality of the test section and thus the required flow quality remains guaranteed.

5.2. Measurement Technique

5.2.1. Data Acquisition Systems

For recording the experimental data in the wind tunnel tests, several measurement systems are required. The wind tunnel operator DNW carries out the steady measurements concerning the test facility with a measurement system that is called DeAs. Data acquisition in connection with the test structure is done by the DLR Institute of Aeroelasticity, which uses two additional systems for different unsteady measurement techniques. After

the data acquisition, the three data sets are combined for each measurement point to enable a subsequent analysis.

DeAs (DNW)

The DeAs system (German: Datenerfassungs- und Anlagensteuerungssoftware) collects steady data of pressure and temperature to monitor and operate the wind tunnel, as described in Section 5.1.2. In the present study, additional data of the flow boundary layer $p_{BL,n}$ with $n = 1...64$ is included. For each measurement point, an ASCII file with the measured quantities, the quantities derived from them and further wind tunnel system data, such as compressor speed and diffuser opening degree, is transferred to the DLR measurement system AMIS (Figure 5.9).

PicColor (DLR)

The PicColor deformation measurement system is a stand-alone system, which is exclusively used to measure the panel deformations caused by the flow and the actuating mechanism. An ASCII format file containing the spatial and temporal information $x(t)$, $y(t)$ and $z(t)$ of multiple points on the structure is submitted to the DLR AMIS measurement system for each measurement point, as shown in Figure 5.9. The dynamic data are subsequently synchronized to the data recorded by the AMIS main measurement system.

AMIS (DLR)

The AMIS (German: Anlage zur Messung Instationärer Signale) measurement system is the main data acquisition system of the DLR Institute of Aeroelasticity's Aeroelastic Experiment department. With the exception of the PicColor measurements, all unsteady measured quantities are recorded by this system, including pressure probes, the actuators' displacement sensors and the acceleration sensors. Using the example of the pressure measurement in Section 5.2.2, the principle of the measurement process is depicted in Figure 5.12. The signal from a sensor is first amplified and then split up into two signals, each connected to one of the two identical data acquisition systems of the Dewetron company [88]. Each Dewetron system consists of a computer unit with an applied front-end that comprises 128 24-bit Delta-Sigma A/D converters with a maximum sampling frequency of $f_{samp,max} = 204.8$ kHz. The first system serves for the acquisition of the data recorded by the AMIS system through an Ethernet connection. The second system is used to display the current measurement data for live monitoring purposes. The same function generator as used for controlling the hydraulics also sends two different TTL (Transistor-Transistor Logic) signals to the AMIS system, which defines the sampling frequency for each measurement point. The first signal frequency f_{S1} corresponds to the actuator excitation signal f_{exc}, whereas the second signal frequency

$$f_{S2} = f_{exc} \cdot 512 \cdot 128 = f_{samp} \cdot 512 \tag{5.8}$$

is the sampling frequency f_{samp} multiplied by an oversampling factor of 512. The sampling frequency allows a recording of $n = 128$ points per period of oscillation. Depending on the excitation frequency and the recording time per measurement point, the recorded numbers of periods are:

$$n_{Per,1-3} = 64, 160, 640 \tag{5.9}$$

A trigger signal of the AMIS releases a synchronized measurement of DeAs and AMIS system, whereas an ideal synchronization of the PicColor system is not possible yet. The recorded raw data is equivalent to the voltage data coming from the sensors that are connected to the Dewetron's analog input. Additional data on sensor sensitivities, offsets, defective sensors etc. is stored in the AMIS system. That additional data is used for the subsequent processing of the raw data. The processed data is then written in a nc-file output that contains the whole data set required for data post processing.

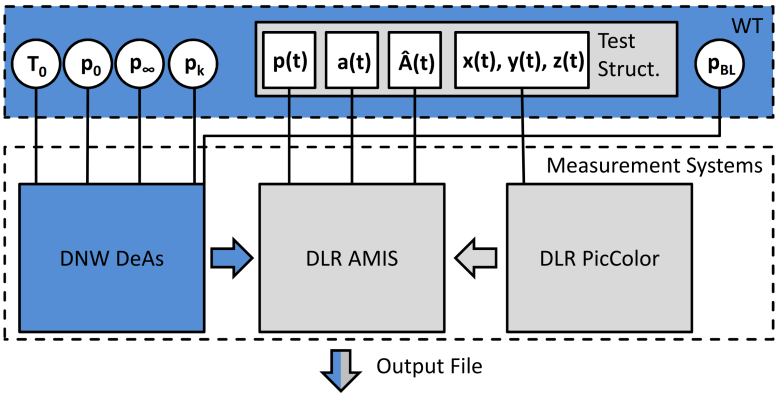

Figure 5.9.: Measurement system compound.

5.2.2. Pressure Probes

Unsteady reference pressure transducers of the type Kulite-XCS-093, illustrated in Figure 5.10 (a), have been fixed on the model to measure the aerodynamic response caused by the oscillating structure. Reference pressure transducers work on basis of the application of two different pressure sources, where each acts on one side of a piezo resistive diaphragm. On the rear side, a reference pressure is applied. On the front side, the pressure to be measured is connected, which leads to a measurement of the pressure difference as shown in Figure 5.10 (b) [89].

- **Pressure sections of Ψ_{11} model:**
  Spanwise: $y_{p,2} = 0.25w_i$, $y_{p,1} = 0.5w_i$, $y_{p,3} = 0.75w_i$
  Streamwise: $x_{p,5} = 0.25l_i$, $x_{p,4} = 0.5l_i$, $x_{p,6} = 0.75l_i$
- **Pressure sections of Ψ_{21} model:**
  Spanwise: $y_{p,2} = 0.25w_i$, $y_{p,1} = 0.5w_i$, $y_{p,3} = 0.75w_i$
  Streamwise: $x_{p,5} = 0.29l_i$, $x_{p,4} = 0.5l_i$, $x_{p,6} = 0.71l_i$

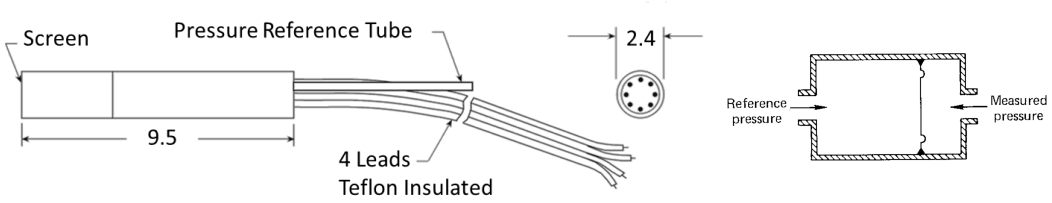

(a) Kulite dimensions (in mm) [90].

(b) Kulite schematical [89].

Figure 5.10.: Unsteady pressure measurement; Reference pressure transducer Kulite-XCS-093 [90].

The pressure differential leads to a change in length and thickness of the diaphragm that causes a detectable change in output voltage due to the associated change in the diaphragm's electric resistance. The used transducers have a pressure range of 0.35 bar and an acceleration sensitivity (transversal) of $2.2 \cdot 10^{-4}$% FSO. The combined maximum error due to non-linearity, hysteresis and repeatability is 0.5% FSO. In the experiment, the applied reference pressure is p_k, which is the total pressure in the plenum. Since all reference tubes are connected, all transducers have the same reference pressure level. The transducers ($n_{p,\Psi 11} = 98$, $n_{p,\Psi 21} = 109$) are arranged in three streamwise and three spanwise sections across the panel, as presented in Figure 5.11.

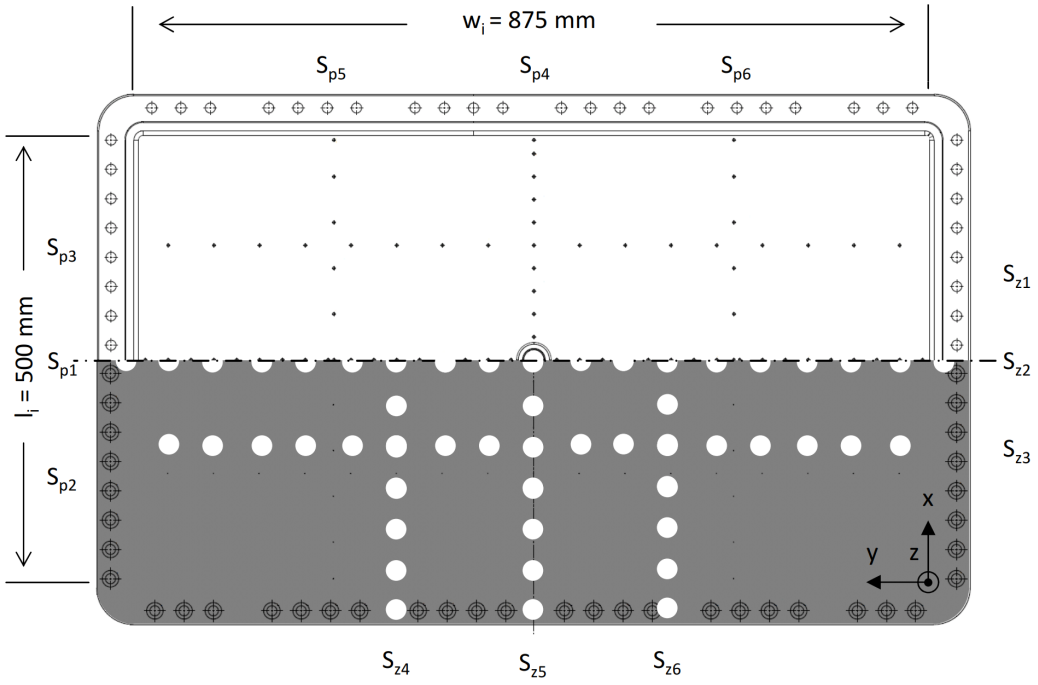

Figure 5.11.: Ψ_{11} test structure with applied pressure probe pattern (top) and marker pattern for deformation measurements (bottom).

98 transducers are applied to the Ψ_{11} panel, whereas 109 transducers are mounted to the Ψ_{21} model. Each transducer is put in a plastics carrier, which is a small tube bent by an angle of 90°. This ensures that the transducer's effective direction is orthogonal to the arising acceleration forces that are caused by the actuator. For a proper fit, each carrier is adhered in a step hole. The short distances between sensor and panel surface lead to small enclosed volumes that have a negligible influence on the resulting transfer function within the frequency range used in the wind tunnel tests. The measurement system for the pressure data acquisition is the DLR-AE AMIS system, which is connected to a Dewetron data acquisition system. Before reaching the DAQ device, each sensor signal passes an amplifier that is located in the plenum, as shown in Figure 5.12.

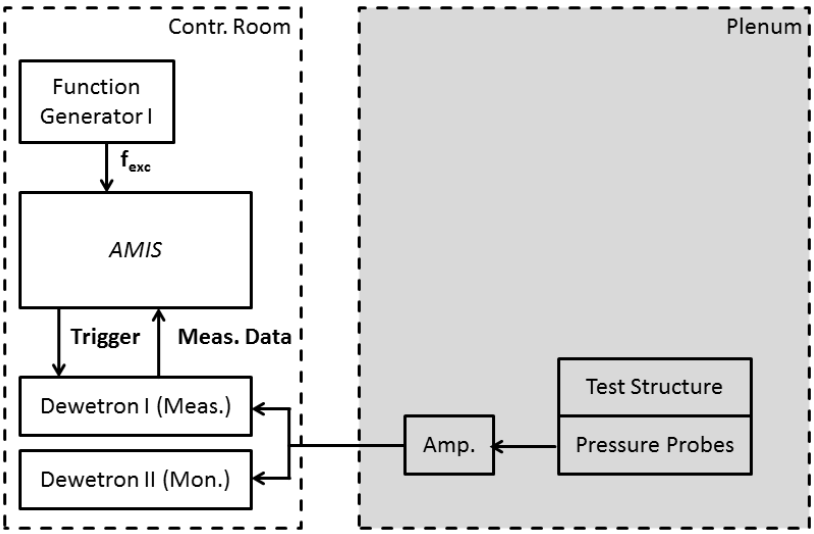

Figure 5.12.: Pressure acquisition system schematic.

At the start of each test run, a calibration of the pressure transducers is done within a pressure range of -21.0 kPa $\leq p_{ref} \leq 21.0$ kPa. During the calibration, a compressor and a vacuum pump provide the required pressures at the reference connection. To perform the calibration, a magnetic valve switches from measurement operation (with the reference p_k) to calibration operation (with the reference p_{ref}). The calibration reference pressure is provided by the pressure calibration device DPI 510 of the Druck Messtechnik GmbH Company. The calibration device can be adjusted with an accuracy of 0.004% FS with a full scale of $p_{FSO} = 50.0$ kPa [20]. The resulting pressure-voltage dependency of each transducer is fitted by a third order polynomial function, whose coefficients are used to prove the calibration. Since a linear dependency corresponds to the manufacturer's specifications, the coefficients representing the higher orders are expected to be negligible. For proving a linear dependency corresponding to the manufacturer's specifications the coefficients representing the higher orders must be negligibly small. The resulting sensitivities are recorded and stored for the following test runs. After a test run is completed, the AMIS software converts the voltage raw data into pressure data,

which is then filed by means of nc-type output files used in the subsequent data analysis. Besides the pressure data, these files contain pressure coefficient data (Equation 5.10) calculated using the steady wind tunnel data that is recorded and transferred to DLR AMIS by the DNW DeAs system:

$$c_p = \frac{p_0 - p_\infty}{\frac{1}{2}\rho {U_\infty}^2} \tag{5.10}$$

The complex amplitude of the pressure coefficients at the excitation frequency is basically used for further analyses and is calculated for each sensor at each MP. A Fast Fourier Transformation (FFT) is used to transfer the measured and calculated pressure coefficient time domain data $c_p(t)$ into the frequency domain $c_p(f)$ as shown in Equation 5.11:

$$c_p(f) = \frac{2.0}{128 \cdot n_{per}} \mathcal{F}\left(c_p(t)\right) \tag{5.11}$$

Due to the chosen resolution per period of $n = 128$ and the set excitation frequency, a time discretization of

$$\Delta t = \frac{T_d}{n_{per} \cdot 128} = \frac{1}{128 \cdot f_{exc}} \tag{5.12}$$

with the total time of measurement T_d results. The frequency discretization

$$\Delta f = \frac{f_{samp}}{n_{per} \cdot 128} = \frac{f_{exc}}{n_{per}} \tag{5.13}$$

is calculated with the sampling frequency f_{samp}. In order to get the complex amplitude of the pressure coefficient belonging to the actuator's excitation frequency, the n_{per}-th element of the frequency domain is selected, which is $c_p(f = f_{exc} = n_{per} \cdot \Delta f)$. The high number of periods recorded in every MP ensures a good signal average value. Figure 5.13 (a) shows five periods of an exemplary recorded sensor time signal at a low excitation frequency, while Figure 5.13 (b) depicts the related FFT results for numerous numbers of periods at the same excitation frequency. The ordinate shows the absolute values of the complex pressure coefficient data. With increased number of periods from $n_{per} = 5$ to $n_{per} = 40$, slight changes in the amplitude are depicted. Amplitudes for a complete set of periods at various excitation frequencies are shown in Figure 5.13 (c). For low numbers of periods, significant changes in the pressure's amplitude occur. For increased numbers of periods, the pressure coefficient's amplitude, normalized by the final value, is going toward its stable average value.
The total maximum of measurement error of the pressure transducers can be calculated

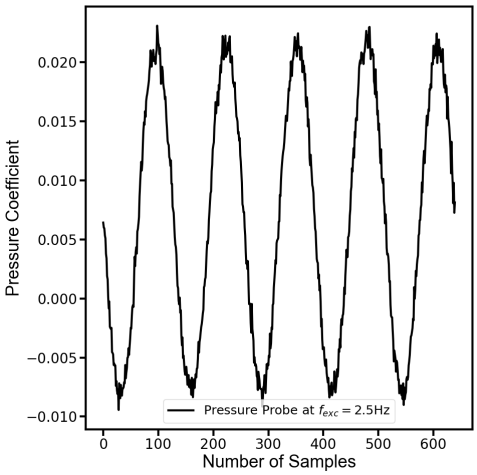

(a) Time signal $c_p(t)$ for $n_{per} = 5$; $f_{exc} = 2.5$ Hz.

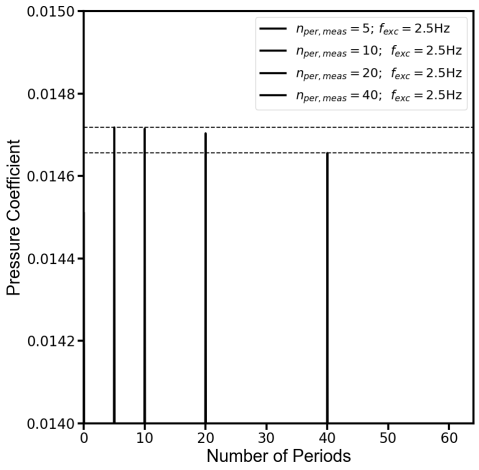

(b) FFT of time signal $c_p(t)$ for different numbers of periods.

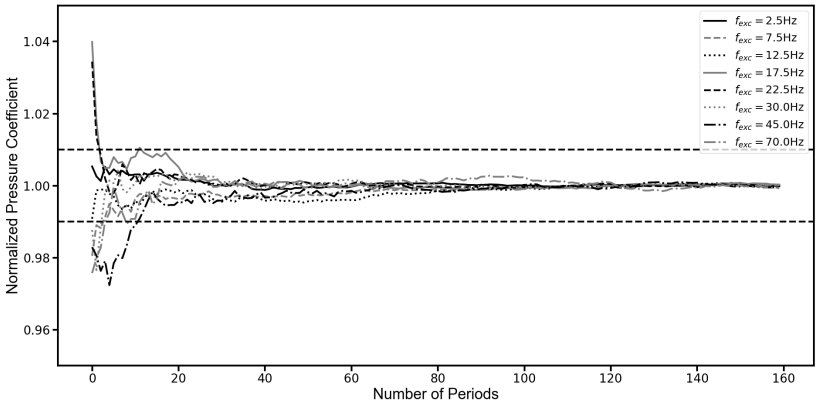

(c) Signal average amplitude depending on the recorded number of periods.

Figure 5.13.: Nondimensional pressure coefficient signal at $x = 0.55 l_i$ and $y = 0.5 w_i$; $M_\infty = 1.2$; $Re = 2.5 \cdot 10^6$; $\hat{A} = 1.8$ mm.

as follows [90]:

$$E_{p,max} = 0.5 \cdot \frac{FSO_p}{100} = 0.5 \cdot \frac{35}{100} = 0.175 \text{ kPa} \tag{5.14}$$

The maximal error in pressure coefficient depends on the dynamic pressure and therefore on the Reynolds number and on the total pressure:

$$E_{c_p,max} = \frac{E(p_0 - p_\infty)}{\frac{1}{2}\rho {c_\infty}^2} = \frac{E_{p,max}}{q_\infty} \tag{5.15}$$

A survey on the possibly maximum measurement errors is shown in Table 5.3.

Re	q_{min} [kPa]	q_{max} [kPa]	$E_{c_p,max}(q_{min})$ [-]	$E_{c_p,max}(q_{max})$ [-]
$2.5 \cdot 10^6$	≈ 10	≈ 15	$17.5 \cdot 10^{-3}$	$12.5 \cdot 10^{-3}$
$5.0 \cdot 10^6$	≈ 20	≈ 30	$8.75 \cdot 10^{-3}$	$5.83 \cdot 10^{-3}$
$7.0 \cdot 10^6$	≈ 31	≈ 44	$5.65 \cdot 10^{-3}$	$3.98 \cdot 10^{-3}$

Table 5.3.: Maximum pressure transducer measurement error.

Dynamic Calibration

Since obtaining the exact temporal phase angle of the pressure's response relative to that of the structure's motion is crucial for the examination of energy transfer between structure and fluid, an observation of the dynamic characteristics of the pressure probes is done. The following analysis is based on the assumption that the pressure, due to inertia forces on an oscillating surface, exhibits a phase angle of $\varphi_{t,p-s} = \pi$ related to the structure's motion. At $M_\infty = 0.0$ conditions, the panel structure is moved at numerous excitation frequencies. The resulting deviation $\Delta\varphi_t$ from the phase angle $\varphi_{t,p-s} = \pi$ is plotted in Figure 5.14 (a) over the range of tested excitation frequencies.

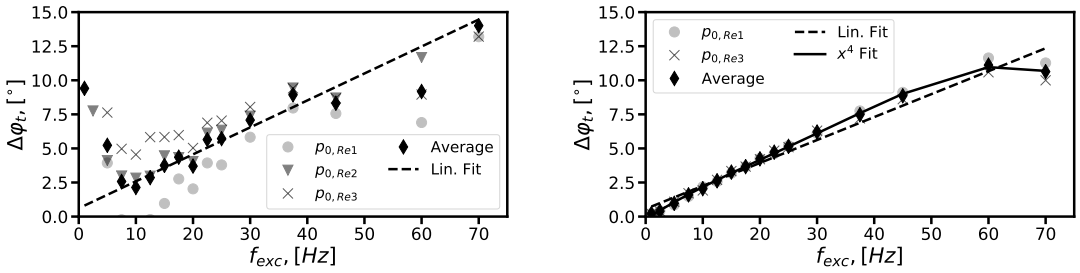

(a) M=0.0; Curve fit.

(b) M=0.7; Curve fit.

Figure 5.14.: Calibration data set; Ψ_{11} test campaign (2017).

The results are approximated by a linear curve fit that shows significant deviations, particularly in the low frequency range. These deviations result from the facility's wind-off conditions that cause very weak measurement signals due to small emerging pressure differences. This is even increased in the low frequency range because slow forced motion induces low inertia forces. Nevertheless, by respecting neither the low frequency range nor the results of the two maximum frequencies, the illustrated linear curve fit of the average values is satisfying.Additional results at $M_\infty = 0.7$ prove the results at $M_\infty = 0.0$. The transducer shows a more distinct signal under these flow conditions within the whole frequency range. The resulting linear fit (and the additional illustrated x^4 fit) is almost identical to the one calculated at $M_\infty = 0.0$. The described procedure is performed for each test campaign only for pressure probes located at points of

large deflections, which ensures distinct signals. Sensors located at the outer domains provide high noise afflicted results. The obtained linear curve fits are used to correct the measured pressures. The belonging figures for the first of the two performed Ψ_{11} test campaigns and the Ψ_{21} campaign are presented in the appendix in Figure C.4 and Figure C.5.

5.2.3. Acceleration Sensors

Acceleration probes of the type 352C22 of the PCB Company, illustrated in Figure 5.15 are used to monitor the test setup's vibrations. The certified measurement range of the uniaxial sensors is $a_{ACC} = \pm 4900$ m/s^2 with a frequency range from $f_{ACC,min} = 1.0$ Hz to $f_{ACC,max} = 10$ kHz [91]. The main purpose of the accelerometers is the observation of structural vibrations that occur during the tests. Due to requirements arisen during the test campaigns, the number of used sensors and their locations were changed several times, of which two major areas of application are discussed in this document.

Figure 5.15.: Accelerometer PCB 352C22 [91].

Sensors attached to the panel and the test frame structure, which is illustrated in Figure 5.16 (a), show if significant motion is transferred to the frame. It must be assured that the panel and the hydraulic actuator behind it are the only moving parts in the experiment. Additional sensors are placed on components of the instrumentation to ensure a proper operation. One of those components is one of the two cameras of the marker tracking deformation measurement SPR system, which is described in detail in the following section. Here, a mechanical decoupling between the camera and the moving test structure is crucial. During the various test series, the frame applied acceleration sensors, with the numbers five to seven, are changed from the panel frame to one of the cameras for monitoring the potentially arising vibrations. Those vibrations may lead to massive errors in the marker tracking (Figure 5.16 (b)). Every motion of the camera means a deviation from its calibration position, which may lead to unpredictable mismeasurements. Thus, not only oscillations at the particular excitation frequency are of interest, but every kind of movement.

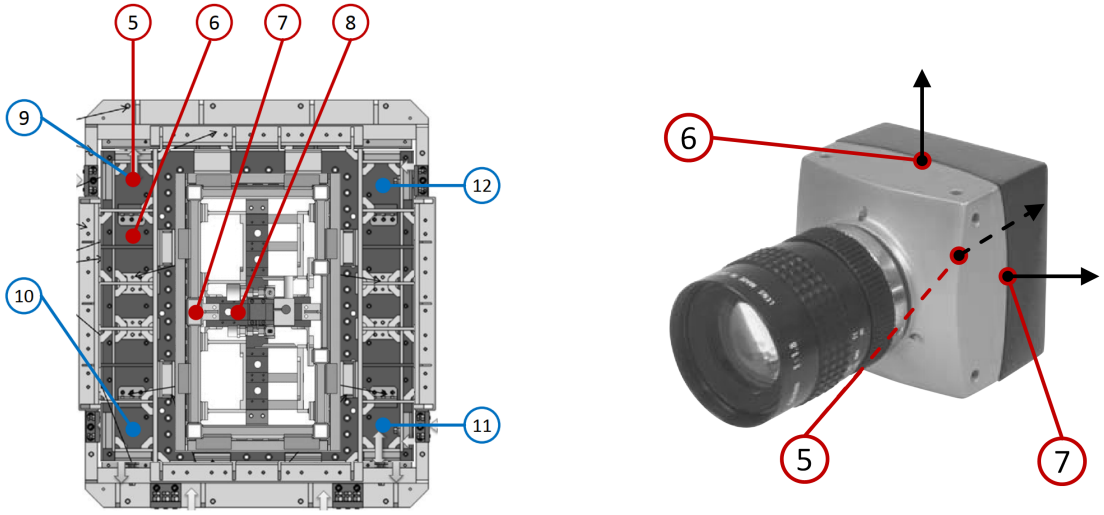

(a) Test setup; Ψ_{11} test campaign 2015 (red) and Ψ_{21} test campaign 2017 (blue).

(b) SPR camera; Ψ_{11} test campaign 2015 alternative positions [92].

Figure 5.16.: Acceleration sensor positions.

5.2.4. Deformation Measurement

Several measurement techniques are used for the determination of structural displacements, some of which have different areas of application and some are giving redundant information. The latter applies for the two main deformation measurement techniques, which are the Stereo Pattern Recognition System (SPR) and the position sensors integrated in the hydraulic cylinders. Both of them give information on the actuator stroke, which is also the structure's deflection amplitude, whereas the SPR system additionally gives data on the entire structure. In addition to those two techniques, further techniques, such as laser vibrometers and laser triangulators, are used.

Position Sensor (Hydraulics)

The actuator's piston stroke is measured by the actuator integrated position sensor Messotron WLH 20 C, whose signal is directly used to control the hydraulic system and thus the actuator's oscillation. In theory, the actuator stroke s is equivalent to the evoked deformation amplitude $\hat{A}$ of the structure (dz in Figure 4.1), which is why the obtained data is in addition essential for the subsequent data analysis. The SPR system measuring the structure's amplitude is not perfectly synchronized to the unsteady instrumentation, which is integrated in the DLR-AMIS system. Therefore, the redundant data on the amplitude ($s(t)$ and $\hat{A}(t)$) also serves the purpose of synchronization. The sensor works on the principle of an inductive bridge circuit with two variable electrical resistances. A ferromagnetic core, which is attached to the moving part of the actuator, changes the impedance of two electromagnetic coils in the center of which it moves, as illustrated in Figure 5.17.

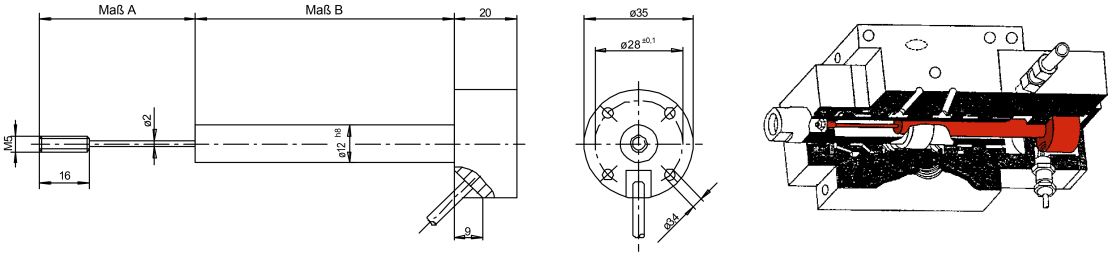

(a) Sensor dimensions [93].

(b) Position in actuator [87].

Figure 5.17.: Position sensor Messotron WLH 20 C.

This counteracting change of each coil's impedance causes a voltage, which is a measure for the core's position. Technical details are given in Table 5.4 and in the data sheet that can be found in Appendix C.

Dimension	**Value**
Nominal Stroke	±10 mm
Nominal Output Signal	80 mV/V
Sensitivity	8 mV/V/mm
Excitation Voltage	5 V
Linearity (Error)	±0.25 % FSO

Table 5.4.: Technical details; position sensor Messotron WLH 20 C.

The sensors are calibrated prior to each test campaign with the use of laser triangulators that exhibit a high accuracy and that are presented in Section 5.2.4. The results of the calibration, which are illustrated in Figure 5.18 for the Ψ_{11} configuration (a) and the Ψ_{21} configuration (b), show the variation of frequencies at different amplitudes, which are divided by the laser measured values, within a frequency range from $f_{exc} = 1.0$ Hz to $f_{exc} = 50.0$ Hz.

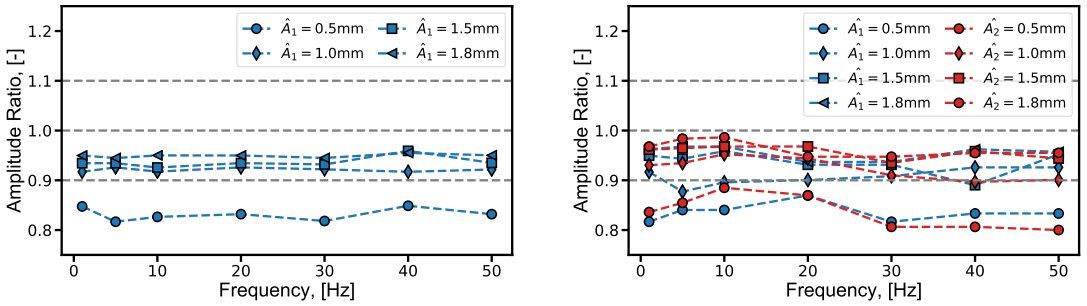

(a) Ψ_{11} calibration.

(b) Ψ_{21} calibration.

Figure 5.18.: Position sensor calibration.

Amplitudes $\hat{A} \geq 1.0$ mm show constant deviations of about 5% compared with the lasertriangulator measured values for the whole tested range of frequencies. The lowest amplitude shows an increased deviation of about 20% compared with the laser reference data. Nevertheless, the deviations are constant for the complete range of tested frequencies. Referring to the representation of pressure measurement data in Figure 5.13 (a) and (b), exemplary sensor time signals and the development of the measured averaged stroke amplitude, as a function of the numbers of measured periods, is depicted in Figure 5.19. Those normalized oscillations, which are shown for three different frequencies in the left figure, have a phase angle shift that is only added to better distinguish the curves. Assuming a pure sinusoidal oscillation being the optimum, no discrepancies at low and medium excitation measurements are recognizable by bare eye. Only for high frequencies at $f_{exc} = 90$ Hz, slight inaccuracies can be observed. The right figure shows the averaged and normalized amplitude for numerous frequencies depending on the measured numbers of periods, which show negligible variations even in the low frequency range. The analysis of the position measurements is done as described in Section 5.2.2.

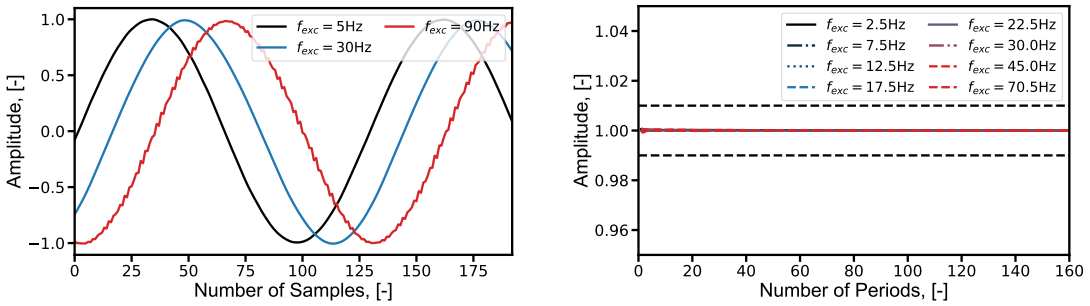

(a) Time signal for $n_{samp} = 1.5 \cdot 128$.

(b) Signal average amplitude $|\hat{A}(f_{exc})|$ depending on the number of periods, based on FFT.

Figure 5.19.: Nondimensional position sensor signal evaluation; Results gained at $\hat{A}_N = 1.8$ mm, $M_\infty = 0.7$ and $Re = 5 \cdot 10^6$.

Laser Vibrometer

A Polytec PSV-400-3D laser scanning vibrometer, whose measurement principle is based on the optical Doppler frequency, is used to get further information on the structure's deformation. The characteristic values enable the recording of data in a frequency range of 0.0 Hz $< f_{LDV} <$ 80 kHz with maximum deformation velocities of $\dot{z} = 10$ m/s. The system's main two components are the control unit, which allows the application of up to three measurement heads and contains the data acquisition unit, and the measurement head with the laser having a wave length of $\lambda_{LDV} = 633$ nm. The latter is deployed in the WT plenum and points through a large optical access located opposite of the test structure into the test section and thus on the test structure, as illustrated in Figure 5.20 (a).

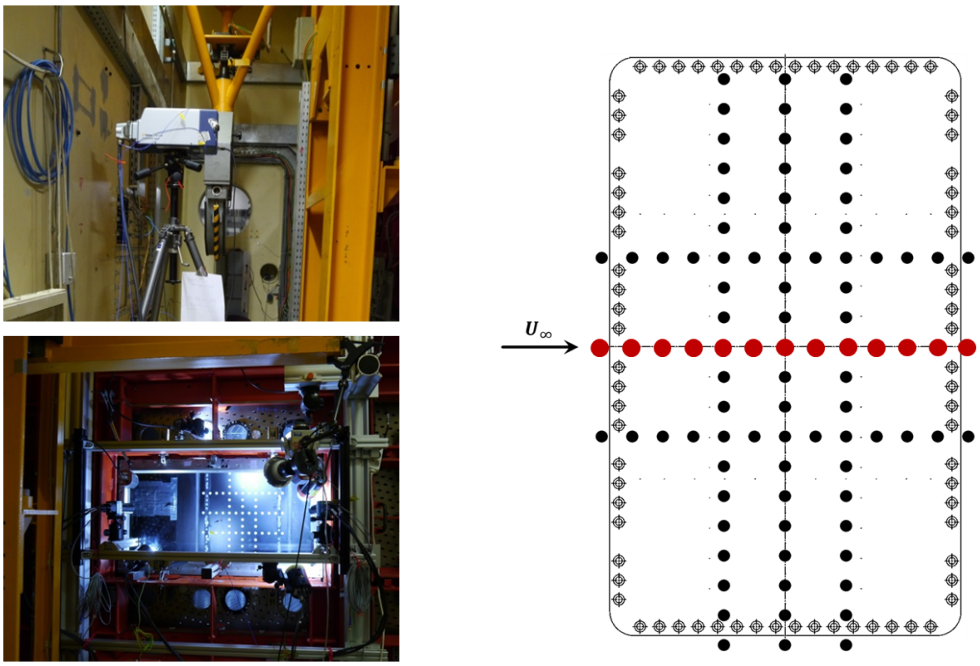

(a) Top: Vibrometer measurement head within the WT plenum. Bottom: View of the measurement head from outside the TS on the test structure.

(b) Positions of laser vibrometer measurements on the test structure (colored red).

Figure 5.20.: Laser vibrometer Polytec PSV-400-3D.

Light emitted by the measurement head's integrated laser and scattered by the moving target structure is captured again by the measurement head and is compared with the initially emitted reference light. A frequency shift is indicated by the integrated interferometer, which is proportional to the surface's velocity [94]. Due to limitations in the device's availability, the scanning pattern is confined to a line of thirteen markers that are located at half-span position and are arranged in flow direction. Figure 5.20 (b) shows the selected pattern, which is a subset of the SPR system's associated marker pattern. The vibrometer's output quantity is the structure velocity, whose analysis is done in the same way as presented in Section 5.2.2. Here, a multiplication by the excitation angle velocity ω_{ext} is needed to obtain the deformations in z-coordinates. Unlike the data acquired by the AMIS system, the sampling frequency is set to a fixed value and is not a function of the excitation frequency. Furthermore, this measurement system is not synchronized with any of the other systems.

Lasertriangulator

The Micro Epsilon ($\mu\epsilon$) Opto 1607-50 non-contact optical displacement measurement systems lasertriangulators are used for the calibration of the hydraulic actuators prior to each test campaign. Furthermore, they were used extensively during the preparatory

test campaigns, which focused on the tests regarding the actuator performance and its limitations due to the attached test structures (Section 5.2.4). For that purpose, the laser devices were directed onto the cylinder piston's upper surface or onto the corresponding part of the attached test structure located directly above. The analogue voltage output of the sensor, linearly related to the travelled distance, is connected via a BNC connection to the Dewetron DAQ systems. Emitted laser light of the triangulator is projected onto a structure, scattered by it and finally collected by a lens that is also located in the triangulator. Depending on the light's angle of incident, a position sensitive device (PSD) calculates data on the distance as shown in Figure 5.21 [95].

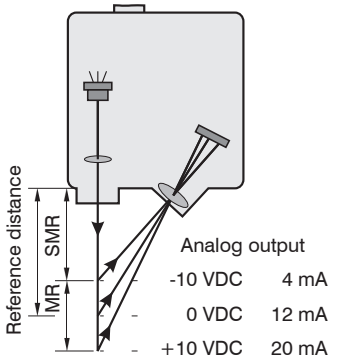

(a) Laser triangulator; Principle [95].

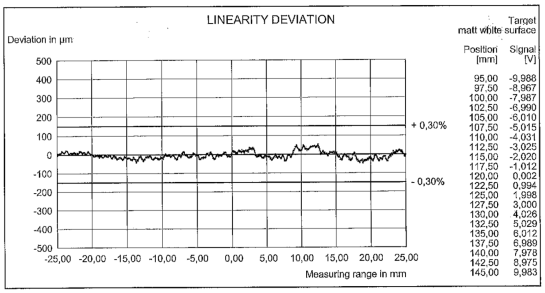

(b) Calibration report; Extract; Serial number 1010-1682; 2014.

Figure 5.21.: Laser triangulator $\mu\epsilon$ Opto 1607-50.

Besides the actual measurement signal, another analogue output line gives information on the intensity of the received signal, which is important to achieve proper measurement results. The laser data gained in this way serves as a reference value, which is compared with the actuator's position sensor information for calibration. The triangulators have a measurement range of ±25.0 mm with a reference distance of 120 mm, which is depicted in Figure 5.21 (a). Further technical details are shown in Table 5.5. The calibration report of one of the used devices is presented in Figure 5.21 (b), which confirms its high precision of measurement with a deviation less than $100\mu m$.

Dimension	**Value**
Output Voltage	-10V ... +10V
Sensitivity	20V/50mm
Ref. Distance (MR)	120mm
Start Meas. (SMR)	95mm
Range	±25mm

Table 5.5.: Technical details; Laser triangulator $\mu\epsilon$ Opto 1607-50.

SPR

The main deformation measurement technique used to measure the complete shape of the structure is the stereo camera based marker tracking (or stereo pattern recognition (SPR)) system PicColor. Two cameras point at different angles on the test structure that exhibits a pattern of markers distributed all over the camera faced surface, which can be seen in the lower half of the panel shown in Figure 5.11. Based on the 2D images recorded by each of the cameras, the position of the captured and tracked markers is calculated and transferred into the 3D space. For both investigated structures, $n_{marker} = 90$ markers are distributed over the panel surface ($n_{marker,panel} = 78$) and its frame ($n_{marker,frame} = 12$) in three streamwise and three spanwise lines (S_{z1} to S_{z6}) (Figures 5.11 and 5.20 (b)):

- **SPR marker sections of Ψ_{11} and Ψ_{21} model:**
  Spanwise: $x_{SPR,1} = 0.70l_i$, $x_{SPR,2} = 0.5l_i$, $x_{SPR,3} = 0.30l_i$
  Streamwise: $y_{SPR,4} = 0.67w_i$, $y_{SPR,5} = 0.5w_i$, $y_{SPR,6} = 0.33w_i$

Due to insufficient illumination during the experiment, the number of markers actually available for each particular MP may differ from these numbers. The cameras are located outside the WT test section with a maximum distance in x- and y-directions, as shown in Figure 5.22 (a).

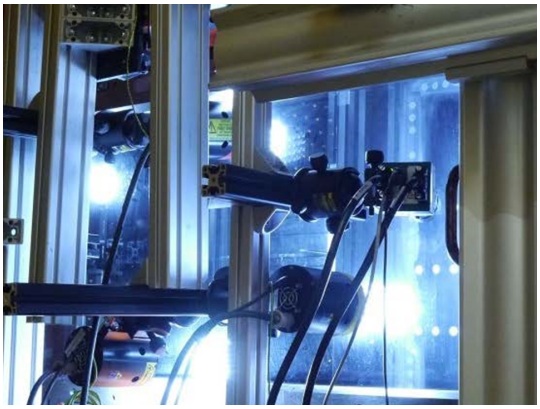

(a) SPR deformation measurement; Experimental setup; Spot lights and cameras point through the test section's optical access on the panel and the markers on its surface.

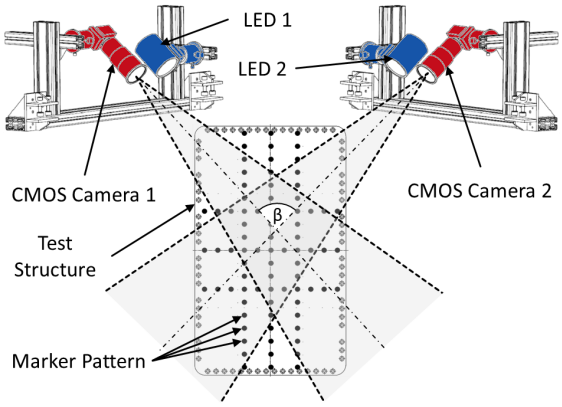

(b) SPR deformation measurement; Experimental setup; Sketch.

Figure 5.22.: SPR application in the wind tunnel test section.

In order to achieve ideal results, an angle of $\beta = 60.0°$ between the two optical axes of the cameras is aspired, which is sketched in Figure 5.22 (b). The Mikrotron MC1310 CMOS cameras provide a maximum resolution of 1280 by 1024 pixels with a maximum frame rate of 500 fps. The sensor diagonal line's dimension is 1.25" with a sensitivity of 1600 LSB/Lux-sec, which means an edge length of the square shaped pixels of $12 \cdot 10^{-6}$ m. Crucial for a proper measurement is the maintenance of high optical contrasts on the one hand. On the other hand, high frame rates not limited by the cameras' shutter

speed assure a sufficient temporal resolution of the structure's oscillations. To satisfy the first, white markers are placed on the black dull panel surface and illuminated by several LED spotlights mounted on the same rack as the cameras (Figure 5.22 (a)). A schematic drawing of the SPR data acquisition process is illustrated in Figure 5.23.

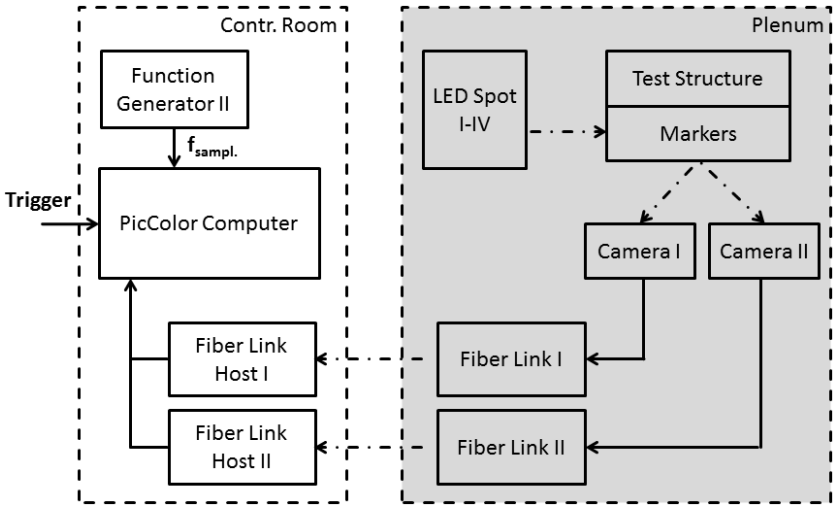

Figure 5.23.: SPR data acquisition system schematic.

For transferring the recorded frames to the frame grabber cards, which are components the SPR DAQ computer, the interconnection of fiber links is established. For each camera, one fiber link module located in the WT plenum, which is connected to another fiber link module located in the WT control room.In contrast to the data acquisition done by the main DAQ system DLR AMIS, the camera sampling frequency, provided by another function generator, is constant and does not depend on the excitation frequency. The only connection between the SPR system and the DLR AMIS system is a trigger signal, which is released by the latter and initiates the SPR measurement. Due to the occurring time delay, which is caused among others by the buffering of the images before being processed, a perfect synchronization of the measurement systems is not guaranteed. The synchronization of the data sets is to be done in the subsequent data post processing by correlation with the actuator position sensor signal. In addition to recording the data, the used software allows the online monitoring of the marker tracking, which is illustrated in Figure 5.24.
The green colored squares enclosing each marker indicate a sound data acquisition, whereas a change in color indicates different error types. Each of those images has a time stamp, given by the frame grabber, which allows the allocation of the image pairs and the computation of the markers' 2D (x- and y-coordinates) and 3D data (x-, y- and z-coordinates). Table 5.6 depicts one block of an exemplary ASCII-format data output file, which shows the coordinates of each tracked marker, the time stamp and an error code, the last having values of zero in this example indicating that no error occurred.
To calculate the 3D data, a matrix is needed, which is set up by a calibration carried out

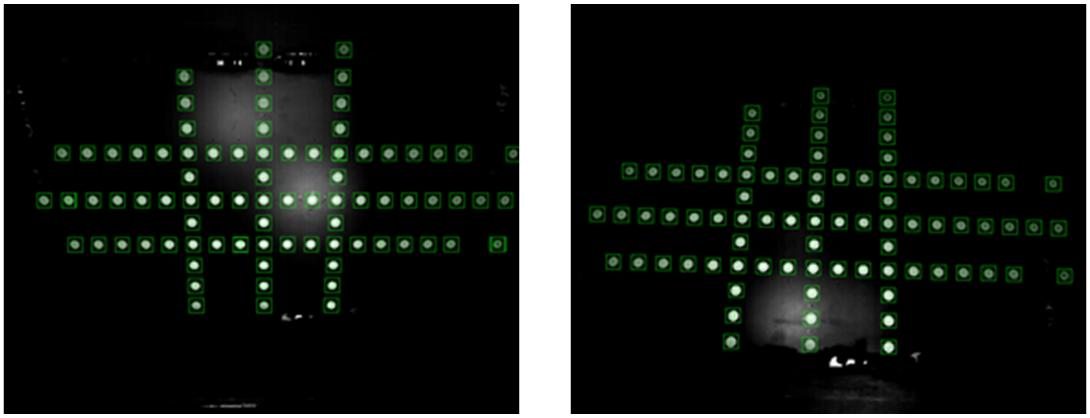

(a) Left CMOS camera image. (b) Right CMOS camera image.

Figure 5.24.: SPR data acquisition system; Screen shot of online marker tracking.

```
*01* Measurement Data File
*39* Enable Writing At Local Date/Time [m/d/y, h:m:s]:
02/15/2017, 16:17:15
*31* Point   x[pix]          y[pix]          z[pix]          status
  1       5.503313e+002   2.869662e+002   1.648870e-001  0
  2       4.997320e+002   2.875412e+002   2.454369e-001  0
  3       4.499418e+002   2.873719e+002   5.279693e-001  0
  4       4.000379e+002   2.872938e+002   9.043795e-001  0
  5       3.501043e+002   2.872190e+002   1.130843e+000  0
  ...       ...                           ...
...                       ...
 85      1.503925e+002   8.370741e+002   3.488108e-001  0
 86      1.502581e+002   9.366944e+002   7.665835e-001  0
*38* WorstError RingDelay IOStatus FrameIndex TimeStamp LostFrame
 0 1541 1 1187 91903421 0
```

Table 5.6.: SPR system; ASCII output-file with 86 tracked markers.

prior to each measurement campaign. One or more calibration bodies are required that are exactly dimensioned and feature trackable markers. The known marker coordinates, deposited in a list, are subsequently allocated to the recorded 2D data set. Based on that a matrix for the 3D calculation is set up. The test bodies used in the experiment are magnets that differ in height with the top side colored white. Since the positioning of the magnets on the surface of the plate is done manually, a certain uncertainty is brought in the calibration process, which should be diminished due to the high number of used calibration bodies ($n_{calib} = 90$). The analysis of the deformation measurement data is carried out in the same way as done for all sensors connected to the DLR AMIS system. The SPR data differs in two characteristics from the data of the AMIS connected sensors, which is to be considered in the analysis: The different sampling approaches

and the non-synchronized data acquisition of the SPR system. In contrast to the AMIS system's data, the SPR data is gained with a fixed sampling frequency. An adaption of the signal allows a post processing as done for the other AMIS related quantities. In a first additional step, the discretization Δt of the signal is increased by interpolation. The new discretized signal has an element, which is on the one hand an integer multiple of its period's resolution and on the other hand an integer number of recorded periods. Here, the signal is cut. Consequently, the shortened signal has an integer number of periods ($n_{per} \in \mathbb{N}$), just as the other signals of the AMIS have. The processing continues as done hitherto. The time-depending displacement function $z(t)$ is transformed into the frequency-depending function $z(f)$ by means of a FFT after which the shortened signal the n_{per}-th element can be picked as usual. The second particularity requires a link between the two measurement systems, which is the signal of one of the hydraulics' position sensors. It can be assumed that the phase of this signal corresponds to the phase of the SPR signal of the marker located at the same x- and y-position of the panel to which the actuator is attached. For each MP, all SPR data must be corrected by the difference in phase angle $\Delta\varphi_{t,SPR-act}$ between the actuator signal $z_{act}(f_{exc})$ and the corresponding marker signal $z_{SPR}(f_{exc})$:

$$\Delta\varphi_{t,SPR-act} = \varphi_t(z_{act}(f_{exc})) - \varphi_t(z_{SPR}(f_{exc})) \tag{5.16}$$

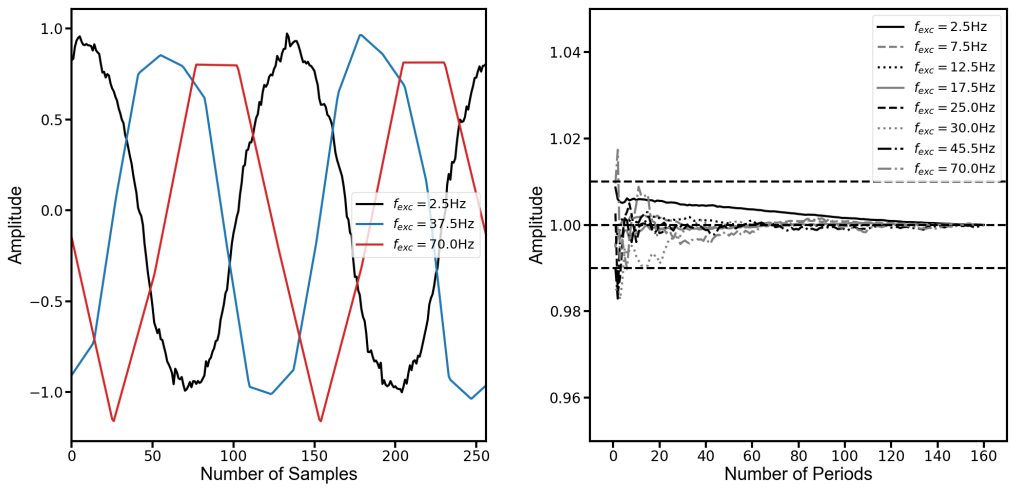

(a) Nondimensional time signal for $n_{per} = 2.0$ after interpolation to a 128 samples per period discretization.

(b) Marker tracking signal average convergence depending on the included number of periods based on FFT.

Figure 5.25.: SPR marker tracking signal evaluation; Results for panel center marker of Ψ_{11} test setup gained at $\hat{A}_N = 1.8$ mm, $M_\infty = 1.2$ and $Re = 2.5 \cdot 10^6$.

Exemplary SPR results with a normalized amplitude of the marker, which is located in the Ψ_{11} panel's center, are presented in Figure 5.25 for three excitation frequencies with the data interpolated linearly to 128 samples per period. The significant decrease in the resolution of a period by increasing the excitation frequency at constant SPR sampling frequency becomes clear by comparing the $f_{exc} = 2.5$ Hz data with the data recorded at increased frequencies, which is illustrated in Figure 5.25 (a). In particular at $f_{exc} = 70.0$Hz, only very few samples per period are available in the original data sets. Nevertheless, the resulting FFT-based average amplitudes for a full measurement series strive toward a stable average value (Figure 5.25 (b)). Here, the curve of the $f_{exc} = 2.5$ data can be regarded as an outlier, since no other data set shows this continuously decreasing trend.

5.2.5. Boundary Layer Wake Rake

The boundary layer wake rake serves to obtain the Mach number profile and the thickness of the flow's boundary layer directly downstream of the test structure. The measurements are done by means of steady pressure measurements using the DeAs DAQ, see Section 5.1.2 and Section 5.2.1. The fluid boundary layer thickness is increasing while running along the panel and is measured by the wake rake applied directly downstream of the panel ($x = 750$ mm, $x_{WT} = 3710$ mm) at half-span position (Figure 5.15), as illustrated in Figure 5.26.

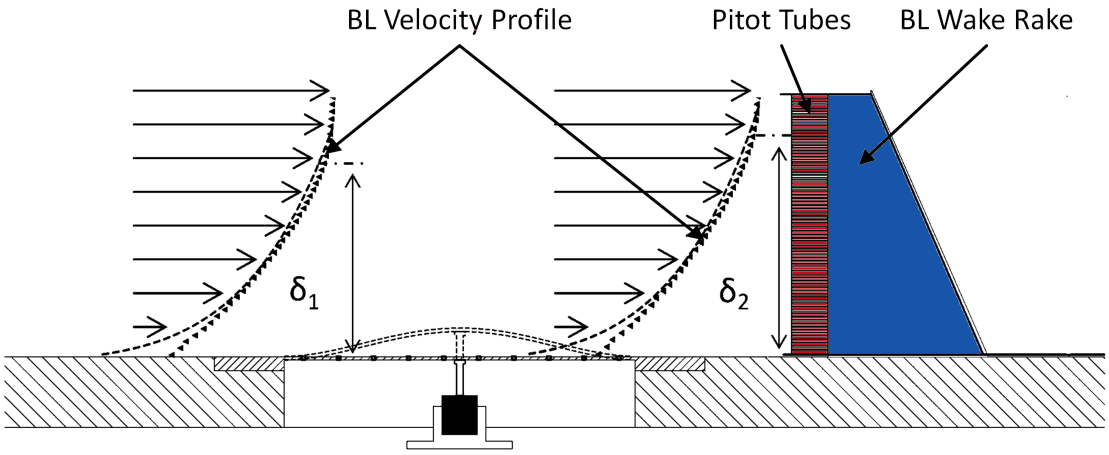

Figure 5.26.: Boundary layer measurement schematic. The indicated boundary layer Mach number profiles are based on an analytic power law approach (dashed lines) and on exemplary test results (markers).

64 Pitot tubes are distributed over a height of $z = 100$ mm (500 mm $\leq y_{WT} \leq$ 400 mm), which is depicted in Figure 5.27. With its inlet directed upstream, a Pitot tube allows the measurement of the fluid's total pressure. As illustrated in Figure 5.27 (a), the fin-shaped rake is mounted to a base plate that is glued to the wind tunnel wall by means of adhesive tape.

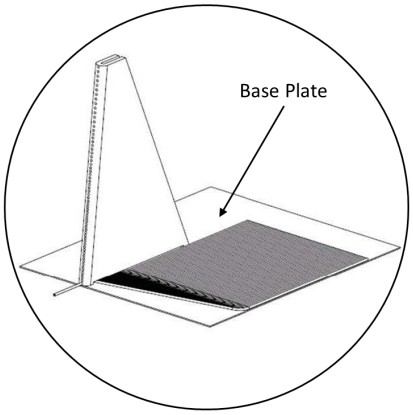

(a) Boundary layer measurements; BL wake rake.

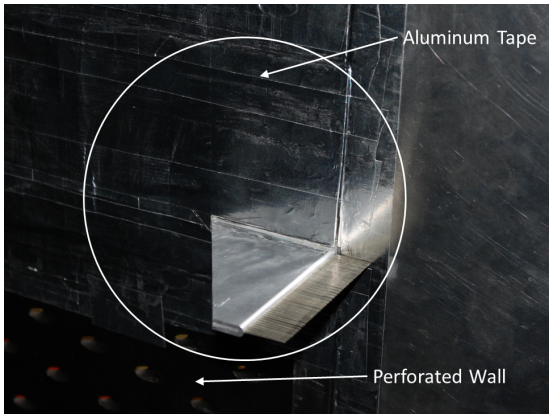

(b) Boundary layer measurements; BL wake rake (flow direction from the right to the left).

Figure 5.27.: Boundary layer wake rake.

All pressure metal tubes pass through the rake and subsequently along its base plate. At its trailing edge, these tubes are connected to flexible ones, which are led through the holes of the Perforated Test Section into the plenum. Figure 5.27 (b) shows a view within the test section in flow direction. The rake's base plate and parts of the perforated wind tunnel wall are covered by aluminum tape in order to ensure a proper attachment of the rake and the pressurized tubes. Based on the gas kinetics relation of Mach number and pressure ratio

$$M_\infty^2 = \frac{2}{\gamma - 1}\left[\left(\frac{p_0}{p_\infty}\right)^{\frac{\gamma-1}{\gamma}} - 1\right] \tag{5.17}$$

with the static pressure p_∞, which is constant in y-direction for $x = const$, the resulting local Mach number for one Pitot tube ($n = 1...64$) can be calculated [96]:

$$M_{pitot,n} = \sqrt{\frac{2}{\gamma - 1}\left[\left(1 + \frac{\gamma - 1}{2}M_\infty^2\right)\left(\frac{p_{pitot,n}}{p_0}\right)^{\frac{\gamma-1}{\gamma}} - 1\right]} \tag{5.18}$$

For supersonic conditions, the Mach number is to be corrected by taking into account the pressure's rise caused by the vertical shock that occurs shortly before the Pitot tube's inlet:

$$M^*_{pitot,n} = \sqrt{\frac{1 + \frac{\gamma-1}{2}M^2_{pitot,n}}{\gamma M^2_{pitot,n} - \frac{\gamma-1}{2}}} \tag{5.19}$$

To determine the flow velocity, the static temperature must be calculated first:

$$T_{n,\infty} = T_0 \cdot \frac{p_\infty}{p_{n,0}}^{\frac{\gamma-1}{\gamma}} \tag{5.20}$$

The total temperature T_0 measured in the WT's settling chamber, the test section's inlet static pressure p_∞ and the BL rake Pitot tube's total pressure $p_{n,0}$ are required. The velocity

$$U_n = \sqrt{2 \cdot c \cdot (T_0 - T_{n,stat})} \tag{5.21}$$

is calculated with the difference between the total temperature T_0 and the static temperature $T_{n,stat}$ and the specific heat capacity $c = 1.0073$ J/kgK. For the comparison of the resulting velocity profiles, the velocities are normalized through the division by U_∞ and the wall distance coordinate z through the division by δ_{99}. The boundary layer thickness δ_{99} used in this document is defined as the normal distance from the wall at which $U(z) = 0.99 \cdot U_\infty$.

5.3. Test Procedure

The present thesis shows results achieved in three wind tunnel campaigns performed at the turn of the year 2015/2016 and in 2017 in the DNW-TWG. Figure 5.28 depicts both the whole range of operation of the DNW-TWG and the extent of flow parameter variation set in the test campaigns discussed hereafter.
The first campaign (2015/2016) focused only on Ψ_{11} model investigations. Besides gaining results on the aeroelastic behavior, the commissioning of the setup and the test of its functionality were of prime importance during that campaign. In 2017, one test campaign dedicated to each panel model was carried out. The second Ψ_{11} test allowed a refinement of the test matrix, a rerun of measurement points and an extent of the set pressure range. Another study on the correlation between deflection amplitude and aerodynamic response, which was done extensively during the first campaign, was omitted. The initial test of the amplitude's impact on the pressure measurements served the purpose of obtaining values, which led to pressure responses large enough to get proper sensor data, but small enough to show a linear mathematical connection. Both of the following WT campaigns were based on those results. Concerning the excitation frequencies, attention was paid to cover a range as broad as possible, which was estimated prior in one of the pre-tests. Within a Mach number range from $M_\infty = 1.0$ to $M_\infty = 1.2$, computations by Alder [74] indicate arising flutter frequencies, which include both single mode flutter and coupled mode flutter, that grow from values close to zero toward values close to the first eigenfrequency of the structure. The experimental results obtained by Muhlstein [8] support those results. Vedeneev [57] also shows single mode flutter frequencies ($1.1 < M\infty < 1.2$) near the first two eigenfrequencies. In case of the currently used structure and with respect to the estimated eigenfrequencies by FEM analyses, the

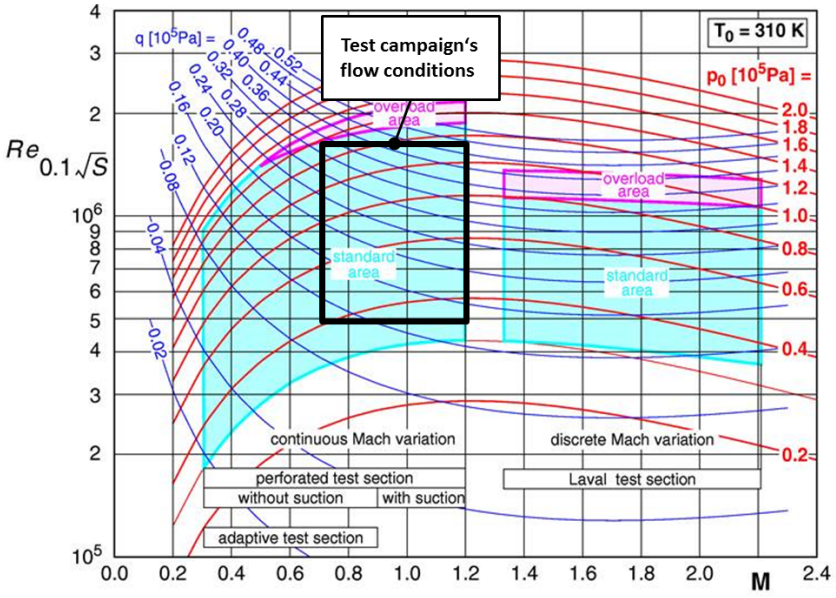

Figure 5.28.: DNW-TWG operation range. In this diagram the Reynolds number is calculated with a reference length of $l_{ref,WT} = 0.1$ m.

intended frequency range up to about $f_{exc} = 100.0$ Hz would be sufficient. The present experiment is based on a forced motion approach though, which means the structure characteristics of elasticity, namely the Young's Modulus and the panel thickness, are excluded or rather simulated by forcing panel eigenfunctions at different frequencies.

5.3.1. Model 1 (Ψ_{11})

The first test campaign is conducted at a relatively low Reynolds number ($Re = 2.5 \cdot 10^6$ based on the reference length $l_{ref} = l_i$), which leads to a low level of aerodynamic loads interacting with the panel. In order to establish the required high subsonic and low supersonic Mach numbers, the total pressure level is varied within 30.0 kPa $< p_0 <$ 40.0 kPa. The Mach number range is divided into equidistant steps of $\Delta M_\infty = 0.05$ in a range of $0.7 \leq M_\infty \leq 1.2$. To cover the aspired broad frequency range, the studies start with static measurement points and stop at $f_{exc,max} = 105.0$ Hz by using a discretization of $\Delta f_{exc} = 7.5$ Hz. The resulting test matrix, which is shown in Figure 5.29 (a), is repeated for three different actuator amplitudes $\hat{A}_1 = 0.6$ mm, $\hat{A}_2 = 1.2$ mm and $\hat{A}_3 = 1.8$ mm. Based on preliminary analyses carried out between the test campaigns a refinement of the test matrices is done for the second test campaign. The step sizes of both the Mach number range and the frequency range are changed. Instead of equidistant steps, the focus is shifted to higher Mach numbers and lower frequencies, as illustrated in Figure 5.29 (b). Instead of a variation of the excitation amplitude, a variation of the Reynolds number is done in the second campaign ($Re_1 = 2.5 \cdot 10^6$, $Re_2 = 5.0 \cdot 10^6$, $Re_3 = 7.5 \cdot 10^6$). Tabular 5.7 outlines the considered variations of amplitude and Reynolds number for

the investigations done on the Ψ_{11} panel test structure.

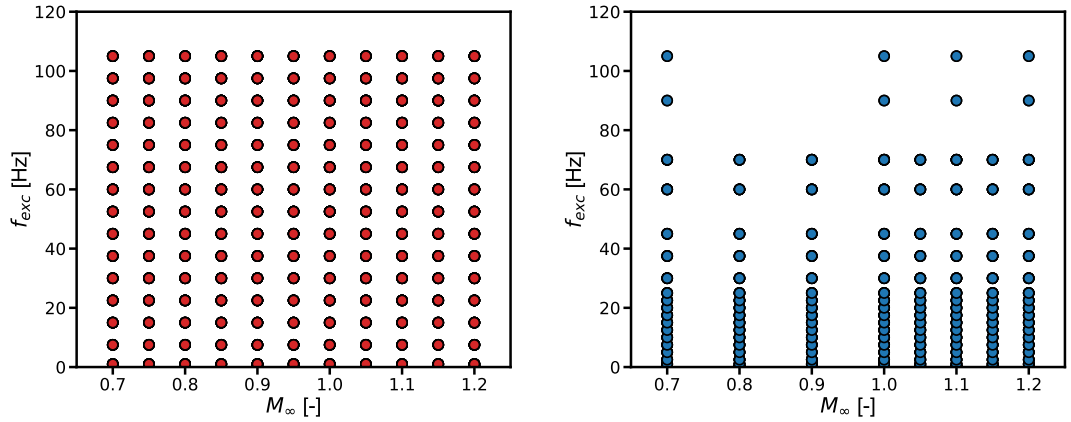

(a) Campaign 1 matrix (2015/16); $Re = 2.5 \cdot 10^6$ and $\hat{A}_1 = 0.6$ mm, $\hat{A}_2 = 1.2$ mm, $\hat{A}_3 = 1.8$ mm.

(b) Campaign 2 matrix (2017); $Re = 2.5 \cdot 10^6$, $Re = 5.0 \cdot 10^6$, $Re = 7.5 \cdot 10^6$ and $\hat{A}_3 = 1.8$ mm.

Figure 5.29.: Variation of excitation frequency and Mach number.

Campaign no.	**1**	**2**	**2**	**2**
Re $[10^6]$	$Re_1 = 2.5$	$Re_1 = 2.5$	$Re_2 = 5.0$	$Re_3 = 7.5$
$\hat{A}_N$ [mm]	$\hat{A}_1 = 0.6$			
	$\hat{A}_2 = 1.2$			
	$\hat{A}_3 = 1.8$	$\hat{A}_3 = 1.8$	$\hat{A}_3 = 1.8$	$\hat{A}_3 = 1.8$

Table 5.7.: Test procedure; Ψ_{11} model.

5.3.2. Model 2 (Ψ_{21})

The experiments done on the Ψ_{21} model are based on the same test matrix as prepared for the 2017 Ψ_{11} tests, which is depicted in Figure 5.29. The results referring to the studies on the amplitude are considered equally valid for the second model. Based on the results gained in the carried out stress analysis, a reduced deflection amplitude of $\hat{A} = 1.2$ mm is chosen, which still ensures significant sensor signals. Tabular 5.8 outlines the considered variations of amplitude and Reynolds number for the investigations done on the Ψ_{21} panel test structure.

Campaign no.	**3**	**3**	**3**
Re $[10^6]$	$Re_1 = 2.5$	$Re_2 = 5.0$	$Re_3 = 7.5$
$\hat{A}_N$ [mm]	$\hat{A}_2 = 1.2$	$\hat{A}_2 = 1.2$	$\hat{A}_2 = 1.2$

Table 5.8.: Test procedure; Ψ_{21} model.

6. Results

This chapter's first three sections illustrate the outcome of the test campaigns with focus on the three main measurement techniques. First, the results of the steady boundary layer measurements, which are done by means of the Pitot-tube equipped wake rake, are presented. Depending on the flow conditions and the dynamic properties of the structure, the focus is put on the boundary layer's velocity profile and its thickness. In the following section, the realized deformations of the test structure are validated by means of the data of the actuator's position sensor and the SPR system. The recorded data is compared to the intended deformation shapes of a flat plate's eigenfunctions Ψ_{11} and Ψ_{21}. The position sensor reveals additional information on the structure's amplitude and the excitation frequency. A satisfactory validation allows in the subsequent sections for the usage of the respective analytic eigenfunction. Finally, the unsteady pressure measurements over the test structure are illustrated and put into context with the underlying structural deformations. The measured phenomena and the impact of the defined structural and fluidic parameters are illustrated and analyzed. The results are compared and validated with analytic approaches. Based on the information on pressure and deformation, the generalized aerodynamic forces are presented in the fourth section, which give information on the transfer of energy between the fluid and the structure. For reasons of simplicity, $l = l_i$ and $w = w_i$ applies in the following chapter.

6.1. Boundary Layer

In order to study the turbulent boundary layer's impact on the aeroelastic stability, its thickness is measured in each measurement point and its dependency on the studied fluidic and structural parameters is analyzed. First, the Mach number's streamwise component is shown as a function of the distance from the WT wall (z-coordinate), which is compared with an analytic approach. It is important to note that the accuracy of the measurements is limited by the rake's Pitot tube resolution, which has a minimum of $\Delta z_{Pitot} \approx 1.0$ mm, and for which no interpolation is done in between.

6.1.1. Velocity Profiles

The measured Mach number profiles discussed in this section are illustrated in the Figure 6.1 to 6.4. The presentation is done by means of graphs in which the wall distance z, which is divided by the calculated boundary layer thickness δ_{99}, is plotted versus the local Mach number M, which is divided by the free stream Mach number M_∞. For comparison, a typical turbulent boundary layer profile based on a 1/n power law approach is depicted. This power law illustrates no Mach number profile, but a velocity profile

u/U_∞. By assuming a temperature that is independent of the wall distance ($dT_0/dz = 0$) both curves are equal. Under consideration of a heat flow through the wind tunnel's wall, that assumption is not correct anymore and a shift of the analytic reference solution must be taken into account. Depending on the direction of the heat flow, the wall near values must be shifted to higher or lower Mach numbers. In order to study the impact of the fluid parameters Reynolds number and Mach number, measurements without an excitation of the structure are presented, which should lead to equal results for the Ψ_{11} and the Ψ_{21} model under equal flow conditions. This agreement is shown by the exemplary profiles for a low Reynolds number and a low Mach number depicted in Figure 6.1.

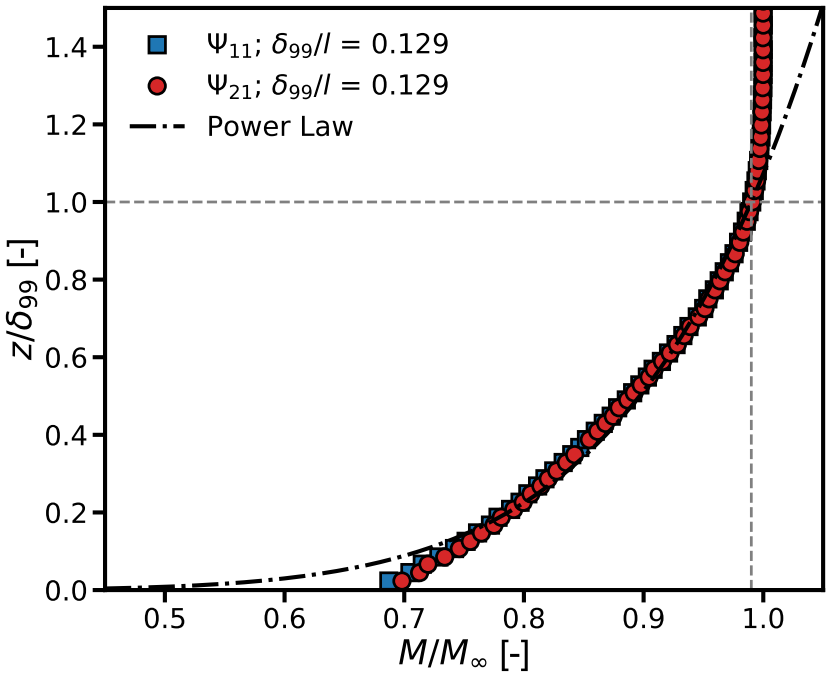

Figure 6.1.: Comparison of velocity profile for Ψ_{11} and Ψ_{21} model test campaigns; $M_\infty = 0.7$; $Re = 2.5 \cdot 10^6$, $\hat{A} = 0.0$ mm; $f_{exc} = 0.0$ Hz.

The power law approach is confirmed here too. The Reynolds number's influence, which is varied from $Re_1 = 2.5 \cdot 10^6$ to $Re_3 = 7.5 \cdot 10^6$, on the Mach number profile is illustrated in Figure 6.2. For both tested structures, no significant dependency is apparent for the here presented subsonic cases, although a linearization of the profile's slope at approximately $0.7 < u/U_\infty < 0.95$ can be noted that increases with increasing Reynolds number. That phenomenon vanishes at supersonic flow conditions as can be seen in Appendix D. The repeatability of the measurements is proven again by comparing the results of the two test campaigns.

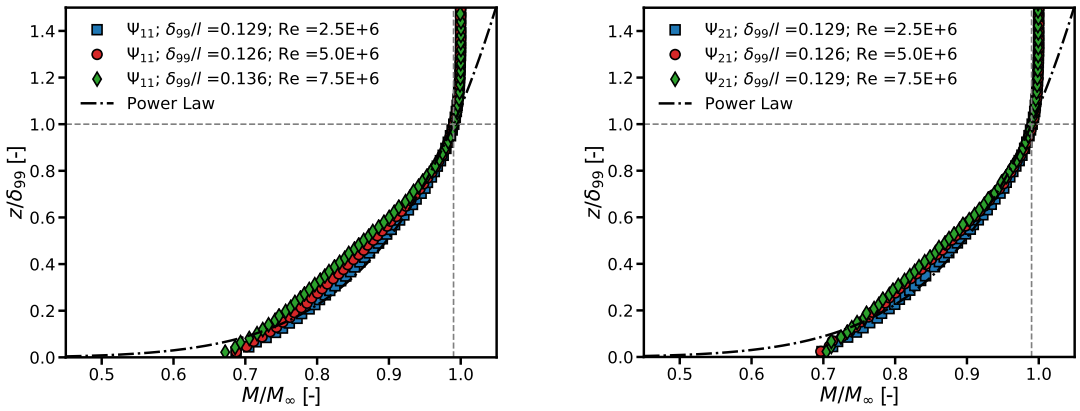

(a) Ψ_{11} model.

(b) Ψ_{21} model.

Figure 6.2.: Impact of Reynolds number on boundary layer velocity profile; $M_\infty = 0.7$; $\hat{A} = 0.0$ mm; $f_{exc} = 0.0$ Hz.

For pointing out the Mach number's influence on the profile, Figure 6.3 shows results of measurements done at two Reynolds numbers for a multitude of Mach numbers. For both Reynolds numbers no general significant dependency can be observed. Results of further Reynolds number comparisons of other test campaigns, which are illustrated in Appendix D, underline that finding.

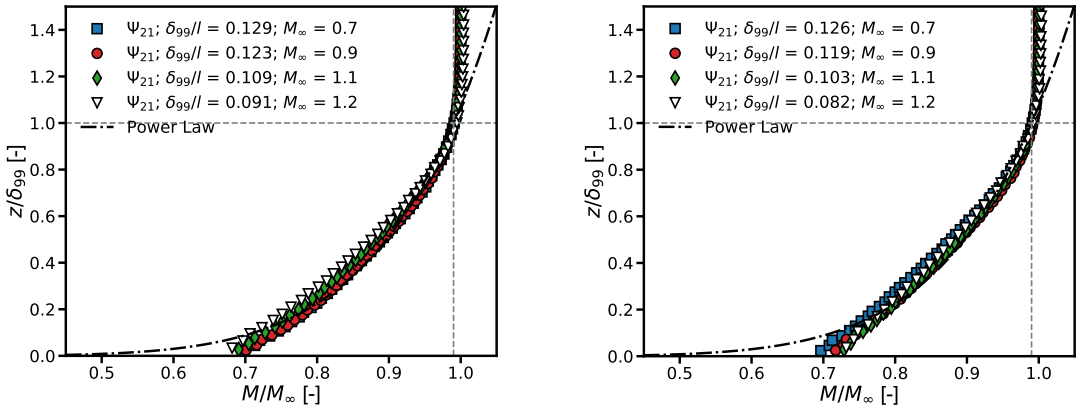

(a) $Re_1 = 2.5 \cdot 10^6$.

(b) $Re_2 = 5.0 \cdot 10^6$.

Figure 6.3.: Mach number influence on boundary layer velocity profile; Ψ_{21}; $\hat{A} = 0.0$ mm; $f_{exc} = 0.0$ Hz.

After showing the Mach number profile's independence of the variation of fluid parameters, the influence of the oscillating structure, which is located upstream of the boundary

layer rake, is studied (Figure 6.4). Results of subsonic and supersonic measurements of the Ψ_{11} campaign are presented for a variation of excitation frequencies, while the amplitude is kept constant at $\hat{A}_2 = 1.2$ mm. Within the range from $f_{exc,min} = 1.0$ Hz to $f_{exc,max} = 60.0$ Hz no influence on the profile is recognized. Noticeable is the change in the profile when comparing the subsonic and the supersonic results. Further results, which contain measurements for further Mach numbers, and corresponding Ψ_{21} measurements can also be found in the appendix. Here, the Ψ_{11} and the Ψ_{21} excitation differ in their particular oscillation amplitude ($\hat{A}(\Psi_{11}) = 1.8$ mm, $\hat{A}(\Psi_{21}) = 1.2$ mm). The mentioned results show the profile's independence of the deflection amplitudes, at least for the two tested magnitudes.

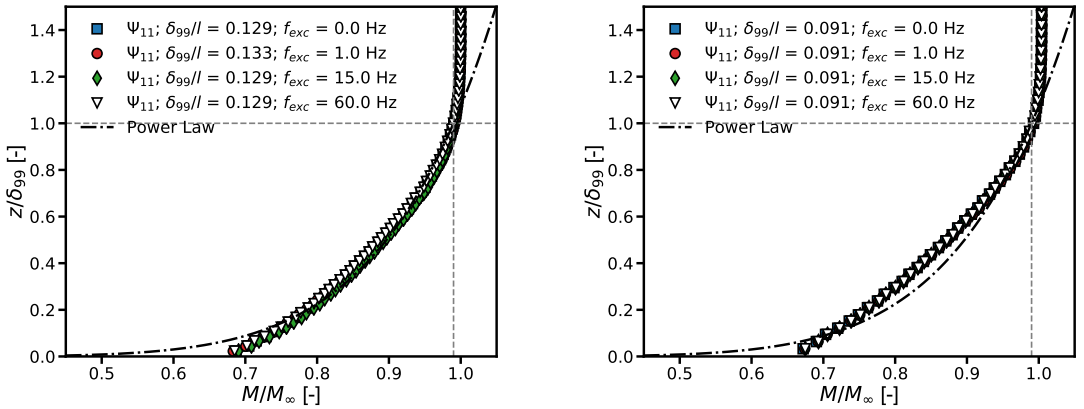

(a) $M_\infty = 0.7$.

(b) $M_\infty = 1.2$.

Figure 6.4.: Excitation frequency influence on boundary layer velocity profile; $Re_1 = 2.5 \cdot 10^6$; $\hat{A}_2 = 1.20$ mm; Ψ_{11}.

The measured time averaged boundary layer profiles generally show a good agreement with the used analytic reference functions and are not influenced by the test structure's oscillation with regard to the amplitude and the frequency. The profile's consistency with the analytic approach slightly changes with increasing Reynolds numbers and with exceeding of the speed of sound. In both cases an increased linearization of the profile can be observed.
Another peculiarity, which is not addressed so far, is the curves' characteristic in the very wall-near region at about $0.0 < z/\varphi_{99} < 0.1$, where the measured slope remains linear and does not decrease in order to meet $M/M_\infty(z = 0) = 0.0$. This phenomenon occurs for numerous measurement points. For gaining a deeper insight into the observed deviations, boundary layer measurements carried out in 2013 in the DNW-TWG are illustrated in Figure 6.5. The measurements, in which the same rake device was used as for the experiment at hand, were performed in another test section of the wind tunnel [97], namely the adaptive Test Section. It has flat and smooth walls, for which the analytic reference power law was actually developed. Besides the analytic solution, the

figure shows results for different Mach numbers $0.3 < M_\infty < 0.8$ and total pressures 39.0 kPa $< p_0 <$ 82.0 kPa, which are measured at $x_{WT} = 3210$ mm. This is the center position of the test section's 3D Position and thus not exactly the same position where the measurements are performed in the present tests. The test section walls have a divergence of $div_{2013} = 2.5$ mm/m, which is less than the divergence set in the Perforated Test Section. The observed characteristics correspond to those found in the present work and show a dependency on the Mach number but no significant dependency on the Reynolds number. The agreement with the analytic approach, shown in Figure 6.5 (a), is almost perfect and neither the linear part in the mid-wall-distance nor the steep linear slope in the wall-near region emerges.

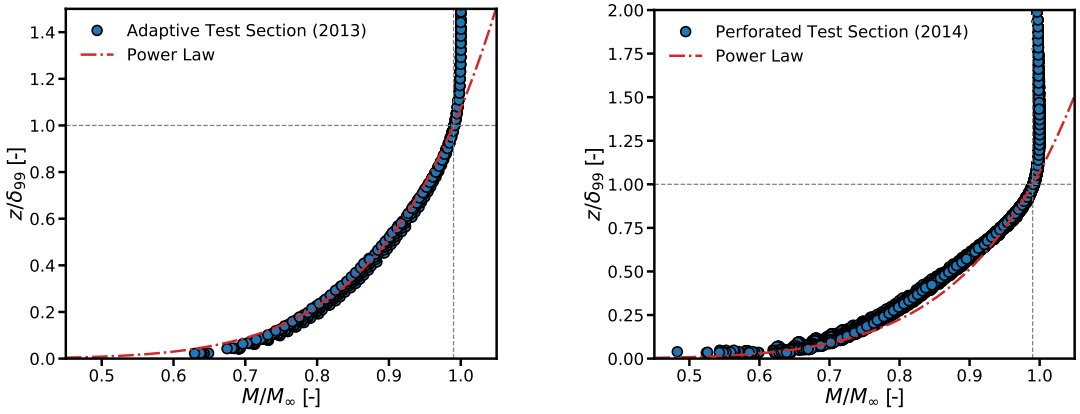

(a) Adaptive Test Section.

(b) Perforated Test Section.

Figure 6.5.: Comparative boundary layer measurements at various Mach numbers in the DNW-TWG.

Additional measurements in the Perforated Test Section were done in 2014 in preparation of the test campaigns discussed in this document [79], presented in Figure 6.5 (b). During this test campaign, the experimental conditions were very close to those later used in the forced motion tests. The Mach number was varied from $M_\infty = 0.7$ to $M_\infty = 1.2$ with a variation of total pressure of 29.0 kPa$< p_0 <$ 80.0 kPa, while the total temperature varied between $T_0 = 292.0$ K and $T_0 = 314.0$ K. For these tests the boundary layer rake was placed at the position $x_{WT} = 3769.5$ mm, which is the same position used in the forced motion experiments, with the slightly diverging walls set to $div_{2014} = 2.8$ mm/m. Here, the change in the profile towards a linear characteristic is very clear. Nevertheless, the deviations in the area close to the wall do not occur.
Measurements done even further back in 1979 show more results of measurements carried out in the Perforated Test Section, which were recorded by a single retractable Pitot tube [96]. The device had a travel distance of 100 mm corresponding to the measurement rake's height that was used in 2013 to 2016. By covering the perforated wall upstream to the Pitot tube, the measurements could be done under smooth wall conditions in the Perforated Test Section. It was found that the walls' angle has a significant

impact on the resulting profile. A large opening angle leads to the same linearization that was observed in the present measurements. Further work on the determination of the DNW-TWG's boundary layer conditions was done in 1996 with the retractable Pitot tube, which again highlighted the wall angle's influence on the boundary layer's profile [98]. The measurements just shown demonstrate the correctness of the measured change in the Mach number profile. The phenomenon can be explained by the change in the streamwise pressure gradient that is caused by the divergent walls' compensation of the fluid's displacement thickness [99, 100]. This characteristic is additionally amplified by a rise of the Reynolds number, which was also observed before [76].

An explanation still remains for the deviations in the wall-near area. None of the former measurements in the DNW-TWG have shown those deviations, not even those in which the same measurement technique was used. In general, it would be unusual to obtain an exact agreement between the measurements and the power law approach in this particular wall distance domain. On the one hand, the equation was introduced to be applied for smooth and flat surface characteristics, which is not available in this experiment as a result of the test section's divergence and its perforation. At high Mach numbers the suction device, allowing for the supersonic Mach numbers, takes mass flow, which is part of the boundary layer, out of the test section. This must have a strong influence on the resulting profile. But even at low Mach numbers, where the device does not work, pressure differences, which arise between the test section and the pressurized plenum, are equalized by the exchange of mass flow through the wall's perforation.
On the other hand, the power law formula is not valid for the whole region of the boundary layer, but is a part of the law of the wall [76]. This law subdivides the boundary layer in three domains. According to that theory, the boundary layer's wall-nearest area, which can reach up to five percent of the boundary layer's thickness, is called the Viscous Sublayer. With increasing distance a buffer layer arises, which forms the transition from the sublayer to that part of the boundary layer, which is described by the power law approach. Those two first layers show a characteristic that is approximately linear. Further, the domains closest to the wall cannot be resolved by the applied measurement device. At the beginning of this section it is stated, that the Mach number profile, related to the free stream Mach number, equals the velocity profile related to the free stream's velocity. This assumption is correct, as long as the total temperature in z-direction is constant. However, in the present case a temperature gradient may be present, since the wind tunnel wall and the fluid most likely do not show the same temperature conditions. This results in a heat flow in a certain direction. As a result, the analytic profiles have to be shifted either to higher or to lower Mach numbers. One other aspect concerning the measurement technique is the averaging of the measurement data over time. The unsteady data of the measured time signal is only used to calculate the time averaged data and is not saved. Thus, unsteady effects cannot be considered, even though they may have a strong impact on the results.
Most likely, the situation at hand is quite different and of rather practical nature. With focus on the alignment of the three Pitot tubes, which are located closest to the WT wall, a change over time can be observed. As mentioned, the first measurements, which

were carried out with the rake device, were done in 2014 and showed very good results as depicted in Figure 6.5. The subsequent test campaign is the investigation on the Ψ_{11} model leading to the results shown in Figure 6.4, which depicts an increased deviation from the analytic curve. The final measurements are performed in the Ψ_{21} test campaign, whose exemplary results are shown in Figure 6.3. The deviation of the $M_\infty = 0.8$ case is in particularly noticeable, since a very steep and linear slope in the results of the three tubes located closest to the wall is shown. The simple explanation is a growing mis-measurement due to a bending of those tubes, which is clearly shown in Figure 6.6. The bending causes a growing offset, which changes the actual position of the inlets of the pitot tubes in z-direction. The distance to the WT wall increases and thus higher velocities of the more distant boundary layer domains are measured.

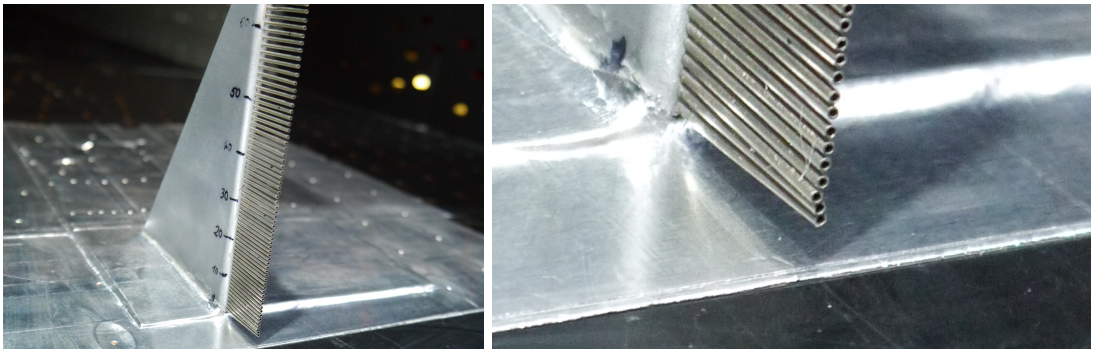

(a) Total. (b) Detail.

Figure 6.6.: Boundary layer rake after three test campaigns.

6.1.2. Thickness Measurements

In addition to the boundary layer thickness δ_{99}, which is here defined as the wall distance, where 99% of the free stream velocity is reached, the belonging displacement thickness δ_1 is an important parameter that can be directly calculated based on the wake rake's measurements. Regarding to Schlichting [76], the displacement thickness

$$\delta_1(x) = \int_{z=0}^{\infty} \left(1 - \frac{u(x,z)}{U_\infty(x)}\right) dz \tag{6.1}$$

is to be calculated with the local flow velocity $u(x,z)$ and the free stream velocity $U_\infty(x)$. The displacement thickness can be regarded as the dislocation of the wall in z-direction necessary to compensate for the narrowing of the flow cross-section and thus keeping the fluid's mass flow constant. The influence of the Reynolds number on these two characteristic quantities is illustrated in Figure 6.7 by using examples of the Ψ_{11} model for various Mach numbers.

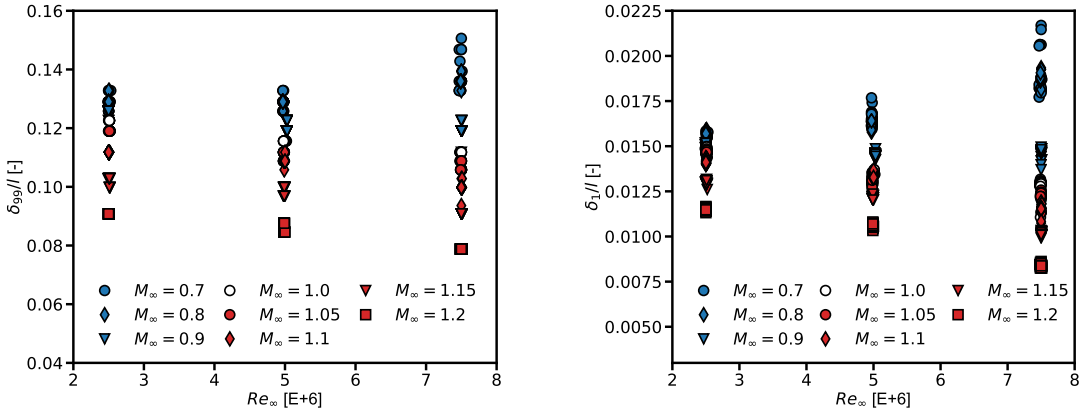

(a) Boundary layer thickness δ_{99}.

(b) Boundary layer displacement thickness δ_1.

Figure 6.7.: Impact of Reynolds number on boundary layer thickness and displacement thickness; Ψ_{11}.

Depending on the Mach numbers, a rise of the Reynolds number can cause increasing as well as decreasing values. The illustrations reveal a noticeable influence of the Reynolds number on the resulting magnitude on the one hand. On the other hand a dominating dependency on the Mach number is shown, which is valid for both the boundary layer thickness and the displacement thickness. The increase in the thickness for subsonic Mach numbers, where a decrease should occur with reference to the flat smooth plate theory [76], can be explained by the divergence of the test section's walls that induces a drop of the accelerating pressure gradient. In contrast, the supersonic domain shows the initially expected decrease of δ_{99} and δ_1. This is additionally supported by the boundary layer suction device, which starts working at $M_\infty \geq 0.9$. The Mach number's impact on the boundary layer is shown in detail for all three tested Reynolds numbers in Figure 6.8.

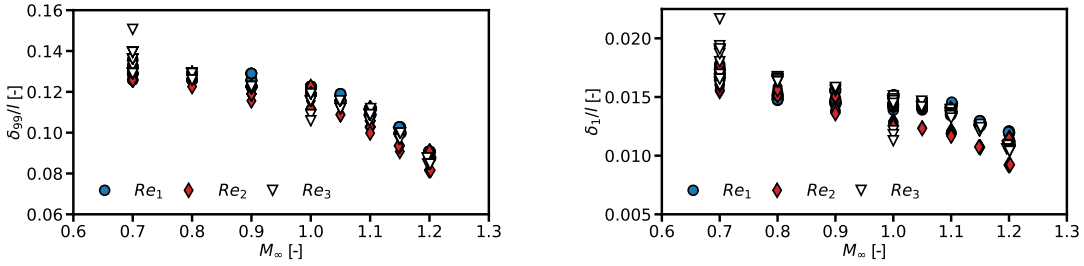

(a) Boundary layer thickness δ_{99}.

(b) Boundary layer displacement thickness δ_1.

Figure 6.8.: Boundary layer thickness and displacement thickness vs. influence of Mach number; $Re = 2.5 \cdot 10^6$; $\hat{A} = 1.2$ mm; Ψ_{21}.

With increasing Mach number the boundary layer thickness decreases from $\delta_{99}/l_i \approx 0.15$ to $\delta_{99}/l_i \approx 0.08$. The characteristics can be broken down into the subsonic and the supersonic domain. In the first domain, a slight decrease of both the boundary layer thickness and the displacement thickness is evident. This characteristic is increased by exceeding $M_\infty = 1.0$, which can be traced back to the beginning suction of the boundary layer, whose mass flow rate increases with rising Mach number. The detected characteristics are conform with the already introduced measurements done in preparation of the test campaigns in 2014 [79] and further measurements carried out at the DLR in 1996 [98]. Corresponding to Figure 6.8, the boundary layer thickness and the displacement thickness are depicted in dependency on the excitation frequency in a range of $0.0 \text{ Hz} \leq f_{exc} \leq 60.0 \text{ Hz}$ in Figure 6.9.

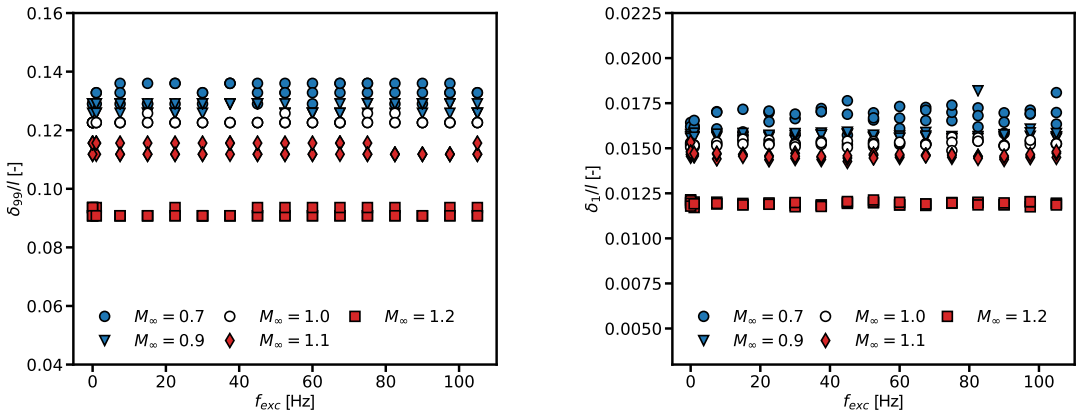

(a) Boundary layer thickness.

(b) Displacement thickness.

Figure 6.9.: Boundary layer thickness and displacement thickness vs. excitation freqeuncy; $Re = 2.5 \cdot 10^6$; Ψ_{11}.

No significant impact of the excitation frequency on the underlying steady pressure measurements is observed. The illustration includes all results of the first test campaign, which comprises measurements under equal flow conditions while the deflection amplitude was varied. No significant influence of the structure's amplitude is detectable. Referring to the conceptual considerations of Chapter 3, it turns out that only small changes in the boundary layer thickness are achievable by the variation of the test facility's flow conditions. However, the measured velocity profiles show good agreements with the analytic approach used. The results should be suitable for serving as a data base for further validations of computational approaches. Additional results of the boundary layer's thickness measurements of the Ψ_{11} campaign can be found in Appendix D.

6.2. Deformation

A requirement in order to achieve meaningful results of the pressure measurements is a proper operation of the structure deflection mechanism. The following discussion focuses on the validation of the realized forced motion, whose resultant shape is compared with the calculated eigenfunctions, on the one hand. On the other hand, the amplitudes of the structural deformation are validated, which is based on the results of the SPR marker tracking system providing data on the entire structure's surface. Those results are compared with data gained by the actuators' position sensors. These deflections, which are measured by the position sensor and by the SPR system, are referred to as amplitude $\hat{A}$. For the Ψ_{21} model, which has two actuators applied, one sensor is chosen for providing the reference signal. Additional data of the laser vibrometer deployed in some Ψ_{11} measurements is available for comparison at low frequencies. Another source of information are several acceleration sensors applied to monitor the SPR system's operation.
It is known from the literature study in Chapter 1 that the structural oscillations, which arise during panel flutter, are dominated by the first and the second streamwise structural eigenmodes. Those eigenmodes in x-direction correspond to the first and the fourth eigenmode of a flat plate (eigenfunctions Ψ_{11} and Ψ_{21}), which extends in x- and y-direction. Therefore, it is of utmost importance to check the quality of the simulation of these shapes forced during the experiments. Associated with the structure's oscillation shape is the amplitude that is given by the actuator's piston and that is measured by the SPR system and by the position sensor integrated in the actuator. Those two sets of results are compared with each other and to the nominal amplitude in order to calculate correction factors. Besides the frequency and the amplitude, the phase angle is part of each oscillation. The temporal phase differences between the signals of the SPR system and the actuator's position sensor are determined. This allows the synchronization of the two data sets. In addition, differences are determined in the phase between the individual SPR measurement positions defined by the markers distributed throughout the test structure. The measurement points used in this section for the verification of the model's deformation are listed in Table 6.1.

Model	M_∞ **[-]**	Re $[10^6]$	$\hat{A}$ **[mm]**	f_{exc} **[Hz]**	U_∞ **[m/s]**	p_0 **[Pa]**	**k [-]**
Ψ_{11}	0.8	5.0	1.8	1.0	281.84	77276.0	0.01
(2017)	0.8	5.0	1.8	15.0	281.75	77306.3	0.17
	0.8	5.0	1.8	30.0	281.80	77322.8	0.33
Ψ_{21}	0.8	5.0	1.2	1.0	282.11	77973.8	0.01
	0.8	5.0	1.2	15.0	281.61	77786.1	0.17
	0.8	5.0	1.2	30.0	281.57	77580.0	0.33

Table 6.1.: Measurement points for the validation of deformation measurement technique.

6.2.1. Vibration Monitoring

Before the actual analysis of the measured data is carried out, it is checked whether the test setup vibrated during the measurements in such a way that may influence the quality of the measurement data. The acceleration sensors used for this purpose serve exclusively for monitoring the experimental setup. Since the actuator mechanism is directly connected to the experimental setup and thus to the WT, it must be ensured that only the panel structure undergoes significant oscillations, whereas the rest of the components related to the test setup remain unaffected. On this account, acceleration sensors are placed at different positions of the test setup's frame structures, as shown in Section 5.2.3. Further data is provided by three of those sensors that were placed on three orthogonal surfaces of one of the two SPR cameras during several measurement series of the first Ψ_{11} test campaign. Additional sensors attached to the panel's rear side provide acceleration data serving as reference for the data presented in this section. Spectra of the measured acceleration $|\ddot{z}|$ of one of these sensors positioned approximately in the panel center are shown in Figure 6.10. Besides the dominating excitation frequency $f/f_{exc} = 1.0$, a multitude of higher harmonics can be clearly identified.

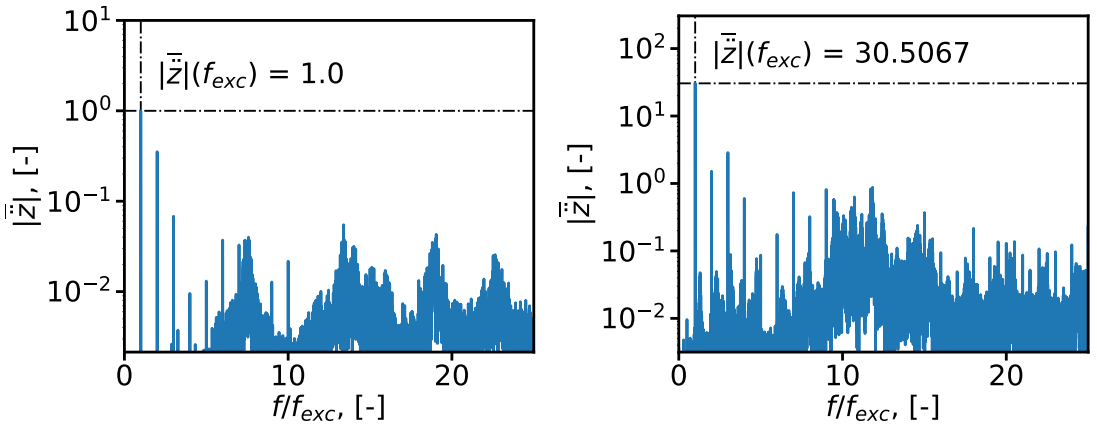

(a) $f_{exc} = 15.0$ Hz.

(b) $f_{exc} = 90.0$ Hz.

Figure 6.10.: Ψ_{11}; $\hat{A} = 1.8$ mm; $M_\infty = 0.8$; $Re = 2.5 \cdot 10^6$; Panel acceleration; ACC Sensor 1; FFT.

The latter are caused by the frequency generator used, the output of which contains these higher harmonic components. Additional components with lower amplitudes occur over the full range of frequencies, which may be caused by the auxiliary equipment of the test facility. Those components that show peaks at about $f/f_{exc} = 8.0$ and $f/f_{exc} = 13.0$ in Figure 6.10 (a) also occur at a excitation frequency of $f_{exc} = 0.0$ Hz. The $f_{exc} = 0.0$ Hz data for the examples of panel, frame and camera vibrations, which are presented in this section, can be found in the appendix in Figure D.12. The illustrated accelerations in all figures in this section are normalized by the reference panel acceleration at a medium

excitation frequency of $f_{exc} = 15.0$ Hz that is shown in Figure 6.10 (a):

$$\overline{|\ddot{z}|} = \frac{|\ddot{z}|}{|\ddot{z}|_{ref}} = \frac{|\ddot{z}|}{|\ddot{z}|_{panel,15Hz}(f/f_{exc} = 1.0)} \tag{6.2}$$

Figure 6.10 (b) presents accelerations for an increased excitation frequency of $f_{exc} = 90.0$ Hz, which, as expected, are also strongly increased. Nevertheless, the characteristics recognized so far remain unchanged. Since the acceleration data do not provide sufficient information on the actual panel deformation, the results serve as reference only, whereas a detailed analysis of the motion and deformation of the panel follows in Section 6.2.3 and Section 6.2.4. Data from the sensors attached to the setup's frame are presented in Figure 6.11.

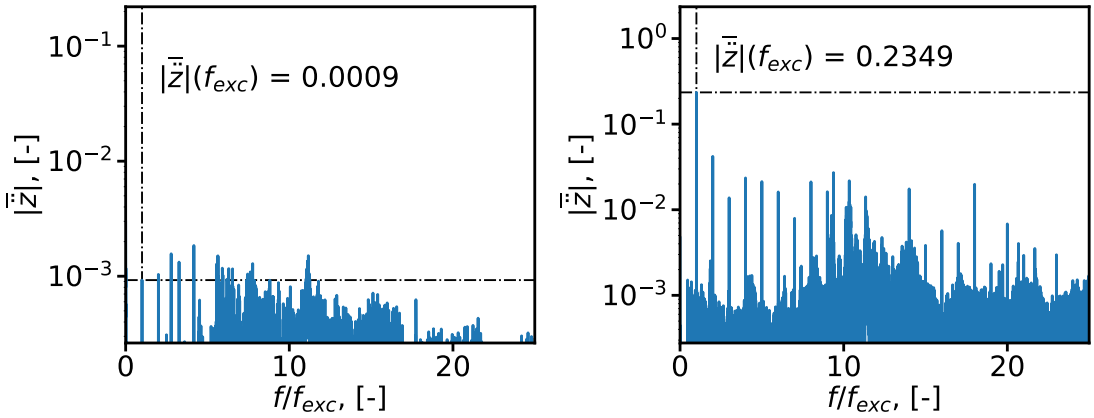

(a) $f_{exc} = 15.0$ Hz. (b) $f_{exc} = 90.0$ Hz.

Figure 6.11.: Ψ_{11}; $\hat{A} = 1.8$ mm; $M_\infty = 0.75$; $Re = 2.5 \cdot 10^6$; Frame acceleration; ACC Sensor 5; FFT.

The slight difference in Mach number can be explained by the fact that vibration data was not recorded simultaneously for camera and frame, since the same sensors were used. The data sets show again a strong increase in the measured acceleration at $f/f_{exc} = 1.0$ for increased excitation frequency from $f_{exc} = 15.0$ Hz to $f_{exc} = 90.0$ Hz. This increase is even more significant as the one recognized for the actuated panel motion. The acceleration data lead to an actual vibration amplitude of the frame structure of approximately one hundredth of a millimeter.
Figure 6.12 shows the third set of accelerations measured on the SPR camera. In contrast to the panel and the frame accelerations, for which only the FFT component at the excitation frequency is of interest, the entire spectrum is considered. The cameras of the SPR system must maintain calibrated positions, since any disturbance of these positions can lead to unpredictable measurement errors. At $f_{exc} = 15.0$ Hz the measured accelerations of the camera are extremely low at $f/f_{exc} = 1.0$, which again changes with

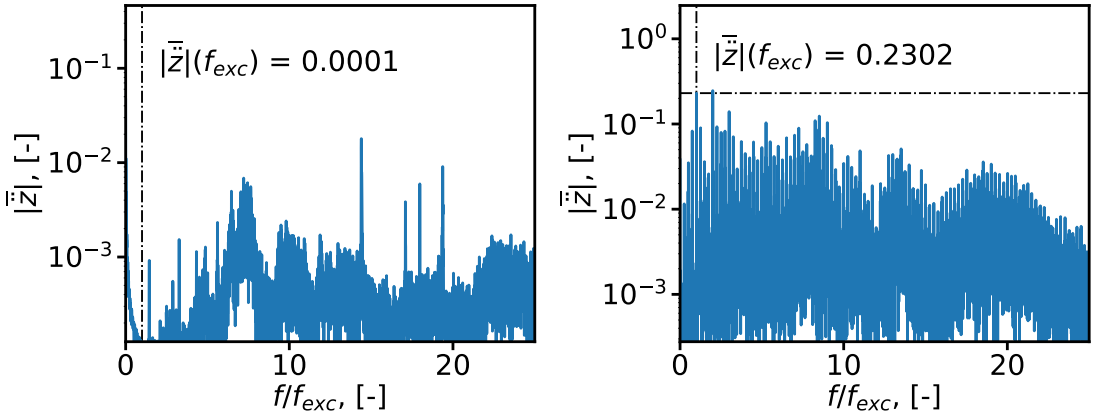

(a) $f_{exc} = 15.0$ Hz. (b) $f_{exc} = 90.0$ Hz.

Figure 6.12.: Ψ_{11}; $\hat{A} = 1.8$ mm; $M_\infty = 0.8$; $Re = 2.5 \cdot 10^6$; SPR camera acceleration; FFT; ACC Sensor 5; FFT.

increasing frequency. The magnitude is even lower here than the one obtained for the setup's frame, whereas the high frequency result is similar to the result of the frame. This means the camera's vibrations at $f/f_{exc} = 1.0$ have increased by at least a factor of 2000, whereas the associated panel accelerations have increased only by a factor of about 30. In addition to the acceleration at $f/f_{exc} = 1.0$, exceptionally large accelerations are measured over the illustrated frequency band, which do not occur for the panel and the frame. Thus, the resulting acceleration and motion of the camera is stronger than indicated by the comparison of the $f/f_{exc} = 1.0$ components. A more detailed estimation of these vibrations' influence on the SPR system is out of the scope of this thesis and therefore no part of it.
In summary, the recorded acceleration data have shown that the test setup is not unaffected by the forced motion equipment of the experiment, but it shows vibrations of acceptable magnitude even at high excitation frequencies. The increase of the excitation frequency is accompanied by substantially increased vibrations. This correlation is also reflected by the results of the SPR system, but which is much more affected than the other components, since large amplitudes are measured throughout the entire spectra. Since vibrations of the cameras means an error in marker tracking, it can be assumed that the measurement technique is strongly affected by vibrations at high excitation frequencies. From a excitation frequency of about $f_{exc} = 60.0$ Hz the substantial increase in vibrations can be observed. Figure D.13 shows this increase over the range of excitation frequencies of the $f/f_{exc} = 1.0$ component for several measurement series.

6.2.2. Reliability of Measurement Data

Before the analysis and evaluation of the deformation data starts, the reliability of the SPR measurements is checked. Exemplary FFT based spectra of the model's mid-span

section ($y/w_i = 0.5$) for five different markers ($x_1/l_i = 0.5$, $x_2/l_i = 0.6$, $x_3/l_i = 0.7$, $x_4/l_i = 0.8$ and $x_5/l_i = 0.9$) are presented in Figure 6.13 and Figure 6.14 for the two tested structures for low and medium excitation frequencies. The measured deflection in z direction is shown over the frequency range, while the frequency is normalized by the particular excitation frequency.

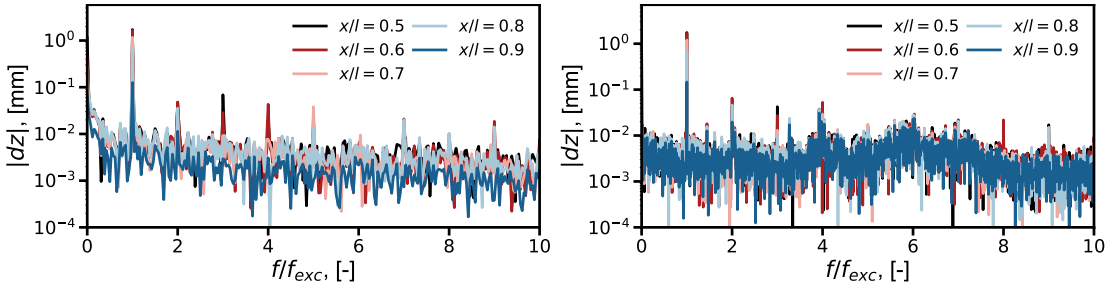

(a) $M_\infty = 0.8$; $f_{exc.} = 1.0$ Hz; $Re = 5.0 \cdot 10^6$. (b) $M_\infty = 0.8$; $f_{exc.} = 15.0$ Hz; $Re = 5.0 \cdot 10^6$.

Figure 6.13.: Spectra of SPR measured absolute deformations $|dz|$; Ψ_{11} model.

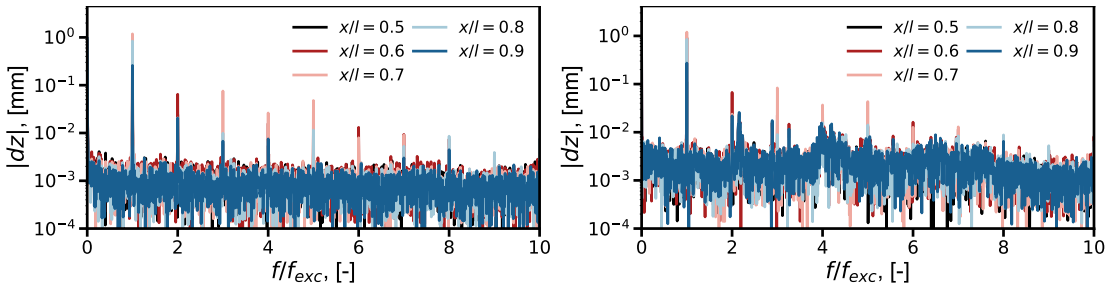

(a) $M_\infty = 0.8$; $f_{exc.} = 1.0$ Hz; $Re = 5.0 \cdot 10^6$. (b) $M_\infty = 0.8$; $f_{exc.} = 15.0$ Hz; $Re = 5.0 \cdot 10^6$.

Figure 6.14.: Spectra of SPR measured absolute deformations $|dz|$; Ψ_{21} model.

The measured Ψ_{11} deformation decreases according to the given marker order, since the $x_1/l_i = 0.5$ position is located at the structure's center, where the largest deformations occur. For the Ψ_{21} model the largest deformations arise at the $x_3/l_i = 0.7$ location, whereas at $x_1/l_i = 0.5$ deformations close to zero occur. Besides the global peaks at $f/f_{exc} = 1.0$, local peaks at multiples of the excitation frequency are detected. That phenomenon can be traced back to the characteristics of the used frequency generator, whose output contains exactly those multiples of the set frequency. In the figures showing results for $f_{exc} = 15.0$ Hz, increased deflection magnitudes between $f_{exc} = 60.0$ Hz and $f_{exc} = 90.0$ Hz Hz emerge. These indicate the test structures' or the test setup's eigenfrequencies. As already stated in Chapter 5, a certain number of periods (from $n_{min} = 160$ to $n_{max} = 640$) is recorded for each measurement point in order to ensure statistically representative results. The standard deviation σ_{SPR} of the measured complex deformations dz is calculated and used as the error bars' magnitudes. Assuming a

normal distribution of the results, the error bars thus defined ensure that approximately 70 percent of the total measurement results lie within this range. Doubling the bar's magnitude means that about 95 percent of the results are within that range. Figure 6.15 and Figure 6.16 show the measured and complex-valued deformations, which are divided in its real and its imaginary part, at $y/w_i = 0.5$ corresponding to the spectra shown above.

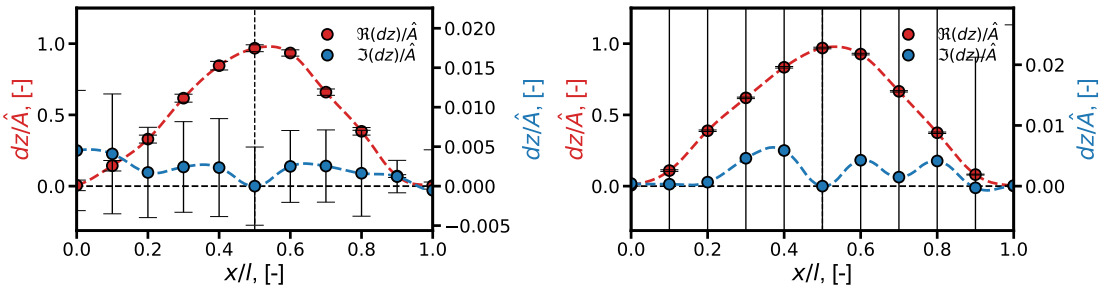

(a) $M_\infty = 0.8$; $f_{exc.} = 1.0$ Hz; $Re = 5.0 \cdot 10^6$. (b) $M_\infty = 0.8$; $f_{exc.} = 15.0$ Hz; $Re = 5.0 \cdot 10^6$.

Figure 6.15.: Deformation measurements with error bars at $y/w_i = 0.5$; Ψ_{11} model.

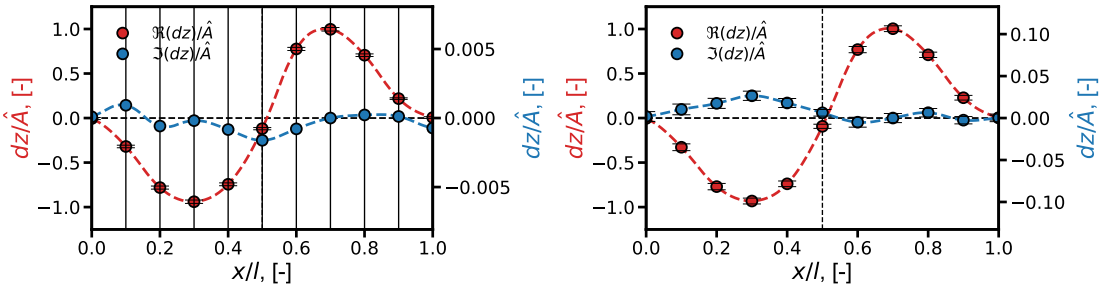

(a) $M_\infty = 0.8$; $f_{exc.} = 1.0$ Hz; $Re = 5.0 \cdot 10^6$. (b) $M_\infty = 0.8$; $f_{exc.} = 15.0$ Hz; $Re = 5.0 \cdot 10^6$.

Figure 6.16.: Deformation measurements with error bars at $y/w_i = 0.5$; Ψ_{21} model.

The SPR data is synchronized to the data of the position sensor with respect to the phase angle, which must be equal for the actuator and the marker applied at the same coordinates. This is why the imaginary part's magnitude is exactly zero at the x-coordinates of the actuator connection. Without intending to anticipate results discussed later, the figures show in almost every example large real part magnitudes with negligible error bars and very small imaginary part values with large error bars. This means that the obtained data is reliable only above a certain magnitude. Especially in the edge-near areas of the structure, where all magnitudes are low, the resulting phase angles can be erroneous. It is still not proven whether the measured results can be regarded as normally distributed. Histograms of measured amplitudes at some of the known positions are illustrated in Figure 6.17 and Figure 6.18.

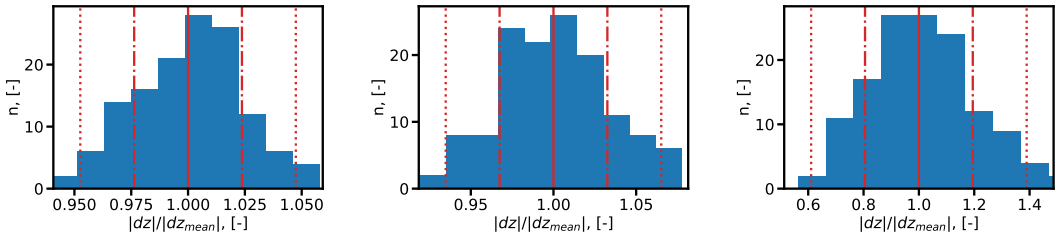

(a) Marker at $x_1/l_i = 0.5$ and $y/w_i = 0.5$.

(b) Marker at $x_3/l_i = 0.7$ and $y/w_i = 0.5$.

(c) Marker at $x_5/l_i = 0.9$ and $y/w_i = 0.5$.

Figure 6.17.: Histograms of measured deflection scattering; $M_\infty = 0.8$; $f_{exc.} = 15.0$ Hz; $Re = 5.0 \cdot 10^6$; Ψ_{11} model. The solid, dashed and dotted red lines indicate the average value, the $1\sigma_{SPR}$ and the $2\sigma_{SPR}$ boundaries.

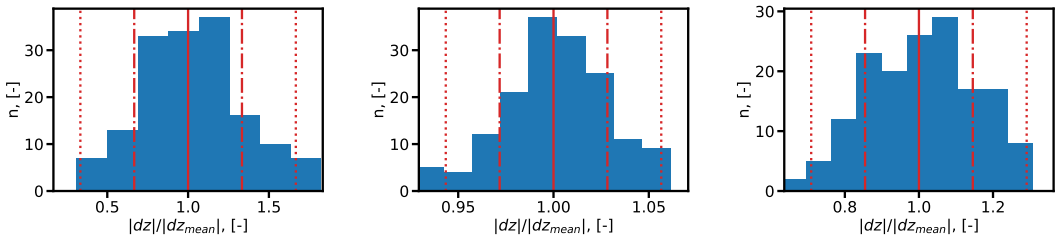

(a) Marker at $x_1/l = 0.5$ and $y/w = 0.5$.

(b) Marker at $x_3/l = 0.7$ and $y/w = 0.5$.

(c) Marker at $x_5/l = 0.9$ and $y/w = 0.5$.

Figure 6.18.: Histograms of measured deflection scattering; $M_\infty = 0.8$; $f_{exc} = 15.0$ Hz; $Re = 5.0 \cdot 10^6$; Ψ_{21} model. The solid, dashed and dotted red lines indicate the average value, the $1\sigma_{SPR}$ and the $2\sigma_{SPR}$ boundaries.

The frequency distribution of all measured oscillation periods is illustrated including the $1\sigma_{SPR}$ and the $2\sigma_{SPR}$ boundaries. The histograms break down the total of recorded amplitudes in a $n = 11$ discretization. Compared with a normal distribution's envelope, which is not shown here, the results show a satisfying agreement. Further, a fair symmetry to the $|dz|/|dz_{mean}| = 1.0$ vertical line can be observed and the majority of results lie within the $1\sigma_{SPR}$ boundaries. This short error consideration is sufficient for the further analysis of the measured data of the structural deformation.

6.2.3. Deformation Shape

The SPR system collects data of the markers distributed in a total of six section lines on the model's surface, which allows for obtaining information throughout the entire structure's surface by interpolation. Since the applied pattern of markers does not allow an interpolation of the structure's corner-near areas though, additional boundary conditions of $dz = 0 + 0j$ are set here. In order to validate the measured data, it is

compared with the results of the FEM calculations described in Chapter 4. For comparison, the complex deformation dz is broken down into its real part and its imaginary part, the latter being a measure for the complex number's phase angle. One objective of the forced motion is to maintain a constant phase angle equal to the actuator's phase angle throughout the entire test structure. The normalized shapes obtained from FEM simulations with applied actuating forces, which are based on the plate's eigenfunctions Ψ_{11} and Ψ_{21}, are illustrated in Figure 6.19. The edge lengths of the model are divided by the panel's length l_i and the displacement in z-direction is normalized by the respective shape's amplitude $\hat{A}$. The total set of tracked markers of the wind tunnel model is shown by means of three streamwise lines and another three spanwise lines of white dots. The illustrated deformations serve as a reference for the following evaluation of the results.

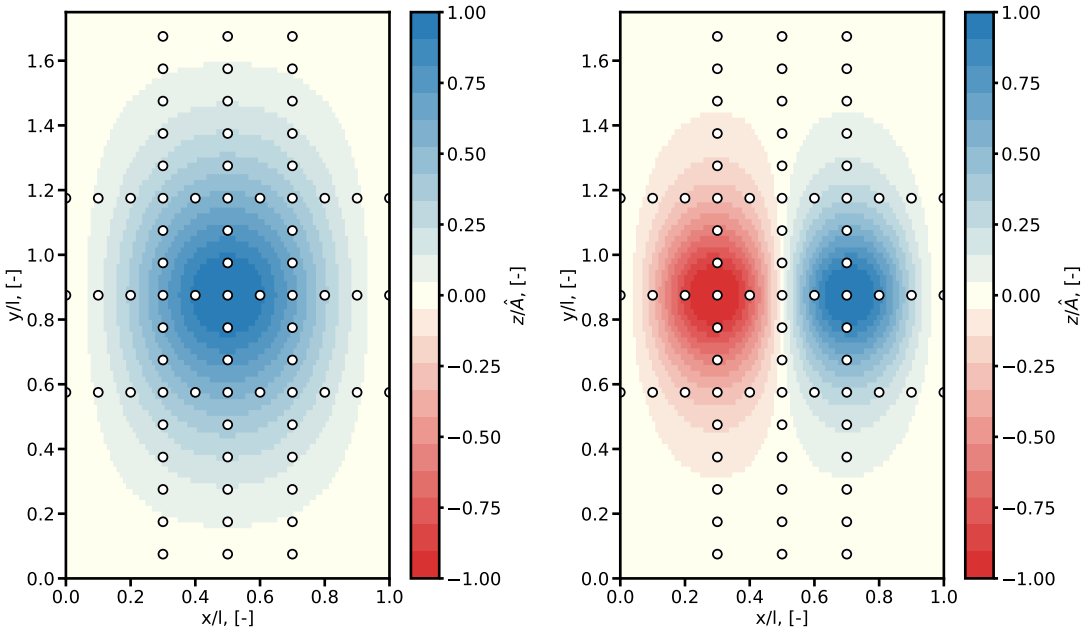

(a) Ψ_{11} simulation.

(b) Ψ_{21} simulation.

Figure 6.19.: Simulated modeshapes; Results of FEM simulated deformation analysis with normalized dimensions.

Imaginary Part

Before the structural deformation that was actually realized is reviewed, it is to be shown that the entire structure is oscillating in-phase. In case it is not, the analysis of the deformation-induced pressure data must take this into account. The imaginary part serves in this section as a measure for the phase angle of the structure's oscillation. Examples for several low and medium frequency measurement points for both tested models are shown in Figure 6.20 and Figure 6.21.

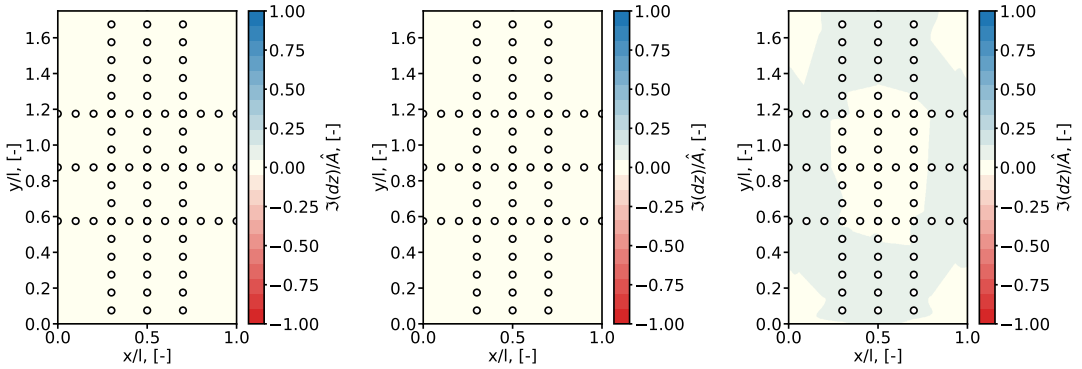

(a) $f_{exc} = 1.0$ Hz. (b) $f_{exc} = 15.0$ Hz. (c) $f_{exc} = 30.0$ Hz.

Figure 6.20.: Imaginary part of structural deformation; Influence of excitation frequency at subsonic flow conditions; $M_\infty = 0.8$; $Re = 5.0 \cdot 10^6$; $\hat{A} = 1.8$ mm; Ψ_{11}.

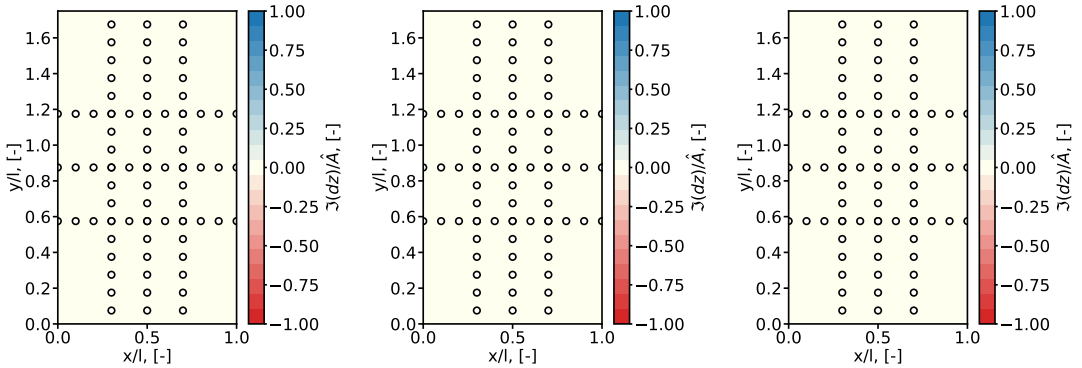

(a) $f_{exc} = 1.0$ Hz. (b) $f_{exc} = 15.0$ Hz. (c) $f_{exc} = 30.0$ Hz.

Figure 6.21.: Imaginary part of structural deformation; Influence of excitation frequency at subsonic flow conditions; $M_\infty = 0.8$; $Re = 5.0 \cdot 10^6$; $\hat{A} = 1.2$ mm; Ψ_{21}.

As described in Section 6.2.2 on the reliability of the measurement data, the phase angle of the markers at the position of the actuator connections is defined as the reference phase angle. Consequently, the phase angles and the imaginary parts at these positions are in all cases zero ($\varphi = 0.0°$ and $\Im(dz) = j0.0$). In case of the Ψ_{21} model the first actuator located down-stream provides the reference signal. Figure 6.20 (a) and Figure 6.20 (b) show a constant value of zero throughout the Ψ_{11} test structure, whereas Figure 6.20 (c) shows small deviations in the outer parts of the structure. These small amplitudes of the imaginary part can affect the resulting phase angle, when the magnitudes of the corresponding real parts are also small. This might occur in the edge-near areas of the panel model.
The results for the Ψ_{21} model with imaginary part values of $\Im(dz) \approx j0.0$ for all exemplary frequencies are shown in Figure 6.21 (a) to (c). Examples of measurements

at supersonic flow conditions of both models are given in the appendix in Figure D.20 and Figure D.21 and show no significant differences compared with the subsonic cases. The impact of the measurements deviating from zero at high excitation frequencies are discussed in the next paragraphs after the corresponding real part results are shown.

Real Part

Since the imaginary part shows almost constant values of zero, it is sufficient to consider only the deformation's real part for the evaluation of the whole measured deformation ($\Re(dz) \approx |dz|$). The real parts presented in Figure 6.22 and Figure 6.23 are illustrated in the same way as was done for the imaginary part examples in the preceding section.

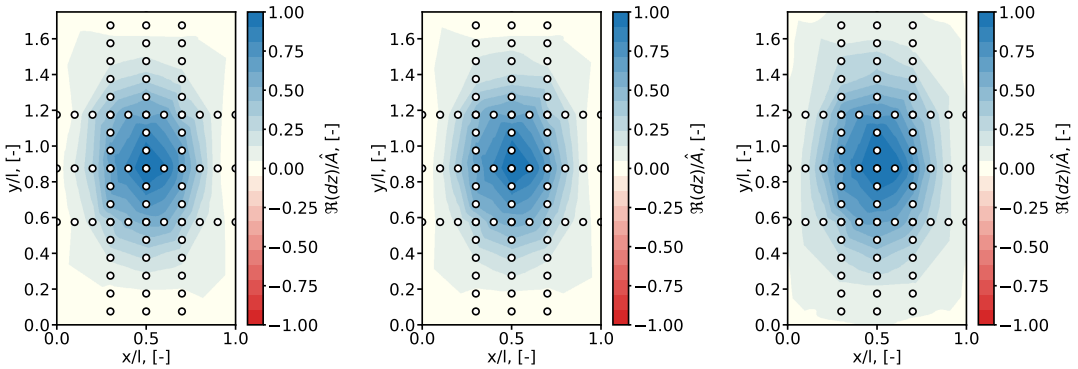

(a) $f_{exc} = 1.0$ Hz. (b) $f_{exc} = 15.0$ Hz. (c) $f_{exc} = 30.0$ Hz.

Figure 6.22.: Real part of structural deformation; Influence of excitation frequency at subsonic flow conditions; $M_\infty = 0.8$, $Re = 5.0 \cdot 10^6$; $\hat{A} = 1.8$ mm; Ψ_{11}.

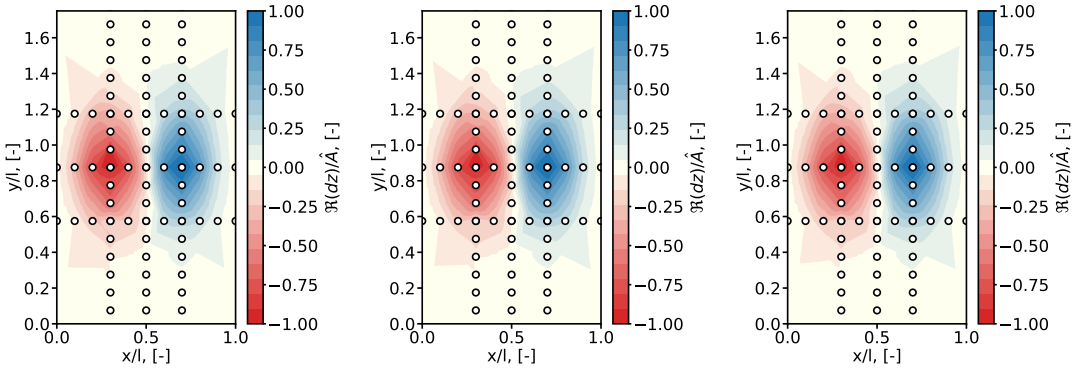

(a) $f_{exc} = 1.0$ Hz. (b) $f_{exc} = 15.0$ Hz. (c) $f_{exc} = 30.0$ Hz.

Figure 6.23.: Real part of structural deformation; Influence of excitation frequency at subsonic flow conditions; $M_\infty = 0.8$, $Re = 5.0 \cdot 10^6$; $\hat{A} = 1.2$ mm; Ψ_{21}.

The results for $f_{exc} = 1.0$ Hz and $f_{exc} = 15.0$ Hz are in good agreement with the reference

results of the FEM simulations shown in Figure 6.19 (a). Analogous to the presented imaginary parts, the Ψ_{11} results show slight deviations for $f_{exc} = 30.0$ Hz. In contrast to this and in accordance to the presented imaginary parts, the Ψ_{21} results show a fair agreement with the simulations presented in Figure 6.19 (b) for all three exemplary frequencies. Following this cursory examination, a more precise evaluation of the results is now required. The common way to correlate vectors to each other is to calculate the dot product of normalized vectors. Especially in the field of structural dynamics and aeroelasticity the Modal Assurance Criterion (MAC) is used:

$$MAC = \frac{|\vec{\Psi}^H_{SPR,ij}\vec{\Psi}_{FEM,ij}|^2}{\vec{\Psi}^H_{SPR,ij}\vec{\Psi}_{SPR,ij}\vec{\Psi}^H_{FEM,ij}\vec{\Psi}_{FEM,ij}} \tag{6.3}$$

This includes in the case at hand the vectorized measured deformation shape of the forced motioned structure $\vec{\Psi}_{SPR,ij}$ and the simulated reference mode shape $\vec{\Psi}_{FEM,ij}$, which is vectorized as well [101]. For identical vectors the result is always $MAC = 1.0$, whereas the result for orthogonal vectors is $MAC = 0.0$. In the present case, the criterion is used to correlate the complete measured and interpolated data sets with the corresponding FEM data sets of the modal analysis (1) and with the FEM forced displacement analysis (2), which is referred to as 3D data. In addition, the results of the mid-section at $y/w_i = 0.5$ are compared with those of the FEM modal analysis data (3) and with the FEM forced displacement data (4) (referred to as 2D data). Figure 6.24 shows the 2D MAC results over the range of excitation frequencies of the experiments. A dotted black line indicates a perfect correlation, whereas the correlation between FEM forced displacement data and FEM modal analysis data is represented by a grey dotted line. In this particular figure both results are almost identical. The results of all measurement points of the test campaign are illustrated, which also includes some outliers.

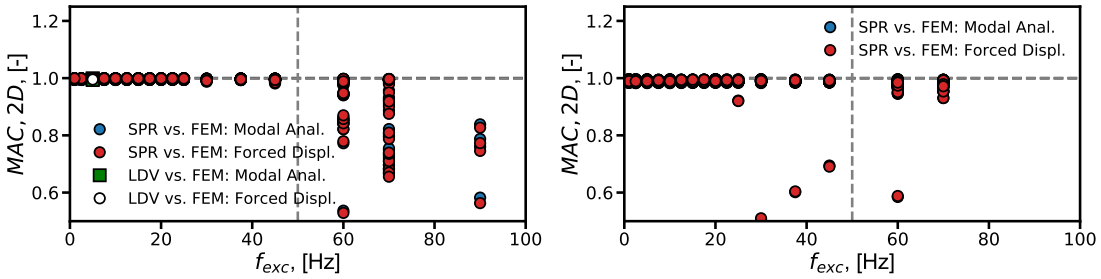

(a) Ψ_{11} model (2017).

(b) Ψ_{21} model.

Figure 6.24.: Correlation of measured structural shape and FEM results of forced displacement and modal analysis approach at $y/w_i = 0.5$.

Additional results of the laser vibrometer are available for $f_{exc} = 5.0$ Hz for the Ψ_{11} model. For both models the match between the two FEM approaches and the measure-

ment deformation is exceptionally good. Furthermore, the FEM modal shape and the FEM forced deformation shape are almost identical. In the second half of the frequency range a strong dispersion of the results occurs, which does not improve again until the end of the investigated frequency range. These deviations are particularly significant for the Ψ_{11} model, whereas the results of the Ψ_{21} model remain satisfactory. The results of the complete data sets shown in Figure 6.25 generally prove the previous observations, but also show significant differences.

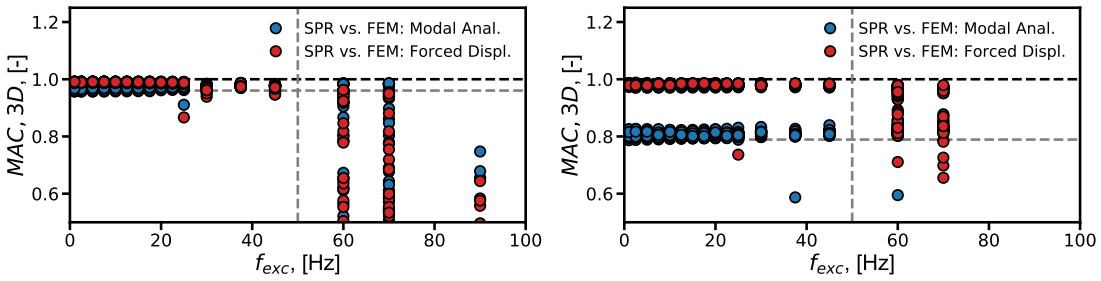

(a) Ψ_{11} model (2017).

(b) Ψ_{21} model.

Figure 6.25.: Correlation of measured structural shape and FEM results of forced displacement and modal analysis approach for the full data set.

The deviations in the high frequency domain are now significant for both the Ψ_{11} model and the Ψ_{21} model. Furthermore, the plots reveal an increased deviation between the FEM calculated mode shape and the corresponding measured and simulated forced displacement results, which applies in particular for the Ψ_{21} model. The results in the low and medium frequency range remain nevertheless satisfying and the correlation between the measured displacements and the forced motion FEM data is as convincing as demonstrated for the half-span section in Figure 6.24. In addition to this, results of the first Ψ_{11} campaign are illustrated in the appendix (Figure D.24), which agree with the results of the second campaign. The occurring deviations at high frequencies, which correspond to the observations for the imaginary values, can be related to the strongly increased accelerations of the cameras of the SPR system shown in Section 6.2.1. If the further results do not contradict this and raise new questions, no further explanation is sought.

6.2.4. Amplitude

In this section the redundant data available for the structure oscillation's amplitude, given on the one side by the SPR system and on the other side by the actuator's position sensor, is compared to each other. Before each test campaign the position sensors are calibrated, for which laser triangulators are used as described in Section 5.2.4. This is why the position sensors' data is considered to be very reliable. Since one SPR marker is located directly at the position of the attached actuator, the SPR amplitude at this

specific location must correspond exactly to the position sensor's data. Figure 6.26 illustrates data sets recorded by the SPR system and comparative measurements of the position sensor, both as a function of the excitation frequencies. All results are divided by the nominal amplitude $\hat{A}_N$. Since the motion of the position sensor is defined as the reference signal, there is no imaginary part and its real part is thus equal to its absolute value $|dz| = \Re(dz)$. This is also valid for the depicted real part of the SPR results, since it represents only the marker synchronized to the actuator's position sensor signal. Imaginary values are nevertheless shown. Those results are not related to the marker at the actuator position, but show only the maximum values found in the whole marker data set.

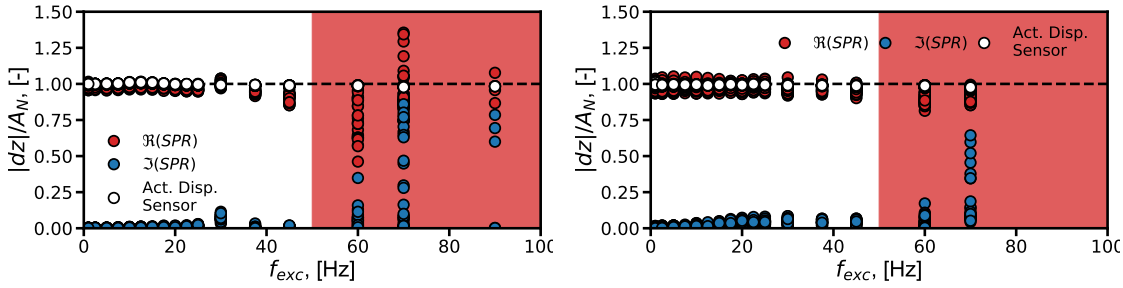

(a) Excitation frequency's influence of measured amplitude; Ψ_{11} model (2017).

(b) Excitation frequency's influence of measured amplitude; Ψ_{21} model.

Figure 6.26.: Comparison of displacement sensor and SPR results related to the nominal amplitude.

Again, strong deviations of the SPR data in the second half of the frequency range emerge, whereas the position sensor's results show a constant behavior throughout the whole range of excitation frequencies. In the first half, both results match well, although the SPR results exhibit certain offsets, which depend on the measurement series but are without connection to the Mach number or the Reynolds number. This behavior may be caused by changes in the temperature, which is subject to significant changes during the test campaigns. The change in temperature depends, among others, on the operating time, the operational point and the outside temperature. Deviations in the position sensor's results can be caused by the manual adjustment of the actuator's stroke by the signal generator at every measurement point. Either way, the characteristics of the SPR results in the high-frequency range are not supported by the displacement sensor's results, which, on the contrary, show constant amplitudes within the entire frequency range. Based on that difference between the two measurement techniques the already presumed faultiness of the SPR system's data in the high frequency range is substantiated.

6.2.5. Summary

To sum up the findings of this section, the shape realized by the applied actuator mechanism was illustrated and compared with the intended design shapes Ψ_{11} and Ψ_{21}. In the low and medium frequency range, the mechanism undoubtedly fulfills its purpose and shows satisfying deformations of the test structure. The consistency of results in the high frequency domain strongly decreases, which may be caused by SPR measurement faults, which is implied by the consistent results of the actuator's position sensor over the full frequency range. Associated acceleration measurements show strongly increased motions of the SPR cameras and thus confirm this assumption. The consistent results of the pressure data throughout the full frequency range support this assumption, as presented in Section 6.3.

6.3. Pressure

The previous section has verified the quality of the forced motion mechanism. Its good outcome allows for the continuation of this work with the analyses of the measured pressure that is induced by the structure's motion. Following the evaluation of the measured pressure's reliability, results are presented in numerous contour plots covering the illustration of results throughout the entire test structure. More detailed insight into the various phenomena is shown afterwards by illustrating results of the panel's mid-span section. The contour plots contain interpolated values, whereas the latter show the complex valued pressure directly derived from the measured data. The reference signal is provided again by the motion of the actuating mechanism that is recorded by the integrated position sensor.
The pressure is represented by means of the pressure coefficient, which was introduced in Section 5.2. The main focus of this chapter lies on the influence of the Mach number (fluid parameter) and the excitation frequency (structure parameter), which strongly affect the aerodynamic response. However, the analysis starts with two short sections, which allow for the simplification of some data sets with respect to the repeatability of results and the impact of the structure's deflection amplitude on the induced pressure. This is followed by the analysis of the influence of the Reynolds number's on the pressure coefficient.

6.3.1. Reliability of Measurement Data

This section refers to the same measurement points and coordinates already used in the previous analysis of the structural deformation for the Ψ_{11} model and the Ψ_{21} model, as presented in Table 6.1. The exemplary spectra shown in Figure 6.27 and Figure 6.28 depict FFT results, that are based on time data for different excitation frequencies of various sensors. All results are obtained for the model's half-span section.

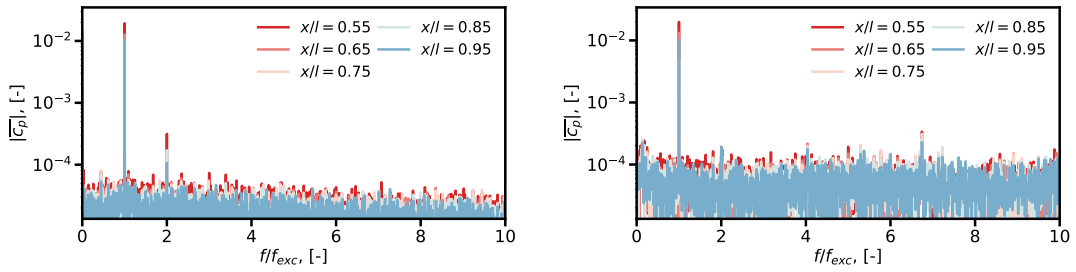

(a) $M_\infty = 0.8$; $f_{exc.} = 1.0$ Hz; $Re = 5.0 \cdot 10^6$. (b) $M_\infty = 0.8$; $f_{exc.} = 15.0$ Hz; $Re = 5.0 \cdot 10^6$.

Figure 6.27.: Spectra of pressure measurements of different sensor positions along the half-span section; Ψ_{11} model.

The presented examples show a dominating global peak of the spectrum at $f/f_{exc} = 1.0$. A second peak emerges at the excitation frequency's second harmonic $f/f_{exc} = 2.0$, as

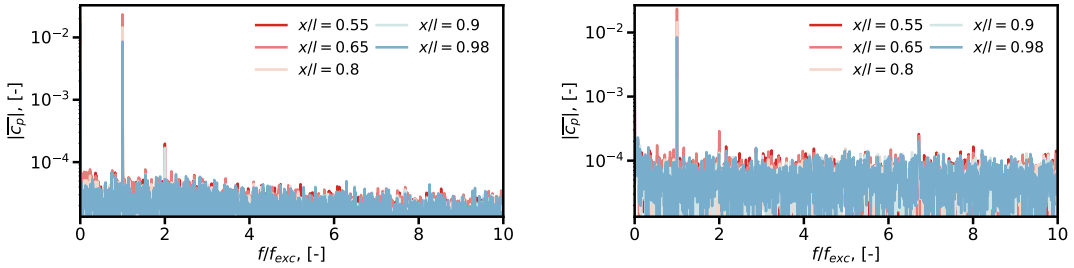

(a) $M_\infty = 0.8$; $f_{exc.} = 1.0$ Hz; $Re = 5.0 \cdot 10^6$. (b) $M_\infty = 0.8$; $f_{exc.} = 15.0$ Hz; $Re = 5.0 \cdot 10^6$.

Figure 6.28.: Spectra of pressure measurements of different sensor positions along the half-span section; Ψ_{21} model.

is shown particularly well by the examples at a low excitation frequency. As discussed earlier, the output of the frequency generator used to set the structure's excitation frequency contains such higher harmonics that ultimately affect the aerodynamic response. Since the ratio between the maximum of the higher harmonics' amplitudes and the amplitude of the excitation frequency is about 100, the impact is considered small. Besides, only the component at $f/f_{exc} = 1.0$ is included in the analysis, which has purely sinusoidal characteristics, as described in Section 5.2.2. The error bars presented in this section represent the standard deviation σ_{cp} of the complex measured pressure amplitudes, according to the same principle as applied to the deformation data. Exemplary histograms of pressure probe signals, plotted in Figure 6.29 and Figure 6.30 for subsonic conditions, show approximately normally distributed results.

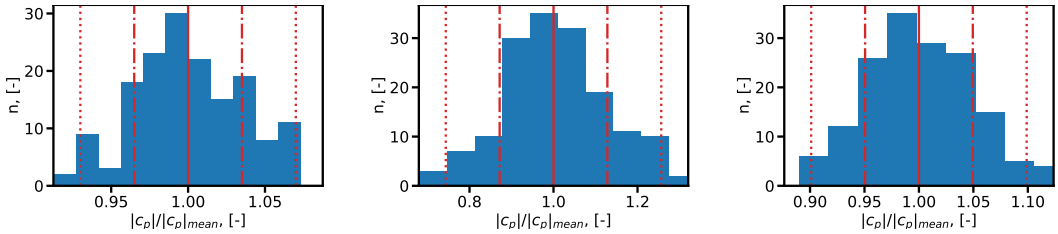

(a) $x_1/l = 0.55$, $y/w_i = 0.5$. (b) $x_3/l = 0.75$, $y/w_i = 0.5$. (c) $x_5/l = 0.95$, $y/w_i = 0.5$.

Figure 6.29.: Histograms of measured pressure amplitude scattering; $M_\infty = 0.8$; $f_{exc.} = 15.0$ Hz; $Re = 5.0 \cdot 10^6$; Ψ_{11} model. The solid, dashed and dotted red lines indicate the average value, the $1\sigma_{cp}$ and the $2\sigma_{cp}$ boundaries.

Each histogram shows the results of the sensor signal for one measurement point. The frequency distribution of the n amplitudes of one full sensor signal is illustrated. Red vertical dash-dotted and dotted boundaries show the distance of the single and the double standard deviation to the average value $|c_p|/|c_p|_{mean} = 1.0$, respectively. The most important characteristics are on the one hand the histograms' symmetry and on the other hand the accumulation of the results' majority within the σ_{cp}-boundaries. Corre-

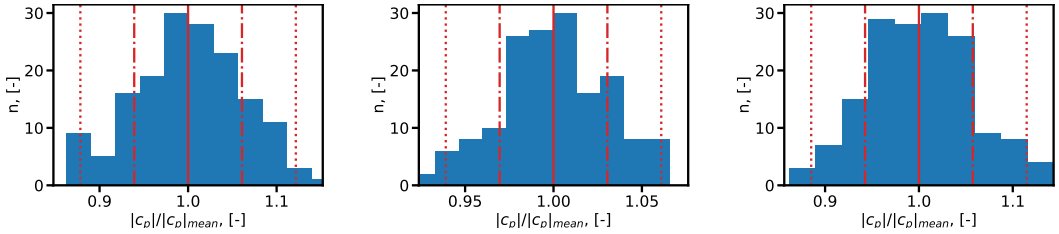

(a) $x_1/l = 0.55$, $y/w = 0.5$. (b) $x_3/l = 0.75$, $y/w = 0.5$. (c) $x_5/l = 0.95$, $y/w = 0.5$.

Figure 6.30.: Histograms of measured pressure amplitude scattering; $M_\infty = 0.8$; $f_{exc.} = 15.0$ Hz; $Re = 5.0 \cdot 10^6$; Ψ_{21} model. The solid, dashed and dotted red lines indicate the average value, the $1\sigma_{cp}$ and the $2\sigma_{cp}$ boundaries.

sponding examples of measurements under supersonic flow conditions are illustrated in Figure D.25 to D.28.

6.3.2. Ψ_{11} Model

In order to analyze the occurring phenomena and dependencies on the different structural and fluidic parameters, the set of measurement points, sufficient for the analyses of the deformation, is extended. The resulting set of measurement points is given in Table 6.2 and Table 6.3. The last column of these tables shows the reduced and thus dimensionless excitation frequency k. This is obtained by dividing the excitation circular frequency ω_{exc}, which is multiplied by half the structure's length, by the free stream velocity.

$$k = \frac{f_{exc} l_i \pi}{U_\infty} \tag{6.4}$$

Another measure, which makes the pressure data comparable, is the introduction of the standardized pressure coefficient, which is the pressure coefficient c_p, divided by the non-dimensional amplitude $\hat{A}/l_i$.

$$\overline{c}_p = c_p \frac{l_i}{\hat{A}} \tag{6.5}$$

Influence of Deflection Amplitude

The first experimental campaign carried out on the Ψ_{11} test structure includes a variation of the actuator stroke, which means a variation of the deflection amplitude. The choice of appropriate amplitudes means a trade-off between experimental requirements and, regarding the following validation activities, numerical requirements. From an experimental point of view, these amplitudes must on the one hand cause displacements throughout the test structure that are large enough in order to obtain accurate response

Model	M_∞ [-]	Re [10^6]	$\hat{A}_N$ [mm]	$f_{exc.}$ [Hz]	U_∞ [m/s]	p_0 [Pa]	k [-]
Ψ_{11}	0.70	2.5	0.6	1.0	242.71	28926.3	0.01
(2015)	0.70	2.49	0.6	60.0	242.87	28845.3	0.78
	0.70	2.5	1.2	1.0	242.5	28893.8	0.01
	0.70	2.49	1.2	60.0	242.59	28825.3	0.78
	0.70	2.49	1.8	1.0	242.5	28819.9	0.01
	0.70	2.49	1.8	60.0	242.5	28835.0	0.78
	1.20	2.48	0.6	1.0	419.33	13872.6	0.01
	1.20	2.49	0.6	60.0	418.5	13898.3	0.45
	1.20	2.5	1.2	1.0	418.5	13901.0	0.01
	1.20	2.5	1.2	60.0	418.43	13902.0	0.45
	1.20	2.49	1.8	1.0	417.94	13900.0	0.01
	1.20	2.49	1.8	60.0	418.91	13878.4	0.45

Table 6.2.: MPs of Ψ_{11} model (2015 Campaign) used in the result's analysis.

signals from the applied measurement technique. On the other hand, the amplitudes are also subject to the limitations of the performed strength calculations. From a numerical point of view, the amplitudes must be kept as small as possible in order to avoid non-linearities in connection with the relation between the induced pressure and the forced motion. Complex pressure results of the first test campaign on the Ψ_{11} model, performed in 2015 and which involved the variation of the excitation amplitude, are illustrated in Figure 6.31.

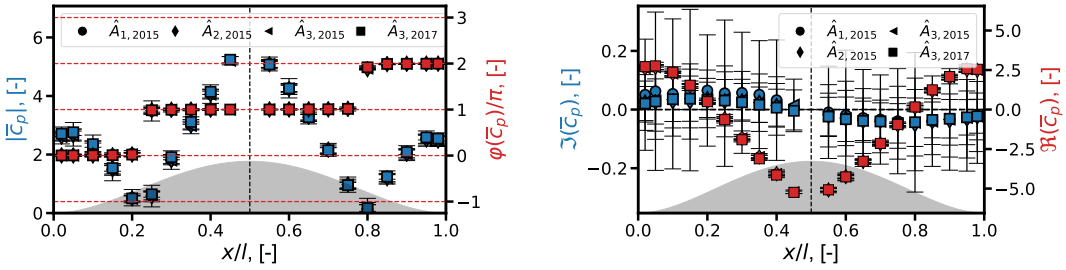

(a) Absolute values and phase angles.

(b) Real and imaginary parts.

Figure 6.31.: Dependency on excitation amplitude and reproducability of results; $y/w_i = 0.5$; $M_\infty = 0.7$; $f_{exc} = 1.0$ Hz; $Re = 2.5 \cdot 10^6$; Ψ_{11} model.

The left hand figure shows the pressure's absolute values and the corresponding temporal phase angels between the structure's motion and the induced pressure for the half-span section at $y/w_i = 0.5$. For now, only a direct comparison of the results is of interest. Analysis of the illustrated characteristics follows in the sections focusing on the influence of the Mach number and the excitation frequency. The three data sets $\hat{A}_{1,2015}$, $\hat{A}_{2,2015}$

Model	M_∞ [-]	Re [10^6]	$\hat{A}_N$ [mm]	$f_{exc.}$ [Hz]	U_∞ [m/s]	p_0 [Pa]	k [-]
Ψ_{11}	0.70	4.98	1.8	1.0	246.41	59977.6	0.01
(2017)	0.70	4.98	1.8	15.0	246.45	59966.9	0.19
	0.70	4.98	1.8	30.0	246.37	59984.8	0.38
	0.70	4.98	1.8	45.0	246.41	59987.1	0.57
	0.70	4.98	1.8	60.0	246.45	59996.5	0.76
	0.80	4.97	1.8	1.0	281.84	50700.4	0.01
	0.80	4.97	1.8	60.0	281.8	50710.2	0.67
	0.90	5.03	1.8	1.0	315.89	43445.7	0.01
	0.90	5.03	1.8	60.0	315.89	43464.9	0.6
	1.05	4.98	1.8	1.0	369.8	34949.2	0.01
	1.05	4.98	1.8	60.0	369.74	34945.2	0.51
	1.10	4.98	1.8	1.0	387.34	32589.7	0.01
	1.10	5.0	1.8	60.0	387.03	32609.6	0.49
	1.20	4.99	1.8	1.0	422.7	28458.2	0.01
	1.20	4.99	1.8	17.5	422.35	28486.6	0.13
	1.20	4.99	1.8	30.0	421.93	28505.8	0.22
	1.20	4.99	1.8	45.0	422.7	28480.6	0.33
	1.20	4.99	1.8	60.0	422.0	28517.9	0.45
	0.70	2.5	1.8	1.0	244.53	29540.3	0.01
	0.70	2.5	1.8	60.0	244.61	29563.0	0.77
	1.20	2.5	1.8	1.0	420.77	14138.4	0.01
	1.20	2.5	1.8	60.0	420.91	14157.3	0.45
	0.70	7.5	1.8	1.0	248.48	92293.7	0.01
	0.70	7.5	1.8	60.0	248.99	92789.4	0.76
	1.20	7.49	1.8	1.0	426.64	43895.2	0.01
	1.20	7.5	1.8	60.0	426.58	43995.0	0.44

Table 6.3.: MPs of Ψ_{11} model (2017 Campaign) used in the result's analysis.

and $\hat{A}_{3,2015}$ are almost congruent, which proves a strictly linear dependence of the pressure on the deformation amplitude within the tested range. This applies for both the pressure's absolute values and the associated phase angles. The plotted error bars are small for the absolute values and the phase angles.
The split of the complex-valued pressure into real parts and imaginary parts results in considerable error bars in the latter, which is the result of its low magnitudes, as is illustrated in Figure 6.31 (b). Remarkable is the agreement of the imaginary parts, which nevertheless occurs. Results for further Mach numbers and amplitudes are presented in Figure D.29 to D.31.

Repeatability of Results

In the second Ψ_{11} test campaign, various of measurement points were recorded under boundary conditions, that were already recorded in the first Ψ_{11} campaign. This provides the opportunity to check the reproducibility of the results and thus to prove the quality of the experimental setup itself. Figure 6.31 (a) and (b) contain, in addition to the results obtained for different amplitudes in the first campaign, results of the second campaign for $\hat{A}_3$. These are compared with the previously performed measurements with the same parameters. No significant differences can be detected. In addition to the experiment's quality demonstrated in this way, the repeatability of the results allows also the combination of the results of the two test campaigns, which are based on different test matrices with different discretizations of the excitation frequency and the Mach number.

Reynolds Number Influence

In Chapter 3, the variation of the flow parameters was chosen in order to adjust the flow's boundary layer and thus to affect the aerodynamic response induced by the panel's deformation. Continuing the analysis and the discussion of the boundary layer measurements of that chapter's first section, this section compares the outcome of the pressure coefficient measurements obtained for the three tested Reynolds numbers. The results obtained at a low Mach number and a low excitation frequency are depicted in Figure 6.32, which reveal a very slight influence on the pressure.

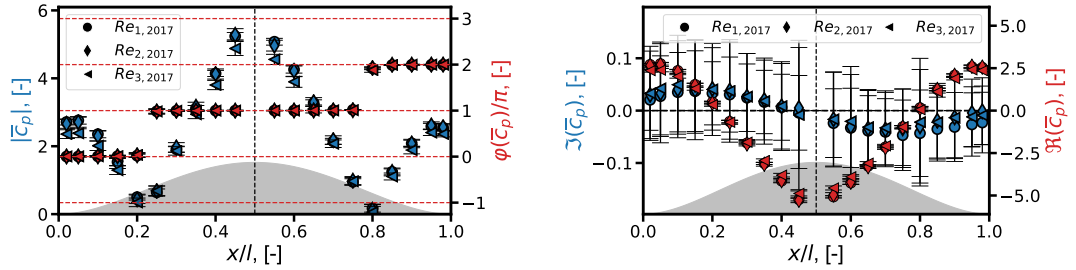

(a) Absolute values and phase angles.

(b) Real and imaginary parts.

Figure 6.32.: Reynolds number influence ($Re_1 = 2.5{\cdot}10^6$, $Re_2 = 5.0{\cdot}10^6$, $Re_3 = 7.5{\cdot}10^6$); $M_\infty = 0.7$; $f_{exc} = 1.0$ Hz; Ψ_{11} model.

Nevertheless, a decrease of the pressure amplitude appears in the subsonic domain for Re_3, whereas the corresponding phase angle remains constant. In contrast to the subsonic example shown here, at supersonic conditions the pressure's magnitude remains unaltered for all tested Reynolds numbers. Those results and additional results for an increased excitation frequency can be found in the appendix in Figure D.32 to Figure D.34. However, Figure D.35 shows that in the very vicinity of $M_\infty = 1.0$ the influence of the Reynolds number is strongly increased and causes a significant increase in the pressure

for increasing Reynolds numbers. Regardless of the selected fluidic and structural boundary conditions, a significant influence of the Reynolds number can only be determined at conditions close to sonic conditions.

Frequency Influence

The figures shown in the last sections give a first clue on what the aerodynamic response on an oscillating flat plate looks like. The presented characteristics are examined in detail in the following sections. Depending on the excitation frequency, the general characteristics and the change in these characteristics are analyzed, which is done first for subsonic conditions and subsequently for supersonic flow conditions. The subsonic contour plots presented in Figure 6.33 and Figure 6.34 show the measured pressure throughout the entire panel for three excitation frequencies. As already known from the deformation's illustrations, the presented interpolated data is based on the totality of the measured pressure probes' data. Additional boundary conditions at the corners of the structure are set in order to complete the data set. In contrast to the contour plots presented in Section 6.2, the plots in this section show the absolute values and the phase angles of the complex-valued pressure.

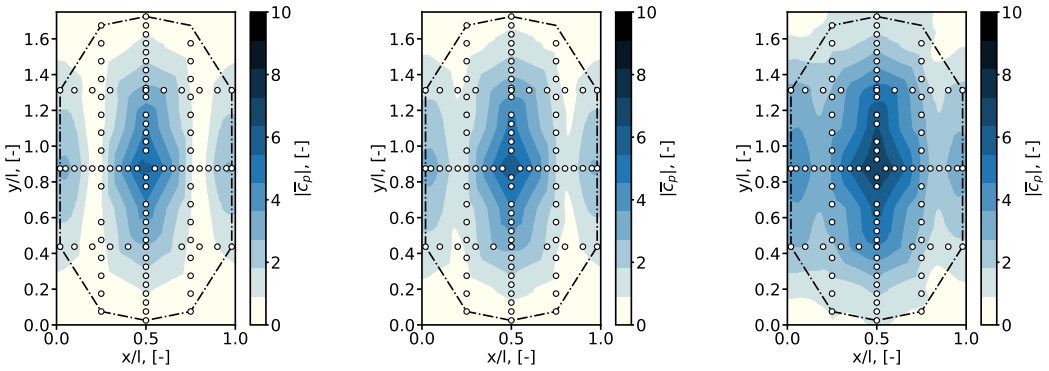

(a) Abs. value; $f_{exc} = 1.0$ Hz. (b) Abs. value; $f_{exc} = 30.0$ Hz. (c) Abs. value; $f_{exc} = 60.0$ Hz.

Figure 6.33.: Influence of excitation frequency at subsonic flow conditions; Ψ_{11} model; $M_\infty = 0.8$; $Re = 5.0 \cdot 10^6$; $\hat{A}_N = 1.8$ mm.

The maximum absolute pressure at a low excitation frequency is located directly in the structure's center, which corresponds with the position of the structure's maximum deformation. Further local peaks arise in the vicinity of the leading edge and the trailing edge, where the minimum deformation of the model can be observed. At the two edges that are limiting the model's extension in spanwise direction (at $y/w_i = 0.0$ and $y/w_i = 1.0$), hardly any induced pressure can be detected. Those three peaks in flow direction are clearly separated at about one-fifth and four-fifth of the panel length with pressure coefficient values of about zero. Figure 6.34 (a) shows the related temporal phase angles, which exhibit two distinct levels.

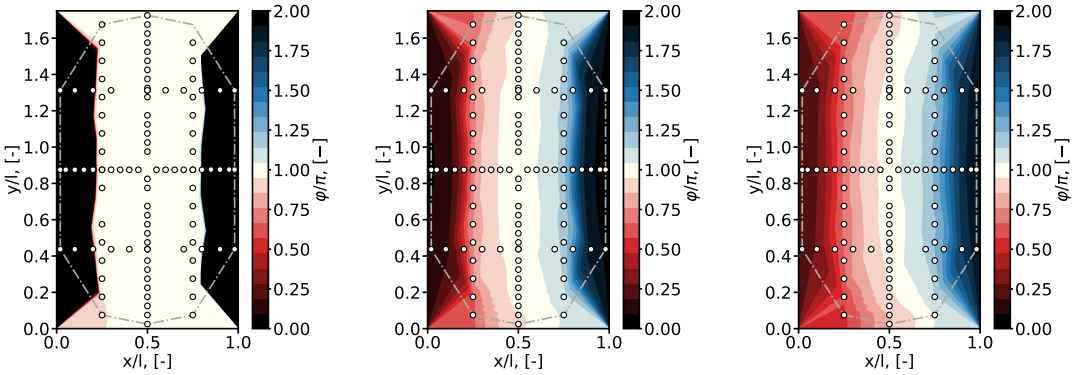

(a) Phase angle; $f_{exc} = 1.0$ Hz. (b) Phase angle; $f_{exc} = 30.0$ Hz. (c) Phase angle; $f_{exc} = 60.0$ Hz.

Figure 6.34.: Influence of excitation frequency at subsonic flow conditions; Ψ_{11} model; $M_\infty = 0.8$; $Re = 5.0 \cdot 10^6$; $\hat{A}_N = 1.8$ mm.

The entire center section has a phase angle of $\varphi = \pi$, whereas the LE and TE areas have a phase angle of $\varphi = 0.0$ or $\varphi = 2\pi$, respectively. Related to the movement of the model, the pressure in the panel center oscillates out of phase, whereas the pressure at the leading edge and the trailing edge oscillates in phase with the actuator. Thus, the pressure on the test structure can be divided into three different domains. The two at the leading edge and the trailing edge oscillate in the same phase as the structure. The third and most pronounced domain, located in the center of the plate, oscillates out of phase. An increase in the frequency, first to $f_{exc} = 30.0$ Hz and finally to $f_{exc} = 60.0$ Hz, causes a growth in the pressure response's magnitude and its spatial extent. As a consequence, the initially obtained spanwise lines, which separate the three domains, vanish and the three areas of high pressure start to merge. Nevertheless, the areas retain the shown phase characteristics, although the originally instantaneous transition from zero to π gives way to a softened transition zone, which is illustrated in Figure 6.34 (b) and (c). Figures depicting the real and the imaginary part of the complex pressure are contained in the appendix in Figure D.36 and Figure D.37. Here, the increase in the imaginary part for increasing excitation frequencies, which is associated with the softening of the phase angle transition, is shown very clearly.
Figure 6.35 shows the results of the half-span section and therefore provides a more detailed insight into the behavior of the aerodynamic response to the test structure's motion. In addition to the absolute values and the phase angles in Figure 6.35 (a) and (b), the complex pressure is divided into its real and imaginary part in Figure 6.35 (c) and (d). Each figure includes a set of five curves recorded at different excitation frequencies. Also, a gray sketch of the underlying structural deformation is presented. For the sake of clarity, the graph's markers representing the actual measured values are connected by solid lines that are based on linear interpolation between the data points.
The illustration of the absolute values clearly shows the above-mentioned rise of the pressure's magnitude and the associated disappearance of the initially distinct dividing

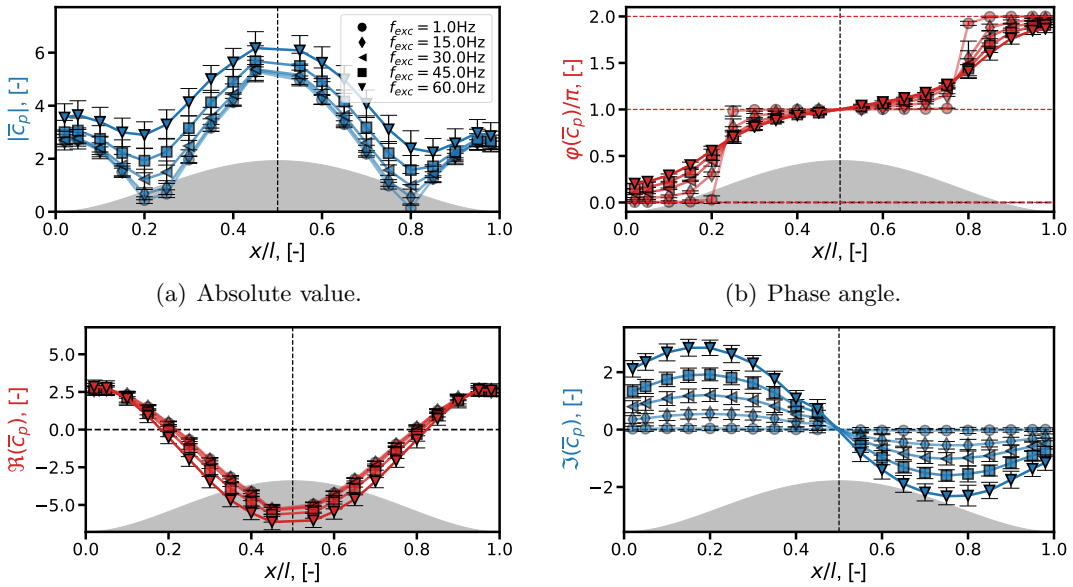

(a) Absolute value.

(b) Phase angle.

(c) Real part.

(d) Imaginary part.

Figure 6.35.: Influence of excitation frequency at subsonic flow conditions; Ψ_{11} model; $M_\infty = 0.7$; $Re = 5.0 \cdot 10^6$; $\hat{A}_N = 1.8$ mm.

lines. The accompanying change in the phase angle shows the development from the initially stepped characteristics at low frequencies to a S-shaped curve at high frequencies. It can clearly be seen, that the separating lines are located where the transition of the phase angle occur at $x/l_i \approx 0.2$ and $x/l_i \approx 0.8$. In the second pair of figures showing the imaginary part and the real part, the latter shows only a very slight dependence on the change in the excitation frequency. Yet, a slight increase of its magnitude is determined. In contrast, the imaginary part is strongly influenced by the increase in the frequency and shows a steep rise in its peak magnitudes. The sinusoidal shape of the imaginary part has a zero-crossing at $x/l_i = 0.5$ and shows opposite signs in the first and the second streamwise half of the model. The peaks are of approximately the same absolute magnitude. The maximum and the minimum are located at the zero points of the real part and at the phase angles' transition from zero to π and from π to 2π.
The observations on the pressure measurements can directly be connected with the underlying structural deformation. Of importance are the locations of maximum and minimum deflections and the inflection points in between. Regarding the absolute pressure values and the real parts, the minima of the former and the zeros of the latter lie at the x-positions where the structure's inflection points are located. Here, the imaginary parts have turning points and thus minima and maxima. However, the turning points of the deformed structure at the leading and the trailing edge and in the panel's center are located where both the pressure's absolute and real part show turning points. Corresponding to the subsonic results shown above, contour plots for supersonic flow conditions for different excitation frequencies are shown in Figure 6.36 and Figure 6.37.

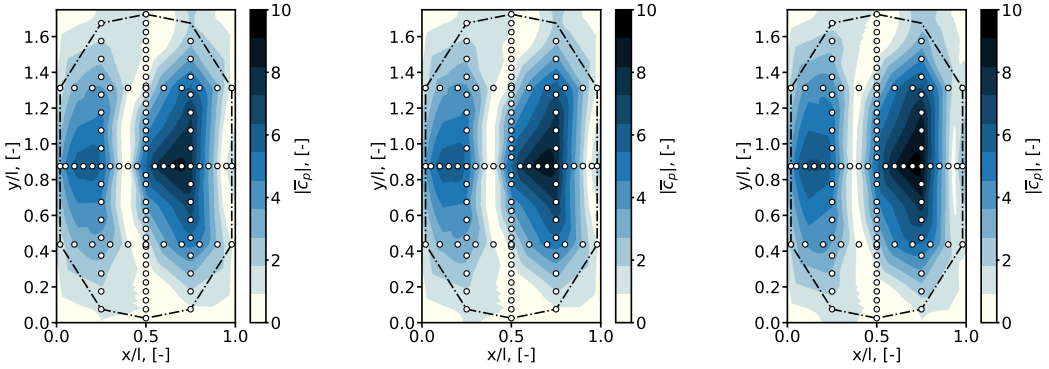

(a) Abs. value; $f_{exc} = 1.0$ Hz. (b) Abs. value; $f_{exc} = 30.0$ Hz. (c) Abs. value; $f_{exc} = 60.0$ Hz.

Figure 6.36.: Influence of excitation frequency at supersonic flow conditions; Ψ_{11} model; $M_\infty = 1.2$; $Re = 5.0 \cdot 10^6$; $\hat{A}_N = 1.8$ mm.

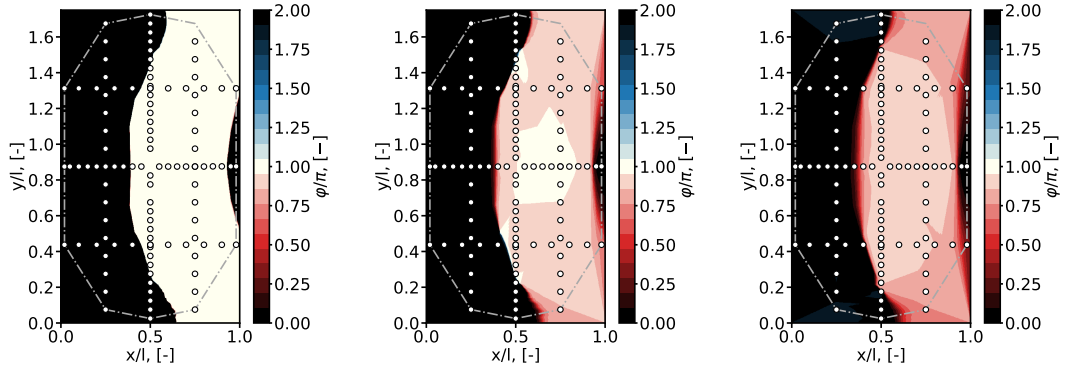

(a) Phase angles; $f_{exc} = 1.0$ Hz. (b) Phase angles; $f_{exc} = 30.0$ Hz. (c) Phase angles; $f_{exc} = 60.0$ Hz.

Figure 6.37.: Influence of excitation frequency at supersonic flow conditions; Ψ_{11} model; $M_\infty = 1.2$; $Re = 5.0 \cdot 10^6$; $\hat{A}_N = 1.8$ mm.

Noticeable at the first glance is that the previously existing symmetry line at $x/l_i = 0.5$ has disappeared for the absolute pressure and the phase angle. A global pressure peak is located in the downstream half of the structure and a local peak emerges in the vicinity of the leading edge. Even though the pressure probes' distribution pattern is rather coarse, the dividing line between the peaks is located at about $x/l_i \approx 0.4$ and a second line is recognizable at about $x/l_i \approx 0.95$. A growth in the pressure's magnitudes, with an accompanying merging of the domains for increasing excitation frequencies, is still present, but much less pronounced as seen before at subsonic conditions. Even at high excitation frequencies, the dividing lines are still clearly visible. The phase angle plots support this observation and show the transition at approximately $x/l_i = 0.4$ and another at $x/l_i = 0.95$. This latter indicates another local pressure domain very close to

the trailing edge. A softening of the phase angle's transition can be determined again, though its significance is small compared with the corresponding subsonic results. A more detailed insight is given in Figure 6.38. Results of the half-span section are shown by splitting up the complex values into absolute values and phase angles on the one hand and into real parts and imaginary parts on the other hand.

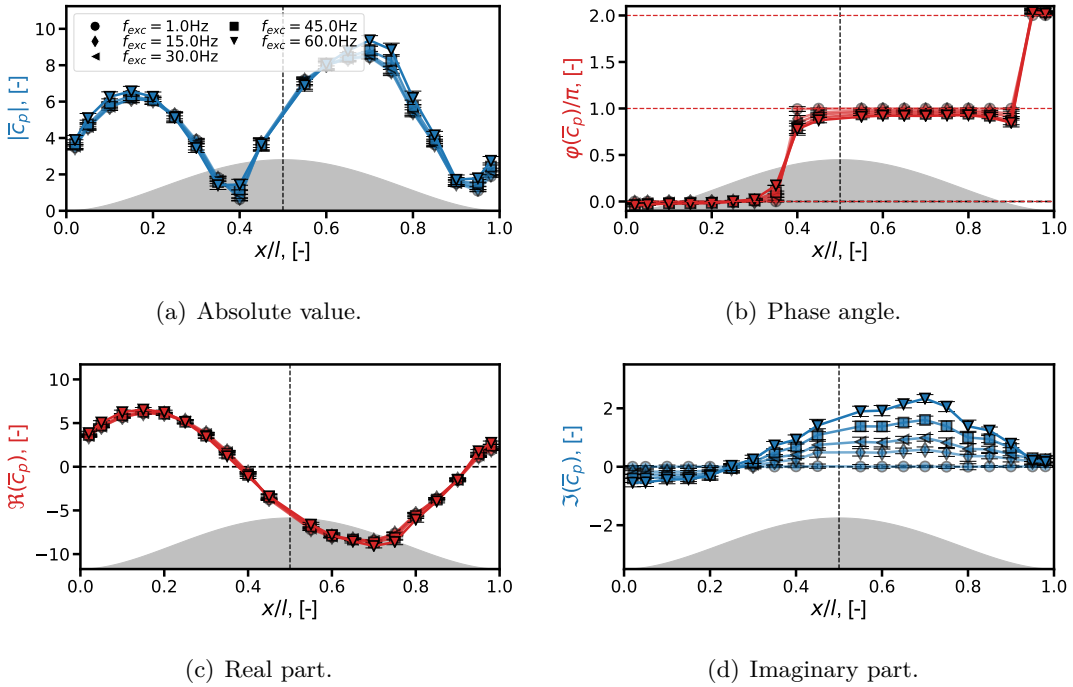

(a) Absolute value.

(b) Phase angle.

(c) Real part.

(d) Imaginary part.

Figure 6.38.: Influence of excitation frequency at supersonic flow conditions; Ψ_{11} model; $M_\infty = 1.2$; $Re = 5.0 \cdot 10^6$; $\hat{A}_N = 1.8$ mm.

By comparing the set of curves with the subsonic measurements, a shift of the curve characteristics in streamwise direction can be seen by about $\Delta x/l_i = 0.15...0.2$. This is particularly clear for the phase angle's transition position and the real part's zero points. The imaginary part's turning points are no longer at the position of the phase angles' transition, which explains the less distinct softening of the transition, although the imaginary part's magnitude is almost unchanged.

Mach Number Influence

In the previous section the frequency's impact on the induced pressure was illustrated for subsonic and supersonic examples. The strong influence of the Mach number on the pressure was observed. In order to analyze that phenomenon, the Mach number's influence is studied in this section for low and for high excitation frequencies. The low frequency results are illustrated in Figure 6.39, the high frequency results are shown in Figure 6.40. Each set of pressure data is divided in a subsonic and a supersonic subset.

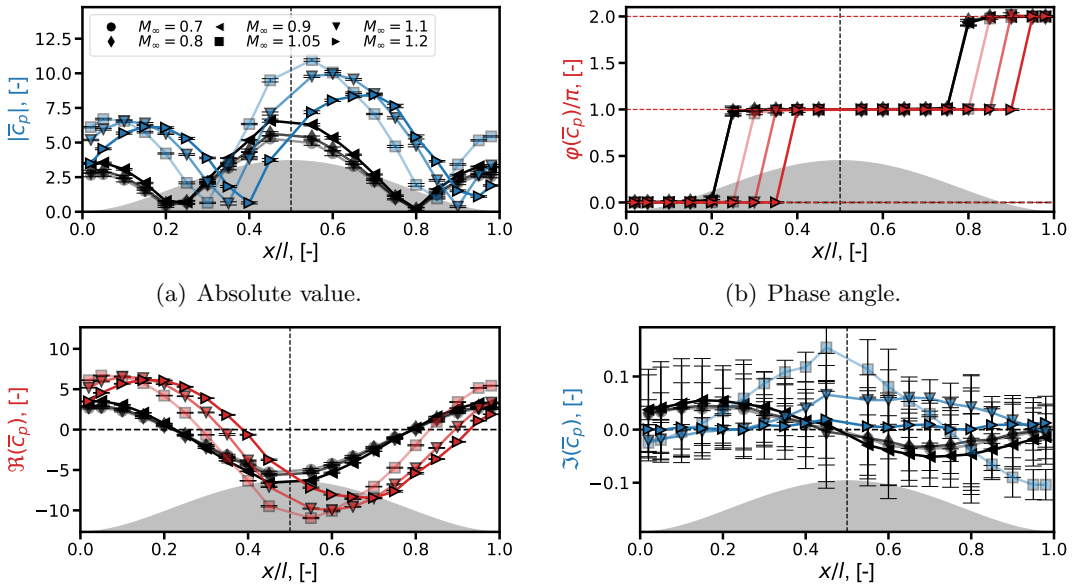

(a) Absolute value.

(b) Phase angle.

(c) Real part.

(d) Imaginary part.

Figure 6.39.: Influence of Mach number at low excitation frequencies; Ψ_{11} model; $f_{exc} = 1.0$ Hz; $Re = 5.0 \cdot 10^6$; $\hat{A}_N = 1.8$ mm.

Despite an increase of the Mach number in the subsonic range from $M_\infty = 0.7$ to $M_\infty = 0.9$ only little change in the pressure magnitude arises at $f_{exc} = 1.0$ Hz. The basic slopes of the four subsonic illustrations in Figure 6.39 (a) to (d) remain unchanged. By exceeding $M_\infty = 1.0$, a sudden change in the pressure coefficient's slope occurs, which leads to a strong rise in its magnitude on the one hand. On the other hand a relocation of the curve's characteristics, such as turning points and inflection points, occurs. That shift of the characteristics can be observed in all four illustrations and is most distinct for the phase angle. The transition between the three domains remains at about $x/l_i = 0.4$ and $x/l_i = 0.8$, while the Mach number is increased within subsonic conditions. At $M_\infty = 1.05$, an initial shift of about five percent of the structure's length is detected. It grows step by step with increasing Mach number until a shift of about 15 percent of the length is reached at $M_\infty = 1.2$. Due to the low amplitude of the pressure's imaginary part, this shift cannot be reliably observed here. In contrast, the real part of the pressure shows this phenomenon very clearly. The Mach number's influence at high excitation frequencies of $f_{exc} = 60.0$ Hz is illustrated in Figure 6.40, which shows phenomena analogous to the previously presented subsonic measurements.
Examining the phase angle, the softening of the phase angle transition, which leads to a clear S-shaped slope for subsonic conditions, is distinctly decreasing with increasing Mach number. The decreasing magnitude of the imaginary part for increasing Mach number proves that observation. The real part remains unchanged by the change in the frequency.

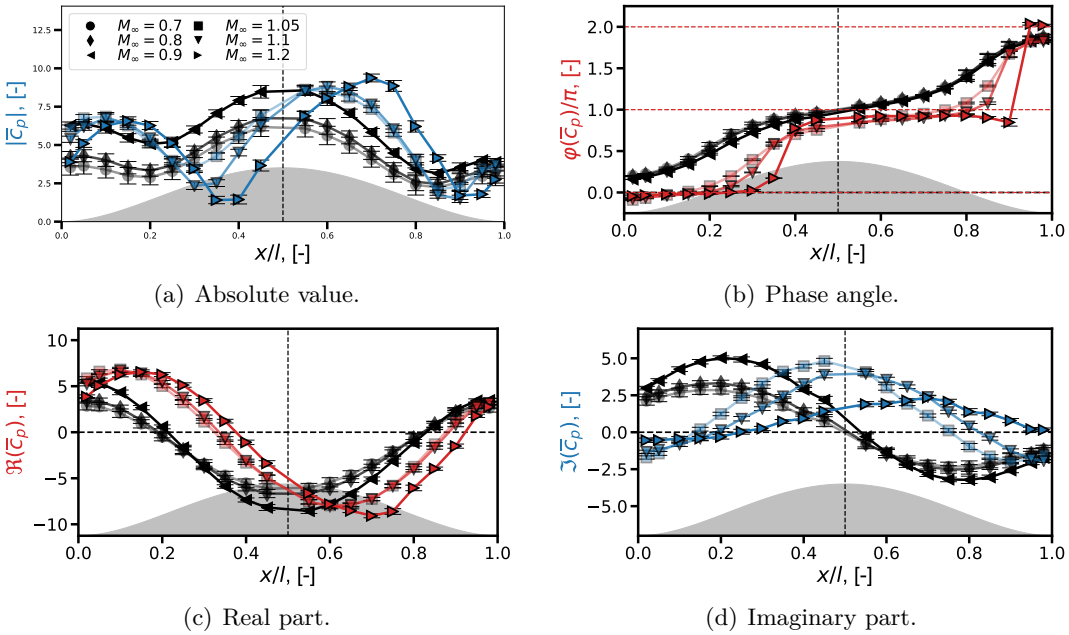

(a) Absolute value.

(b) Phase angle.

(c) Real part.

(d) Imaginary part.

Figure 6.40.: Influence of Mach number at high excitation frequencies; Ψ_{11} model; $f_{exc} = 60.0$ Hz; $Re = 5.0 \cdot 10^6$; $\hat{A}_N = 1.8$ mm.

6.3.3. Ψ_{21} Model

Since the results of the Ψ_{21} model basically show the same phenomena as the Ψ_{11} model does, the already known emerging phenomena are discussed here only in brief. The results are presented in the same way as in the previous section. Only one test campaign was carried out with this model, which means an analysis regarding the repeatability of results cannot be performed here. Regarding the analysis of the excitation amplitude's variation and the influence of the Reynolds number, reference is also made to the results of the Ψ_{11} model presented in Section 6.3.2. The measurement points used in this section's analysis are presented in Table 6.4.

Frequency Influence

Figure 6.41 and Figure 6.42 depict the contour plots of the pressure's absolute values and the belonging phase angle of the Ψ_{21} model for a variation of the excitation frequency under subsonic flow conditions. The corresponding results of the section at $y/w_i = 0.5$ are shown in Figure 6.43 broken down in four subplots, which contain on the one hand the absolute values and the phase angles and on the other hand the real and the imaginary components of the complex-valued pressure. The results resemble results, which could be obtained by arranging two Ψ_{11} structures in a row, each with a global maximum in its center. The pressure characteristics correspond to the deformations of the structure,

Model	M_∞ [-]	Re [10^6]	$\hat{A_N}$ [mm]	$f_{exc.}$ [Hz]	U_∞ [m/s]	p_0 [Pa]	k [-]
Ψ_{21}	0.70	5.0	1.2	1.0	247.21	60694.9	0.01
(2017)	0.70	5.0	1.2	15.0	247.57	60924.6	0.19
	0.70	5.0	1.2	30.0	247.69	60988.4	0.38
	0.70	5.0	1.2	45.0	247.65	61003.5	0.57
	0.70	5.0	1.2	60.0	247.61	60994.3	0.76
	0.80	5.0	1.2	1.0	282.11	51152.8	0.01
	0.80	5.0	1.2	60.0	281.57	50910.6	0.67
	0.90	5.01	1.2	1.0	316.35	43456.9	0.01
	0.90	5.0	1.2	60.0	316.3	43392.7	0.6
	1.05	5.0	1.2	1.0	368.9	34891.0	0.01
	1.05	5.01	1.2	60.0	368.9	34909.0	0.51
	1.10	5.0	1.2	1.0	386.17	32570.7	0.01
	1.10	5.0	1.2	60.0	386.53	32540.1	0.49
	1.20	4.99	1.2	1.0	421.6	28380.6	0.01
	1.20	4.99	1.2	15.0	422.44	28317.6	0.11
	1.20	4.99	1.2	30.0	421.6	28380.0	0.22
	1.20	4.99	1.2	45.0	421.6	28382.9	0.34
	1.20	4.99	1.2	60.0	421.6	28360.2	0.45

Table 6.4.: Measurement points of Ψ_{21} model used in the result's analysis.

which exhibits turning points at the same locations. Including the local pressure maxima at the leading edge and the trailing edge, there are four complex pressure domains divided by three spanwise lines at $x/l_i \approx 0.1$, $x/l_i \approx 0.5$ and $x/l_i \approx 0.9$, as is shown in Figure 6.41.

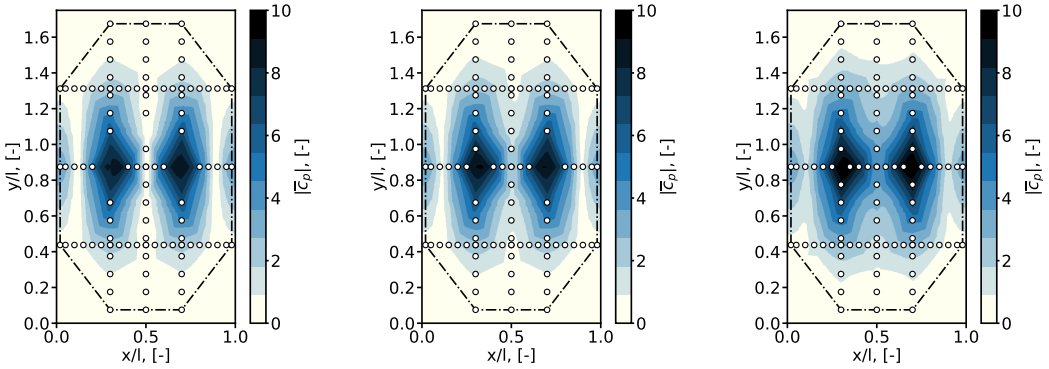

(a) Abs. values, $f_{exc} = 1.0$ Hz (b) Abs. values, $f_{exc} = 30.0$ Hz (c) Abs. values, $f_{exc} = 60.0$ Hz

Figure 6.41.: Influence of excitation frequency at subsonic flow conditions; Ψ_{21} model; $M_\infty = 0.7$; $Re = 5.0 \cdot 10^6$; $\hat{A}_N = 1.2$ mm.

In accordance with the first model, those domains grow larger with rising excitation frequency. This growth is accompanied with the domains' merging and the dissolution of the dividing lines. In contrast to the Ψ_{11} structure, the Ψ_{21} test structure is dynamically deflected by two counteracting actuators, each with an integrated position sensor. The sensor located downstream provides the signal used as a reference for the whole Ψ_{21} pressure data. The phase transition between each of the pressure domains indicates that each pressure domain is in phase opposition to its adjacent domains, which is illustrated in Figure 6.42 (a) showing domains of either zero or π.

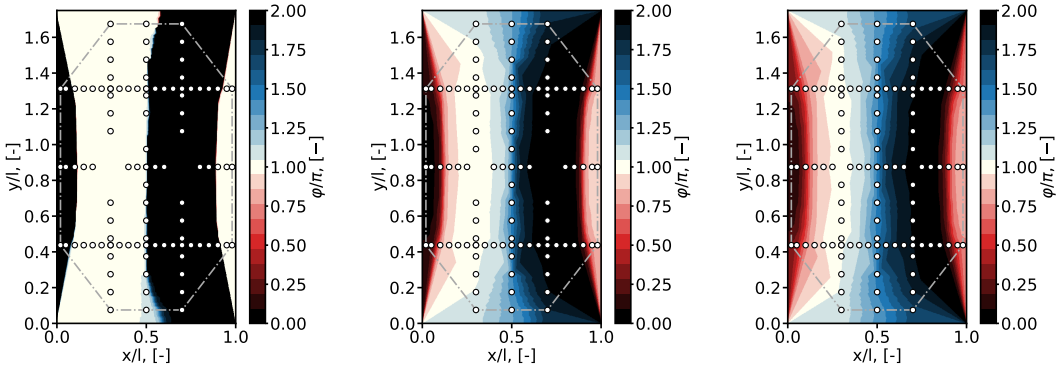

(a) Phase angles, $f_{exc} = 1.0$ Hz (b) Phase angles, $f_{exc} = 30.0$ Hz (c) Phase angles, $f_{exc} = 60.0$ Hz

Figure 6.42.: Influence of excitation frequency at subsonic flow conditions; Ψ_{21} model; $M_\infty = 0.7$; $Re = 5.0 \cdot 10^6$; $\hat{A}_N = 1.2$ mm.

The disappearance of the initially distinct dividing lines between the pressure domains becomes apparent by observing the successive merging of the two center domains with rising frequency from $f_{exc} = 1.0$ Hz to $f_{exc} = 60.0$ Hz at high subsonic Mach numbers of $M_\infty = 0.7$, which is depicted in Figure 6.42 (a) to (c). Apart from the two domains in the panel center, the same effect occurs at the leading and the trailing edge where additional small pressure domains are located. Here, the phase angles show again the development from an instantaneous step of $\Delta\varphi = \pi$ towards a continuous transition zone.

Interpolated results throughout the entire test structure for supersonic conditions as a function of the excitation frequency are shown in Figure 6.44 and Figure 6.45. The former shows the pressure's absolute values, whereas the latter illustrates the associated phase angles. A dependency of the absolute pressure on the rising frequency is hard to recognize, whereas the changes in the phase angle can be nicely detected. The remaining illustrations on the pressure's real and imaginary part are content of the appendix in Figure D.40 to Figure D.43.

Of the four parameters shown in Figure 6.46, only the imaginary part, that illustrates the connection between the shape of the structure's deflection and the resulting pressure, is strongly influenced by an increase in the excitation frequency. The influence on the phase angle is small, since the imaginary part's maxima and minima emerge at the x-

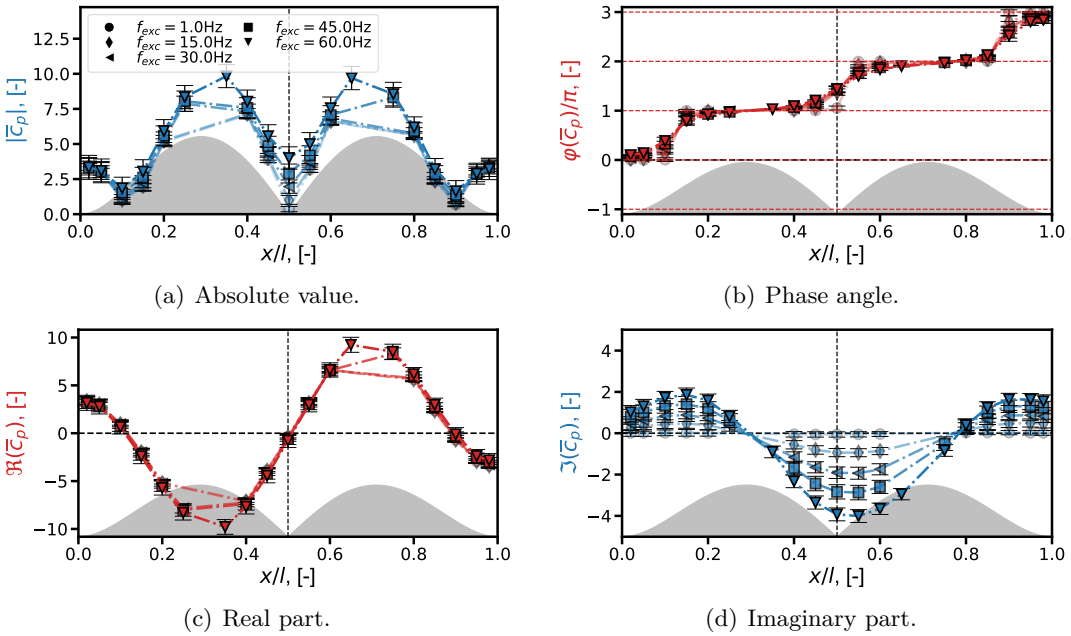

(a) Absolute value. (b) Phase angle.

(c) Real part. (d) Imaginary part.

Figure 6.43.: Influence of excitation frequency at subsonic flow conditions; Ψ_{21} model; $M_\infty = 0.7$; $Re = 5.0 \cdot 10^6$; $\hat{A}_N = 1.2$ mm.

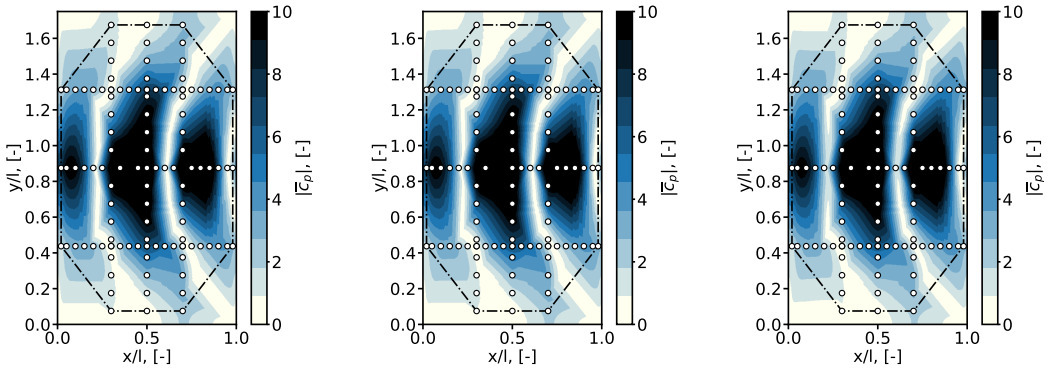

(a) Abs. values, $f_{exc} = 1.0$ Hz (b) Abs. values, $f_{exc} = 30.0$ Hz (c) Abs. values, $f_{exc} = 60.0$ Hz

Figure 6.44.: Influence of excitation frequency at supersonic flow conditions; Ψ_{21} model; $M_\infty = 1.2$; $Re = 5.0 \cdot 10^6$; $\hat{A}_N = 1.2$ mm.

coordinates where also the real part shows high amplitudes. Thus, the imaginary part's influence remains small and also the absolute values remain almost unchanged. Since some sensor errors occurred in the half-span section, the depicted interpolation lines between $x/l_i = 0.35$ and $x/l_i = 0.45$ might be misleading on the first glance.

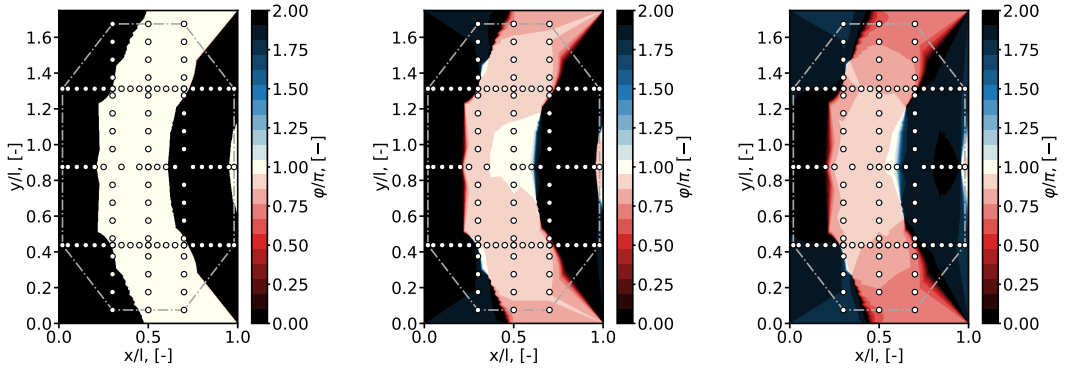

(a) Phase angles, $f_{exc} = 1.0$ Hz (b) Phase angles, $f_{exc} = 30.0$ Hz (c) Phase angles, $f_{exc} = 60.0$ Hz

Figure 6.45.: Influence of excitation frequency at supersonic flow conditions; Ψ_{21} model; $M_\infty = 1.2$; $Re = 5.0 \cdot 10^6$; $\hat{A}_N = 1.2$ mm.

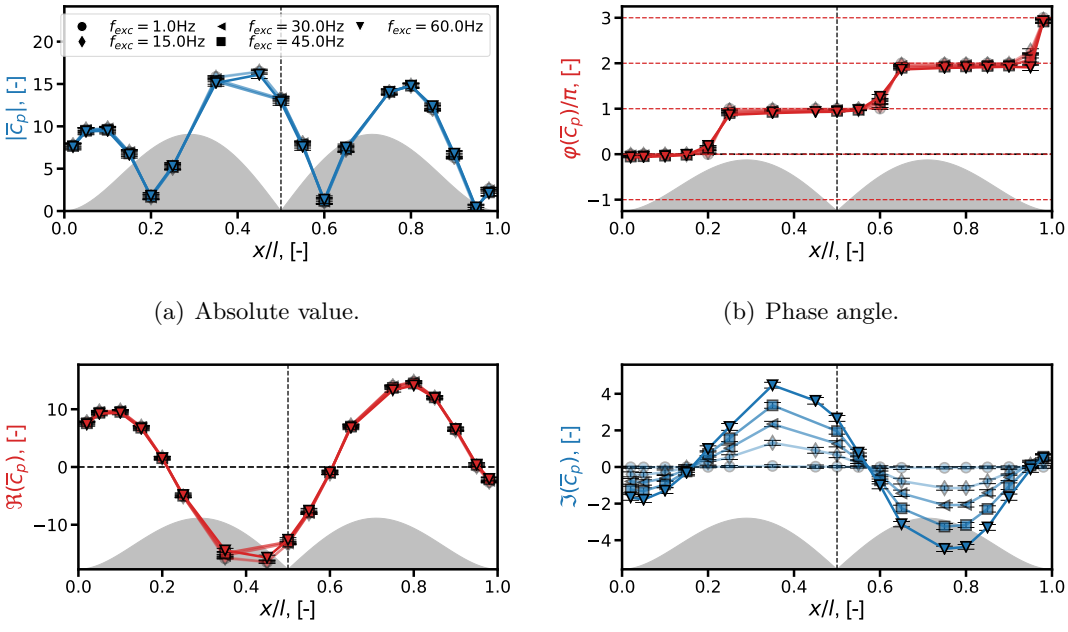

(a) Absolute value.

(b) Phase angle.

(c) Real part.

(d) Imaginary part.

Figure 6.46.: Influence of excitation frequency at supersonic flow conditions; Ψ_{21} model; $M_\infty = 1.2$; $Re = 5.0 \cdot 10^6$; $\hat{A}_N = 1.2$ mm.

Mach Number Influence

The impact of the Mach number is shown in Figure 6.47 and 6.48 for low and high excitation frequencies. At the lower frequency, the characteristics of all associated illus-

trations remain almost unchanged by the variation of the Mach number in the subsonic range. Again, this changes by exceeding the $M_\infty = 1.0$ boundary. The three phase angle transition points of the Ψ_{21} model at $x/l_i \approx 0.1$, $x/l_i \approx 0.5$ and $x/l_i \approx 0.9$ are shifted successively with increasing Mach number in streamwise direction with $\Delta x \approx 0.05 x/l_i$ per step. Since the tested supersonic Mach numbers are limited to a number of three and the resolution of the applied pressure transducers is $\Delta x_p = 0.05 x/l_i$, the occurring shift increment is estimated only roughly. This shift can be observed for all components of the complex pressure. In addition, the pressure's real as well as the imaginary part show an increase in its magnitude. Since the latter's magnitude remains very small, its influence is limited.

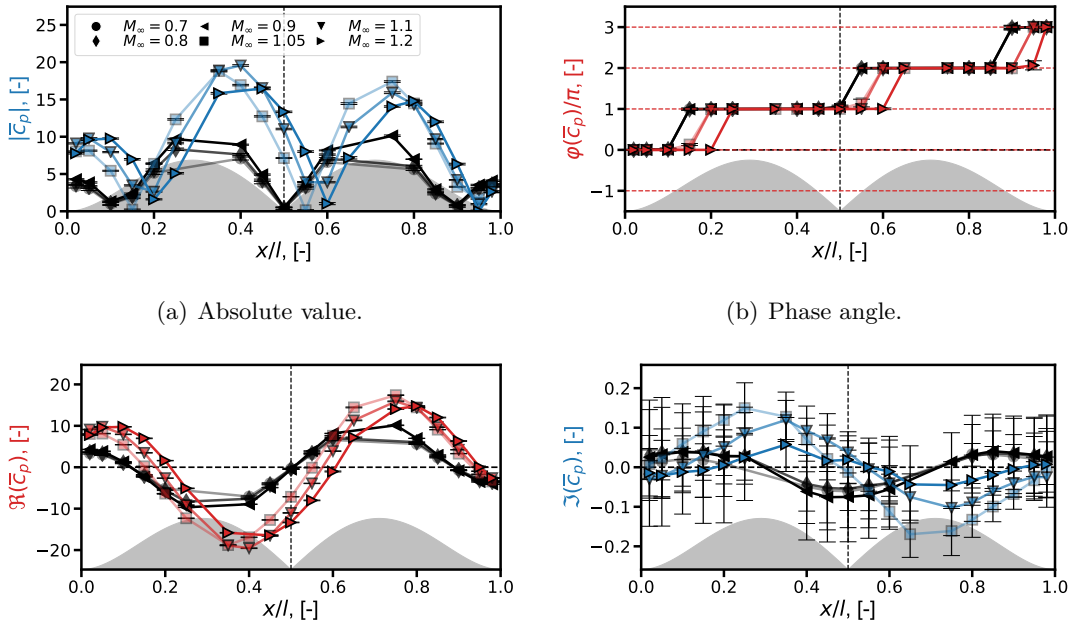

(a) Absolute value.

(b) Phase angle.

(c) Real part.

(d) Imaginary part.

Figure 6.47.: Influence of Mach number at low excitation frequencies; Ψ_{21} model; $f_{exc} = 1.0$ Hz; $Re = 5.0 \cdot 10^6$; $\hat{A}_N = 1.2$ mm.

The results of the higher frequency measurements generally show the same characteristics as observed for the lower frequency. The shift of the curve characteristics, which can be observed clearly in the phase angle's illustration at the lower frequency, is still there, even though it has become less distinct. This is caused by the high imaginary part's magnitude that occurs at the higher excitation frequency and has a significant influence on the phase angle. Nevertheless, the real part exhibits small changes in its magnitude and remains almost unchanged for increasing excitation frequency (compare Figure 6.47 (c) with Figure 6.48 (c)).

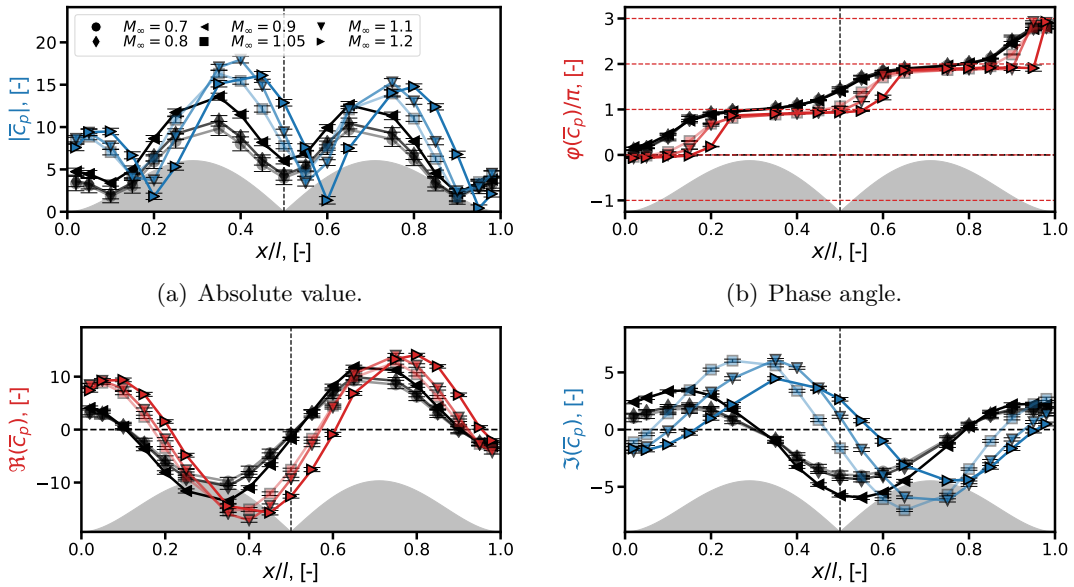

(a) Absolute value.

(b) Phase angle.

(c) Real part.

(d) Imaginary part.

Figure 6.48.: Influence of Mach number at high excitation frequencies; Ψ_{21} model; $f_{exc} = 60.0$ Hz; $Re = 5.0 \cdot 10^6$; $\hat{A}_N = 1.2$ mm.

6.3.4. Verification of Pressure Measurements

After the measured pressures of the test campaigns have been discussed and described, the purpose of this section is to prove the plausibility of the measured data by using the analytic approaches presented in Section 2.3. Due to their limitations in terms of the Mach number's validity range and the viscous characteristics of the flow, which are not considered in the equations, a perfect agreement is not expected. The main focus is to ensure that the measured trends are confirmed. The comparison of results that is carried out in this section is done for the half-span section at $y = 0.5w$. In a first step, exemplary subsonic and supersonic Ψ_{11} measurements are compared with the subsonic potential flow theory and the piston theory. Subsequently, the qualitative trends and the measured and calculated pressure magnitudes are compared in two separate paragraphs. A comparison of subsonic measured pressures with the subsonic potential flow theory approach at $M_\infty = 0.7$ and $f_{exc} = 25.0$ Hz is illustrated in Figure 6.49. The analytic function applied in order to describe the eigenfunction Ψ_{11} is Equation 2.39. The pressure's real parts, measured and calculated, show a cosinusoidal shape. In contrast to the calculated values, the measured pressures show a slightly shifted slope with regard to its x-axis symmetry. Further, the amplitudes of the measured pressure's real parts are significantly smaller than those obtained by theory. The calculated pressure's imaginary parts describe an ideal sine over the panel length, which is approximated very good by the measurements. Both the curve's trend and the associated amplitudes are met well. Only at the leading and the trailing edge, the characteristics differ.

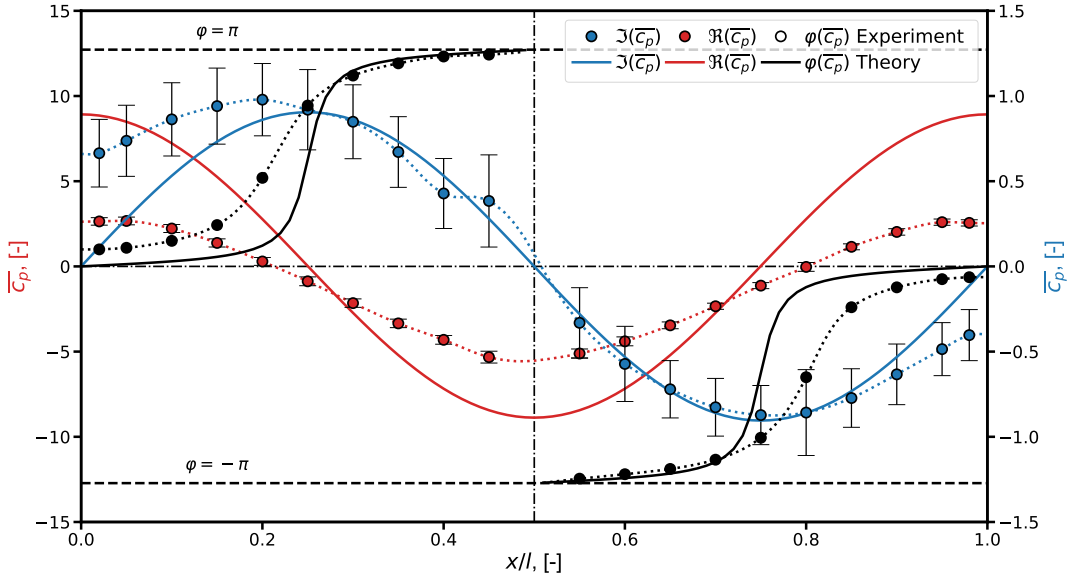

Figure 6.49.: Subsonic results; $M_\infty = 0.7$; $f_{exc} = 25.0$ Hz; $Re = 5 \cdot 10^6$; Ψ_{11}.

This is reflected by the temporal phase angle's slope ($\varphi_t = \varphi$). The imaginary parts, which differ from zero at LE and TE, and the small amplitudes of the real parts lead to phase angles also differing from zero in these areas. In the panel center the differences are equalized, the consequence being that experiment and theory are almost congruent.

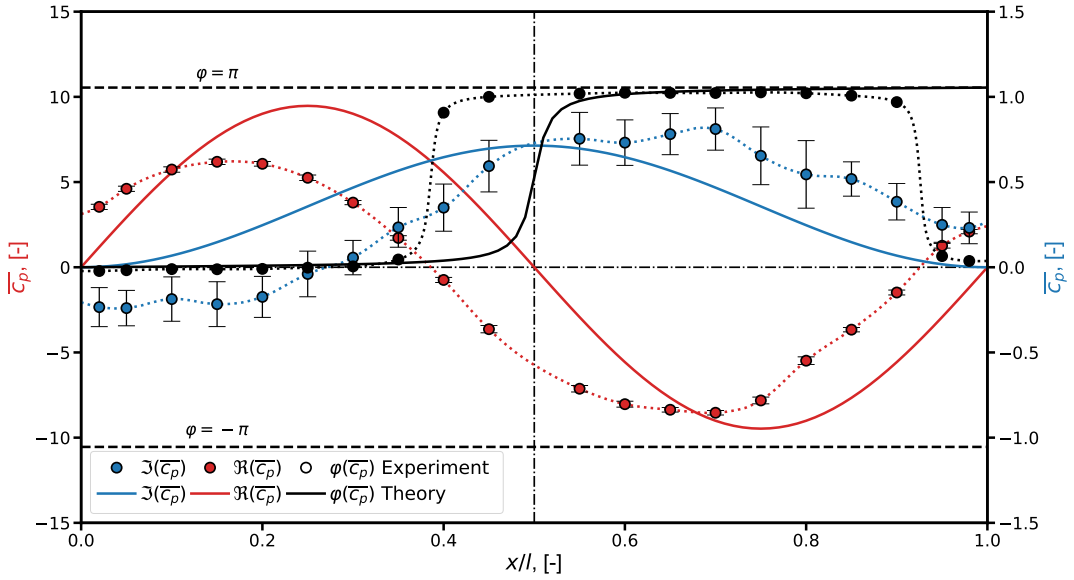

Figure 6.50.: Supersonic results; $M_\infty = 1.2$; $f_{exc} = 25.0$ Hz; $Re = 5 \cdot 10^6$; Ψ_{11}.

Supersonic results for $M_\infty = 1.2$ are shown in Figure 6.50, which is based on the same analytic deformation function as the subsonic calculations are. The supersonic pressure distribution is calculated based on Equation 2.46 with the correction formula (Equation 2.49) for the low supersonic Mach number range. The resulting slope of the pressure's real part amplitudes is purely sinusoidal, whereas the curve of the associated measured results exhibits a phase shift. As observed for subsonic conditions, the calculated amplitudes again exceed the measured ones. The imaginary part of the measured pressure does not show characteristics as clear as the subsonic results does, nevertheless a rough agreement with the analytic results is present. The maximum amplitudes match very well, whereas another shift along the x-axis between the two results is evident. This becomes particularly clear in the resulting phase angles. The calculated phase angle transition from zero to π going along with the real part's zero crossing of the measured data is shifted downstream.

Qualitative Evaluation

After this comparison of the results, a detailed discussion of the obtained characteristics is carried out in the following. Further subsonic results are examined by applying the subsonic potential flow theory approach by Ackeret [70] and Dowell [7] and the traveling waves theory based on the work by Fung [11]. Additional supersonic results are compared to the piston theory by Lighthill [69] and Ashley [10] and with the traveling waves approach as well. In order to study the impact of the Mach number, results at $M_\infty = 0.7$, $M_\infty = 0.9$, $M_\infty = 1.05$ and $M_\infty = 1.2$ are discussed for $f_{exc} = 25.0$ Hz. Since the focus is put on a qualitative analysis, the theoretical data are normalized by the associated maximum values and the presented phase angles are divided by π.
The subsonic measured real parts of the pressure of the Ψ_{11} data shown in Figure 6.51 resemble a $\Delta\varphi_x = \pi/2$ shifted $sin(\pi x/l_i)$ function, hence $cos(\pi x/l_i)$. This, in consequence, equals the $\Delta\varphi_x = \pi$ shifted shape of the underlying deformation Ψ_{11} that is shown by the gray shape in the figures. This characteristic does not change with the increase in the Mach number from $M_\infty = 0.7$ to $M_\infty = 0.9$.

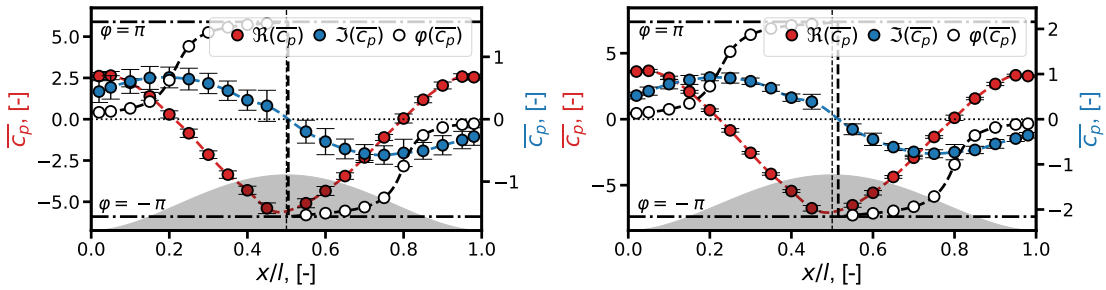

(a) $M_\infty = 0.7$.

(b) $M_\infty = 0.9$.

Figure 6.51.: Subsonic measurement results; $f_{exc} = 25.0$ Hz; $Re = 5 \cdot 10^6$; Ψ_{11}.

This matches with the theory, which is in this thesis referred to as subsonic potential

flow theory, as is depicted in Figure 6.52. In contrast to Figure 6.49, the deformation applied in these cases is based on Equation 2.38, which leads to changes in the vicinity of the leading and the trailing edge. These changes indicate an increased deviation from the experimentally realized deformation on the one hand. On the other hand, this theoretical approach allows also the description of the eigenfunction Ψ_{21}, which is required for further verification in this paragraph.

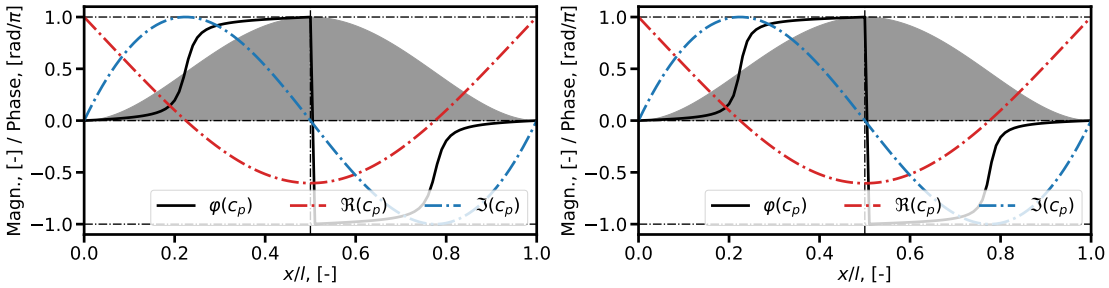

(a) $M_\infty = 0.7$. (b) $M_\infty = 0.9$.

Figure 6.52.: Subsonic and normalized analytic results using potential flow theory; $f_{exc} = 25.0$ Hz; Ψ_{11}.

The traveling waves theory shown in Figure 6.53, for which again Equation 2.39 is used in order to describe the deformation, agrees to the former results and shows a full sinusoidal real part with the same phase shift as shown in Figure 6.51 and Figure 6.52. For both Mach numbers, the measured imaginary part (Figure 6.51) is almost sinusoidal. However, the curve appears truncated at LE and TE in such a way that no complete sine results. The two analytic imaginary data sets are in complete agreement and show an ideal sinusoidal shape for both subsonic Mach numbers.

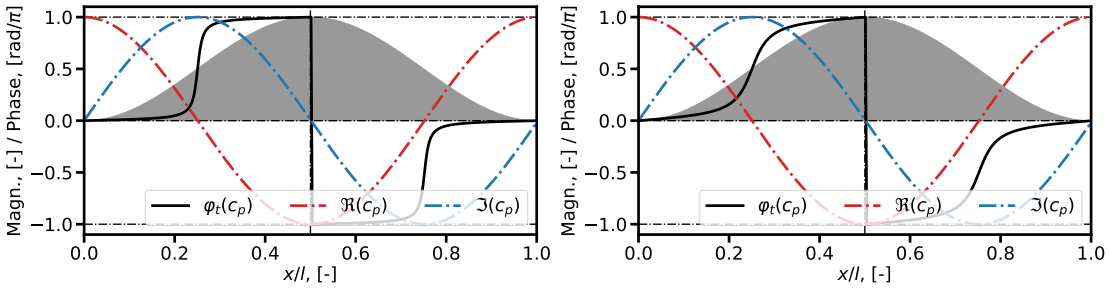

(a) $M_\infty = 0.7$. (b) $M_\infty = 0.9$.

Figure 6.53.: Subsonic and normalized analytic results using traveling waves theory; $f_{exc} = 25.0$ Hz; Ψ_{11}.

On the whole, the trend of the phase angle between the pressure's and the structure's oscillations is in a good agreement for all data sets and Mach numbers. Throughout the panel's length, the phase angle first rises from about $\varphi_t(x/l = 0) \approx 0.0\pi$ to

$\varphi_t(x/l = 0.5) \approx 1\pi$ and then from about $\varphi_t(x/l = 0.5) \approx -1\pi$ to $\varphi_t(x/l = 1) \approx 0.0\pi$. Since $-\pi \mathrel{\hat{=}} \pi$, this is equivalent to a rise from $\varphi_t(x/l = 0) \approx 0.0\pi$ to $\varphi_t(x/l = 1) \approx 2\pi$. The measured data, illustrated in Figure 6.51, show clearly the characteristics of a traveling wave denoted by the continuous rise of the phase angle, which does not significantly change for increased Mach numbers. The φ_t-curves for both Mach numbers show more or less pronounced S-shapes, which is generally confirmed by both analytic approaches. The φ_t-data of the potential flow theory is merely insensitive to a change in the Mach number, whereas results of the traveling wave theory show a significant increase of traveling wave characteristic. This increase, which means an increased ratio of the imaginary part and the real part, can be recognized by the increased continuous rise of the depicted phase angle over the panel length. Results of the subsonic potential flow approach for Ψ_{21} are shown in Figure 2.3 (b), whereas Figure 6.54 shows the associated experimental results. The same agreement between theory and experiment can be observed, just as in the Ψ_{11} case.

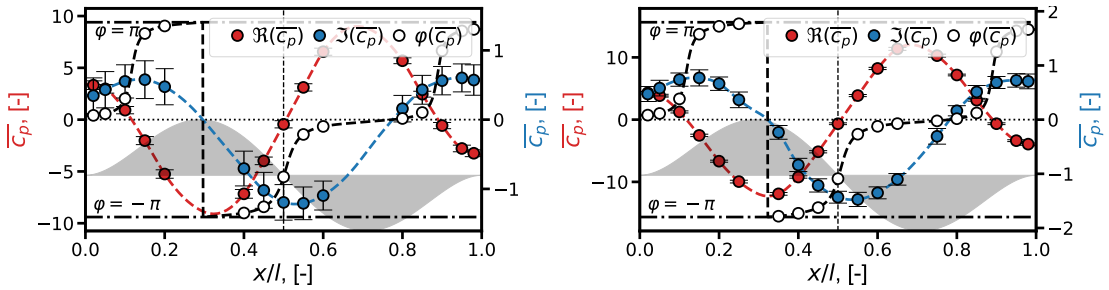

(a) $M_\infty = 0.7$. (b) $M_\infty = 0.9$.

Figure 6.54.: Subsonic experimental data; $f_{exc} = 25.0$ Hz; $Re = 5 \cdot 10^6$; Ψ_{21}.

Following, a detailed discussion of the supersonic findings is carried out. The pressure's real parts $\Re(\overline{c}_p(x))$ of the Ψ_{11} test campaigns show shifted, but clearly recognizable, sinusoidal characteristics at very low supersonic conditions ($M_\infty = 1.05$), as shown in Figure 6.55 (a).

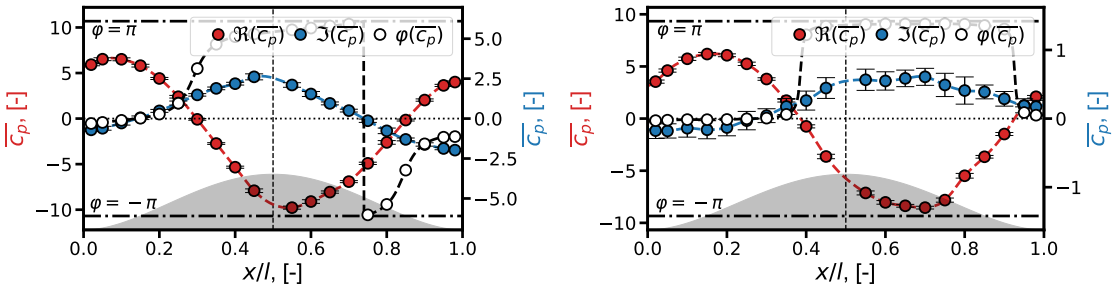

(a) $M_\infty = 1.05$. (b) $M_\infty = 1.2$.

Figure 6.55.: Supersonic measurement results; $Re = 5 \cdot 10^6$; $f_{exc} = 25.0$ Hz; Ψ_{11}.

This characteristic does not change for the increased Mach number of $M_\infty = 1.2$ shown in Figure 6.55 (b), although a slightly increased shift $\Delta\varphi_x$ can be observed. Those streamwise shifts are already known from the analysis of the Mach number's influence and are shown in Figure 6.39 and Figure 6.40. After the flow exceeds $M_\infty = 1.0$, those shifts appear and grow stronger with further increasing Mach number. Due to the lack of data obtained at Mach numbers $M_\infty > 1.2$, the assumption that a further increase in the Mach number would cause a propagation of this shift, which finally results in an ideal sinusoidal characteristic over the panel length, is not verifiable at this stage. Such an ideal sine function, which does not depend on the Mach number, is indicated by the piston theory as depicted in Figure 6.56.

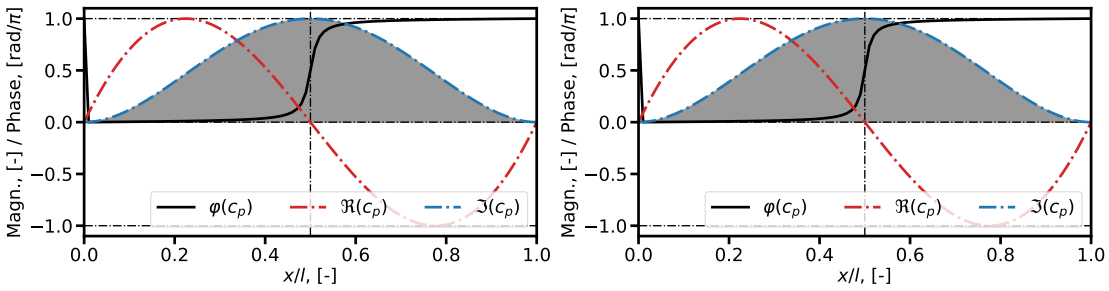

(a) $M_\infty = 1.05$. (b) $M_\infty = 1.2$.

Figure 6.56.: Supersonic and normalized analytic results using piston theory; $f_{exc} = 25.0$ Hz; Ψ_{11}.

The real part data, presented in Figure 6.57 for low supersonic Mach numbers, by the traveling waves theory agree with the piston theory. The trend of the imaginary parts of the measured pressure is not as clear as the previously discussed real part data. Nevertheless, a sinusoidal characteristic is present, which shows strong similarities to the shape of the underlying structure.

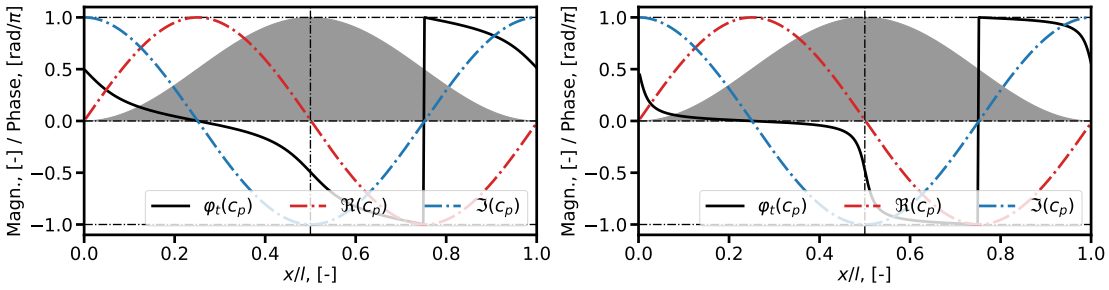

(a) $M_\infty = 1.05$. (b) $M_\infty = 1.2$.

Figure 6.57.: Supersonic and normalized analytic results using traveling waves theory; $f_{exc} = 25.0$ Hz; Ψ_{11}.

This agrees with the piston theory, whose imaginary part matches exactly the shape of

the structural deformation, the motion of which induces the pressure distribution. Compared with the piston theory and the measured pressure, the traveling waves theory's results show a change of sign that equals a spatial phase shift of π in x-direction. The measured phase angles at low supersonic Mach numbers rise over the panel with distinct traveling wave characteristics, as seen before in the case of the subsonic verification. This behavior changes for increased Mach numbers though. The initially continuous rise in the phase angle changes to a stepwise characteristic, which indicates growing standing wave conditions, which is in agreement with the piston theory. The phase angle trend based on the traveling waves theory, which shows a negative slope over the panel's length differs completely from piston theory as well as measured pressure. For the traveling waves theory, this change in the phase angle's slope is connected with the changed algebraic sign of the pressure's imaginary part. All described observations for the Ψ_{11} model are also valid for the Ψ_{21} model, whose comparative data are shown in Figure 6.58 and Figure 2.4 (b).

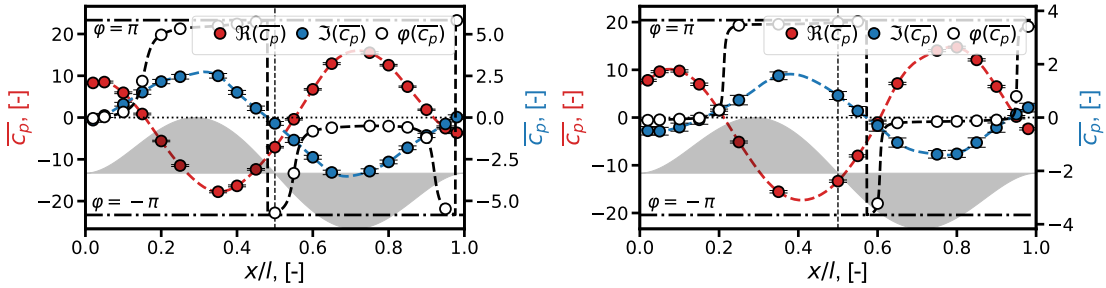

(a) $M_\infty = 1.05$. (b) $M_\infty = 1.2$.

Figure 6.58.: Supersonic measurement results; $f_{exc} = 25.0$ Hz; $Re = 5 \cdot 10^6$; Ψ_{21}.

Quantitative Evaluation

Figure 6.59 (a) compares the experimentally obtained magnitudes of the pressure coefficients with the results of the subsonic potential flow theory and the results of the piston theory for the complete investigated Mach number range. Figure 6.59 (b) shows the comparison of the measured data with the results of the traveling waves theory. Both illustrations focus on the Ψ_{11} model being subject to an excitation frequency of $f_{exc} = 25.0$ Hz. As a reminder: all three applied theories are actually not valid in the vicinity of $M_\infty = 1.0$. The closer the corrected theories come to $M_\infty = 1.0$, the more erroneous are the results. At this Mach number, the theory is approaching a singularity, which does not occur in the experiment.
With a constant excitation frequency, the illustrated data represent the maximum values emerging over the panel depending only on the Mach number. The trends of the measured and the calculated real parts regarding the dependency on the Mach number are in good agreement, on the one hand. On the other hand, the measured magnitudes are much smaller than predicted by theory. The subsonic results show a constant

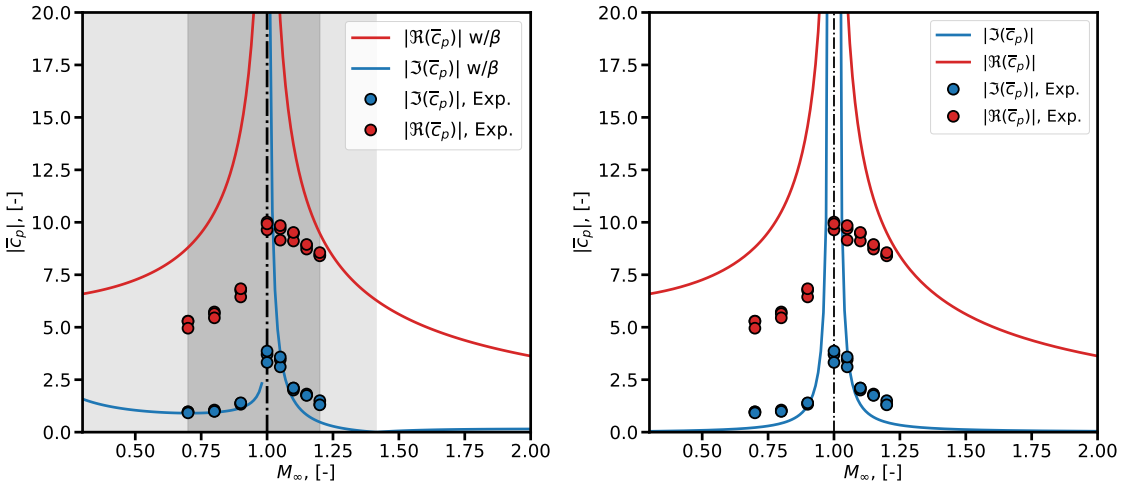

(a) Potential flow theory and piston theory.

(b) Traveling waves theory.

Figure 6.59.: Test results vs. theory; $Re = 5 \cdot 10^6$; $f_{exc} = 25.0$ Hz; Ψ_{11}.

deviation, whereas the measured supersonic results approach the theory's results with increasing Mach number. In contrast, the imaginary parts in the subsonic and the supersonic domain show a good agreement in terms of trend and magnitude. There might be various reasons for the differences that occurred between the theoretically and the experimentally achieved pressure magnitudes:

1. The applied theories ignore viscous effects of the fluid. In the experiment, the fluid's viscosity leads to a boundary layer, whose impact is roughly estimated in the following:
   a) Although it was not possible to vary flow conditions sufficiently to allow for a quantification of the boundary layer's impact on the pressure, an influence has been shown by the results of the presented measurements. For low Reynolds numbers, thus a high boundary layer thickness, decreased pressure amplitudes are measured.
   b) A more extensive variation of the boundary layer was shown by the experiments of Muhlstein [8], in which the boundary layer's influence became particularly clear. Even if in the thesis at hand the actual flutter boundaries are not studied, Muhlstein's work shows how strong the boundary layer's impact can be. A boundary layer with a thickness of about $\delta_{99} = 2.5$ cm ($\delta_{99}/l \approx 0.1$) showed a flutter boundary at about $q_\infty = 48$ kPa (1000.0 psf), which was reduced by more than 50% to $q_\infty = 19$ kPa (400.0 psf) by extrapolating results for a complete absence of a boundary layer.
   c) In contrast to the used theoretical approaches, which do not consider any kind of friction, a boundary layer of $\delta_{99}/l \geq 0.1$ was present during the experimental activities. That boundary layer's influence is also determined in

calculations, which were accompanying the preparation of the illustrated WT experiment [102]. A comparison of those 2D simulations at $x/l_i = 0.6$ with $\delta_{99}/l_i = 0.0$ and viscous flow simulations with $\delta_{99}/l_i \geq 0.13$ shows a pressure loss of about 30%. This loss in pressure leads consequently to a loss in the associated GAFs.

d) Applying the presented simple piston theory approach for an aeroelastic system with two structural eigenmodes, as presented in Section 2.1, a reduction of the aerodynamic forces Q_{21} by 30%, under flow conditions similar to those of the presented WT tests, results in an increase in the critical dynamic pressure by nearly 50%. This impact is illustrated in Figure 6.50, which shows the real and the imaginary parts of the aeroelastic system's eigenfrequencies ω_1 and ω_2 for a reduced pressure. The critical dynamic pressure, which is depicted for 100% and for 70% of the GAFs, is reached as soon as the branching of the imaginary parts and the debranching of the real parts occur. This result supports the previous assumption about the boundary layer's influence on an aeroelastic system, although no results for a direct comparison with the experiments at hand are provided here.

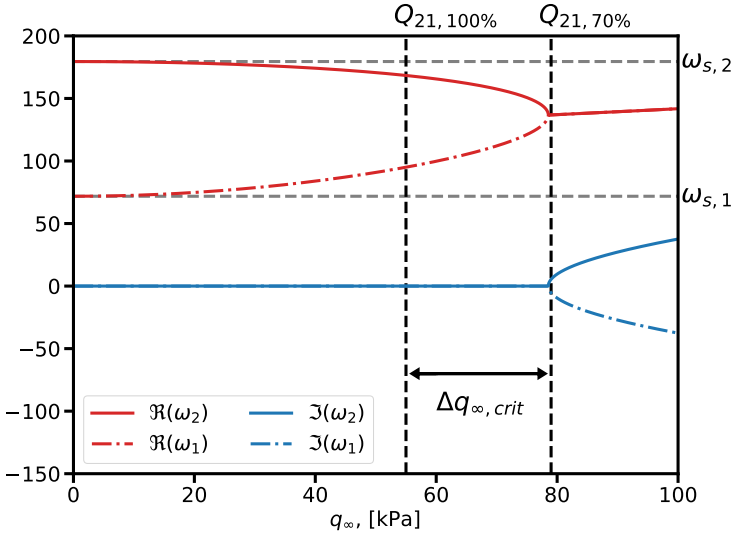

Figure 6.60.: Influence of a pressure amplitude reduced by 30% on the critical dynamic pressure based on 2 DOF piston theory.

2. The equations used for the comparison do not take 3D flow effects into account, which emerge as a result of cross-flows in spanwise direction that lead to a significant pressure decrease in the structure's half-span section. At deflection amplitudes which are about twice as high as those set in the experiment reductions of approximately 25% can occur [102].

3. Since the used wind tunnel setup has a wall opposing the test structure, which

spatially limits the test section's extend in z-direction, its influence on the pressure on the panel surface is not negligible. The corrected results

$$c_{p,corr} = c_p \cdot coth\left(\frac{g}{l} 2\pi \sqrt{|1 - M_\infty^2|}\right) \tag{6.6}$$

depend on the geometric wind tunnel parameter g/l, which indicates the ratio of the structure's length to the distance between the structure and the opposing wall g [103, 104]. The correction leads in the present case to very small correction factors of about $c_p^* = 1.005 c_p$. Besides the small resulting influence, it is not known to what extent that influence is reduced by the perforated WT wall.

4. Another influence arises from the differences between the analytic deformation shape used in theory and the actually realized deformation in the test campaigns, on which the results are based. The comparison of the eigenfunction with the measured shape has shown a good agreement, which is why this influence is considered very small.

5. The presented error bars represent the standard deviation of the current measurements and must be considered.

Summary of Verification

Summarizing the verification, one can state that the local pressure distribution under subsonic conditions has been confirmed by both the potential flow theory and the traveling waves theory. The measurements under supersonic conditions were confirmed by the piston theory and show a growing agreement for increased Mach numbers. The traveling waves theory shows a good agreement for the complex-valued pressure's real part, but poor agreement for the imaginary part. For the latter, a change in the algebraic sign of the obtained traveling wave characteristic occurs. As shown in Section 2.3.3, at supersonic Mach numbers, beyond the maximum set in the WT experiments, the results by traveling waves theory approach the ones by the piston theory. A precise consideration of the boundary layer of the incoming flow might resolve the discrepancies.

6.3.5. Summary of Pressure Coefficient Results

Results of the measured aerodynamic response by using the normalized pressure coefficient have been presented for both investigated structures, with which the first and the second streamwise eigenfunctions Ψ_{11} and Ψ_{21} were simulated. The analysis comprised the investigation on the flow parameters, such as Reynolds number and Mach number and on the structural parameters, such as excitation frequency and amplitude. Subsequently, the subsonic and supersonic results were validated with theoretical approaches. In the following, the findings are summarized in brief:

1. The dependence of the aerodynamic response on the moving structure's amplitude is strictly linear, which suggests a normalization of the pressure by the deflection amplitude.

2. A comparison of measurement points with equal fluidic and structural parameters of the two test campaigns, which were performed on the Ψ_{11} model in 2015 and 2017, respectively, confirms a sound repeatability of the results and thus a high reliability of the test setup.

3. The Reynolds number, adjusted by a variation of the total pressure, shows a minor impact on the measured pressure coefficients. This behavior was anticipated with regard to the small effect of the Reynolds number on the flow's boundary layer obtained in the first section of this chapter.

4. At low frequencies counter-oscillating pressure domains over the test structure occur, which are either in phase or out of phase with the underlying oscillation of the test structure. Initially, those domains are clearly separated by spanwise lines of zero-crossings, which changes with an increase of the excitation frequency. Increasing pressure's imaginary parts are induced, which attenuates the initially observed step in the phase angle transition between $\varphi_t = 0.0$ and $\varphi_t = \pi$. Thus, the initially observed standing wave characteristic of the pressure receives characteristics of a traveling wave. In contrast to the imaginary part, the corresponding real part remains almost unaffected. The analytic verification confirms the general pressure curves' characteristics over the structure's half-span section and the observations on the influence of the frequency.

5. Of particular interest is the influence of the Mach number on the aerodynamic response, since data achieved at subsonic and supersonic flow conditions are available. In the subsonic domain a variation of the Mach number leads to a negligible change of the measured pressure. The real part's curve corresponds to that of the deformed structure with changed algebraic sign, which means a dependence of its curvature. In contrast, the imaginary part exhibits a characteristic shifted by $\Delta\varphi_x = \pi/2$ compared to test structure's shape.
   Once the speed of sound is exceeded, major changes appear in the pressure curves. Both real and imaginary parts are subject to a spatial shift in the direction of flow, which progresses with increasing supersonic Mach number. The applied piston theory only partially confirms these results, since it is not fully valid for low supersonic flows. A more pronounced shift is indicated, which is also suspected for the experimental results in case of a further increase of the Mach number. Unfortunately those Mach numbers needed for a completion of the supersonic verification are outside the performance range of the used test section.

6.4. Generalized Aerodynamic Forces

In this section the previously presented results of the structural deformation and the measured pressure are combined in order to calculate the Generalized Aerodynamic Forces (GAFs). The GAFs, introduced in Chapter 2, represent the aerodynamic loads referring to the individual eigenmodes of a structure. By weighting the induced pressures according to the shape of the respective mode, the GAFs are also a measure of the work carried out. Only temporal phase shifts between the aerodynamic response and the structural motion that differ from $\varphi_t = n \cdot \pi$ can lead to an exchange of energy between the structure and the fluid. That means that the pressure's oscillation related to the structure's oscillation must show an imaginary component in order to induce mechanical work. Consequently, the focus of this section is put on the GAFs' imaginary parts to achieve information on the system's aeroelastic stability by means of the aerodynamic damping. Data is required for the whole structure, which justifies the addition of boundary conditions for pressure and deformation at the corners of the test structure, for which no experimental data are available. Since the agreement between simulated deformation and measured deformation is remarkably good, the forces are determined based on the analytic shape of the test structure. This also prevents incorrect measurements of the complex-valued deformation data, which occur in particular in the edge near areas, from affecting the final results. Based on Equation 2.5 for a one-dimensional plate, the two-dimensional and normalized equation is used in the following presentation of the results:

$$\overline{Q}_{ij,ij} = \int_0^w \int_0^l \overline{c}_{p,ij} \Psi_{ij} dx dy \tag{6.7}$$

Figure 6.61 and Figure 6.62 show the locally measured complex pressures and the resulting GAFs for the half-span section. The multiplication of the pressure with the structure's eigenfunction that is equal to the structure's normalized deformation leads to the disappearance of the pressure's influence at the LE and the TE, whereas the largest influence is found in the plate's center for Ψ_{11}.

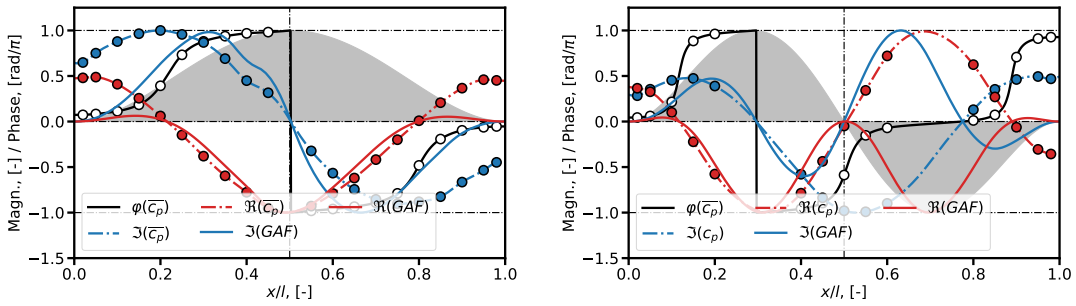

(a) $M_\infty = 0.7$; $f_{exc} = 25.0$ Hz; Re_2; Ψ_{11}.

(b) $M_\infty = 0.7$; $f_{exc} = 25.0$ Hz; Re_2; Ψ_{21}.

Figure 6.61.: GAFs; Subsonic experimental data.

For Ψ_{21}, the most pronounced domains are consequently $x/l_i \approx 0.3$ and $x/l_i \approx 0.7$. The subsonic real parts of the complex-valued GAFs have exclusively a negative sign, which is caused by the exclusively negative sign of the pressure's real part. Thus, the integration over the structure ($\int_0^w dy$ and $\int_0^w \int_0^l dxdy$) to get global information will result also in a negative value. The situation is different for the imaginary data, which show alternating positive and negative domains of roughly the same size. Since those domains equalize each other, integration leads to very small values. For supersonic Mach numbers illustrated in Figure 6.62 the characteristics change.

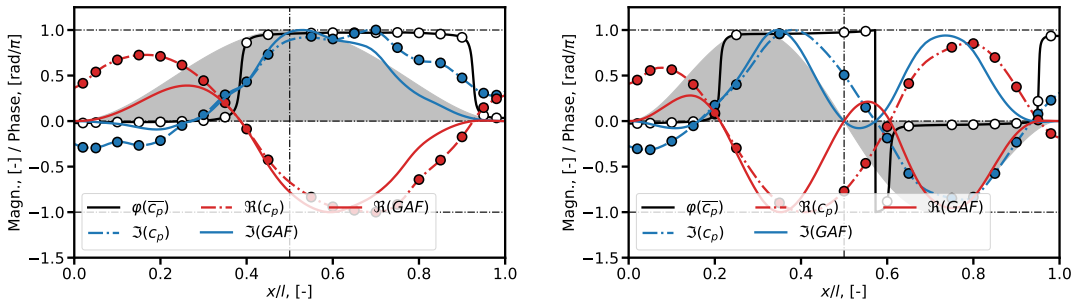

(a) $M_\infty = 1.2$; $f_{exc} = 25.0$ Hz; Re_2; Ψ_{11}.

(b) $M_\infty = 1.2$; $f_{exc} = 25.0$ Hz; Re_2; Ψ_{21}.

Figure 6.62.: GAFs; Supersonic experimental data.

The imaginary part has almost an exclusively positive algebraic sign over the entire structure, whereas the real part shows alternating areas with positive and negative values. Thus, integration leads to summed positive imaginary values, but mutually canceling real values. The resulting imaginary parts $\Im(GAF)$ are presented in Figure 6.63 as a function of the Mach number and the excitation frequency, which are taken into account in the experiments. The figure illustrates the Ψ_{11} results (a) and the Ψ_{21} results (b) for the highest Reynolds number tested. In addition, all individual measurement points, on which the interpolated results over the whole M_∞-f_{exc}-range are based on, are indicated by white dots.

Both maps show equal basic characteristics, which can roughly be divided into three domains. The first domain is located in the subsonic Mach number range and extends from $f_{exc} = 0.0$ Hz to medium and, in particular for Ψ_{21}, to high excitation frequencies. Here, the imaginary part's magnitude of the aerodynamic forces is close to zero, which is in agreement with the local GAF distribution in Figure 6.61 for which the positive and negative areas are in balance. From low frequencies at low supersonic Mach numbers to low and medium frequencies at maximum supersonic Mach numbers, a second domain with very low values for $Im(Q_{11,11})$ and $Im(Q_{21,21})$ is discernible. The third and actually eye-catching characteristic is the wedge-shaped domain of high magnitudes, which extends from high frequencies, where it covers almost the entire Mach number range (in particular for Ψ_{11}), to low frequencies where its tip points on a Mach number of about $1.05 < M_\infty < 1.1$. The Ψ_{21} wedge-shaped domain shows, in contrast to the Ψ_{11} results, a smaller base in the high frequency range, which covers only half the Mach number

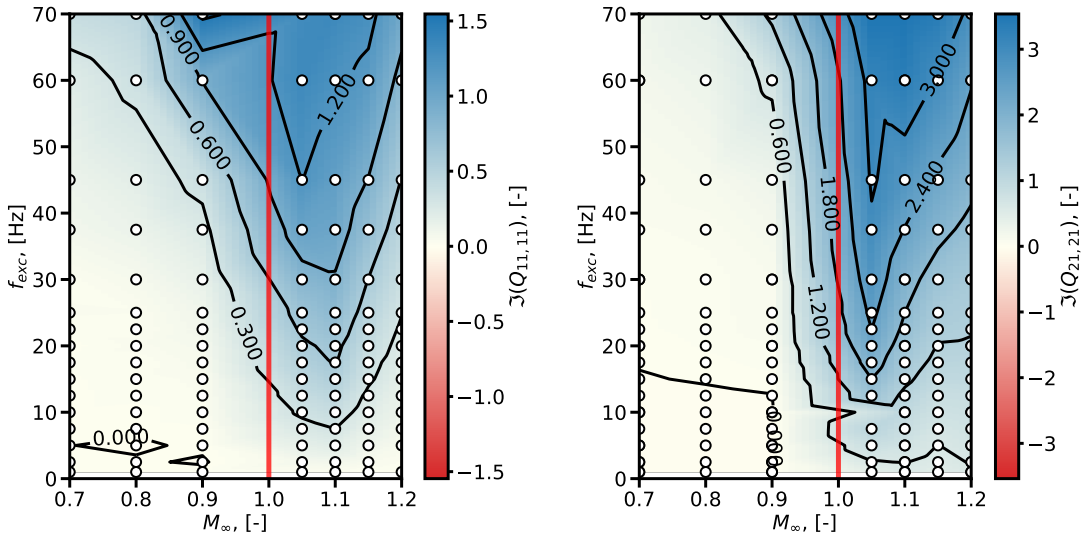

(a) Ψ_{11}; Re_3; $\hat{A}_3$.

(b) Ψ_{21}; Re_3; $\hat{A}_2$.

Figure 6.63.: $\Im(GAF)$ as a function of the excitation frequency f_{exc} and the Mach number M_∞.

range and starts in the subsonic range close to $M_\infty = 1.0$. Another remarkable difference occurs for the Ψ_{21} amplitudes, which are almost twice as high as the values of the Ψ_{11} measurements. With regard to the maximum values, which are located in the high frequency domain at a Mach number of about $M_\infty = 1.1$, a slight increase occurs with an increase of the Reynolds numbers. This is illustrated in Figure 6.64, which depicts the results of all three tested Reynolds numbers.

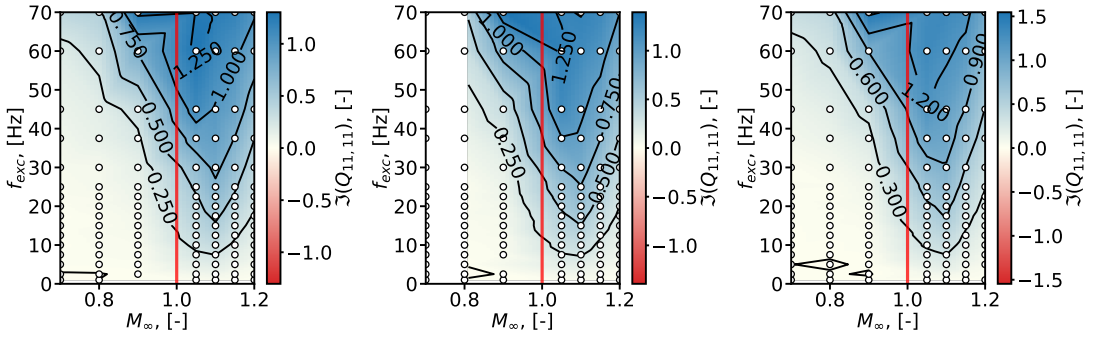

(a) Re_1; $\hat{A}_3$.

(b) Re_2; $\hat{A}_3$.

(c) Re_3; $\hat{A}_3$.

Figure 6.64.: $\Im(GAF)$ as a function of the excitation frequency f_{exc} and the Mach number M_∞; Ψ_{11}; Test campaign 2017.

Unfortunately, no results are available for $M_\infty = 0.7$ at Re_2 (Figure 6.64 (b)) to complete the map. In agreement to this observation is the outcome of Section 6.3.2, which proves a slight increase in the pressure amplitude for conditions close to $M_\infty = 1.0$ for high Reynolds numbers. At those flow conditions the maximum magnitudes are located. Depending on the Mach number, the boundary layer thickness is only very slightly affected by the change in the Reynolds number, as was shown in Section 6.1.2. All $f_{exc} - M_\infty$-maps containing the integrated GAFs' imaginary part, illustrated in Figure 6.63 and Figure 6.64, show only positive domains and thus positive aerodynamic damping. A positive damping means stable conditions of the aeroelastic system. The representation of the measured values is now followed by a comparison based on the theoretical approaches. These, as seen before for the validation of the pressure measurement, are based on equations representing the structure's half-span section. Corresponding to the theoretical results in Section 6.3.4 on the pressure validation, Figure 6.65 and Figure 6.66 show the generalized aerodynamic forces and the complex pressure coefficients based on the theory.

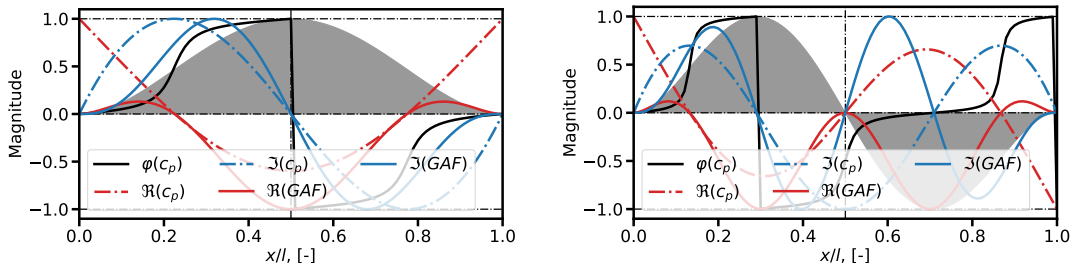

(a) Ψ_{11}. (b) Ψ_{21}.

Figure 6.65.: GAFs; Analytic approach with potential flow theory equation; Subsonic conditions; $f_{exc} = 25.0$ Hz; $M_\infty = 0.7$.

For subsonic conditions there is a reasonable agreement between theory and experiment. The domains of positive and negative imaginary values for both the theory and the experiment are about the same size, which leads to integrated values of about zero. In contrast to Ψ_{11}, where the pressure can only be related to one phase of the structure, the Ψ_{21} structure has two counteracting domains (shifted by $\Delta\varphi_t = \pi$). Here, attention must be paid to the fact that the pressure data of the structure's first half ($x/l_i < 0.5$) and of the second half ($x/l_i > 0.5$) are related to the same actuator's phase. Due to the weighting with the structure's shape in the calculation of the GAFs, the resulting magnitude near LE and TE goes toward zero. Thus, all differences between theory and experiment in the pressure data near the leading and the trailing edge, observed in Section 6.3.4, become negligible. The comparison of the experimental real values with the theoretical results shows no significant differences. For supersonic conditions shown in Figure 6.66, the properties of the pressure's and the force's imaginary parts and real parts are exchanged compared with the subsonic data. The real part shows for both introduced eigenfunctions Ψ_{11} and Ψ_{21} equal positive and negative domains, whereas the imaginary part shows exclusively positive values.

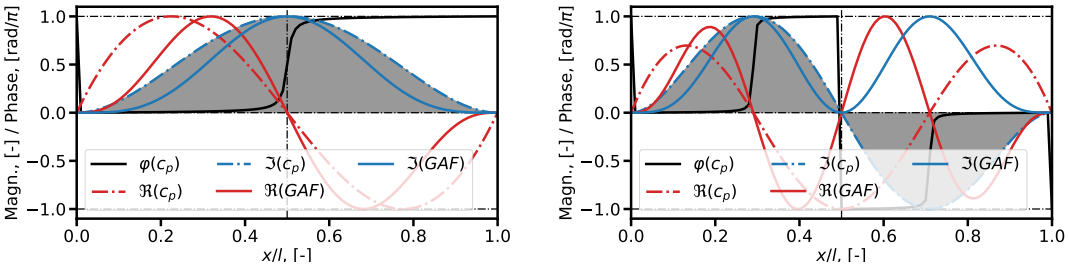

(a) Ψ_{11}. (b) Ψ_{21}.

Figure 6.66.: GAFs; Analytic approach with piston theory equation; Supersonic conditions; $f_{exc} = 25.0$ Hz; $M_\infty = 1.2$.

The integrated $\Im(GAF(M_\infty, f_{exc}))$ data calculated with the potential flow theory and the piston theory is presented in Figure 6.67. In the subsonic Mach number range the resulting imaginary parts are all equal to zero, since the positive and the negative domains are at equilibrium. For supersonic conditions, the imaginary part shows solely positive values, but its amplitude depends strongly on the combination of excitation frequency and the free stream Mach number, as described in Section 2.3.

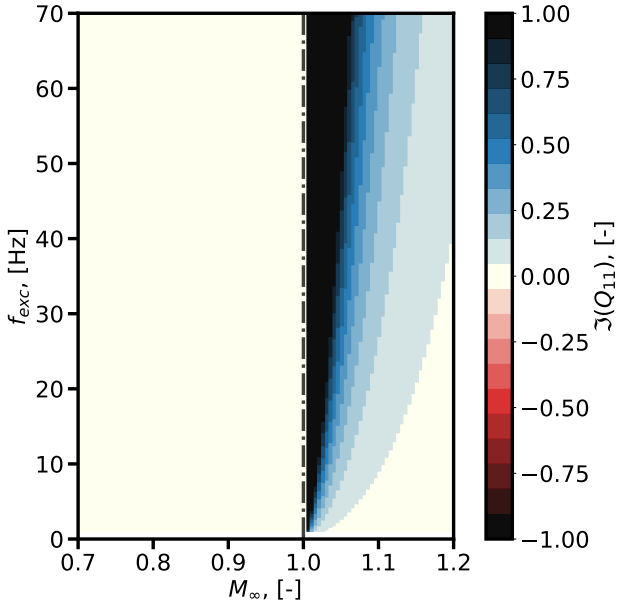

Figure 6.67.: $\Im(GAF)$ as a function of f_{exc} and M_∞ based on potential flow and piston theory; Qualitative progression; Ψ_{11}.

Consequently, the maximum is located at supersonic Mach numbers close to $M_\infty = 1.0$ and at high excitation frequencies. With decreasing frequency and increasing Mach number (Prandtl-Glauert transformation) the magnitude drops and the result is a wedge

shaped characteristic that resembles the experimental results. In contrast to the theory, the experimental data shows also significant imaginary part amplitudes in the subsonic domain. The phenomenon of the imaginary domains' equalization under subsonic conditions, which is shown by experimental and theoretical results, can be studied by the observation of the zero-crossing of the sinusoidal function $\Im(GAF)(x/l_i)$ at half-span. The theoretical results show those crossings at each eigenfunction's minimum and maximum, which leads to the shown complete equalization. The location of the experimental obtained zero-crossings $x_{\Im,null}/l$ for Ψ_{11} and Ψ_{21} are illustrated in Figure 6.68 (a) and (b) as a function of the free stream Mach number.

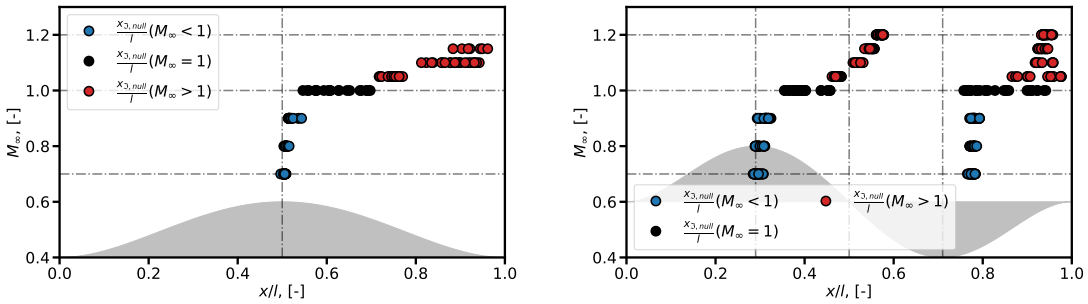

(a) Ψ_{11} (2017).

(b) Ψ_{21}.

Figure 6.68.: Shift of $\Im(GAF)(x/l_i)$ zero crossings depending on the free stream Mach number.

At low Mach numbers, the zero-crossings are located exactly at the coordinates predicted by the theory. With increasing Mach number, they start to move down stream. The deviation from the theory's results leads to differently sized positive and negative domains, which prevents a complete cancellation. A similar mechanism emerges by using the traveling wave theory and occurs between the two critical Mach numbers $M_{crit,\oplus}$ and $M_{crit,\ominus}$ for a given excitation frequency. Figure 6.69 shows results for the GAFs based on the traveling wave theory as a function of f_{exc} and M_∞.
Wedge shaped domains with imaginary values even in the subsonic domain emerge in this case, as was also observed for the experimental data. The wedge's solely positive subsonic edge denotes the domain where the upstream traveling wave reaches the critical Mach number of $M_{crit,\oplus}$, while the downstream traveling wave still shows subsonic conditions. Corresponding to the subsonic edge, a supersonic edge is present as well, which indicates an additional exceeding of the speed of sound of the downstream traveling wave $M_{crit,\ominus}$. In this domain, where both waves are subject to supersonic flow conditions, negative work is indicated, which is not detected for the experimental data. Recalling the findings of Section 2.3.3 and Section 6.3.4, the dominating amplitude of either the upstream or the downstream directed traveling wave determines the resulting traveling wave characteristic. A dominant amplitude of the downstream wave produces a temporal phase angle characteristic with a negative slope over the panel, which results in a negative imaginary part of the resulting integrated aerodynamic forces (Figure 6.69).

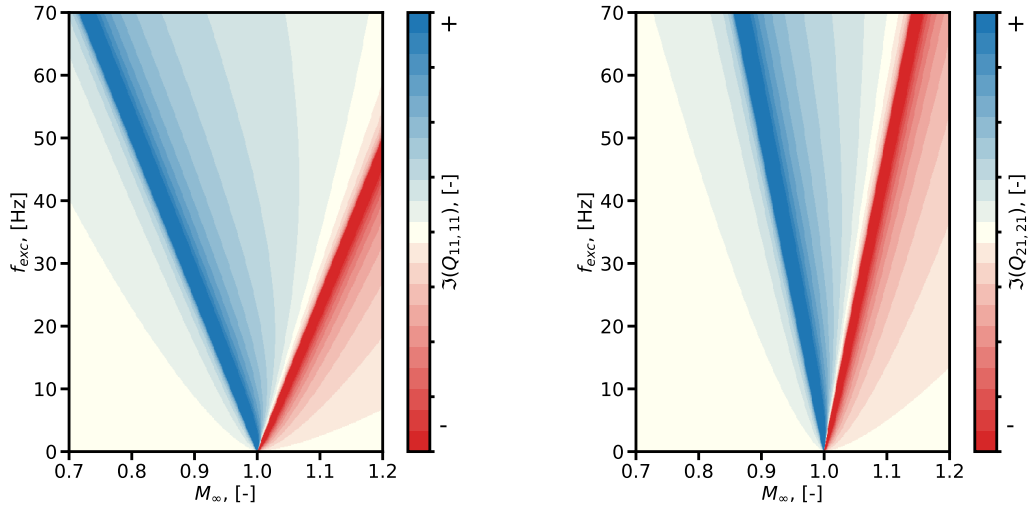

(a) Ψ_{11} model (2017).

(b) Ψ_{21} model.

Figure 6.69.: $\Im(GAF)$ as a function of the excitation frequency f_{exc} and the Mach number M_∞ based on traveling wave theory; Qualitative progression.

This is not achieved for a single measurement point (Figure 6.64). Since no negative $\Im(Q_{ij})$ is measured, according to the traveling wave theory the downstream traveling wave cannot be dominant.
The complete theory of Fung [11] contains beside the traveling wave approach also an implementation of the flow's boundary layer, which is not considered in the results presented here. In this case a boundary layer profile according to the power law approach is considered, which leads to an average velocity over the panel being below the free stream velocity M_∞. In the boundary layer an average Mach number of $M_\delta < M_\infty$ is established at a supersonic free stream Mach number. Due to the decrease in the Mach number, the critical Mach numbers $M_{crit,\oplus}$ and $M_{crit,\ominus}$ are reached at higher free stream Mach numbers. This acts like an offset in the shown GAFs characteristic. As a result, the tip of the GAFs-wedge does not point at $M_\infty = 1.0$, but at $M_\infty > 1.0$.
In addition, the presence of a boundary layer induces a decrease of the resulting pressure, in particular in the vicinity of the singularity of both traveling waves. For the upstream traveling wave, these conditions are in the subsonic domain, whereas the downstream traveling wave meets the critical conditions in the low supersonic domain. Consequently, the impact is here stronger than for the upstream traveling wave and leads to a shrinkage of the domain of positive work illustrated in Figure 6.69. Assuming a decrease of the downstream amplitude below the amplitude of the upstream wave, properties similar to those of the measured data in Figure 6.63 and Figure 6.64 would appear. Since no sufficient experimental data on the variation of the boundary layer is available though, a closer investigation of this mechanism is outside the scope of the current thesis.
The complete set of results for all measurement series is content of the appendix, which

includes three M_∞-f_{exc}-maps of each test campaign. The illustrations of the first Ψ_{11} campaign in Figure D.45 show the variation of the excitation amplitude. As already indicated in the presentation of the pressure measurements in Section 6.3.2, the deflection amplitude has no significant influence on the imaginary part of the GAFs that are calculated with $\overline{c}_p$. The results of the second Ψ_{11} campaign and the Ψ_{21} campaign in Figure D.46 and Figure D.47 show data for different Reynolds numbers.

7. Conclusions

Due to the poor predictability of dynamic aeroelastic instabilities of plates and shells that are subjected to high subsonic and low supersonic flows, experimental activities were performed in order to achieve detailed insight into the arising physical phenomena and to provide comparative data for subsequent numerical validation work.
Literature has shown that so-called single mode flutter is predominant in the low supersonic flow domain, i. e. only one of the low structural eigenmodes becomes unstable. Thus, the focus is on the integrated values of the imaginary part of the generalized aerodynamic forces, which are a direct measure of the aerodynamic damping of such a single DOF system. These values are negative, in case aeroelastic instabilities emerge. The domain of the Mach numbers in question is of particular interest because of two phenomena acting contrarily. On the one hand, a strongly decreased critical dynamic pressure can be observed in this domain. On the other hand, the boundaries of aeroelastic stability are largely affected by the boundary layer of the incoming flow, which shows a stabilizing impact on the aeroelastic system.
In contrast to previous tests, the present experiments allow for the separation of the structural dynamics and the unsteady aerodynamics. The applied forced motion approach assures a defined structural motion and thus allows a focus on the measurement of the aerodynamics. The latter are measured by unsteady pressure probes, which additionally assure a high resolved measurement of the local aerodynamics generated on the panel model's surface. The activities focused on the fluid mechanics induced by the motion that simulated the first and the second streamwise eigenmode shapes of a panel structure, which is subjected to high subsonic and low supersonic Mach numbers. First, the outcome of the performed experiments, corresponding to the objectives stated in Chapter 1.2, is summarized. Finally, an outlook on following steps is given, in view of the data obtained and future experimental activities.

Summary of Results

1. Preceding the experimental activities presented in this thesis, its features were to be defined and the test setup was to be designed. Besides the demands on the flow conditions, additional parameters were determined and prioritized, based on literature.
   The Transonic Wind Tunnel Göttingen (DNW-TWG) was selected to perform the tests, since it provides the required range of high subsonic and low supersonic Mach numbers. Furthermore, it allows the variation of the total pressure and thus the Reynolds number, which enables to control the boundary layer properties of the incoming flow. The actual test setup, which was embedded in the test facility,

operates on the forced motion principle. An actuating system allows control of the selected structural parameters. It consists of one or two linear hydraulic cylinders, which deform the test structure dynamically according to its first and second streamwise eigenfunction. The actuators are mounted on the back of the structure, whereas the structure's front faces the wind tunnel's flow. In order to minimize the structural and geometric parameters to be considered, a generic structure was studied, which is a flat and rectangular plate. The two structural parameters extensively studied in the experiments, in addition to the two afore mentioned fluidic parameters, are the excitation frequency and the amplitude of the structure's deformation, both of which are controlled by the actuating system. Since future experiments with changed focal points were considered as well, a highly versatile setup was designed. This enables investigations of a variety of structural and fluidic parameters related to the aeroelasticity of shell and plate structures. The outcome is a modular test setup, which is able to be adapted to the scientific objective of a wide variety of test campaigns. The experimental activities shown in this thesis present the first configurations of this new test environment, where two different test models were used.
The forced motion principle and the applied measurement techniques aim at the correlation of the aerodynamic response with the underlying defined structural deformation inducing it. Accordingly, the flow-faced side of the test structure was extensively equipped with highly sensitive dynamic pressure transducers, which allow the pressure data to be obtained over the entire surface. The corresponding deformation measurement was done by a stereo marker tracking system and position sensors, which are integrated in the hydraulic actuators. Accelerometers were used to monitor the vibrations of the whole test setup. Additionally, a wake rake mounted downstream of the test structure measured the boundary layer characteristics.

2. A database for subsequent analysis and validation was acquired, which basically comprises the above stated information on the induced pressure, the structure's forced motion and the flow's boundary layer. Data was recorded in a Mach number range from $M_\infty = 0.7$ to $M_\infty = 1.2$ with a step size of $\Delta M_\infty = 0.05$ for three different Reynolds numbers $Re_1 = 2.5 \cdot 10^6$, $Re_2 = 5.0 \cdot 10^6$ and $Re_3 = 7.5 \cdot 10^6$. The Reynolds numbers result from the maximum range of total pressure, which can be set in test facility. The excitation frequency of the simulated first streamwise eigenfunctions Ψ_{11} and Ψ_{21} was varied from $f_{exc} = 0.0$ Hz to $f_{exc} = 70.0$ Hz. In case of the Ψ_{11} tests, three different amplitudes $\hat{A}_1 = 0.6$ mm, $\hat{A}_2 = 1.2$ mm and $\hat{A}_3 = 1.8$ mm were tested. The Ψ_{21} tests were performed at a constant amplitude of $\hat{A}_2 = 1.2$ mm.

3. The measurements of pressure, deformation and boundary layer were analyzed to achieve insight into the local phenomena that emerge on the test structure's surface: Data of the wake rake provided information on the velocity profiles inside the boundary layer, which show satisfactory agreement with classical power law

equations. Nevertheless, slight mismeasurements occurred for the Pitot tubes that are located closest to the WT wall. These discrepancies were caused by an erroneous operation of mechanical nature, which increased from one test campaign to the next. No indication was found that the structural parameters excitation frequency, amplitude and simulated mode shape affect the boundary layer characteristics in any way. Calculated from the velocity distributions, the boundary layer thickness and the displacement thickness show only a slight dependence on the WT's total pressure. This means a limitation of the investigations on the boundary layer's influence on aeroelastic stability in this test campaign.
The evaluation of the panel's deformation demonstrates that the intended design shapes are met satisfactorily. This allows the intended correlation of the measured aerodynamic response with the underlying structural oscillations and theoretical approaches. Special attention was paid to the measured phase angle characteristic, which proves to be completely in phase over the structure with the actuator's phase angle. The aerodynamic response, which is represented by the measured and complex-valued pressure over the panel, was studied with respect to all mentioned structural and fluidic parameters:

- The structure's deflection amplitude affects the pressure's absolute value. The dependence between deflection amplitude and induced pressure amplitude is strictly linear within the tested range. In the following, the obtained pressure is normalized by the deflection amplitude, which allows the comparison of the data sets measured with different deflection amplitudes.
- By controlling the total pressure in the WT's test section, the Reynolds number was changed. The resulting effect on the unsteady pressure is small. This observation is consistent with the previously stated negligible influence of the WT's total pressure on the flow's boundary layer. Consequently, a clear statement about the BL's influence on the aerodynamic response cannot be made with the fluidic boundary conditions of the experiment at hand.
- The excitation frequency determines the normalized pressure's imaginary part. A rise in the frequency means a rise in the imaginary part's magnitude, whereas the real part remains stable. With a low or no imaginary value, the induced pressure acting on the structure is of a standing wave type. A rise of the pressure's imaginary part goes along with a change in the temporal phase characteristic, which results in a successive increase of traveling wave characteristics. Under subsonic conditions, this influence is very significant. For low supersonic flows and in opposition to subsonic flows, the maximum values of the real and imaginary parts are located at about the same positions ($x(\Im_{max}) \approx x(\Re_{max})$), which means that the imaginary part's influence is strongly reduced.
- The Mach number strongly affects the pressure, whereby the change from the subsonic domain to the supersonic domain is of particular interest. This transition leads to qualitative and quantitative changes in both the real part

and the imaginary part of the pressure. At subsonic conditions, the pressure's real part corresponds to the structural deformation, which can be assumed to be sinusoidal, with a spatial phase shift of $\Delta\varphi_x = \pi$, whereas the imaginary part shows a phase shift of $\Delta\varphi_x = \pi/2$. When exceeding the speed of sound those properties switch. Now, the real part shows the $\Delta\varphi_x = \pi/2$ shift and the imaginary part has a $\Delta\varphi_x = \pi$ shift. These properties are best pronounced at the high supersonic conditions of the used test range. In the vicinity of $M_\infty = 1.0$, a blending of subsonic and supersonic characteristics occurs.

A verification of the measured data was carried out by means of potential flow theory approaches. Those show a good agreement with the measurements for subsonic and supersonic flow conditions. Nevertheless, the agreement between theory and experiment is poor for conditions close to $M_\infty = 1.0$, where a merging of supersonic and subsonic characteristics was measured. A theory based on traveling waves, whose results show also subsonic and supersonic characteristics at flow conditions near to $M_\infty = 1.0$, can rudimentary verify the subsonic results of this particular domain. A consideration of the flow's boundary layer in this theory should significantly improve the agreement between measurement and theory for $M_\infty \geq 1.0$.

4. Based on the measured pressure and the structure's deformation, the generalized aerodynamic forces (GAFs) were calculated. These represent the acting aerodynamic loads based on one particular structural eigenmode shape. These indicate the aerodynamic loads that act on the individual structural eigenmode shapes. The GAF's imaginary part, which is considered in the following, is a measure for the energy transfer between fluid and structure. Since the Mach number M_∞ and the excitation frequency f_{exc} are the most influential parameters, the analysis of the GAFs is done by illustrating the results as a function of these two quantities.

   - Regardless of the particular test campaign, the results show three different domains in the M_∞-f_{exc} plots. At low subsonic conditions and at high supersonic conditions, the imaginary parts of the determined force remain small and mostly close to zero. Depending on the excitation frequency, a large positive-valued domain is detectable at low supersonic Mach numbers. This wedge-shaped domain extends from low frequencies at a Mach number of about $M_\infty = 1.1$ to the high frequency domain, where the full range of Mach numbers is covered, even the subsonic domain.
     According to the Piston Theory, this domain arises only under supersonic flow conditions due to the exclusively positive sign of the pressure's imaginary part over the structure's length. Here, the imaginary part increases with increasing frequency and decreases with increasing Mach number. However, the measured pressure shows blended characteristics of pure subsonic and pure supersonic characteristics in the vicinity of $M_\infty = 1.0$. This leads to an increased influence of the imaginary part with increased integrated values even in the high subsonic domain. This characteristic can be described to

some extent by the traveling waves theory.

- None of the results of the test campaigns show domains of energy transfer from the fluid into the structure. For the first and second streamwise bending mode shape the global GAFs were determined whose imaginary part indicates the aerodynamic damping. Consequently, no negative aerodynamic damping occurs in the tested parameter range, which could cause single mode flutter of one of the simulated mode shapes.
- As the test results have shown, the variation of the Reynolds number has an influence on the pressure. But this effect is too small to draw detailed conclusions about its influence. A wider range of Reynolds numbers and thus boundary layer variations would show the influence on the aeroelastic stability more precisely.

The theoretical approaches used to verify the pressure measurements also serve to explain the achieved GAF characteristics. The results are in good agreement, whereby the occurring deviations are already known from verification the pressure. In order to achieve an improved match, it is therefore assumed that the massive reduction of the boundary layer thickness of the incoming flow could lead to domains of negative imaginary aerodynamic forces and thus to a destabilization of the aeroelastic system, as is indicated by theory.

Outlook

Due to the only minor changes in BL thickness, which is induced by the variation of the WT's total pressure and thus the Reynolds umber, the impact of the boundary layer on the pressure and thus on the GAFs, as they are calculated based on the pressure measurements, cannot be determined sufficiently. Thus, assumptions concerning the different domains of positive and negative damping of the obtained GAF maps cannot be verified based on the present experimental data. In order to achieve distinct changes in BL thickness, an additional control device should be mounted upstream of the test structure that allows an adjustment of the boundary layer thickness over a wide range. Preliminary design considerations have already been carried out in this thesis, which prove a feasible and employable device that operates on the principle of fluid suction. A final design needs to be developed that is suitable for the different subsonic and supersonic operating points of the WT.
After comprehensive investigations of the BL's influence and on the condition of obtained negative damping would have been performed, a free panel flutter experiment would provide valuable insight in actually emerging flutter mechanisms. The focus of such an experiment should be onto the associated limit cycle oscillations, which occur during panel flutter, and even on possible structural failure mechanisms. The presented test setup is well suited for this kind of experiment. The current structures are designed with focus on the prevention of dynamic instabilities. So, only a new test structure

needs to be designed and manufactured, which is relatively simple compared with the development of a new test setup.
An improvement of the presented experiment could be achieved by extending the studied range of Mach numbers. A completion of the data for supersonic Mach numbers could reinforce the agreement of the measured data with the simple piston theory approach. Further work connected with the current experimental activities has been carried out at the DLR in the recent years by means of numerical investigations that comprise coupled fluid-structure-interaction calculations. Final comparisons and analyses of the numerical data with the data presented in this thesis have not yet been completed.
Besides the above mentioned extensions of the presented experiments, the developed test setup allows for investigations focusing on completely different structures and different experimental approaches. In contrast to the isotropic structures of the experiments shown in this thesis, which have a simple geometry, more complex structures can be applied to the test setup. At the beginning of this thesis, several influencing parameters were named, which strongly affect the aeroelastic stability of plates and shells. Those parameters, which address the structure's geometry and its material properties, may be worth being studied in further WT activities. The introduction of curved structures would enable studies on structures being more related to aerospace applications, which also applies for models made of composite materials. Based on the modular design of the test setup, improved and changed test approaches are conceivable: On the one hand, the actuator mechanism could be enhanced in order to include more mode shapes by adding actuator devices. On the other hand the mechanism could be completely removed in order to add other measurement technique and test equipment, such as a pressurizable cavity, which was already foreseen in the setup's design phase.

Bibliography

[1] H. W. Foersching. *Grundlagen der Aeroelastik*, chapter 1, pages 15–18. Springer Verlag Berlin Heidelberg New York, 1 edition, 1974.

[2] A. R. Collar. THE EXPANDING DOMAIN OF AEROELASTICITY. *THE ROYAL AERONAUTICAL SOCIETY*, pages 613–636, June 1946.

[3] E. H. Dowell. Generalized Aerodynamic Forces on a Flexible Plate Undergoing Transient Motion in a Shear Flow with an Application to Panel Flutter. *AIAA Journal*, 9(5):834–841, 1971.

[4] H. W. Foersching. *Grundlagen der Aeroelastik*, chapter 6, pages 538–552. Springer Verlag Berlin Heidelberg New York, 1 edition, 1974.

[5] F. E. Kordes and R. B. Noll. FLIGHT FLUTTER RESULTS FOR FLAT RECTANGULAR PANELS. Technical Note D-1058, NASA, 1962.

[6] T. R. Lall. INTERSTAGE ADAPTER PANEL FLUTTER ON ATLAS-CENTAUR AC-2. AC-3 AND AC-4 VEHICLES. Technical Memorandum X-1179, NASA, 1965.

[7] E. H. Dowell. *Aeroelasticity of Plates and Shells*. Noordhoff International, Leyden, The Netherlands, 1975.

[8] L. Muhlstein, P. A. Gaspers, and PD. W. Riddle. An experimental study of the influence of the turbulent boundary layer on panel flutter. Technical Note D-5798, NASA, 1968.

[9] P. A. Gaspers, L. Muhlstein, and D. N. Petroff. Further experimental results on the influence of the turbulent boundary layer on panel flutter. Technical Note D-5798, NASA, 1970.

[10] H. Ashley and G. Zartarian. Piston Theory: A New Aerodynamic Tool for the Aeroelastician. *Journal of the Aeronautical Sciences*, 23(12):1109–1118, 1956.

[11] Y. C. Fung. Some Recent Contributions to Panel Flutter Research. *AIAA Journal*, 1(4):898–909, 1963.

[12] E. H. Dowell. Panel Flutter. SP 8004, NASA, 1972.

[13] E. H. Dowell and H. M. Voss. Theoretical and Experimental Panel Flutter Studies in the Mach Number Range 1.0 to 5.0. *AIAA Journal*, 3(12):2292–2304, 1965.

[14] D. J. Johns. A Survey on Panel Flutter. Advisory Report 1, AGARD, 1965.

[15] C. Mei, K. Abdel-Motagaly, and K. Chen. REVIEW OF NONLINEAR PANEL FLUTTER AT SUPERSONIC AND HYPERSONIC SPEEDS. In *CEAS/AIAA/ICASE/NASA Langley International Forum on Aeroelasticity and Structural Dynamics 1999*, 1999.

[16] E. H. Dowell and O. Bendiksen. Panel Flutter. In *Encyclopedia of Aerospace Engineering*. John Wiley & Sons, Ltd, 2010.

[17] A. Hashimoto, T. Aoyama, and Y. Nakamura. Effects on Turbulent Boundary Layer on Panel Flutter. *AIAA Journal*, 47(12):2785–2791, 2009.

[18] E. H. Dowell. Aerodynamic Boundary Layer Effects on Flutter and Damping of Plates. *Journal of Aircraft*, 10(12):734–738, 1973.

[19] A. Hebler. Vorhersage der Stabilitätsgrenze eines Laminarprofils mit einer Doublet-Lattice-Korrekturmethode basierend auf instationären Versuchsdaten. Master thesis, TU Dresden, December 2014.

[20] H. Mai. Untersuchung der Druckverteilung eines schwingenden Ringflügels in transsonischer Strömung. DLR-Forschungsbericht 2011-12, Deutsches Zentrum für Luft- und Raumfahrt e. V., 2011.

[21] H. U. Meier. *Die deutsche Luftfahrt, Die Pfeilflügelentwicklung in Deutschland bis 1945*, page 251. Bernhard & Graefe Verlag, Bonn, pp.251, 2006.

[22] P. F. Jordan. Über das Flattern von Beplankungen. Technical Report B 45/J/3, AVA, 1945.

[23] P. F. Jordan. The Physical Nature of PANEL FLUTTER. *AERO DIGEST*, pages 34–38, 1956.

[24] M. A. Sylvester and E. J. Baker. Some experimental studies of panel flutter at mach number 1.3,. Technical Note 3914, NACA, 1955.

[25] M. A. Sylvester, H. C. Neslon, and H. J. Cunningham. Experimental and Theoretical Studies of Flutter at Mach Numbers 1.2 to 3.0. Research Memorandum L55E18b, NACA, 1955.

[26] M. A. Sylvester. Experimental Studies of Flutter of Buckled Rectangular Panels at Mach Numbers From 1.2 to 3.0 Including Effects of Pressure Differential and of Panel Width-Length Ratio. Research Memorandum L55130, NACA, 1955.

[27] E. Beeler De. THE X-15 RESEARCH PROGRAM. Report 289, AGARD, 1960.

[28] National Aeronautics and Space Administration. Proceedings of the X-15 First Flight 30th Anniversary Celebration. In *NASA Conference Publication 3105; pp. 157-164*, 1989.

[29] F. E. Kordes and W. J. Tuovilla. FLUTTER RESEARCH OF SKIN PANELS. Technical Note D-451, NASA, 1960.

[30] H. L. Bohon. PANEL FLUTTER TESTS ON FULL-SCALE X-15 LOWER VERTICAL STABILIZER AT MACH NUMBER OF 3.0. Technical Note D-1385, NASA, 1962.

[31] W. R. Baird. Summary of the Aerothermoelastic Development Program for the X-20A (Dyna-Soar). Technical Documentary Report SEG TDR 64-30, Defense Documentation Center, 1964.

[32] S. C. Dixon and G. E. Griffith. EXPERIMENTAL INVESTIGATION AT MACH NUMBER 3.0 EFFECTS OF THERMAL STRESS AND BUCKLING ON THE FLUTTER OF FOUR-BAY ALUMINUM ALLOY PANELS WITH LENGTH-WIDTH RATIO OF 10. Technical Note D-921, NASA, 1961.

[33] S. C. Dixon. EXPERIMENTAL INVESTIGATION AT MACH NUMBER 3.0 EFFECTS OF THERMAL STRESS AND BUCKLING ON FLUTTER CHARACTERISTICS OF FLAT SINGLE-BAY PANELS OF LENGTH-WIDTH RATIO 0.96. Technical Note D-1485, NASA, 1962.

[34] S. C. Dixon and C. P. Shore. EFFECTS OF DIFFERENTIAL PRESSURE, THERMAL STRESS, AND BUCKLING ON FLUTTER OF FLAT PANELS WITH LENGTH-WIDTH RATIO OF 2. Technical Note D-2047, NASA, 1963.

[35] D. J. Shideler, S. C. Dixon, and C. P. Shore. FLUTTER AT MACH 3 OF THERMALLY STRESSED PANELS AND COMPARISON WITH THEORY FOR PANELS WITH EDGE ROTATIONAL RESTRAINT. Technical Note D-3498, NASA, 1966.

[36] W. T. Schaefer. CHARACTERISTICS OF MAJOR ACTIVE WIND TUNNELS AT THE LANGLEY RESEARCH CENTER. Technical Memorandum X-1130, NASA, 1965.

[37] H. L. Bohon. FLUTTER OF CORRUGATION-STIFFENED PANELS AT MACH 3 AND COMPARISON WITH THEORY. Technical Note D-4321, NASA, 1968.

[38] J. G. Presnell and R. L. McKinney. EXPERIMENTAL PANEL FLUTTER RESULTS FOR SOME FLAT AND CURVED TITANIUM SKIN PANELS AT SUPERSONIC SPEEDS. Technical Report D-1600, NASA, 1963.

[39] D. J. Weidman. EXPERIMENTAL FLUTTER RESULTS FOR CORRUGATION-STIFFENED AND UNSTIFFENED PANELS. Technical Report D-3301, NASA, 1966.

[40] C. J. Geiger. History of the X-20A Dyna-Soar Volume I (Narrative). Technical Report ASD-TR-63-50-I, Historical Division of Aeronautical Systems Division; Wright-Patterson AFB, 1963.

[41] R. F. Houchin. *The Rise and Fall of Dyna-Soar: A History of Air Force Hypersonic R&D, 1944-1963*. PhD thesis, Auburn University, 1995.

[42] E. G. Czarnecki. Dyna-Soar-Glider Flight-Envelope Structural Parameters. In *Langley Res. Center Joint Conf. on Lifting Manned Hypervelocity and Reentry Vehicles, part 2*, pages pp. 147–160, 1960.

[43] H. Mielke. *Lexikon der Raumfahrt*, pages 37, 44–45. Transpress VEB Verlag für Verkehrswesen, 5 edition, February 1977.

[44] R. W. Walker. FLUTTER INVESTIGATION OF STREAMWISE-ORIENTED ARRAYS OF CURVED PANELS UNDER COMPRESSIVE LOADING AND AERODYNAMIC HEATING. Technical Note D-2910, NASA, 1965.

[45] N.N. Atlas-Centaur AC-17 Performance For Applications Technology Satellite ATS-D Mission. Technical Memorandum X-2525, NASA, May 1972.

[46] M. L. Nach and R. L. Greene. Panel Flutter Studies of Boost-Vehicle Full-Scale Flight Insulation Panels. Tchnical Memorandum TM X-1417, NASA, 1967.

[47] L. Muhlstein. A FORCED VIBRATION TECHNIQUE FOR INVESTIGATION OF PANEL FLUTTER. In *AIAA Aerodynamic Testing Conference*, number 66-769, September 21-23 1966.

[48] H. J. Cunningham. Flutter Analysis of Flat Rectangular Panels Based on Three-Dimensional Supersonic Potential Flow. *AIAA Journal*, 1(8):1795–1801, 1967.

[49] T.M. Perkins. Aeroelastic Stability of an Array of Full-Scale Panels from the Saturn S-IVB Stage at Transonic Mach numbers. Technical Report 67-9, AEDC, 1967.

[50] T. M. Perkins. Flutter Test of an Array of Full-Scale Panels from the Saturn S-IVB Stage at Transonic Mach numbers. Technical Report 68-30, AEDC, 1968.

[51] J. J. Nichols. Final Report: Saturn V, S-IVB Panel Flutter Qualification Test. Technical Note D-5439, NASA, 1969.

[52] T.M. Perkins. Narrative End Item Report Saturn S-IVB-504N. Douglas Report DAC-56562, McDonnell Douglas Corporation, 1968.

[53] H. L. Bohon and C. P. Shore. APPLICATION OF RECENT PANEL FLUTTER RESEARCH TO THE SPACE SHUTTLE PART II - INFLUENCE OF EDGE CLIPS AND FLOW ANGULARITY. In *NASA SPACE SUTTLE TECHNOLGY CONFERENCE Volume III - Dynamics and Aeroelasticity*, Langley Research Center, Hampton, March 2-4 1971.

[54] L. H. Bohon, J. L. Shideler, and D. R. Rummler. Radiative Metallic Thermal Protection Systems: A Status Report; Journal of Spacecraft. *Journal of Spacecraft*, 14(10):626–632, 1977.

[55] P. Shyprykevich. EXPERIMENTAL INVESTIGATION OF ORTHOTROPIC PANEL FLUTTER AT ARBITRARY YAW ANGLES, AND COMPARISON WITH THEORY. Contractor Report CR-2265, NASA, 1973.

[56] P. Shyprykevich and J. W. Sawyer. Flutter of Orthotropic Panels at Arbitrary Yaw Angles- Experiment and Theory. *Journal of Aircraft*, 11(1):15–20, 1974.

[57] V. V. Vedeneev, S. V. Guvernyuk, and M. E. Kolotnikov. Experimental observation of single-mode panel flutter in a supersonic gas flow. In *7th EUROMECH Solid Mechanics Conference*, Lisbon, Portugal, 7-11 September 2009.

[58] V. V. Vedeneev, S. V. Guvernyuk, S. V. Zubkov, and M. E. Kolotnikov. Experimental Investigations of Single-Mode Panel Flutter in Supersonic Gas Flow. *Fluid Dynamics*, 45(2):312–324, 2009.

[59] V. V. Vedeneev, S. V. Guvernyuk, S. V. Zubkov, and M. E. Kolotnikov. Experimental observation of single-mode panel flutter in a supersonic gas flow. *Doklady Physics*, 54(8):389–391, 2009.

[60] V. V. Vedeneev. Panel flutter at low supersonic speeds. *Journal of Fluids and Structures*, 29:79–96, 2012.

[61] E. Carrera, E. Zappino, and K. Patocka. Aeroelastic analysis of versatile thermal insulation (VTI) panels with pinched boundary conditions. *CEAS Space J*, 6:23–35, 2013.

[62] E. Carrera, E. Zappino, A. Farrarese, and M. Montabone. AEROELASTIC DESIGN OF VERSATILE THERMAL INSULATION (VTI) PANELS. In *AIDAA XXII Conference*, Napoli, 9-12 September 2013. AIDAA.

[63] E. H. Dowell. Panel Flutter: A Review of the Aeroelastic Stability of Plates and Shells. *AIAA Journal*, 8(3):385–399, 1970.

[64] E. Dowell, J. Edwards, and T. Strganac. Nonlinear Aeroelasticity. *Journal of Aircraft*, 40(5):857–874, 2003.

[65] C. E. Lemley. Design criteria for the prediction and prevention of panel flutter Volume I: Criteria Presentation. Technical Report AFFDL-67-140, McDonnel Douglas Corperation, 1968.

[66] M. Laurenson and J. L. McPherson. DESIGN PROCEDURES FOR FLUTTER-FREE SURFACE PANELS. CR 2801, NASA, 1977.

[67] H. Irretier. *Grundlagen der Schwingungstechnik 2*. Vieweg & Sohn., first edition edition, 2001.

[68] T. H. G. Megson. *Aircraft Structures for Engineering Students*. Elsevier Ltd., fourth edition edition, 2007.

[69] M. J. Lighthill. Oscillating Airfoils at High Mach Number. *Journal of the Aeronautical Sciences*, 20(6):402–406, 1953.

[70] J. Ackeret. über Luftkräfte bei sehr grossen Geschwindigkeiten insbesondere bei ebenen Strömungen. *Helvetica Physica Acta*, 1 (1928):301–322, 1928.

[71] H. Glauert. The Effect of Compressibility on the Lift of an Aerofoil. *Proceeding of the Royal Society A*, 118(779):113–119, March 1927.

[72] J. W. Miles. On the Aerodynamic Instability of Thin Panels. *Journal of the Aeronautical Sciences*, pages 771–780, August 1956.

[73] E. H. Dowell. Nonlinear Oscillations of a Fluttering Plate. *AIAA Journal*, 4(7):1267–1274, July 1966.

[74] M. Alder. Development and Validation of a Fluid-Structure Solver for Transonic Panel Flutter. *AIAA Journal*, 53(12):3509–3520, December 2015.

[75] P. R. Hakenesch. Aerodynamik des Flugzeugs. Lecture Notes, Munich University of Applied Sciences, 2007.

[76] H. Schlichting and K. Gersten. *Boundary Layer Theory*, chapter 11, pages 293–294. Springer Berlin Heidelberg New York, 8th revised and enlarged edition edition, 2003.

[77] J. M. Kay. Boundary-Layer Flow along a Flat Plate with Uniform Suction. Technical Report R. & M. No.2628, Aeronautical Research Council Reports and Memoranda, Ministry of Supply, 1953.

[78] M. Lutz. Numerische Untersuchung zur Erstellung einer Einlaufkontur zwecks einer Grenzschichtdickenvariation im Transsonischen Windkanal Göttingen (DNW-TWG). DLR-Interner Bericht DLR-IB-AE-GO-2016-259, Deutsches Zentrum für Luft- und Raumfahrt e. V., 2016.

[79] J. Lübker. Druckmessungen im DNW-TWG (Perforierte Messstrecke), 2014. IB 232-2014 J 11, DLR, 2014.

[80] M. Lock. *A study of two-dimensional panel flutter*. PhD thesis, California Institute of Technology, Pasadena, California, 1961.

[81] E. H. Dowell and H. M. Voss. The Effect of a Cavity on Panel Vibration. *AIAA Journal*, 1(2):476–477, February 1963.

[82] H. L. Bohon. Flutter Design of Stiffened-Skin Panels for Hypersonic Aircraft. Technical Note NASA TN D-5555, NASA, December 1969.

[83] M. A. Kouchakzadeh, M. Rasekh, and H. Haddadpour. Panel flutter analysis of general laminated composite plates. *Composite Structures*, 92:2906–2915, 2010.

[84] M. Ganapathi and T. K. Varadan. Supersonic Flutter of Laminated Curved Panels. *Defense Science Journal*, 45(2):147–159, April 1995.

[85] S. C. Dixon. Application of Transtability Concept to Flutter of Finite Panels and Experimental Results. Technical Note NASA TN D-1948, NASA, September 1963.

[86] Forschungskuratorium Maschinenbau (FKM), editor. *FKM-Richtlinie - "Rechnerischer Festigkeitsnachweis für Maschinenbauteile"*. VDMA-Verlag, 6 edition, 2012.

[87] N.N. *Hydropuls Spezifikation 1 PLF 7 8905*. Carl Schenck AG.

[88] S. Wiggen. Bewegungsinduzierte instationäre Luftkräfte bei wirbeldominierter Strömung. DLR-Forschungsbericht 2016-50, Deutsches Zentrum für Luft- und Raumfahrt e. V., 2016.

[89] N.N. *Kulite Pressure Transducer Handbook*. Kulite Semiconductor Products, Inc.

[90] N.N. *Kulite XCS-093 Data Sheet*. Kulite Semiconductor Products, Inc.

[91] N.N. *PCB Model Number 352C22 ICP ACCELEROMETER*. PCB PIEZOTRONICS, revision h edition.

[92] N.N. *Hochgeschwindigkeits megaPixel CMOS-Kamera MC1310/11*. Mikrotron GmbH, 2007.

[93] N.N. *Induktive Wegaufnehmer Differentialdrosselausführung Sonderbauform WLH ... C*. Messotron Hennig GmbH & Co KG, 2001.

[94] S.J. Rothberg, M.S. Allen, and P. Castellini. An international review of laser Doppler vibrometry: making light work of vibration measurement. *ics and Lasers in Engineering*, 99:11–22, December 2017.

[95] N.N. *Betriebsanleitung opto NCDT 1607/1627*. Micro-Epsilon Messtechnik GmbH & Co. KG, 2008.

[96] W. Lorenz-Meyer. Grenzschichtmessungen an der perforierten Messstreckenwand des 1m x 1m transsonischen Windkanals der DFVLR-AVA Göttingen. Master's thesis, DFVLR-AVA Göttingen, 1979.

[97] J. Lübker. DNW-TWG Grenzschichtvermessung 2013. IB 232-2014 J 01, DLR, 2013.

[98] P. Potin. Grenzschichtuntersuchungen im Transsonischen Windkanal Göttingen (TWG). IB 29112-96 B 02, DLR, 1996.

[99] F. M. White. *Viscous Fluid Flow*. McGraw-Hill, NewYork, 1974.

[100] H. Schlichting and E. Truckenbrodt. *Aerodynamik des Flugzeuges, Erster Band, Grundlagen aus der Strömungsmechanik, Aerodynamik des Tragflügels (Teil I)*. Springer-Verlag, 1959.

[101] R. J. Allemang. The Modal Assurance criterion - Twenty Years of Use and Abuse. *Sound and Vibration*, August:14–21, 2003.

[102] O. Luderer. Numerische Untersuchung des Einflusses experimenteller Randbedingungen auf die aerodynamischen Lasten einer oszillierenden Platte. Master's thesis, Technische Universität Hamburg Harburg, TUHH, 2017.

[103] G. H. Schnerr. Vorlesung Gasdynamik. Lecture Script, 2009.

[104] K. Burg, S. Viriyabhun, and J. Zierep. Die Überschallströmung längs einer welligen Wand mit gerader Gegenwand. *Acta Mechanica - ACTA MECH*, 16:271–278, 09 1973.

List of Tables

List of Figures

Appendices

A. Experimental Conception

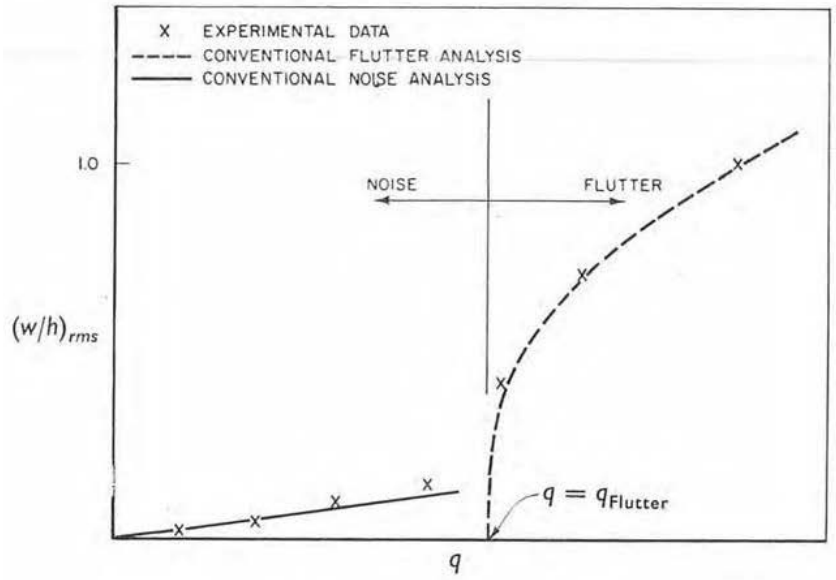

Figure A.1.: Schematic of plate response by means of normalized panel deflection vs. dynamic pressure [7].

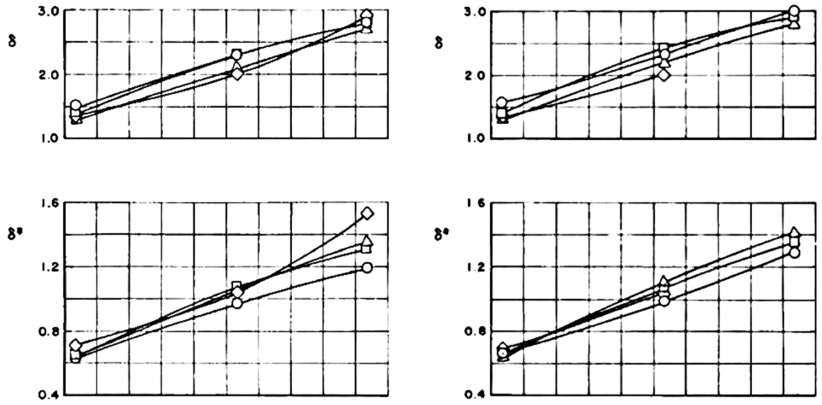

Figure A.2.: Variation of boundary layer characteristics with rake position and Mach Number at low Reynolds Number (left) and at high Reynolds Number (right) and for different Mach Numbers ($\circ$ $M_\infty = 1.1$; $\square$ $M_\infty = 1.2$; $\triangle$ $M_\infty = 1.3$; $\Diamond$ $M = 1.35$) [49].

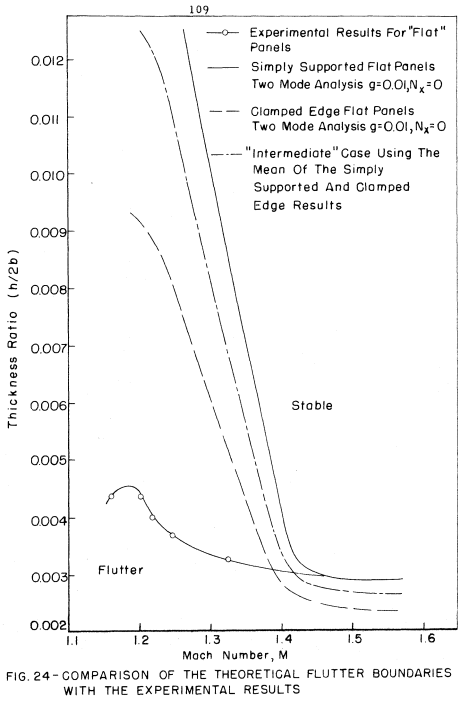

Figure A.3.: Influence of Mechanical Boundary Conditions on flutter. Comparison of the theoretical flutter boundaries with the experimental results [80].

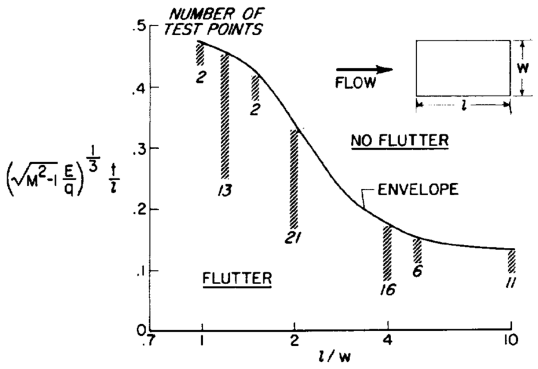

Figure A.4.: Influence of the aspect ratio on flutter. Critical dynamic pressure vs. aspect ratio of a flat rectangular panel [29].

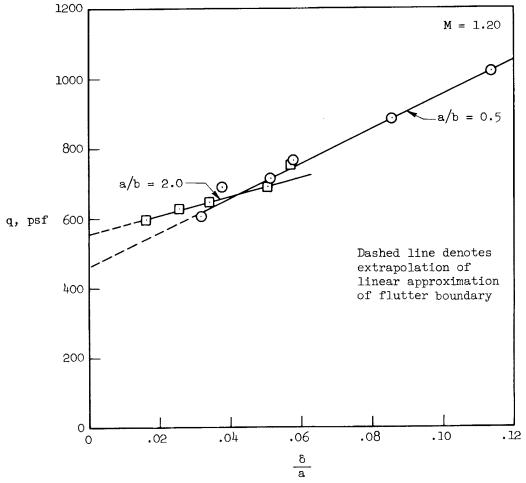

Figure A.5.: Influence of aspect ratio on flutter. Flutter dynamic pressure is presented as a function of boundary-layer thickness and aspect ratio [8].

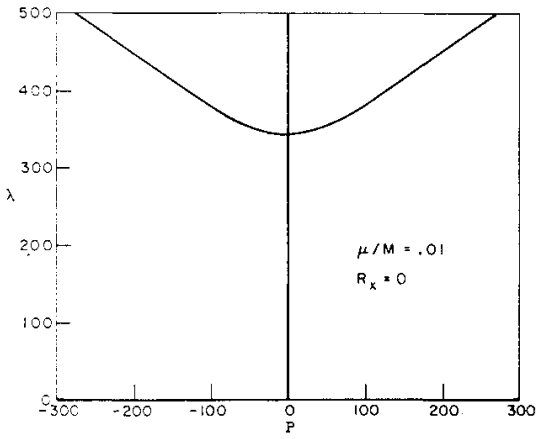

Figure A.6.: Flutter dynamic pressure vs static pressure differential [73].

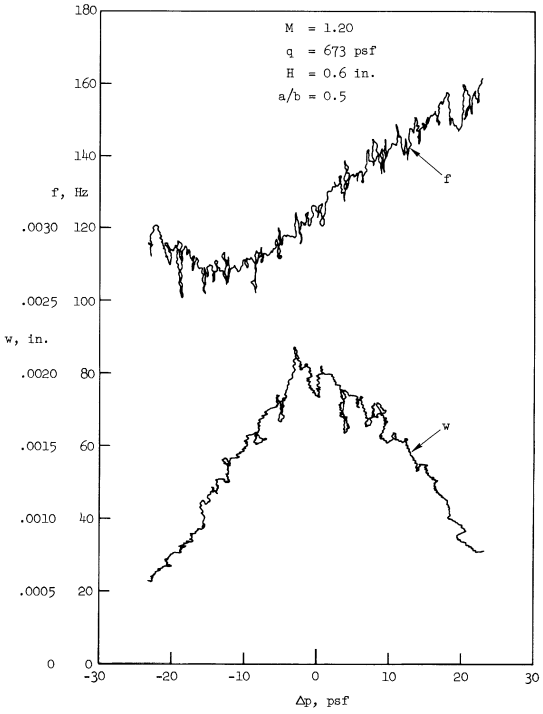

Figure A.7.: Influence of cavity effects on panel flutter. Typical variation of frequency and amplitude of dominant panel response mode with cavity differential pressure [8].

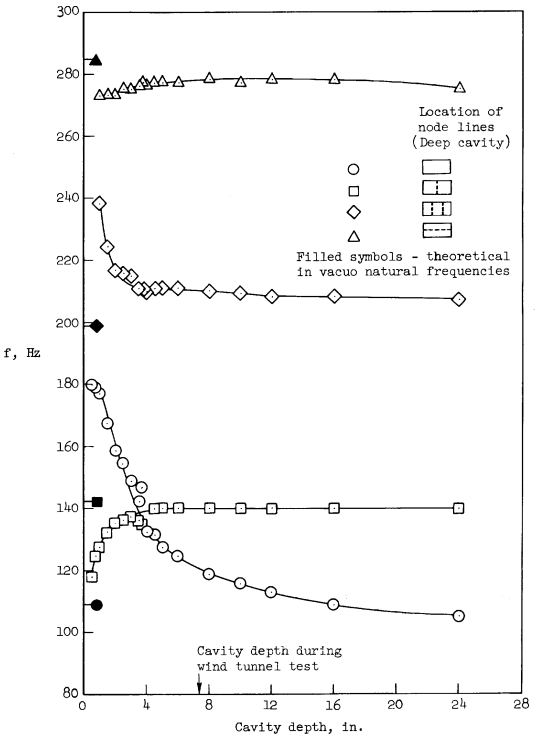

Figure A.8.: Influence of cavity effects on panel flutter. Effect of cavity depth on panel natural frequencies at atmospheric pressure [8].

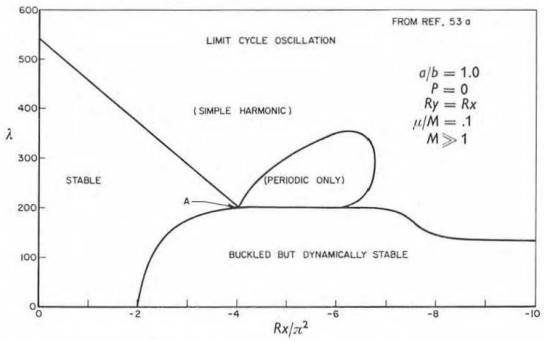

Figure A.9.: Influence of in-plane loads on panel flutter. Stability regions for panels with in-plane loads in x-direction Rx [7].

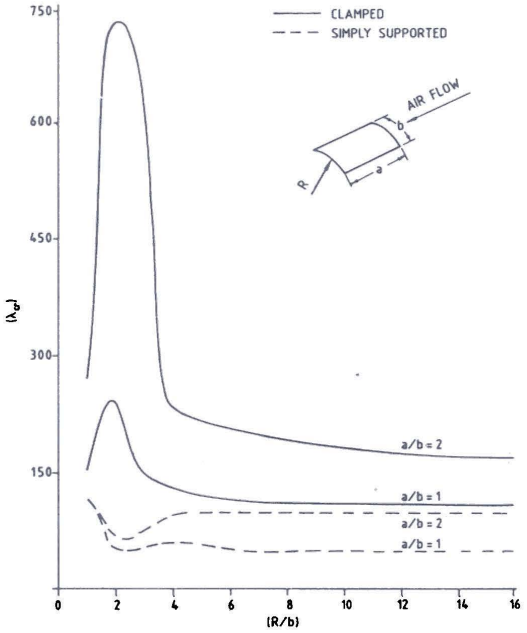

Figure A.10.: Influence of in-plane loads and curvature on panel flutter. Critical dynamic pressure vs radius-to-arc-length ratio for isotropic panels ($b/h = 100$) [84].

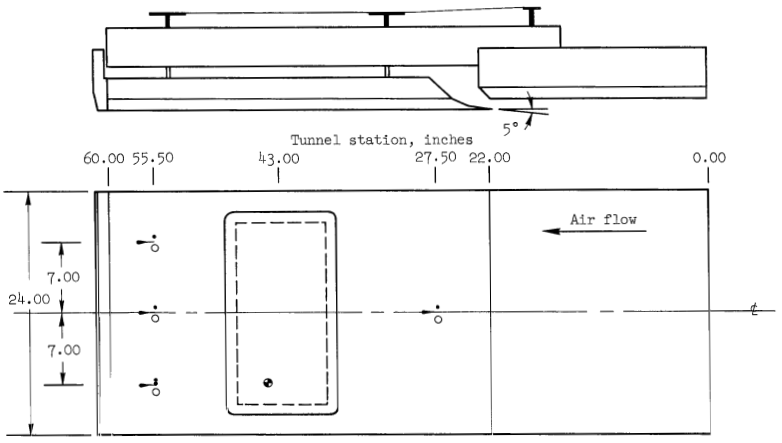

Figure A.11.: WT setup by Gaspers [9].

B. Setup

Technische Information
TOOLOX33

Anwendung

TOOLOX33 ist ein neuer gehärteter und angelassener Werkzeugstahl mit hoher Zähigkeit und sehr geringer Restspannung für gute Formstabilität. TOOLOX 33 ist dank seines geringen Karbidinhaltes sehr gut zu bearbeiten. TOOLOX 33 eignet sich hervorragend zur Herstellung von Formwerkzeugen, z.B. Kunststoff-, Gummiformen und Maschinenkomponenten. Durch geeignete Oberflächenbehandlung lässt sich die Standzeit des Werkzeugs oder der Komponente verlängern.

Typische Werte

Chemische Zusammensetzung

C	0,22-0,24%
Si	0,6-1,1%
Mn	0,8%
P	max 0,010%
S	max 0,003%
Cr	1,0-1,2%
Mo	0,30%
V	0,10-0,11%
Ni	max 1%
CE_{IIW}	0,62-0,71
CET	0,40-0,44

Mechanische Eigenschaften

	+20°C	+200°C	+300°C	+400°C	+500°C
Zugfestigkeit, R_m [MPa]	1080	1000			
Streckgrenze, $R_{p0,2}$ [MPa]	950	860			
Bruchdehnung, A_5 [%]	16	12			
Stauchgrenze, $R_{c0,2}$ [MPa]	880	750	700	590	560
Kerbschlagarbeit [J/20°C]	100	170	180	180	
Härte, [HBW]	310				
Härte, [HRC]	29				

Einschlussgehalt

Einschlussgröße (äquival. Drm.)	6µm
Flächenanteil	0,015%
Länge/Breite Verhältnis	1,2

Physikalische Eigenschaften

	+20°C	+200°C	+400°C	+600°C
Wärmeleitung [W/m • K]	35	35	30	23
Wärmeausdehnungs-koeffizient[10^{-6}/K]	13,1	13,1		

Oberflächentechnik

Hart und Zäh

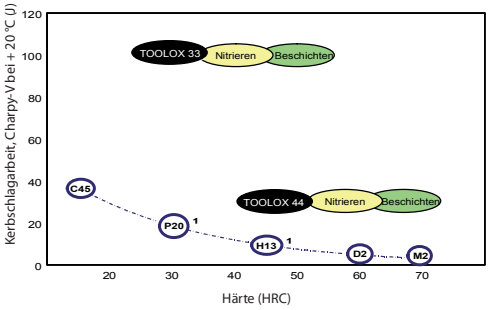

Gasnitrieren, 510 °C

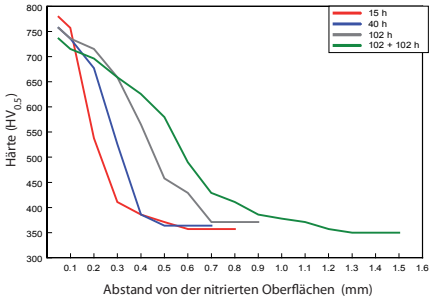

Fussnote 1: P20 ≈ W.Nr 1.2311 and H13 ≈ W.Nr 1.2344

TOOLOX33®
PREHARDENED TOOL STEEL

SSAB Oxelösund AB, SE-613 80 Oxelösund, Sweden. Tel +46(0)155 25 40 00, Fax +46(0)155 25 55 34. www.toolox.com

SSAB OXELÖSUND

Figure B.1.: Toolox 33 data sheet (extract).

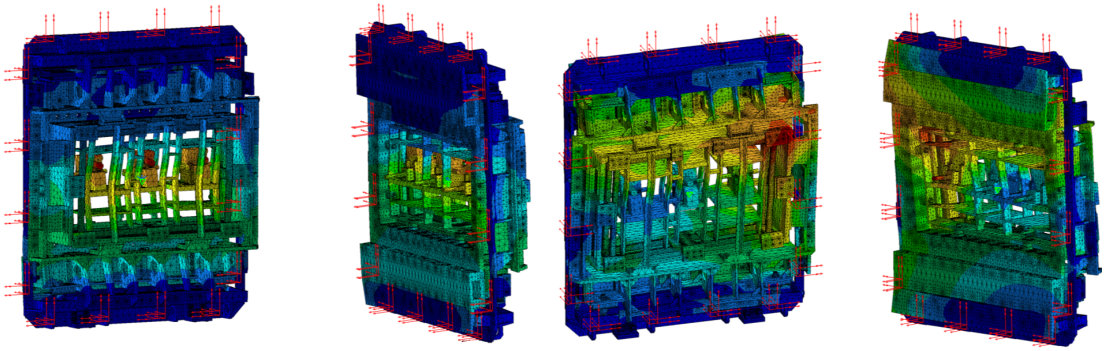

(a) Third eigenfrequency at $f = 232.4$ Hz. (b) Fourth eigenfrequency at $f = 276.8$ Hz.

Figure B.2.: Test setup eigenfrequencies ($\alpha = 90°$ configuration).

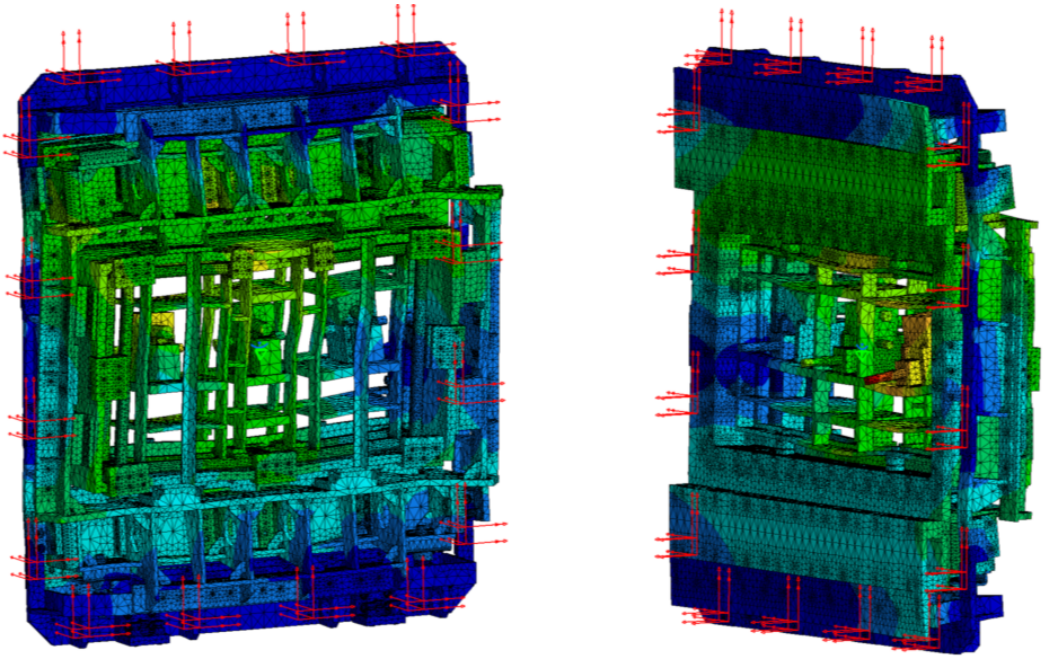

Figure B.3.: Test setup eigenfrequencies ($\alpha = 90°$ configuration); Fifth eigenfrequency at $f = 289.2$ Hz.

C. Testing Technology

Data Sheets

Induktive Wegaufnehmer
Differentialdrosselausführung
Sonderbauform **WLH ... C** (kalibriert auf 80 mV/V)

MESSOTRON

radialer Kabelanschluß

Anschluß:

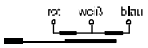

Teflon-Kabel 500 mm lang;
Kernkanal durchgängig

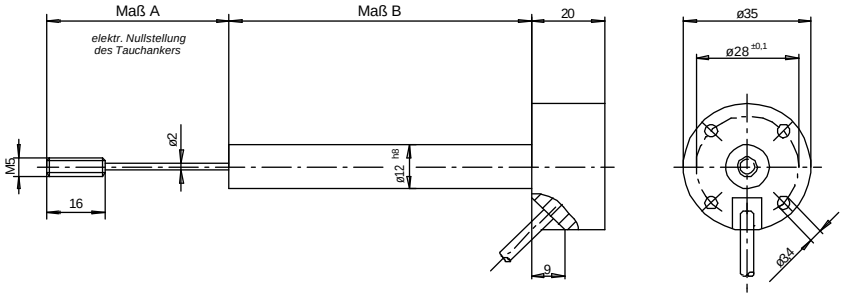

Bestellbeispiel: WLH 50 C

		WLH 10	WLH 20	WLH 40	WLH 50	WLH 100	WLH 150	WLH 200	WLH 250	WLH 300	WLH 400	WLH 500
Nennmeßweg	**mm**	±5	±10	±20	±25	±50	±75	±100	±125	±150	±200	±250
Arbeitsspanne	**mm**	20	30	60	60	120	170	220	270	320	420	516
Maß A	**mm**	40	55	50	50	100	130	150	180	200	250	300
Maß B	**mm**	80	100	145	145	245	355	455	565	675	875	1065
Aufnehmergewicht (ca.)	**g**	40	60	85	85	120	150	200	230	280	350	440
Tauchankergewicht (ca.)	**g**	6	8	9	9	12	15	20	25	30	40	50
Nennausgangssignal **)	**mV/V**	80	80	80	80	80	80	80	80	80	80	80
Empfindlichkeit	**mV/V/mm**	16	8	4	3,2	1,6	1,07	0,8	0,64	0,53	0,4	0,32
Speisespannung	**V eff**	bis 5										
Trägerfrequenz	**kHz**	5 ... 10										
Linearitätsfehler		±0,25% des Gesamtmeßweges										
Temperaturfehler des Nullpunktes		±0,02% / 10K										
Temperaturfehler der Empfindlichkeit		±0,05% / 10K										
Betriebstemperatur *)		-50°C ... +80°C Option: bis120°C										
Schutzart nach Din 40050		IP 64										

*) Optionen bei Bestellung angeben **) Toleranz der Kalibrierung: ±3 mV/V

MESSOTRON
Hennig GmbH&Co.KG
Industrie-Messtechnik
Friedr.-Ebert-Str. 37, Tel.. (06257)82331
D-64342 Seeheim-Jugenheim

Serie WLH ... C
10 ... 500 mm

Maßblatt
16.47.00
Stand 07/96

Bei der äußeren Gestaltung der Wegaufnehmer können wir Ihre Wünsche weitgehend berücksichtigen

Änderungen vorbehalten
11/01

Figure C.1.: Position sensor data sheet.

kulite®

STANDARD VERSION MINIATURE IS® PRESSURE TRANSDUCER

XCQ-093 SERIES

- Industry Standard
- Superb Stability
- Program Qualified in U.S.A. And Europe
- Size And Shape Ideal For Incorporation In User Designed Probes

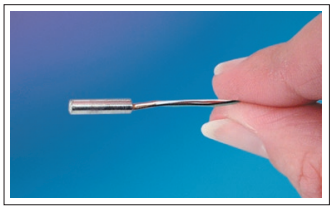

The XCQ-093 Series allows for a very rugged package suited for probes, pressure rakes and other similar test set ups. This transducer is well suited for both dynamic and static pressure measurements in benign or harsh environments.

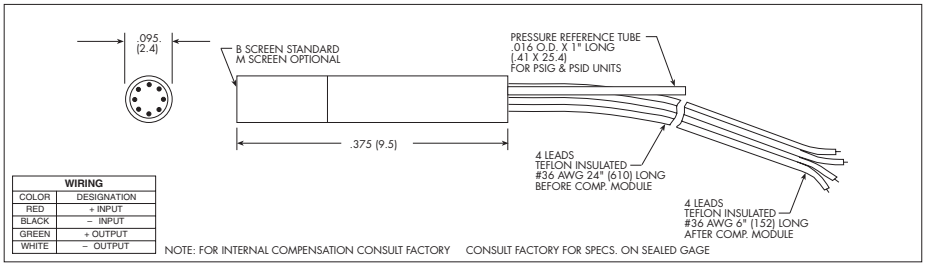

WIRING	
COLOR	DESIGNATION
RED	+ INPUT
BLACK	– INPUT
GREEN	+ OUTPUT
WHITE	– OUTPUT

NOTE: FOR INTERNAL COMPENSATION CONSULT FACTORY CONSULT FACTORY FOR SPECS. ON SEALED GAGE

INPUT Pressure Range	0.35 5	0.7 10	1.7 25	3.5 50	7 100	17 250	35 500	70 BAR 1000 PSI
Operational Mode	Absolute, Gage, Sealed Gage, Differential					Absolute, Sealed Gage		
Over Pressure	2 Times Rated Pressure With No Change In Calibration							
Burst Pressure	3 Times Rated Pressure							
Pressure Media	All Nonconductive, Noncorrosive Liquids or Gases							
Rated Electrical Excitation	10 VDC/AC							
Maximum Electrical Excitation	15 VDC/AC							
Input Impedance	1000 Ohms (Min.)							
OUTPUT Output Impedance	1000 Ohms (Nom.)							
Full Scale Output (FSO)	100 mV (Nom.)							
Residual Unbalance	± 5 mV (Typ.)							
Combined Non-Linearity, Hysteresis and Repeatability	± 0.1% FSO BFSL (Typ.), ± 0.5% FSO (Max.)							
Resolution	Infinitesimal							
Natural Frequency (KHz) (Typ.)	150	175	240	300	380	550	700	1000
Acceleration Sensitivity % FS/g Perpendicular Transverse	$1.5x10^{-3}$ $2.2x10^{-4}$	$1.0x10^{-3}$ $1.4x10^{-4}$	$5.0x10^{-4}$ $6.0x10^{-5}$	$3.0x10^{-4}$ $4.0x10^{-5}$	$1.5x10^{-4}$ $2.0x10^{-5}$	$1.0x10^{-4}$ $9.0x10^{-6}$	$6.0x10^{-5}$ $6.0x10^{-6}$	$4.5x10^{-5}$ $3.0x10^{-6}$
Insulation Resistance	100 Megohm Min. @ 50 VDC							
ENVIRONMENTAL Operating Temperature Range	-65°F to +250°F (-55°C to +120°C)							
Compensated Temperature Range	80°F to +180°F (25°C to +80°C) Any 100°F Range Within The Operating Range on Request							
Thermal Zero Shift	± 1% FS/100°F (Typ.)							
Thermal Sensitivity Shift	± 1% /100°F (Typ.)							
Steady Acceleration	10,000g. (Max.)							
Linear Vibration	10-2,000 Hz Sine, 100g. (Max.)							
PHYSICAL Electrical Connection	4 Leads 36 AWG 30" Long							
Weight	.4 Gram (Nom.) Excluding Module and Leads							
Pressure Sensing Principle	Fully Active Four Arm Wheatstone Bridge Dielectrically Isolated Silicon on Silicon							

Note: Custom pressure ranges, accuracies and mechanical configurations available. Dimensions are in inches. Dimensions in parenthesis are in millimeters.
Continuous development and refinement of our products may result in specification changes without notice - all dimensions nominal. (I)

KULITE SEMICONDUCTOR PRODUCTS, INC. • One Willow Tree Road • Leonia, New Jersey 07605 • Tel: 201 461-0900 • Fax: 201 461-0990 • http://www.kulite.com

Figure C.2.: Pressure sensor data sheet.

Model Number	ICP® ACCELEROMETER	Revision: H
352C22		ECN #: 42346

Performance	ENGLISH	SI	
Sensitivity(± 15 %)	10 mV/g	1.0 mV/(m/s²)	
Measurement Range	± 500 g pk	± 4900 m/s² pk	
Frequency Range(± 5 %)	1.0 to 10,000 Hz	1.0 to 10,000 Hz	
Frequency Range(± 10 %)	0.7 to 13,000 Hz	0.7 to 13,000 Hz	
Frequency Range(± 3 dB)	0.3 to 20,000 Hz	0.3 to 20,000 Hz	
Resonant Frequency	≥ 50 kHz	≥ 50 kHz	
Broadband Resolution(1 to 10,000 Hz)	0.004 g rms	0.04 m/s² rms	[1]
Non-Linearity	≤ 1 %	≤ 1 %	[2]
Transverse Sensitivity	≤ 5 %	≤ 5 %	
Environmental			
Overload Limit(Shock)	± 10,000 g pk	± 98,000 m/s² pk	
Temperature Range(Operating)	-65 to +250 °F	-54 to +121 °C	
Temperature Response	See Graph	See Graph	[1]
Electrical			
Excitation Voltage	18 to 30 VDC	18 to 30 VDC	
Constant Current Excitation	2 to 20 mA	2 to 20 mA	
Output Impedance	≤ 300 Ohm	≤ 300 Ohm	
Output Bias Voltage	7 to 12 VDC	7 to 12 VDC	
Discharge Time Constant	1.0 to 3.5 sec	1.0 to 3.5 sec	
Settling Time(within 10% of bias)	<3 sec	<3 sec	
Spectral Noise(1 Hz)	800 µg/√Hz	7840 (µm/sec²)/√Hz	[1]
Spectral Noise(10 Hz)	250 µg/√Hz	2450 (µm/sec²)/√Hz	[1]
Spectral Noise(100 Hz)	60 µg/√Hz	590 (µm/sec²)/√Hz	[1]
Spectral Noise(1 kHz)	50 µg/√Hz	490 (µm/sec²)/√Hz	[1]
Spectral Noise(10 kHz)	40 µg/√Hz	392 (µm/sec²)/√Hz	[1]
Electrical Isolation(Base)	$>10^8$ Ohm	$>10^8$ Ohm	
Physical			
Size (Height x Length x Width)	0.14 in x 0.45 in x 0.25 in	3.6 mm x 11.4 mm x 6.4 mm	
Weight	0.017 oz	0.5 gm	[1]
Sensing Element	Ceramic	Ceramic	
Sensing Geometry	Shear	Shear	
Housing Material	Anodized Aluminum	Anodized Aluminum	
Sealing	Epoxy	Epoxy	
Electrical Connector	3-56 Coaxial Jack	3-56 Coaxial Jack	
Electrical Connection Position	Side	Side	
Mounting	Adhesive	Adhesive	

CE[3]

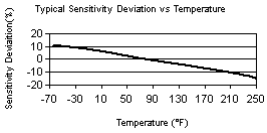

All specifications are at room temperature unless otherwise specified.
In the interest of constant product improvement, we reserve the right to change specifications without notice.
ICP® is a registered trademark of PCB Group, Inc.

OPTIONAL VERSIONS
Optional versions have identical specifications and accessories as listed for the standard model except where noted below. More than one option may be used.

NOTES:
[1] Typical.
[2] Zero-based, least-squares, straight line method.
[3] See PCB Declaration of Conformance PS023 for details.

SUPPLIED ACCESSORIES:
Model 030A10 Coax Cable, 10 ft (3 m), 3-56 plug to 10-32 plug. (1)
Model 039A27 One-piece removal tool for Models 352C22, 357C10, 352A21, & 357A09 (1)
Model 080A109 Petro Wax (1)
Model ACS-1 NIST traceable frequency response (10 Hz to upper 5% point). (1)

Entered: AP	Engineer: JJB	Sales: WDC	Approved: JJB	Spec Number:
Date: 12/16/2013	Date: 12/16/2013	Date: 12/16/2013	Date: 12/16/2013	10668

PCB PIEZOTRONICS
3425 Walden Avenue, Depew, NY 14043
Phone: 716-684-0001
Fax: 716-684-0987
E-Mail: info@pcb.com

Figure C.3.: Acceleration sensor data sheet.

Calibration Data

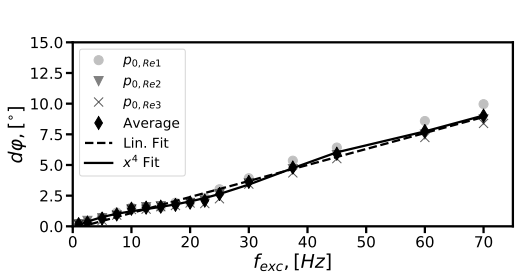

(a) M=0.7; Curve fit, Actuator 1.

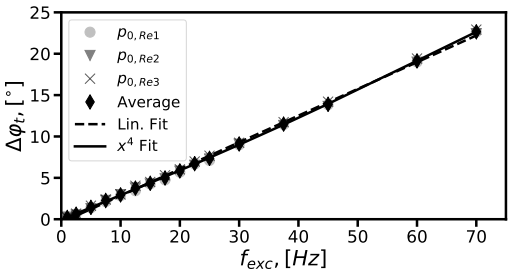

(b) M=0.7; Curve fit, Actuator 2.

Figure C.4.: Calibration data set; Ψ_{21} model; 2017.

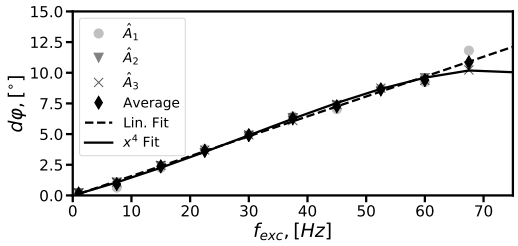

(a) M=0.7; Curve fit.

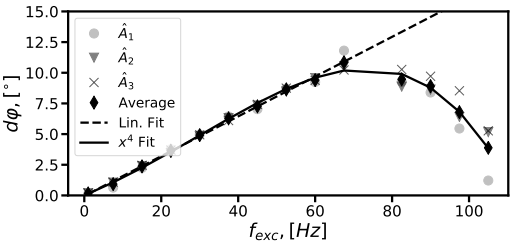

(b) M=0.7; Curve fit, full frequency range.

Figure C.5.: Calibration data set; Ψ_{11} model; 2015.

D. Results

Boundary Layer

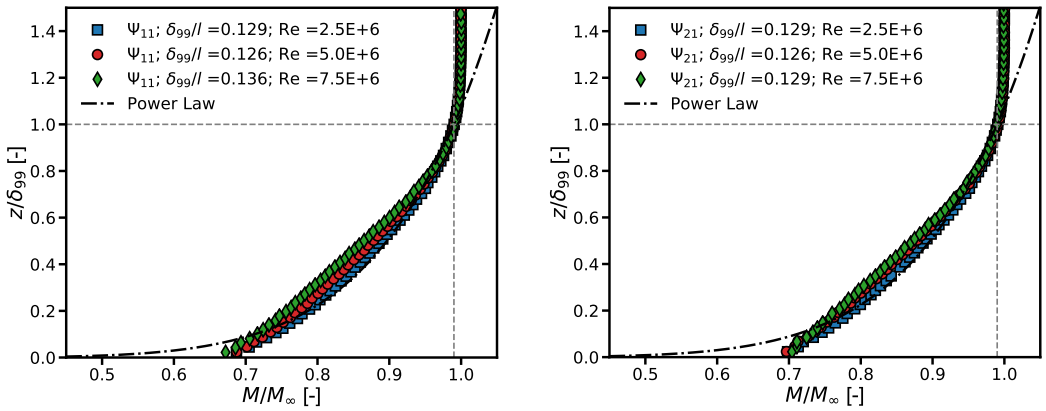

(a) Ψ_{11} model; $M_\infty = 0.7$.

(b) Ψ_{21} model; $M_\infty = 0.7$.

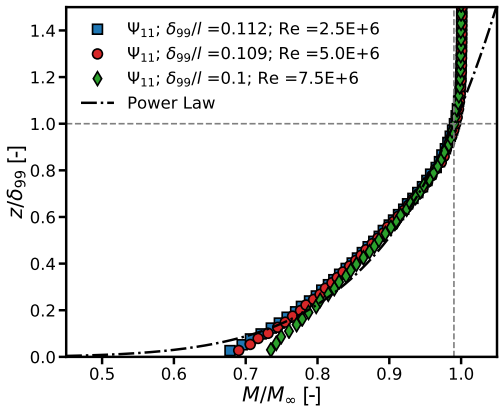

(c) Ψ_{11} model; $M_\infty = 1.1$.

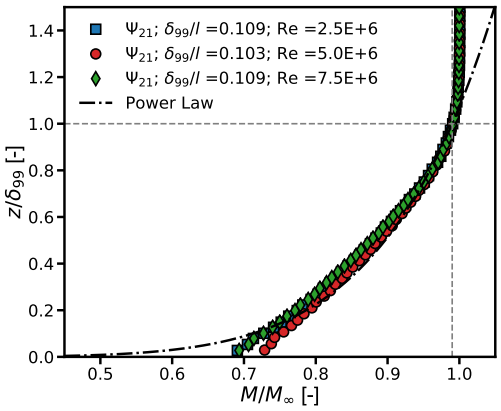

(d) Ψ_{21} model; $M_\infty = 1.1$.

Figure D.1.: Impact of Reynolds number on boundary layer velocity profile; $\hat{A} = 0.0$ mm; $f_{exc} = 0.0$ Hz.

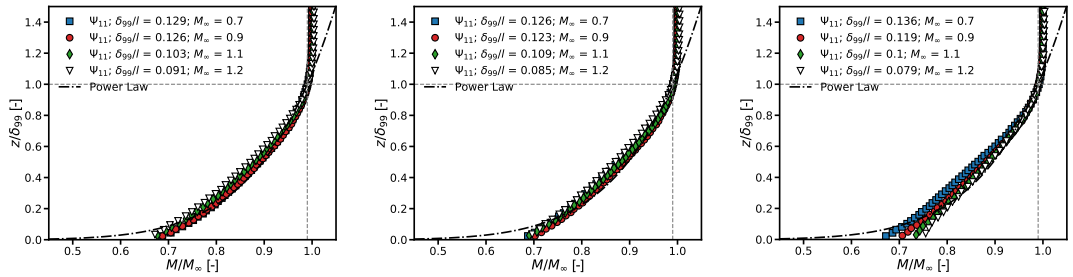

(a) $Re = 2.5 \cdot 10^6$. (b) $Re = 5.0 \cdot 10^6$. (c) $Re = 7.5 \cdot 10^6$.

Figure D.2.: Mach number influence on boundary layer velocity profile; Ψ_{11} model; $\hat{A} = 0.0$ mm; $f_{exc} = 0.0$ Hz.

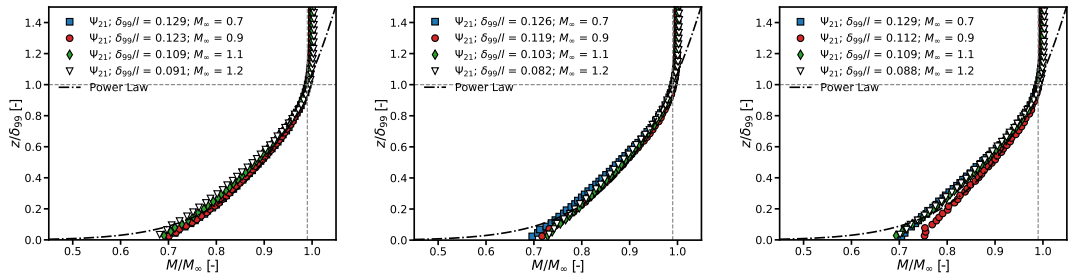

(a) $Re = 2.5 \cdot 10^6$. (b) $Re = 5.0 \cdot 10^6$. (c) $Re = 7.5 \cdot 10^6$.

Figure D.3.: Mach number influence on boundary layer velocity profile; Ψ_{21} model; $\hat{A} = 0.0$ mm; $f_{exc} = 0.0$ Hz.

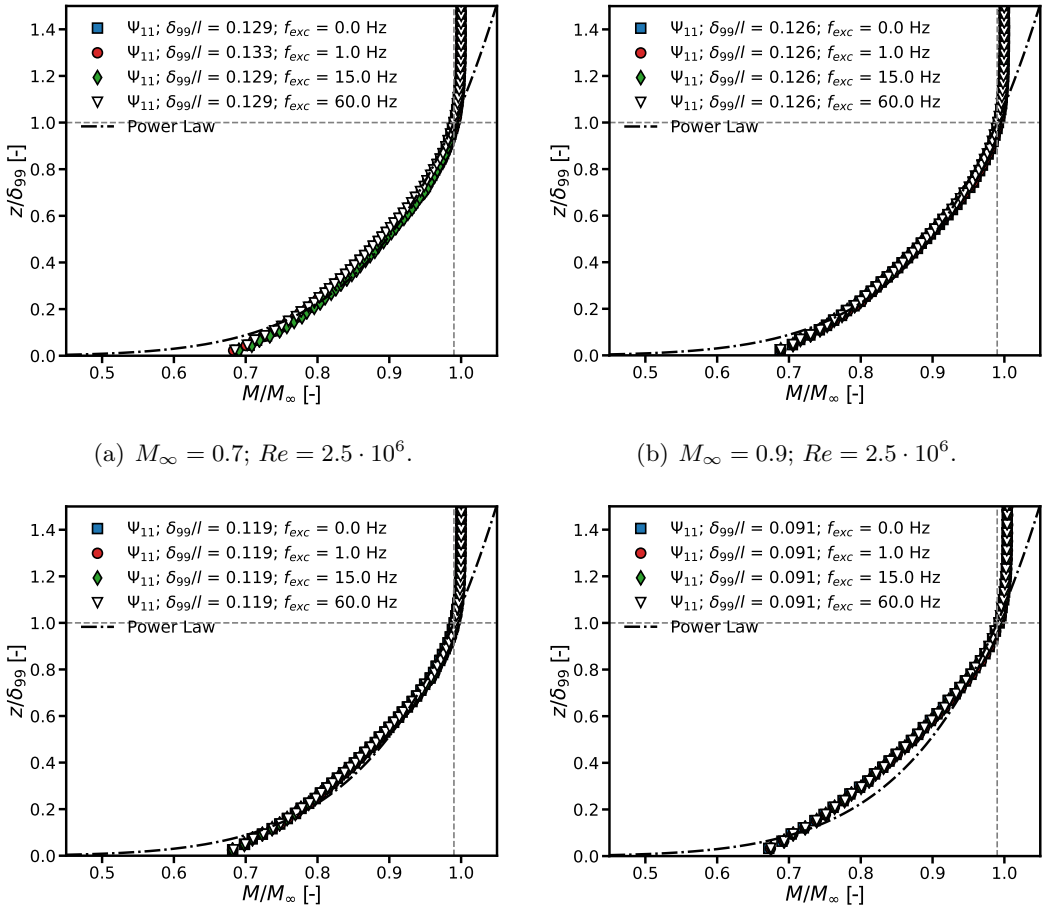

(a) $M_\infty = 0.7$; $Re = 2.5 \cdot 10^6$.

(b) $M_\infty = 0.9$; $Re = 2.5 \cdot 10^6$.

(c) $M_\infty = 1.05$; $Re = 2.5 \cdot 10^6$.

(d) $M_\infty = 1.2$; $Re = 2.5 \cdot 10^6$.

Figure D.4.: Frequency dependency; Ψ_{11} model.

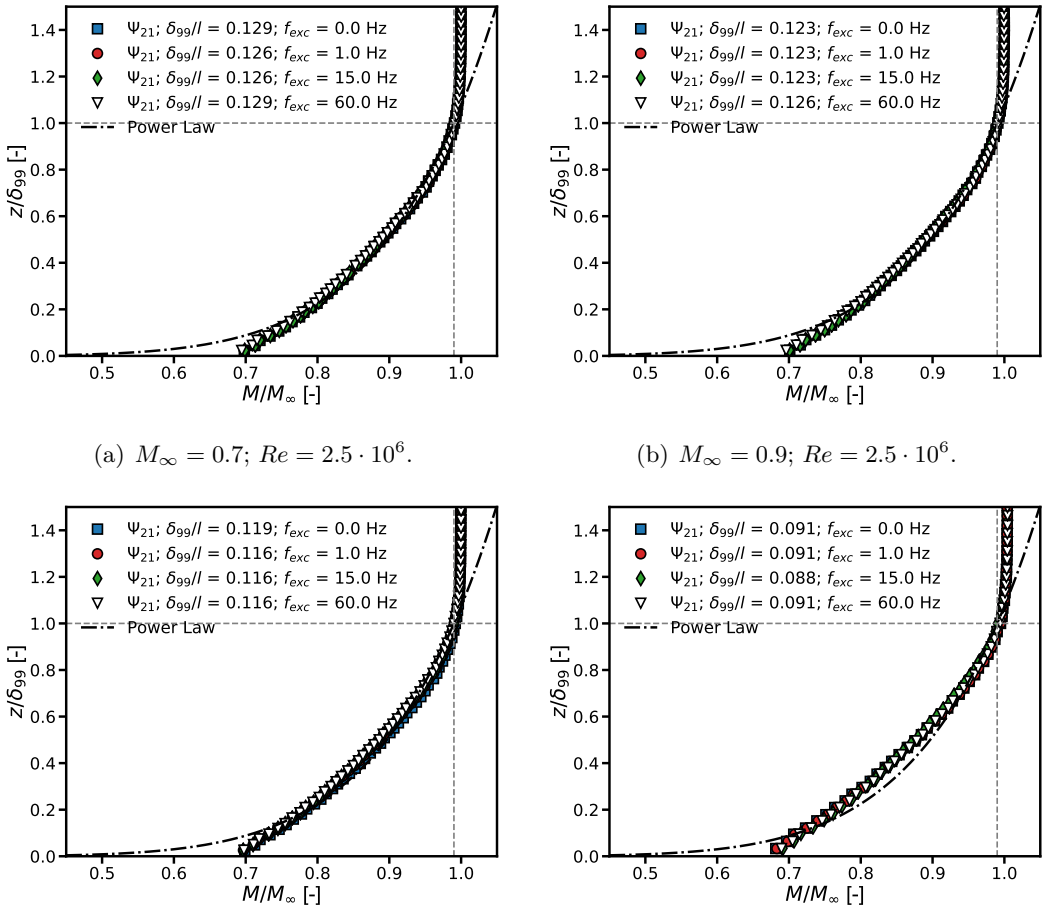

(a) $M_\infty = 0.7$; $Re = 2.5 \cdot 10^6$.

(b) $M_\infty = 0.9$; $Re = 2.5 \cdot 10^6$.

(c) $M_\infty = 1.05$; $Re = 2.5 \cdot 10^6$.

(d) $M_\infty = 1.2$; $Re = 2.5 \cdot 10^6$.

Figure D.5.: Excitation frequency influence on boundary layer velocity profile; $Re = 2.5 \cdot 10^6$; $\hat{A} = 1.2$ mm; Ψ_{21} model.

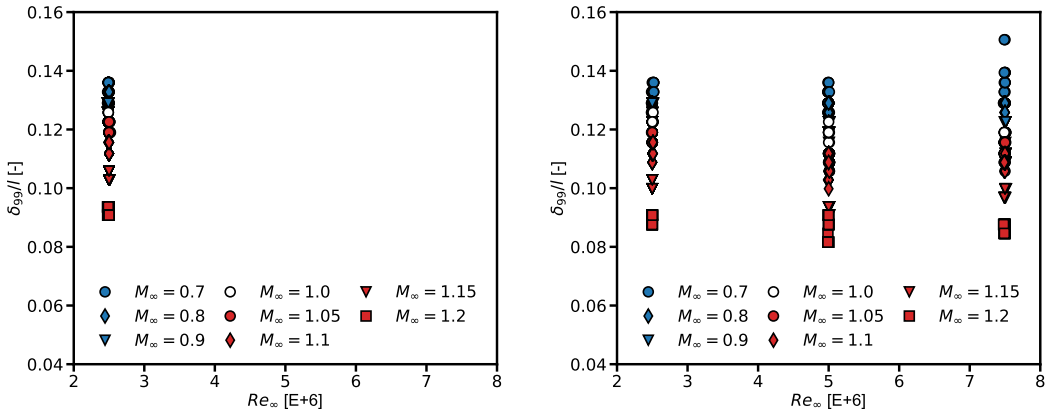

(a) Ψ_{11} model (First Test Campaign). (b) Ψ_{21} model.

Figure D.6.: Boundary layer thickness vs. Reynolds number.

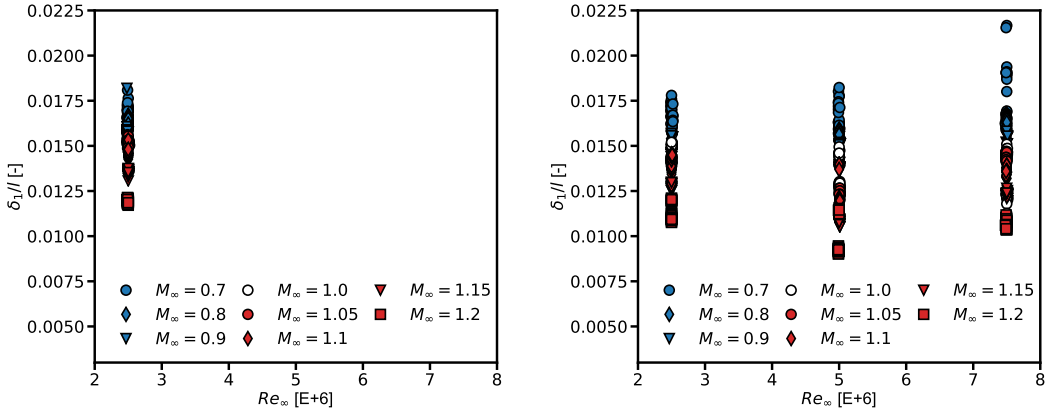

(a) Ψ_{11} model (First Test Campaign). (b) Ψ_{21} model.

Figure D.7.: Boundary layer displacement thickness vs. Reynolds number.

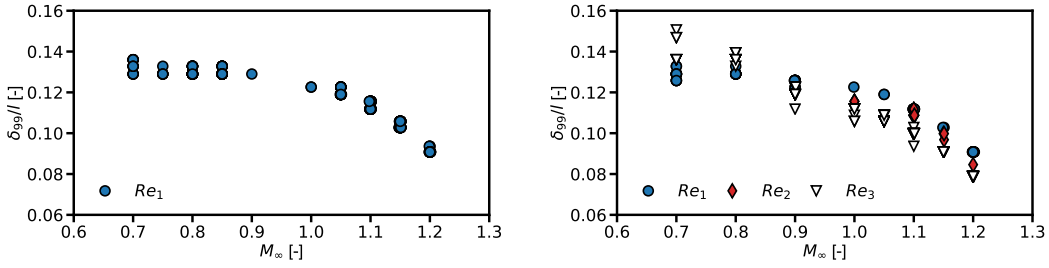

(a) Ψ_{11} model (First Test Campaign). (b) Ψ_{11} model (Second Test Campaign).

Figure D.8.: Boundary layer thickness vs. Mach number.

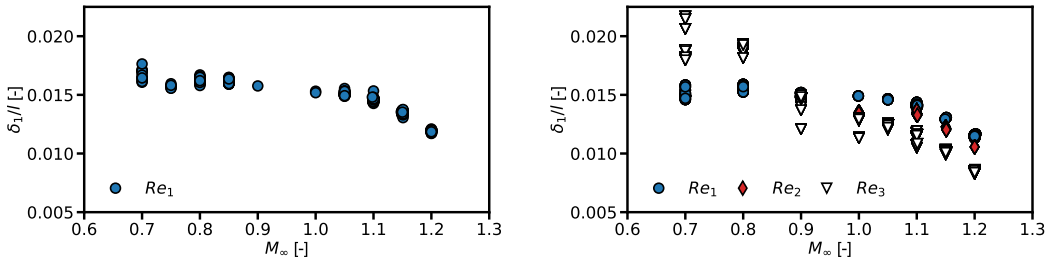

(a) Ψ_{11} model (First Test Campaign). (b) Ψ_{21} model (Second Test Campaign).

Figure D.9.: Boundary layer displacement thickness vs. Mach number.

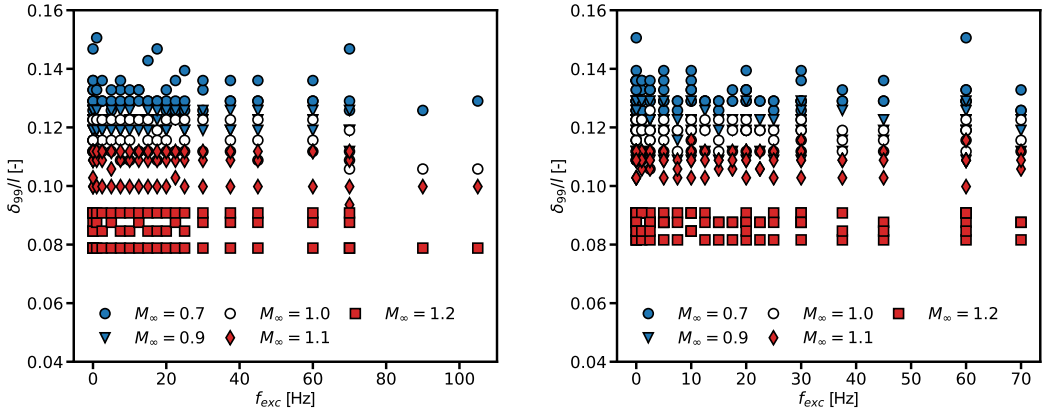

(a) Ψ_{11} model (First Test Campaign). (b) Ψ_{21} model.

Figure D.10.: Boundary layer thickness vs. excitation frequency.

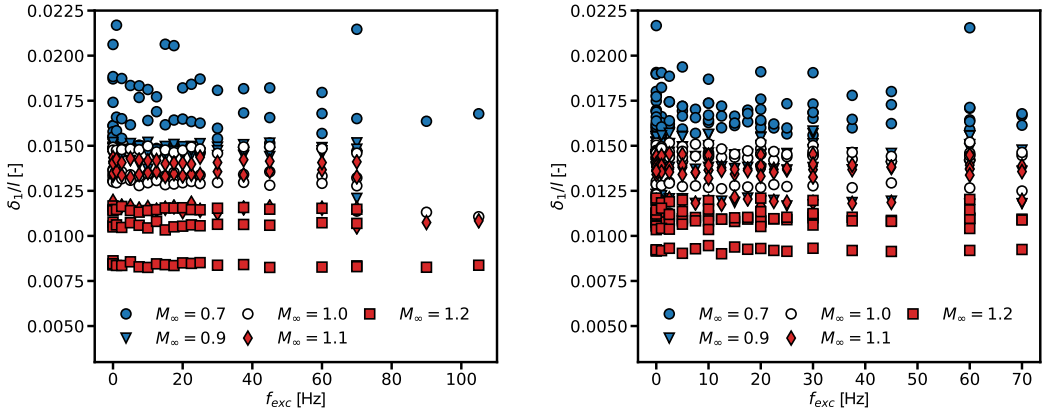

(a) Ψ_{11} model (First Test Campaign). (b) Ψ_{21}.

Figure D.11.: Boundary layer displacement thickness vs. excitation frequency.

Deformation

Model	M_∞ [-]	Re [10^6]	$\hat{A}$ [mm]	f_{exc} [Hz]	U_∞ [m/s]	p_0 [Pa]	k [-]
Ψ_{11}	1.2	5.0	1.8	1.0	422.7	69126.2	0.01
(2017)	1.2	5.0	1.8	15.0	422.35	69107.5	0.11
	1.2	5.0	1.8	30.0	421.93	69066.4	0.22
Ψ_{21}	1.2	5.0	1.2	1.0	421.6	68807.5	0.01
	1.2	5.0	1.2	15.0	422.44	68801.5	0.11
	1.2	5.0	1.2	30.0	421.6	68778.1	0.22

Table D.1.: Measurement points presented for validation of applied deformation technique; Supersonic flow.

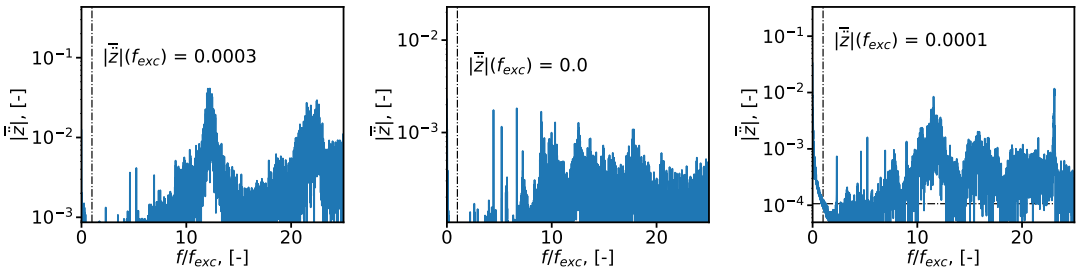

(a) $M_\infty = 0.8$; Panel; Sensor 1. (b) $M_\infty = 0.75$; Frame; Sensor 5. (c) $M_\infty = 0.8$; Camera; Sensor 5.

Figure D.12.: Ψ_{11}; $f_{exc} = 0.0$ Hz; $Re = 2.5 \cdot 10^6$; Acceleration; FFT; The reference excitation frequency used for division is $f_{exc} = 9.375$ Hz.

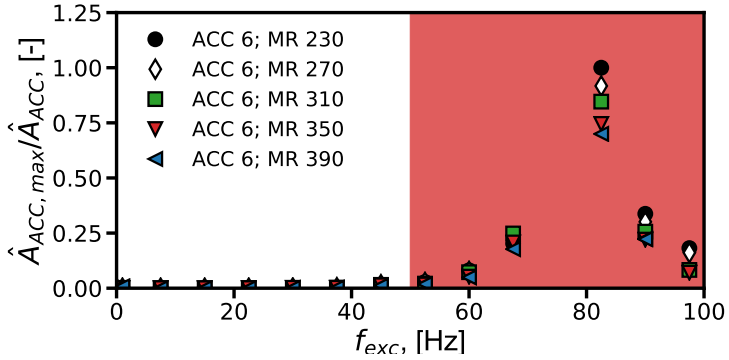

Figure D.13.: Qualitative rise of the $f/f_{exc} = 1.0$ acceleration component over the applied excitation frequencies.

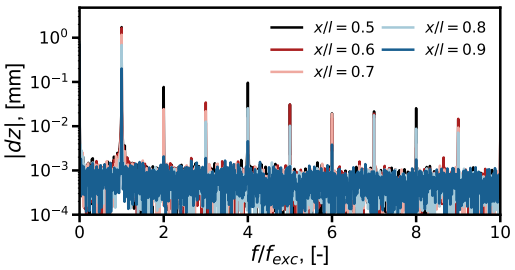

(a) $M_\infty = 1.2$; $f_{exc.} = 1.0$ Hz; $Re = 5.0 \cdot 10^6$.

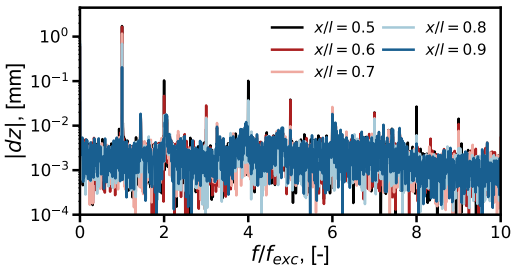

(b) $M_\infty = 1.2$; $f_{exc.} = 15.0$ Hz; $Re = 5.0 \cdot 10^6$.

Figure D.14.: Spectra of SPR measured absolute deformations $|dz|$; Ψ_{11} model.

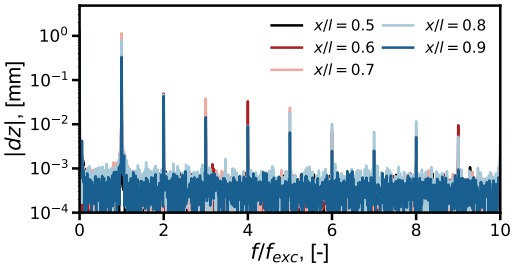

(a) $M_\infty = 1.2$; $f_{exc.} = 1.0$Hz; $Re = 5.0 \cdot 10^6$.

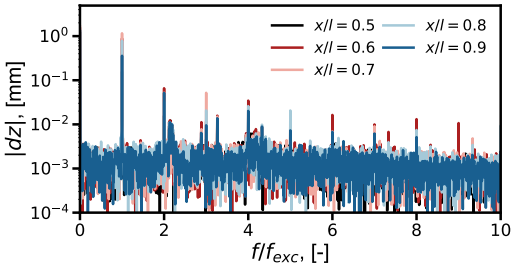

(b) $M_\infty = 1.2$; $f_{exc.} = 15.0$Hz; $Re = 5.0 \cdot 10^6$.

Figure D.15.: Spectra of SPR measured absolute deformations $|dz|$; Ψ_{21} model.

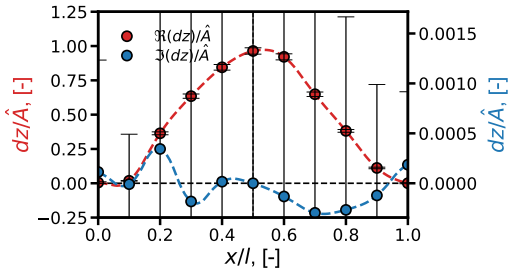

(a) $M_\infty = 1.2$; $f_{exc.} = 1.0$Hz; $Re = 5.0E + 6$.

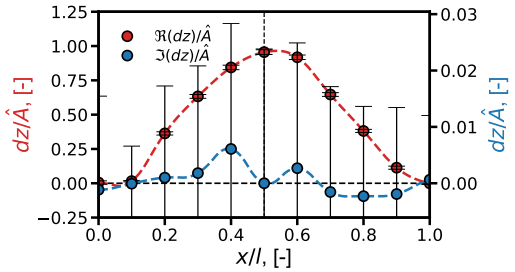

(b) $M_\infty = 1.2$; $f_{exc.} = 15.0$Hz; $Re = 5.0E + 6$.

Figure D.16.: Deformation measurements with error bars at $y/w = 0.5$; Ψ_{11} model.

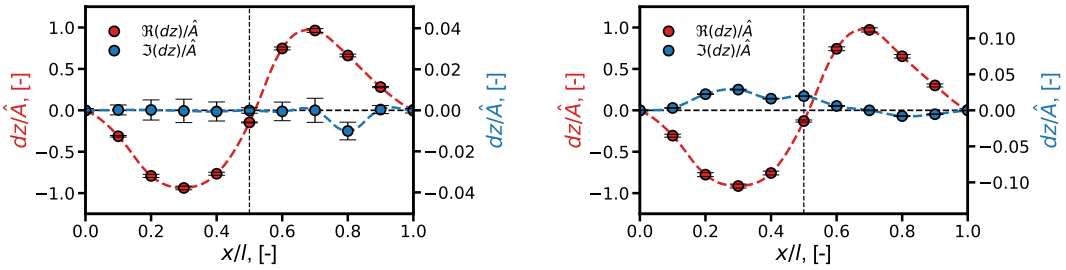

(a) $M_\infty = 1.2$; $f_{exc.} = 1.0$ Hz; $Re = 5.0 \cdot 10^6$. (b) $M_\infty = 1.2$; $f_{exc.} = 15.0$ Hz; $Re = 5.0 \cdot 10^6$.

Figure D.17.: Deformation measurements with error bars at $y/w = 0.5$; Ψ_{21} model.

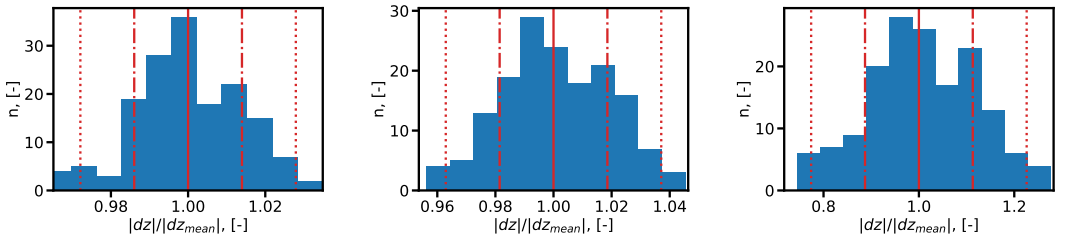

(a) Marker at $x_1/l_i = 0.5$, $y/w_i = 0.5$. (b) Marker at $x_3/l_i = 0.7$, $y/w_i = 0.5$. (c) Marker at $x_5/l_i = 0.9$, $y/w_i = 0.5$.

Figure D.18.: Histograms of measured deflection scattering; $M_\infty = 1.2$; $f_{exc.} = 15.0$ Hz; $Re = 5.0 \cdot 10^6$; Ψ_{11} model.

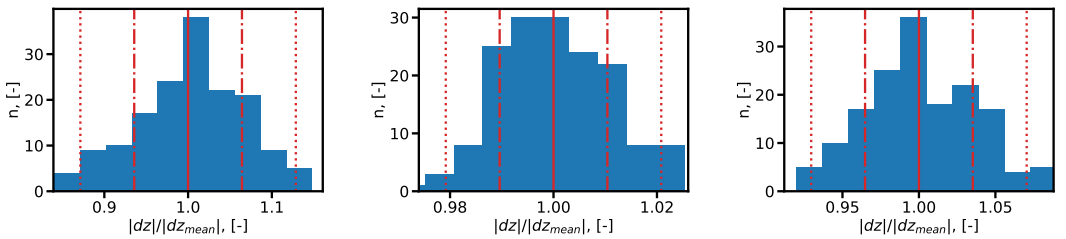

(a) Marker at $x_1/l_i = 0.5$, $y/w_i = 0.5$. (b) Marker at $x_3/l_i = 0.7$, $y/w_i = 0.5$. (c) Marker at $x_5/l_i = 0.9$, $y/w_i = 0.5$.

Figure D.19.: Histograms of measured deflection scattering; $M_\infty = 1.2$; $f_{exc.} = 15.0$ Hz; $Re = 5.0 \cdot 10^6$; Ψ_{21} model.

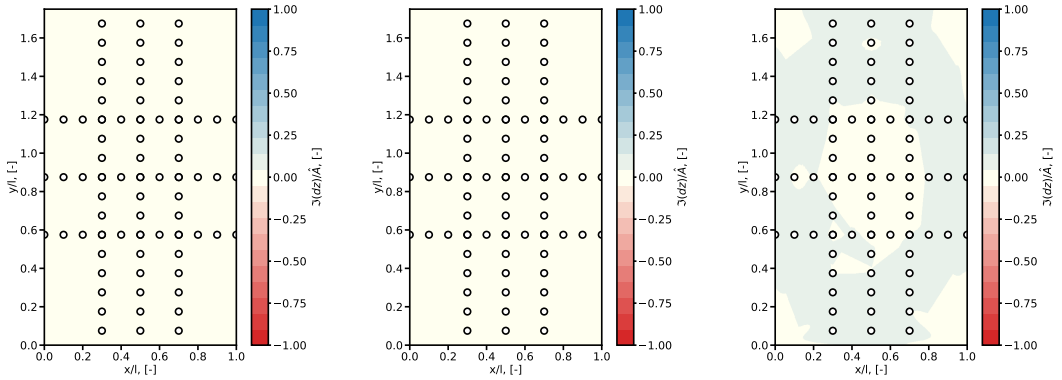

(a) $f_{exc} = 1.0$ Hz. (b) $f_{exc} = 15.0$ Hz. (c) $f_{exc} = 30.0$ Hz.

Figure D.20.: Imaginary part of structural deformation; Influence of excitation frequency at subsonic flow conditions; $M_\infty = 1.2$; $Re = 5.0 \cdot 10^6$; $\hat{A} = 1.8$ mm; Ψ_{11} model.

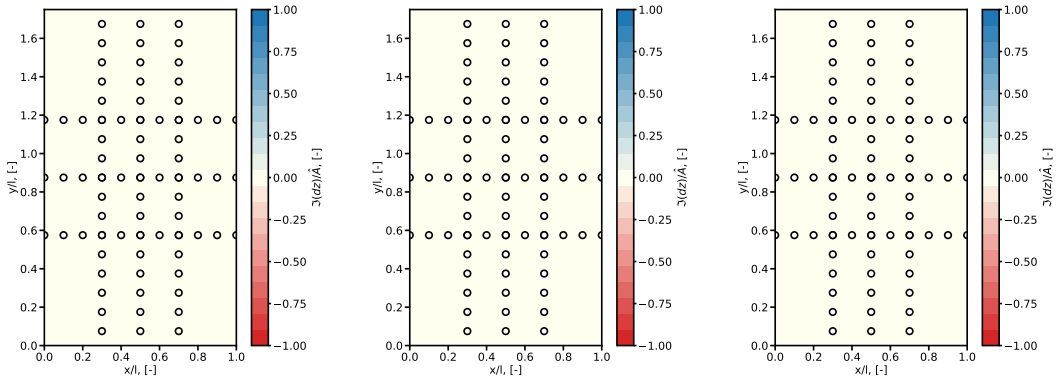

(a) $f_{exc} = 1.0$ Hz (b) $f_{exc} = 15.0$ Hz (c) $f_{exc} = 30.0$ Hz

Figure D.21.: Imaginary part of structural deformation; Influence of excitation frequency at subsonic flow conditions; $M_\infty = 1.2$; $Re = 5.0 \cdot 10^6$; $\hat{A} = 1.2$ mm; Ψ_{21} model.

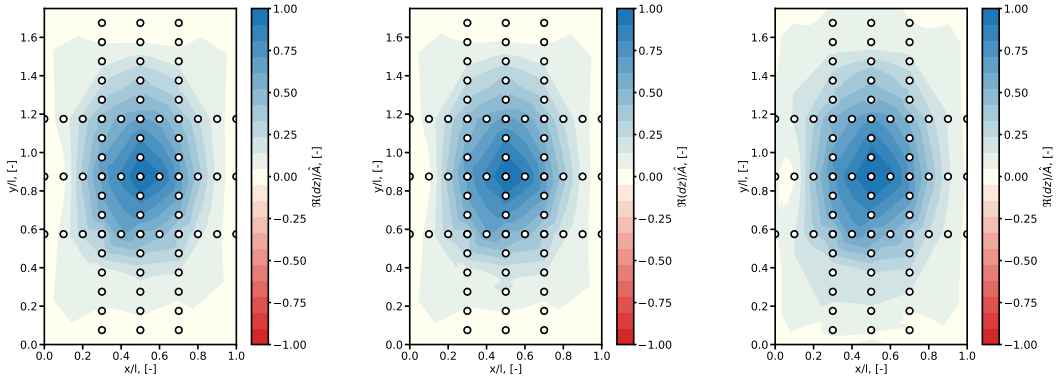

(a) $f_{exc} = 1.0$ Hz (b) $f_{exc} = 15.0$ Hz (c) $f_{exc} = 30.0$ Hz

Figure D.22.: Real part of measured deflection; Influence of excitation frequency at subsonic flow conditions; Measured results at $M_\infty = 1.2$; $Re = 5.0 \cdot 10^6$; $\hat{A} = 1.8$ mm; Ψ_{11} model.

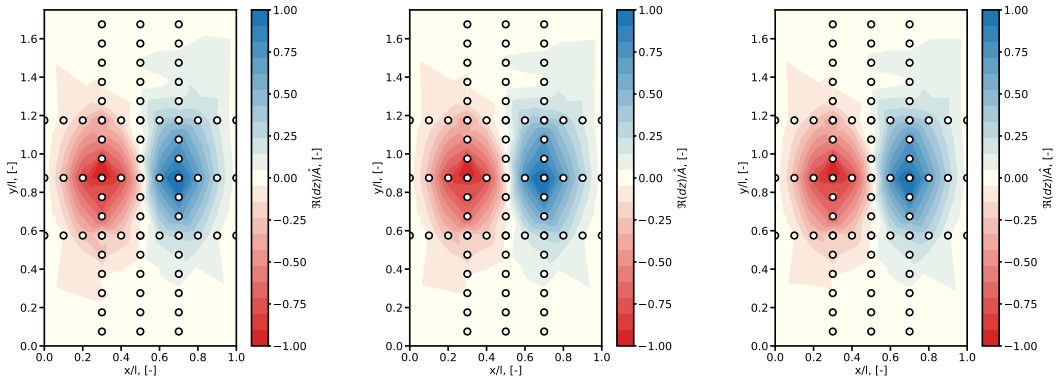

(a) $f_{exc} = 1.0$ Hz (b) $f_{exc} = 15.0$ Hz (c) $f_{exc} = 30.0$ Hz

Figure D.23.: Real part of measured deflection; Influence of excitation frequency at subsonic flow conditions; Measured results at $M_\infty = 1.2$; $Re = 5.0 \cdot 10^6$; $\hat{A} = 1.2$ mm; Ψ_{21} model.

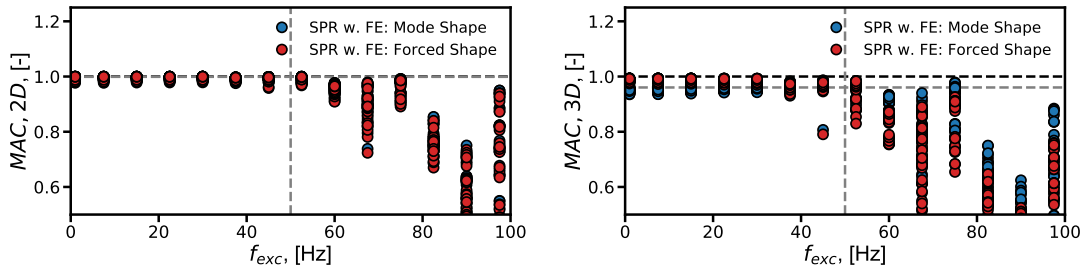

(a) Ψ_{11} model (2015); $y/w_i = 0.5$ section.

(b) Ψ_{11} model (2015); Full data set.

Figure D.24.: Correlation of measured and calculated structural shapes due to FE forced displacement and FE mode shape data.

Pressure

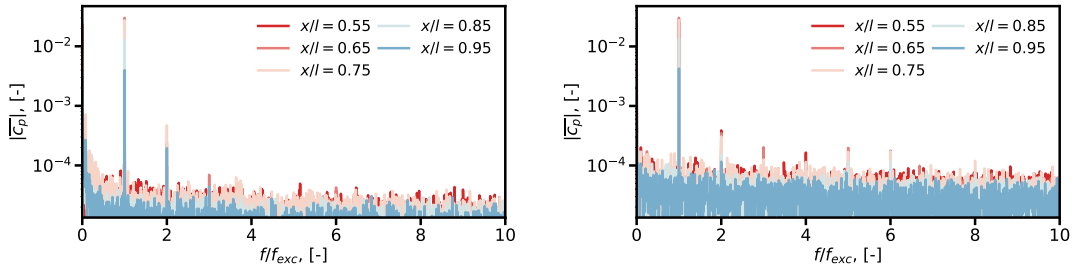

(a) $M_\infty = 1.2$; $f_{exc.} = 1.0$ Hz; $Re = 5.0 \cdot 10^6$. (b) $M_\infty = 1.2$; $f_{exc.} = 15.0$ Hz; $Re = 5.0 \cdot 10^6$.

Figure D.25.: Spectra of pressure measurements; Ψ_{11} model.

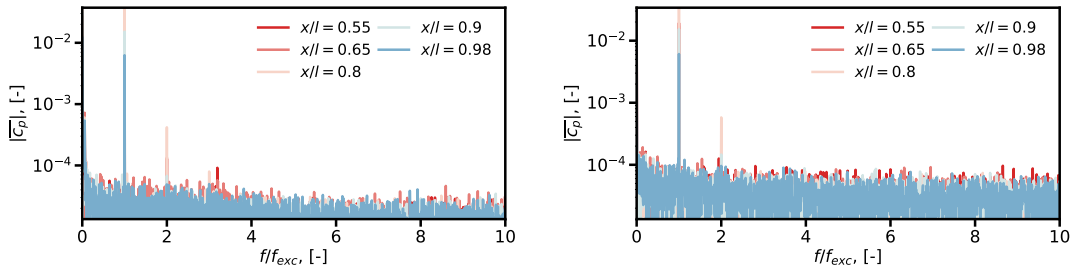

(a) $M_\infty = 1.2$; $f_{exc.} = 1.0$ Hz; $Re = 5.0 \cdot 10^6$. (b) $M_\infty = 1.2$; $f_{exc.} = 15.0$ Hz; $Re = 5.0 \cdot 10^6$.

Figure D.26.: Spectra of pressure measurements; Ψ_{21} model.

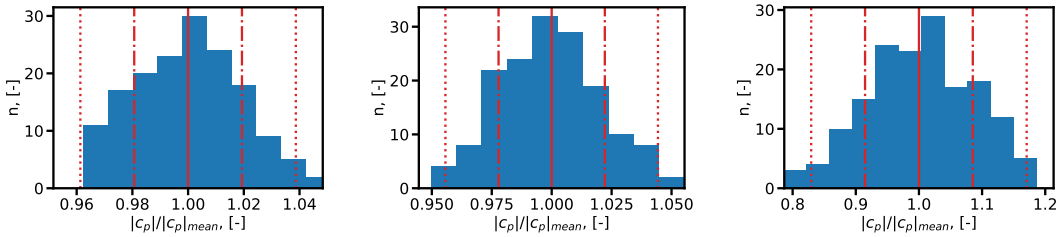

(a) Sensor at $x_1/l_i = 0.55$, $y/w_i = 0.5$. (b) Sensor at $x_3/l_i = 0.75$, $y/w_i = 0.5$. (c) Sensor at $x_5/l_i = 0.95$, $y/w_i = 0.5$.

Figure D.27.: Histograms of measured pressure amplitude scattering; $M_\infty = 1.2$; $f_{exc.} = 15.0$ Hz; $Re = 5.0$; Ψ_{11} model.

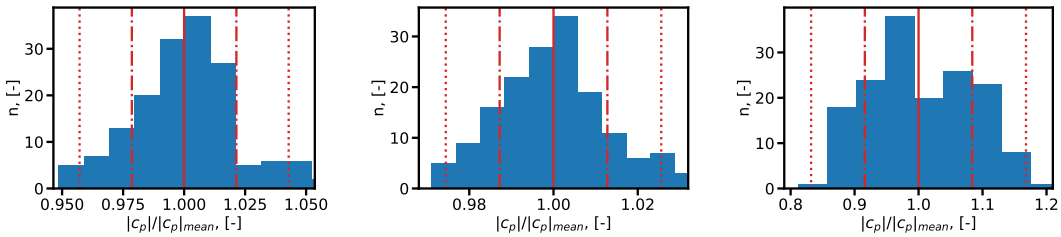

(a) Sensor at $x_1/l_i = 0.55$, $y/w_i = 0.5$. (b) Sensor at $x_3/l_i = 0.75$, $y/w_i = 0.5$. (c) Sensor at $x_5/l_i = 0.95$, $y/w_i = 0.5$.

Figure D.28.: Histograms of measured pressure amplitude scattering; $M_\infty = 1.2$; $f_{exc.} = 15.0$ Hz; $Re = 5.0$; Ψ_{21} model.

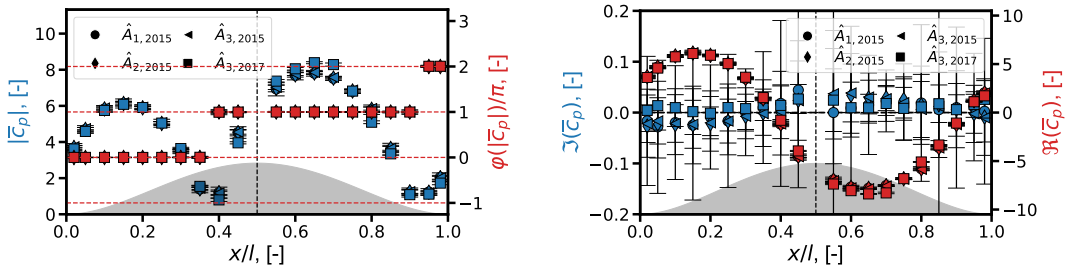

(a) Absolute values values and phase angles. (b) Real and imaginary parts.

Figure D.29.: Dependency on excitation amplitude and reproducability of results; $y/w_i = 0.5$; $M_\infty = 1.2$; $f_{exc} = 1$ Hz; $Re = 2.5 \cdot 10^6$; Ψ_{11} model.

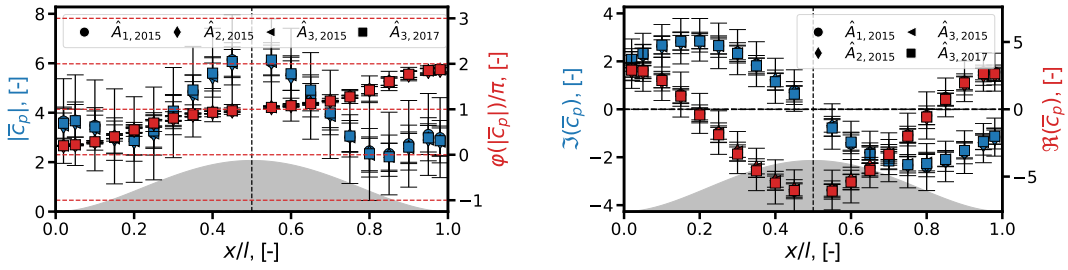

(a) Absolute values values and phase angles. (b) Real and imaginary parts.

Figure D.30.: Dependency on excitation amplitude and reproducability of results; $y/w_i = 0.5$; $M_\infty = 0.7$; $f_{exc} = 60$ Hz; $Re = 2.5 \cdot 10^6$; Ψ_{11} model.

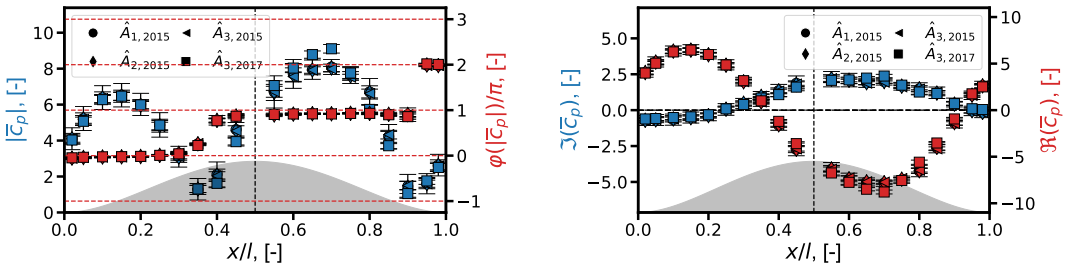

(a) Absolute values values and phase angles.

(b) Real and imaginary parts.

Figure D.31.: Dependency on excitation amplitude and reproducability of results; $y/w_i = 0.5$; $M_\infty = 1.2$; $f_{exc} = 60$ Hz; $Re = 2.5E + 6$; Ψ_{11} model.

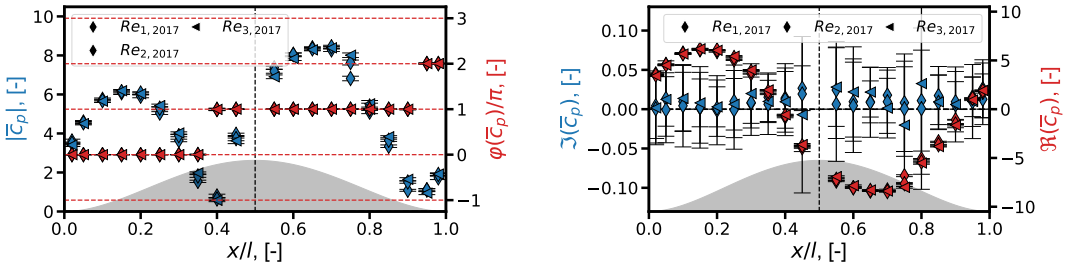

(a) Absolute values values and phase angles.

(b) Real and imaginary parts.

Figure D.32.: Reynolds number influence; $M_\infty = 1.2$; $f_{exc} = 1$ Hz; Ψ_{11} model.

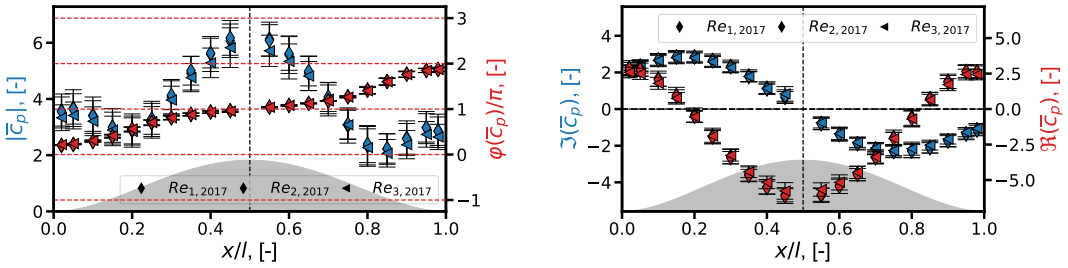

(a) Absolute values values and phase angles.

(b) Real and imaginary parts.

Figure D.33.: Reynolds number influence; $M_\infty = 0.7$; $f_{exc} = 60$ Hz; Ψ_{11} model.

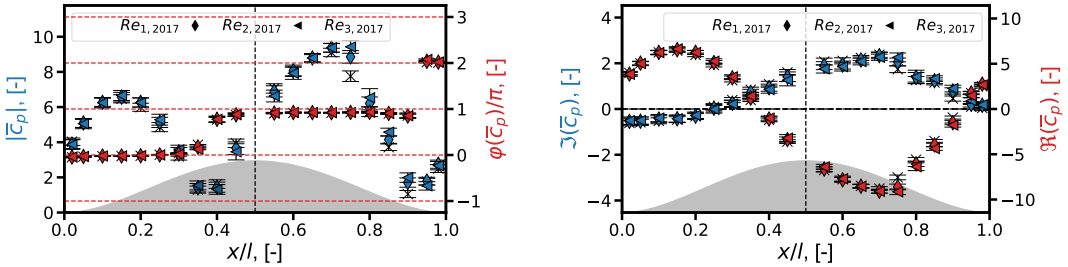

(a) Absolute values values and phase angles.

(b) Real and imaginary parts.

Figure D.34.: Reynolds number influence; $M_\infty = 1.2$; $f_{exc} = 60$ Hz; Ψ_{11} model.

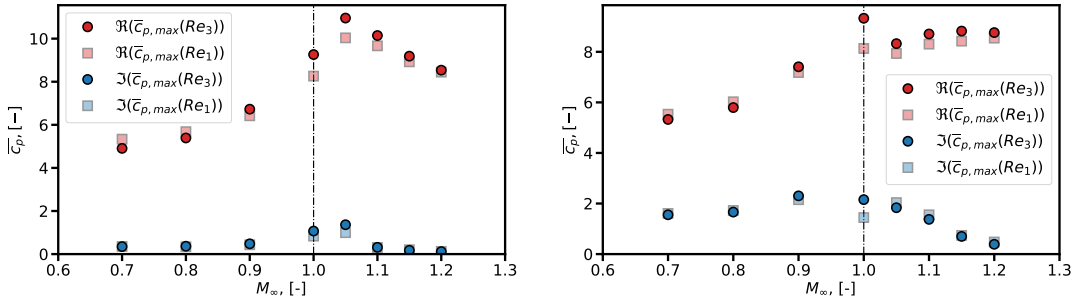

(a) $f_{exc} = 10$ Hz.

(b) $f_{exc} = 45$ Hz.

Figure D.35.: Reynolds number influence on the pressure versus free stream Mach number; Ψ_{11} model (2017).

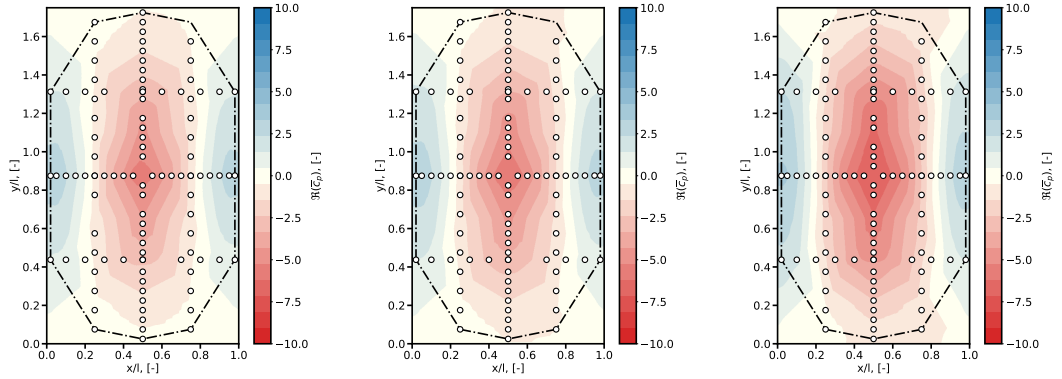

(a) Real part; $f_{exc} = 1.0$ Hz.

(b) Real part; $f_{exc} = 30.0$ Hz.

(c) Real part; $f_{exc} = 60.0$ Hz.

Figure D.36.: Influence of excitation frequency at subsonic flow conditions; $M_\infty = 0.8$; $Re = 5.0 \cdot 10^6$; $\hat{A} = 1.8$ mm; Ψ_{11} model.

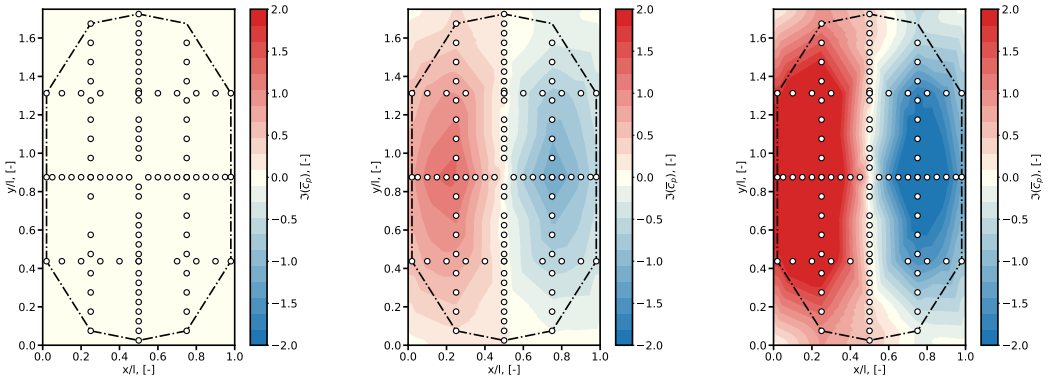

(a) Imag. part; $f_{exc} = 1.0$ Hz (b) Imag. part; $f_{exc} = 30.0$ Hz (c) Imag. part; $f_{exc} = 60.0$ Hz

Figure D.37.: Influence of excitation frequency at subsonic flow conditions; $M_\infty = 0.8$; $Re = 5.0 \cdot 10^6$; $\hat{A} = 1.8$ mm; Ψ_{11} model.

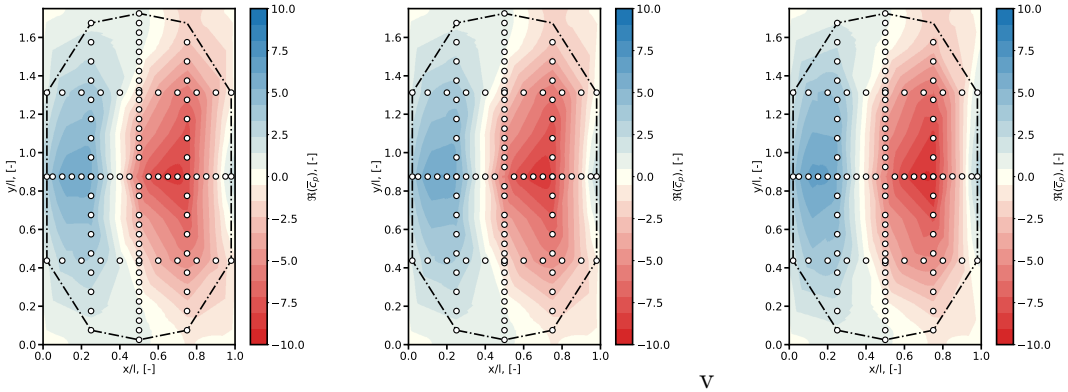

(a) Real part; $f_{exc} = 1.0$ Hz (b) Real part; $f_{exc} = 30.0$ Hz (c) Real part; $f_{exc} = 60.0$ Hz

Figure D.38.: Influence of excitation frequency at supersonic flow conditions; $M_\infty = 1.2$; $Re = 5.0 \cdot 10^6$; $\hat{A}_N = 1.8$ mm; Ψ_{11} model.

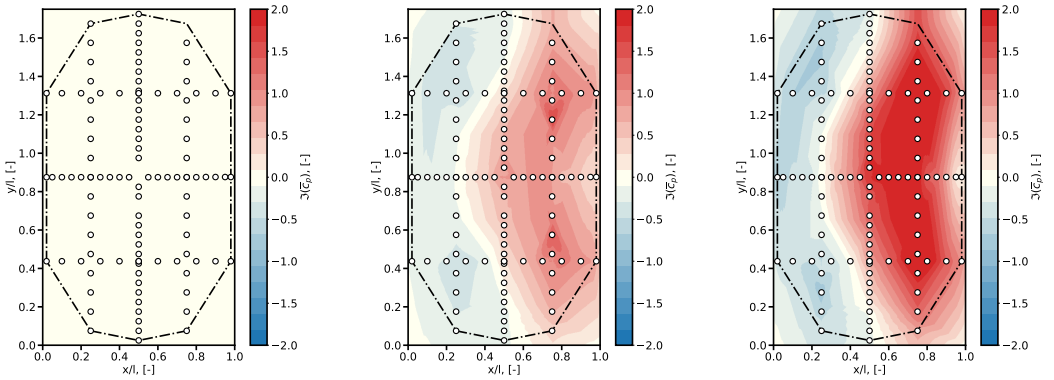

(a) Imag. part; $f_{exc} = 1.0$ Hz (b) Imag. part; $f_{exc} = 30.0$ Hz (c) Imag. part; $f_{exc} = 60.0$ Hz

Figure D.39.: Influence of excitation frequency at supersonic flow conditions; $M_\infty = 1.2$; $Re = 5.0E \cdot 10^6$; $\hat{A}_N = 1.8$ mm; Ψ_{11} model.

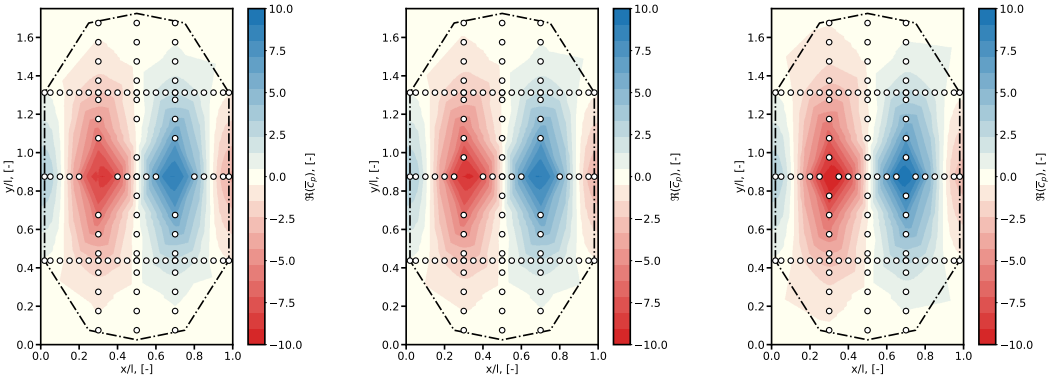

(a) Abs. values; $f_{exc} = 1.0$ Hz (b) Abs. values; $f_{exc} = 30.0$ Hz (c) Abs. values; $f_{exc} = 60.0$ Hz

Figure D.40.: Influence of excitation frequency at supersonic flow conditions; $M_\infty = 1.2$; $Re = 5.0 \cdot 10^6$; $\hat{A}_N = 1.2$ mm; Ψ_{21} model.

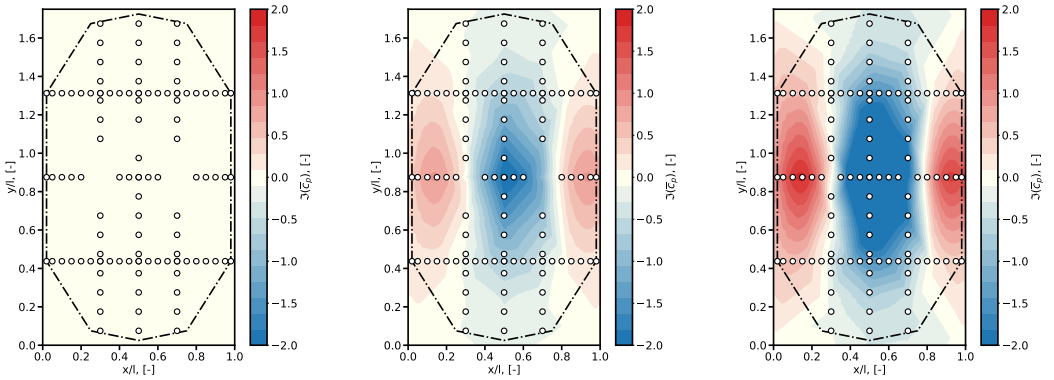

(a) Phase angles; $f_{exc} = 1.0$ Hz (b) Phase angles; $f_{exc} = 30.0$ Hz (c) Phase angles; $f_{exc} = 60.0$ Hz

Figure D.41.: Influence of excitation frequency at supersonic flow conditions; $M_\infty = 1.2$; $Re = 5.0 \cdot 10^6$; $\hat{A}_N = 1.2$ mm; Ψ_{21} model.

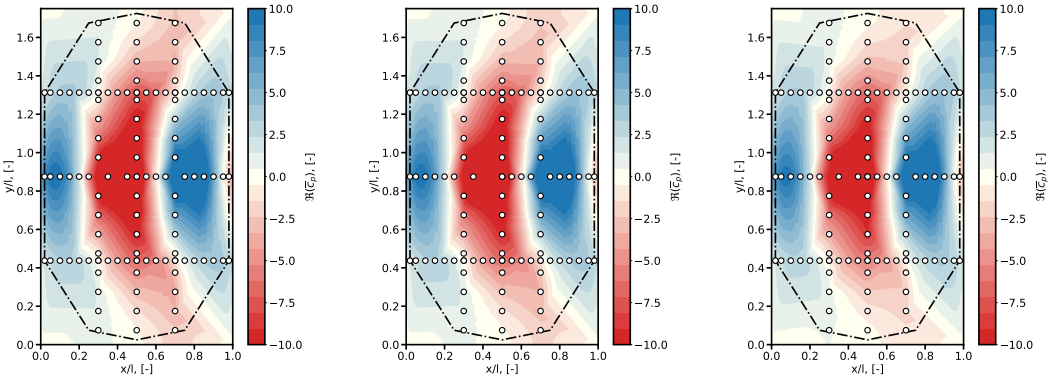

(a) Abs. values; $f_{exc} = 1.0$ Hz (b) Abs. values; $f_{exc} = 30.0$ Hz (c) Abs. values; $f_{exc} = 60.0$ Hz

Figure D.42.: Influence of excitation frequency at supersonic flow conditions; $M_\infty = 1.2$; $Re = 5.0 \cdot 10^6$; $\hat{A}_N = 1.2$ mm; Ψ_{21} model.

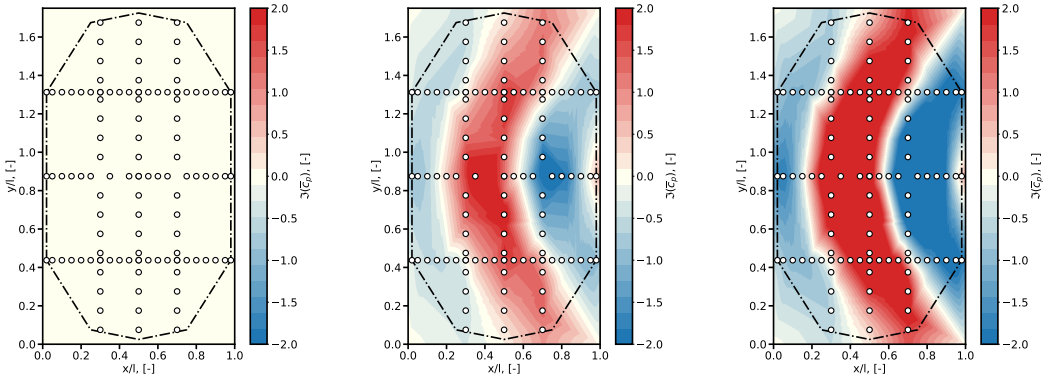

(a) Phase angles; $f_{exc} = 1.0$ Hz (b) Phase angles; $f_{exc} = 30.0$ Hz (c) Phase angles; $f_{exc} = 60.0$ Hz

Figure D.43.: Influence of excitation frequency at supersonic flow conditions; $M_\infty = 1.2$; $Re = 5.0 \cdot 10^6$; $\hat{A}_N = 1.2$ mm; Ψ_{21} model.

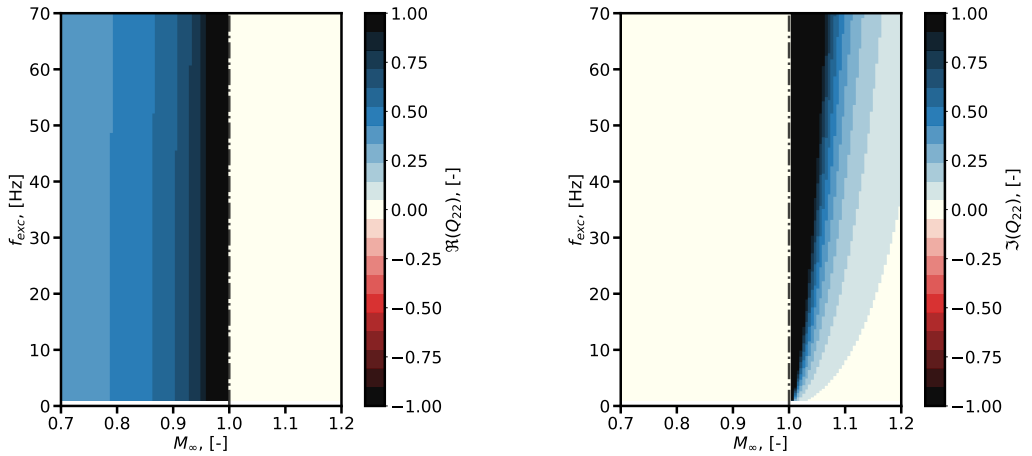

(a) Ψ_{21}; Real part. (b) Ψ_{21}; Imaginary part.

Figure D.44.: Resulting GAFs of theoretical approaches.

GAF

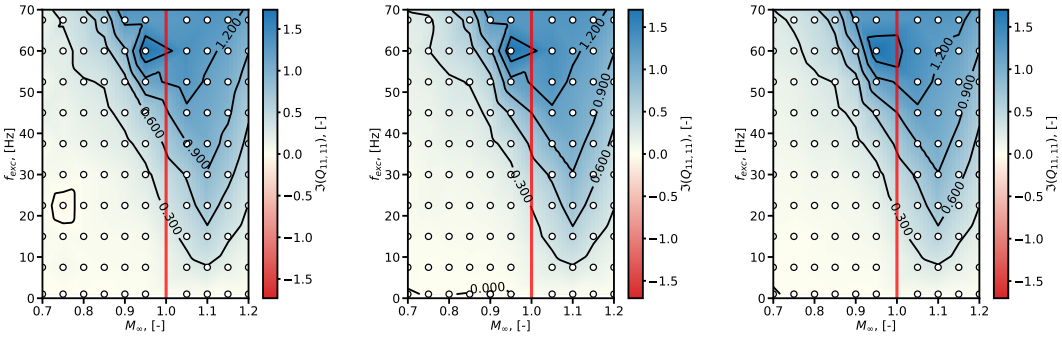

(a) Re_1; $\hat{A}_1$. (b) Re_1; $\hat{A}_2$. (c) Re_1; $\hat{A}_3$.

Figure D.45.: GAF (Imag) as a function of f_{exc} and M_∞; Ψ_{11} model; 2015.

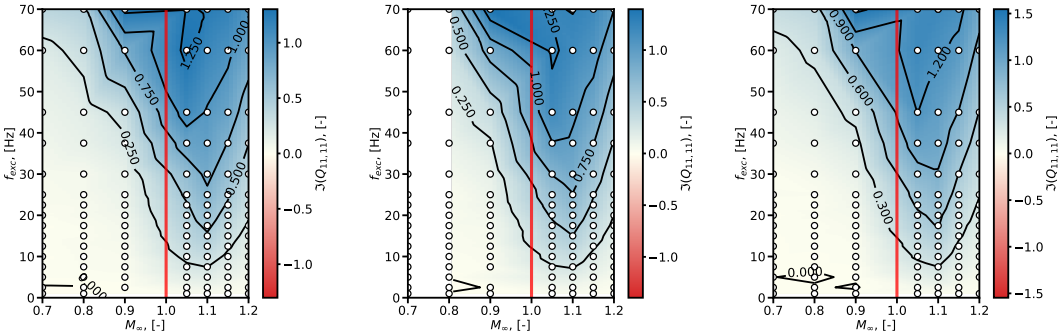

(a) Re_1; $\hat{A}_3$. (b) Re_2; $\hat{A}_3$. (c) Re_3; $\hat{A}_3$.

Figure D.46.: GAF (Imag) as a function of f_{exc} and M_∞; Ψ_{11} model; 2017.

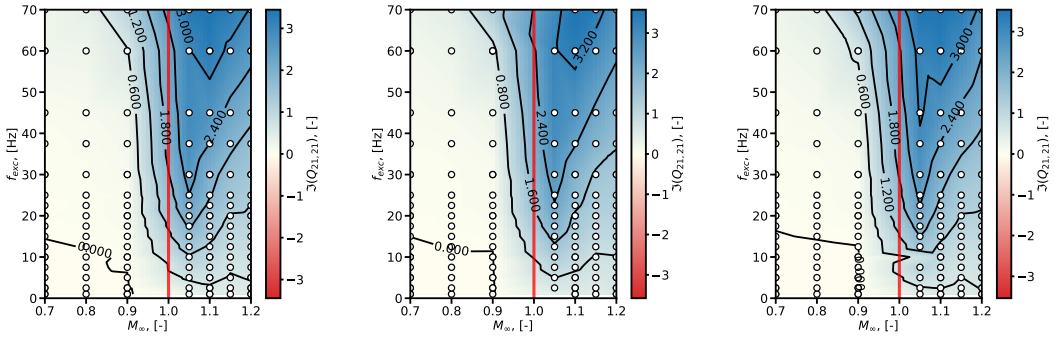

(a) Re_1; $\hat{A}_2$. (b) Re_2; $\hat{A}_2$. (c) Re_3; $\hat{A}_2$.

Figure D.47.: GAF (Imag) as a function of f_{exc} and M_∞; Ψ_{21} model.

E. List of Pressure Transducer Positions

No.	y [mm]	x [mm]	No.	y [mm]	x [mm]	No.	y [mm]	x [mm]
1	-425	0	37	0	200	73	-300	-125
2	-400	0	38	0	175	74	-250	-125
3	-375	0	39	0	150	75	-200	-125
4	-350	0	40	0	125	76	-150	-125
5	-325	0	41	0	100	77	-100	-125
6	-300	0	42	0	75	78	-50	-125
7	-275	0	43	0	50	79	50	-125
8	-25	0	44	0	25	80	100	-125
9	-225	0	45	0	-25	81	150	-125
10	-200	0	46	0	-50	82	200	-125
11	-175	0	47	0	-75	83	250	-125
12	-150	0	48	0	-100	84	300	-125
13	-125	0	49	0	-125	85	350	-125
14	-100	0	50	0	-150	86	400	-125
15	-75	0	51	0	-175	87	-218.75	240
16	-50	0	52	0	-200	88	-218.75	200
17	-25	0	53	0	-225	89	-218.75	150
18	25	0	54	0	-240	90	-218.75	100
19	50	0	55	-400	125	91	-218.75	50
20	75	0	56	-350	125	92	-218.75	0
21	100	0	57	-300	125	93	-218.75	-50
22	125	0	58	-250	125	94	-218.75	-100
23	150	0	59	-200	125	95	-218.75	-150
24	175	0	60	-150	125	96	-218.75	-200
25	200	0	61	-100	125	97	-218.75	-240
26	225	0	62	-50	125	98	218.75	240
27	250	0	63	50	125	99	218.75	200
28	275	0	64	100	125	100	218.75	150
29	300	0	65	150	125	101	218.75	100
30	325	0	66	200	125	102	218.75	50
31	350	0	67	250	125	103	218.75	0
32	375	0	68	300	125	104	218.75	-50
33	400	0	69	350	125	105	218.75	-100
34	425	0	70	400	125	106	218.75	-150
35	0	240	71	-400	-125	107	218.75	-200
36	0	225	72	-350	-125	108	218.75	-240

Table E.1.: Ψ_{11} model; $y = y_{panel}$-w/2 ; $x = x_{panel}$-l/2

No.	y [mm]	x [mm]	No.	y [mm]	x [mm]	No.	y [mm]	x [mm]
1	-400	100	37	-250	-100	73	0	200
2	-350	100	38	-200	-100	74	0	175
3	-300	100	39	-150	-100	75	0	150
4	-250	100	40	-100	-100	76	0	125
5	-200	100	41	-50	-100	77	0	75
6	-150	100	42	50	-100	78	0	50
7	-100	100	43	100	-100	79	0	25
8	-50	100	44	150	-100	80	0	-25
9	50	100	45	200	-100	81	0	-50
10	100	100	46	250	-100	82	0	-75
11	150	100	47	300	-100	83	0	-125
12	200	100	48	350	-100	84	0	-150
13	250	100	49	400	-100	85	0	-175
14	300	100	50	-218,75	240	86	0	-200
15	350	100	51	-218,75	225	87	0	-225
16	400	100	52	-218,75	200	88	0	-240
17	-400	0	53	-218,75	175	89	218,75	240
18	-350	0	54	-218,75	150	90	218,75	225
19	-300	0	55	-218,75	125	91	218,75	200
20	-250	0	56	-218,75	100	92	218,75	175
21	-200	0	57	-218,75	75	93	218,75	150
22	-150	0	58	-218,75	50	94	218,75	125
23	-100	0	59	-218,75	25	95	218,75	100
24	-50	0	60	-218,75	0	96	218,75	75
25	0	0	61	-218,75	-25	97	218,75	50
26	50	0	62	-218,75	-50	98	218,75	25
27	100	0	63	-218,75	-75	99	218,75	0
28	150	0	64	-218,75	-100	100	218,75	-25
29	200	0	65	-218,75	-125	101	218,75	-50
30	250	0	66	-218,75	-150	102	218,75	-75
31	300	0	67	-218,75	-175	103	218,75	-100
32	350	0	68	-218,75	-200	104	218,75	-125
33	400	0	69	-218,75	-225	105	218,75	-150
34	-400	-100	70	-218,75	-240	106	218,75	-175
35	-350	-100	71	0	240	107	218,75	-200
36	-300	-100	72	0	225	108	218,75	-225
						109	218,75	-240

Table E.2.: Ψ_{21} model; $y = y_{panel}$-w/2 ; $x = x_{panel}$-l/2

F. List of Measurement Points

M_∞	Re	$\hat{A}$	f_{exc}	MP
0.70	2.5	0.6	1.0	90002
0.70	2.5	0.6	7.5	90003
0.70	2.5	0.6	15.0	90004
0.70	2.5	0.6	22.5	90005
0.70	2.5	0.6	30.0	90006
0.70	2.5	0.6	37.5	90007
0.70	2.5	0.6	45.0	90008
0.70	2.5	0.6	52.5	90009
0.70	2.5	0.6	60.0	90010
0.70	2.5	0.6	67.5	90011
0.70	2.5	0.6	82.5	90015
0.70	2.5	0.6	90.0	90016
0.70	2.5	1.2	1.0	100002
0.70	2.5	1.2	7.5	100003
0.70	2.5	1.2	15.0	100004
0.70	2.5	1.2	22.5	100005
0.70	2.5	1.2	30.0	100006
0.70	2.5	1.2	37.5	100007
0.70	2.5	1.2	45.0	100008
0.70	2.5	1.2	52.5	100009
0.70	2.5	1.2	60.0	100010
0.70	2.5	1.2	67.5	100011
0.70	2.5	1.2	82.5	100013
0.70	2.5	1.2	90.0	100014
0.70	2.5	1.8	1.0	110002
0.70	2.5	1.8	7.5	110003
0.70	2.5	1.8	15.0	110004
0.70	2.5	1.8	22.5	110005
0.70	2.5	1.8	30.0	110006
0.70	2.5	1.8	37.5	110007
0.70	2.5	1.8	45.0	110008
0.70	2.5	1.8	60.0	110010
0.70	2.5	1.8	67.5	110011
0.70	2.5	1.8	82.5	110013
0.70	2.5	1.8	90.0	110014

M_∞	Re	$\hat{A}$	f_{exc}	MP
0.75	2.5	0.6	1.0	130002
0.75	2.5	0.6	7.5	130003
0.75	2.5	0.6	15.0	130004
0.75	2.5	0.6	22.5	130005
0.75	2.5	0.6	30.0	130006
0.75	2.5	0.6	37.5	130007
0.75	2.5	0.6	45.0	130008
0.75	2.5	0.6	52.5	130009
0.75	2.5	0.6	60.0	130010
0.75	2.5	0.6	67.5	130011
0.75	2.5	0.6	82.5	130013
0.75	2.5	0.6	90.0	130014
0.75	2.5	1.2	1.0	140002
0.75	2.5	1.2	7.5	140003
0.75	2.5	1.2	15.0	140004
0.75	2.5	1.2	22.5	140005
0.75	2.5	1.2	30.0	140006
0.75	2.5	1.2	37.5	140007
0.75	2.5	1.2	45.0	140008
0.75	2.5	1.2	52.5	140009
0.75	2.5	1.2	60.0	140010
0.75	2.5	1.2	67.5	140011
0.75	2.5	1.2	82.5	140013
0.75	2.5	1.2	90.0	140014
0.75	2.5	1.8	1.0	150002
0.75	2.5	1.8	7.5	150003
0.75	2.5	1.8	15.0	150004
0.75	2.5	1.8	22.5	150005
0.75	2.5	1.8	30.0	150006
0.75	2.5	1.8	37.5	150007
0.75	2.5	1.8	45.0	150008
0.75	2.5	1.8	52.5	150009
0.75	2.5	1.8	60.0	150010
0.75	2.5	1.8	67.5	150011
0.75	2.5	1.8	82.5	150013
0.75	2.5	1.8	90.0	150014

M_∞	Re	$\hat{A}$	f_{exc}	MP
0.80	2.5	0.6	1.0	170002
0.80	2.5	0.6	7.5	170003
0.80	2.5	0.6	15.0	170004
0.80	2.5	0.6	22.5	170005
0.80	2.5	0.6	30.0	170006
0.80	2.5	0.6	37.5	170007
0.80	2.5	0.6	45.0	170008
0.80	2.5	0.6	52.5	170009
0.80	2.5	0.6	60.0	170010
0.80	2.5	0.6	67.5	170011
0.80	2.5	0.6	82.5	170013
0.80	2.5	0.6	90.0	170014
0.80	2.5	1.2	1.0	180002
0.80	2.5	1.2	7.5	180003
0.80	2.5	1.2	15.0	180004
0.80	2.5	1.2	22.5	180005
0.80	2.5	1.2	30.0	180006
0.80	2.5	1.2	37.5	180007
0.80	2.5	1.2	45.0	180008
0.80	2.5	1.2	52.5	180009
0.80	2.5	1.2	60.0	180010
0.80	2.5	1.2	67.5	180011
0.80	2.5	1.2	82.5	180013
0.80	2.5	1.2	90.0	180014
0.80	2.5	1.8	1.0	190002
0.80	2.5	1.8	7.5	190003
0.80	2.5	1.8	15.0	190004
0.80	2.5	1.8	22.5	190005
0.80	2.5	1.8	30.0	190006
0.80	2.5	1.8	37.5	190007
0.80	2.5	1.8	45.0	190008
0.80	2.5	1.8	52.5	190009
0.80	2.5	1.8	60.0	190010
0.80	2.5	1.8	67.5	190011
0.80	2.5	1.8	82.5	190013
0.80	2.5	1.8	90.0	190014

M_∞	Re	$\hat{A}$	f_{exc}	MP
0.85	2.5	0.6	1.0	210002
0.85	2.5	0.6	7.5	210003
0.85	2.5	0.6	15.0	210004
0.85	2.5	0.6	22.5	210005
0.85	2.5	0.6	30.0	210006
0.85	2.5	0.6	37.5	210007
0.85	2.5	0.6	45.0	210008
0.85	2.5	0.6	52.5	210009
0.85	2.5	0.6	60.0	210010
0.85	2.5	0.6	67.5	210011
0.85	2.5	0.6	82.5	210013
0.85	2.5	0.6	90.0	210014
0.85	2.5	1.2	1.0	220002
0.85	2.5	1.2	7.5	220003
0.85	2.5	1.2	15.0	220004
0.85	2.5	1.2	22.5	220005
0.85	2.5	1.2	30.0	220006
0.85	2.5	1.2	37.5	220007
0.85	2.5	1.2	45.0	220008
0.85	2.5	1.2	52.5	220009
0.85	2.5	1.2	60.0	220010
0.85	2.5	1.2	67.5	220011
0.85	2.5	1.2	82.5	220013
0.85	2.5	1.2	90.0	220014
0.85	2.5	1.8	1.0	230002
0.85	2.5	1.8	7.5	230003
0.85	2.5	1.8	15.0	230004
0.85	2.5	1.8	22.5	230005
0.85	2.5	1.8	30.0	230006
0.85	2.5	1.8	37.5	230007
0.85	2.5	1.8	45.0	230008
0.85	2.5	1.8	52.5	230009
0.85	2.5	1.8	60.0	230010
0.85	2.5	1.8	67.5	230011
0.85	2.5	1.8	82.5	230013
0.85	2.5	1.8	90.0	230014

Table F.1.: List of Measurement Points; M_∞ [-]; Re [10E6]; $\hat{A}$ [mm]; f_{exc} [Hz]; Ψ_{11} model (2015); Table 1 of 3.

M_∞	Re	$\hat{A}$	f_{exc}	MP
0.90	2.5	0.6	1.0	250002
0.90	2.5	0.6	7.5	250003
0.90	2.5	0.6	15.0	250004
0.90	2.5	0.6	22.5	250005
0.90	2.5	0.6	30.0	250006
0.90	2.5	0.6	37.5	250007
0.90	2.5	0.6	45.0	250008
0.90	2.5	0.6	52.5	250009
0.90	2.5	0.6	60.0	250010
0.90	2.5	0.6	67.5	250011
0.90	2.5	0.6	82.5	250013
0.90	2.5	0.6	90.0	250014
0.90	2.5	1.2	1.0	260002
0.90	2.5	1.2	7.5	260004
0.90	2.5	1.2	15.0	260005
0.90	2.5	1.2	22.5	260006
0.90	2.5	1.2	30.0	260007
0.90	2.5	1.2	37.5	260008
0.90	2.5	1.2	45.0	260009
0.90	2.5	1.2	52.5	260010
0.90	2.5	1.2	60.0	260011
0.90	2.5	1.2	67.5	260012
0.90	2.5	1.2	82.5	260014
0.90	2.5	1.2	90.0	260015
0.90	2.5	1.8	1.0	270002
0.90	2.5	1.8	7.5	270003
0.90	2.5	1.8	15.0	270004
0.90	2.5	1.8	22.5	270005
0.90	2.5	1.8	30.0	270006
0.90	2.5	1.8	37.5	270007
0.90	2.5	1.8	45.0	270008
0.90	2.5	1.8	52.5	270009
0.90	2.5	1.8	60.0	270010
0.90	2.5	1.8	67.5	270011
0.90	2.5	1.8	82.5	270013
0.90	2.5	1.8	90.0	270014

M_∞	Re	$\hat{A}$	f_{exc}	MP
0.95	2.5	0.6	1.0	290002
0.95	2.5	0.6	7.5	290003
0.95	2.5	0.6	15.0	290004
0.95	2.5	0.6	22.5	290005
0.95	2.5	0.6	30.0	290006
0.95	2.5	0.6	37.5	290007
0.95	2.5	0.6	45.0	290008
0.95	2.5	0.6	52.5	290009
0.95	2.5	0.6	60.0	290010
0.95	2.5	0.6	67.5	290011
0.95	2.5	0.6	82.5	290013
0.95	2.5	0.6	90.0	290014
0.95	2.5	1.2	1.0	300002
0.95	2.5	1.2	7.5	300004
0.95	2.5	1.2	15.0	300005
0.95	2.5	1.2	22.5	300006
0.95	2.5	1.2	30.0	300007
0.95	2.5	1.2	37.5	300008
0.95	2.5	1.2	45.0	300009
0.95	2.5	1.2	52.5	300010
0.95	2.5	1.2	60.0	300011
0.95	2.5	1.2	67.5	300012
0.95	2.5	1.2	82.5	300014
0.95	2.5	1.2	90.0	300015
0.95	2.5	1.8	1.0	310002
0.95	2.5	1.8	7.5	310003
0.95	2.5	1.8	15.0	310004
0.95	2.5	1.8	22.5	310005
0.95	2.5	1.8	30.0	310006
0.95	2.5	1.8	37.5	310007
0.95	2.5	1.8	45.0	310008
0.95	2.5	1.8	52.5	310009
0.95	2.5	1.8	60.0	310010
0.95	2.5	1.8	67.5	310011
0.95	2.5	1.8	82.5	310013
0.95	2.5	1.8	90.0	310014

M_∞	Re	$\hat{A}$	f_{exc}	MP
1.0	2.5	0.6	1.0	330003
1.0	2.5	0.6	7.5	330004
1.0	2.5	0.6	15.0	330005
1.0	2.5	0.6	22.5	330006
1.0	2.5	0.6	30.0	330007
1.0	2.5	0.6	37.5	330008
1.0	2.5	0.6	45.0	330009
1.0	2.5	0.6	52.5	330010
1.0	2.5	0.6	60.0	330011
1.0	2.5	0.6	67.5	330012
1.0	2.5	0.6	82.5	330014
1.0	2.5	0.6	90.0	330015
1.0	2.5	1.2	1.0	340003
1.0	2.5	1.2	7.5	340004
1.0	2.5	1.2	15.0	340005
1.0	2.5	1.2	22.5	340006
1.0	2.5	1.2	30.0	340007
1.0	2.5	1.2	37.5	340008
1.0	2.5	1.2	45.0	340009
1.0	2.5	1.2	52.5	340010
1.0	2.5	1.2	60.0	340011
1.0	2.5	1.2	67.5	340012
1.0	2.5	1.2	82.5	340015
1.0	2.5	1.2	90.0	340016
1.0	2.5	1.8	1.0	350003
1.0	2.5	1.8	7.5	350004
1.0	2.5	1.8	15.0	350005
1.0	2.5	1.8	22.5	350006
1.0	2.5	1.8	30.0	350007
1.0	2.5	1.8	37.5	350008
1.0	2.5	1.8	45.0	350009
1.0	2.5	1.8	52.5	350010
1.0	2.5	1.8	60.0	350012
1.0	2.5	1.8	67.5	350013
1.0	2.5	1.8	82.5	350015
1.0	2.5	1.8	90.0	350016

M_∞	Re	$\hat{A}$	f_{exc}	MP
1.05	2.5	0.6	1.0	370003
1.05	2.5	0.6	7.5	370004
1.05	2.5	0.6	15.0	370005
1.05	2.5	0.6	22.5	370006
1.05	2.5	0.6	30.0	370007
1.05	2.5	0.6	37.5	370008
1.05	2.5	0.6	45.0	370009
1.05	2.5	0.6	52.5	370010
1.05	2.5	0.6	60.0	370011
1.05	2.5	0.6	67.5	370012
1.05	2.5	0.6	82.5	370014
1.05	2.5	0.6	90.0	370015
1.05	2.5	1.2	1.0	380003
1.05	2.5	1.2	7.5	380004
1.05	2.5	1.2	15.0	380005
1.05	2.5	1.2	22.5	380006
1.05	2.5	1.2	30.0	380007
1.05	2.5	1.2	37.5	380008
1.05	2.5	1.2	45.0	380009
1.05	2.5	1.2	52.5	380010
1.05	2.5	1.2	60.0	380011
1.05	2.5	1.2	67.5	380012
1.05	2.5	1.2	82.5	380014
1.05	2.5	1.2	90.0	380015
1.05	2.5	1.8	1.0	390003
1.05	2.5	1.8	7.5	390004
1.05	2.5	1.8	15.0	390005
1.05	2.5	1.8	22.5	390006
1.05	2.5	1.8	30.0	390007
1.05	2.5	1.8	37.5	390008
1.05	2.5	1.8	45.0	390009
1.05	2.5	1.8	52.5	390010
1.05	2.5	1.8	60.0	390011
1.05	2.5	1.8	67.5	390012
1.05	2.5	1.8	82.5	390014
1.05	2.5	1.8	90.0	390015

Table F.2.: List of Measurement Points; M_∞ [-]; Re [10E6]; $\hat{A}$ [mm]; f_{exc} [Hz]; Ψ_{11} model (2015); Table 2 of 3.

M_∞	Re	$\hat{A}$	f_{exc}	MP
1.1	2.5	0.6	1.0	410003
1.1	2.5	0.6	7.5	410004
1.1	2.5	0.6	15.0	410005
1.1	2.5	0.6	22.5	410006
1.1	2.5	0.6	30.0	410007
1.1	2.5	0.6	37.5	410008
1.1	2.5	0.6	45.0	410009
1.1	2.5	0.6	52.5	410010
1.1	2.5	0.6	60.0	410011
1.1	2.5	0.6	67.5	410012
1.1	2.5	0.6	82.5	410014
1.1	2.5	0.6	90.0	410015
1.1	2.5	1.2	1.0	420003
1.1	2.5	1.2	7.5	420004
1.1	2.5	1.2	15.0	420005
1.1	2.5	1.2	22.5	420006
1.1	2.5	1.2	30.0	420007
1.1	2.5	1.2	37.5	420008
1.1	2.5	1.2	45.0	420009
1.1	2.5	1.2	52.5	420010
1.1	2.5	1.2	60.0	420011
1.1	2.5	1.2	67.5	420012
1.1	2.5	1.2	82.5	420014
1.1	2.5	1.2	90.0	420015
1.1	2.5	1.8	1.0	430003
1.1	2.5	1.8	7.5	430004
1.1	2.5	1.8	15.0	430005
1.1	2.5	1.8	22.5	430006
1.1	2.5	1.8	30.0	430007
1.1	2.5	1.8	37.5	430008
1.1	2.5	1.8	45.0	430009
1.1	2.5	1.8	52.5	430010
1.1	2.5	1.8	60.0	430011
1.1	2.5	1.8	67.5	430012
1.1	2.5	1.8	82.5	430014
1.1	2.5	1.8	90.0	430015

M_∞	Re	$\hat{A}$	f_{exc}	MP
1.15	2.5	0.6	1.0	450003
1.15	2.5	0.6	7.5	450004
1.15	2.5	0.6	15.0	450005
1.15	2.5	0.6	22.5	450006
1.15	2.5	0.6	30.0	450007
1.15	2.5	0.6	37.5	450008
1.15	2.5	0.6	45.0	450009
1.15	2.5	0.6	52.5	450010
1.15	2.5	0.6	60.0	450011
1.15	2.5	0.6	67.5	450012
1.15	2.5	0.6	82.5	450014
1.15	2.5	0.6	90.0	450015
1.15	2.5	1.2	1.0	460003
1.15	2.5	1.2	7.5	460004
1.15	2.5	1.2	15.0	460005
1.15	2.5	1.2	22.5	460006
1.15	2.5	1.2	30.0	460007
1.15	2.5	1.2	37.5	460008
1.15	2.5	1.2	45.0	460009
1.15	2.5	1.2	52.5	460010
1.15	2.5	1.2	60.0	460011
1.15	2.5	1.2	67.5	460012
1.15	2.5	1.2	82.5	460014
1.15	2.5	1.2	90.0	460015
1.15	2.5	1.8	1.0	470003
1.15	2.5	1.8	7.5	470004
1.15	2.5	1.8	15.0	470005
1.15	2.5	1.8	22.5	470006
1.15	2.5	1.8	30.0	470007
1.15	2.5	1.8	37.5	470008
1.15	2.5	1.8	45.0	470009
1.15	2.5	1.8	52.5	470010
1.15	2.5	1.8	60.0	470011
1.15	2.5	1.8	67.5	470012
1.15	2.5	1.8	82.5	470014
1.15	2.5	1.8	90.0	470015

M_∞	Re	$\hat{A}$	f_{exc}	MP
1.2	2.5	0.6	1.0	490003
1.2	2.5	0.6	7.5	490004
1.2	2.5	0.6	15.0	490005
1.2	2.5	0.6	22.5	490006
1.2	2.5	0.6	30.0	490007
1.2	2.5	0.6	37.5	490008
1.2	2.5	0.6	45.0	490009
1.2	2.5	0.6	52.5	490010
1.2	2.5	0.6	60.0	490011
1.2	2.5	0.6	67.5	490012
1.2	2.5	0.6	82.5	490014
1.2	2.5	0.6	90.0	490015
1.2	2.5	1.2	1.0	500004
1.2	2.5	1.2	7.5	500005
1.2	2.5	1.2	15.0	500006
1.2	2.5	1.2	22.5	500007
1.2	2.5	1.2	30.0	500008
1.2	2.5	1.2	37.5	500009
1.2	2.5	1.2	45.0	500010
1.2	2.5	1.2	52.5	500011
1.2	2.5	1.2	60.0	500012
1.2	2.5	1.2	67.5	500013
1.2	2.5	1.2	82.5	500015
1.2	2.5	1.2	90.0	500016
1.2	2.5	1.8	1.0	510003
1.2	2.5	1.8	7.5	510004
1.2	2.5	1.8	15.0	510005
1.2	2.5	1.8	22.5	510006
1.2	2.5	1.8	30.0	510007
1.2	2.5	1.8	37.5	510009
1.2	2.5	1.8	45.0	510010
1.2	2.5	1.8	52.5	510011
1.2	2.5	1.8	60.0	510012
1.2	2.5	1.8	67.5	510013
1.2	2.5	1.8	82.5	510015
1.2	2.5	1.8	90.0	510016

Table F.3.: List of Measurement Points; M_∞ [-]; Re [10E6]; $\hat{A}$ [mm]; f_{exc} [Hz]; Ψ_{11} model (2015); Table 3 of 3.

M_∞	Re	$\hat{A}$	f_{exc}	MP
0.70	5.0	1.8	1.0	150004
0.70	5.0	1.8	2.5	150005
0.70	5.0	1.8	5.0	150006
0.70	5.0	1.8	7.5	150007
0.70	5.0	1.8	10.0	150008
0.70	5.0	1.8	12.5	150010
0.70	5.0	1.8	15.0	150011
0.70	5.0	1.8	17.5	150012
0.70	5.0	1.8	20.0	150013
0.70	5.0	1.8	22.5	150014
0.70	5.0	1.8	25.0	150015
0.70	5.0	1.8	30.0	150016
0.70	5.0	1.8	37.5	150017
0.70	5.0	1.8	45.0	150018
0.70	5.0	1.8	60.0	150019
0.70	5.0	1.8	70.0	150020
0.70	2.5	1.8	1.0	310004
0.70	2.5	1.8	2.5	310005
0.70	2.5	1.8	5.0	310006
0.70	2.5	1.8	7.5	310007
0.70	2.5	1.8	10.0	310008
0.70	2.5	1.8	12.5	310009
0.70	2.5	1.8	15.0	310010
0.70	2.5	1.8	17.5	310011
0.70	2.5	1.8	20.0	310012
0.70	2.5	1.8	22.5	310013
0.70	2.5	1.8	25.0	310014
0.70	2.5	1.8	30.0	310015
0.70	2.5	1.8	37.5	310016
0.70	2.5	1.8	45.0	310017
0.70	2.5	1.8	60.0	310018
0.70	2.5	1.8	70.0	310019
0.70	7.5	1.8	1.0	440004
0.70	7.5	1.8	2.5	440005
0.70	7.5	1.8	5.0	440006
0.70	7.5	1.8	7.5	440007
0.70	7.5	1.8	10.0	440008
0.70	7.5	1.8	12.5	440009
0.70	7.5	1.8	15.0	440010
0.70	7.5	1.8	17.5	440011
0.70	7.5	1.8	20.0	440012
0.70	7.5	1.8	22.5	440013
0.70	7.5	1.8	25.0	440014
0.70	7.5	1.8	30.0	440015
0.70	7.5	1.8	37.5	440016
0.70	7.5	1.8	45.0	440017
0.70	7.5	1.8	60.0	440018
0.70	7.5	1.8	70.0	440019

M_∞	Re	$\hat{A}$	f_{exc}	MP
0.80	5.0	1.8	1.0	170004
0.80	5.0	1.8	2.5	170005
0.80	5.0	1.8	5.0	170006
0.80	5.0	1.8	7.5	170007
0.80	5.0	1.8	10.0	170008
0.80	5.0	1.8	12.5	170009
0.80	5.0	1.8	15.0	170010
0.80	5.0	1.8	17.5	170011
0.80	5.0	1.8	20.0	170012
0.80	5.0	1.8	22.5	170013
0.80	5.0	1.8	25.0	170014
0.80	5.0	1.8	30.0	170015
0.80	5.0	1.8	37.5	170016
0.80	5.0	1.8	45.0	170017
0.80	5.0	1.8	60.0	170018
0.80	5.0	1.8	70.0	170019
0.80	2.5	1.8	1.0	320005
0.80	2.5	1.8	2.5	320005
0.80	2.5	1.8	5.0	320006
0.80	2.5	1.8	7.5	320007
0.80	2.5	1.8	10.0	320008
0.80	2.5	1.8	12.5	320009
0.80	2.5	1.8	15.0	320010
0.80	2.5	1.8	17.5	320011
0.80	2.5	1.8	20.0	320012
0.80	2.5	1.8	22.5	320013
0.80	2.5	1.8	25.0	320014
0.80	2.5	1.8	30.0	320015
0.80	2.5	1.8	37.5	320016
0.80	2.5	1.8	45.0	320017
0.80	2.5	1.8	60.0	320018
0.80	2.5	1.8	70.0	320019
0.80	7.5	1.8	1.0	450004
0.80	7.5	1.8	2.5	450005
0.80	7.5	1.8	5.0	450006
0.80	7.5	1.8	7.5	450007
0.80	7.5	1.8	10.0	450008
0.80	7.5	1.8	12.5	450009
0.80	7.5	1.8	15.0	450010
0.80	7.5	1.8	17.5	450011
0.80	7.5	1.8	20.0	450012
0.80	7.5	1.8	22.5	450013
0.80	7.5	1.8	25.0	450014
0.80	7.5	1.8	30.0	450015
0.80	7.5	1.8	37.5	450016
0.80	7.5	1.8	45.0	450017
0.80	7.5	1.8	60.0	450018
0.80	7.5	1.8	70.0	450019

M_∞	Re	$\hat{A}$	f_{exc}	MP
0.90	5.0	1.8	1.0	180004
0.90	5.0	1.8	2.5	180005
0.90	5.0	1.8	2.5	180006
0.90	5.0	1.8	7.5	180007
0.90	5.0	1.8	10.0	180008
0.90	5.0	1.8	12.5	180009
0.90	5.0	1.8	15.0	180010
0.90	5.0	1.8	17.5	180011
0.90	5.0	1.8	20.0	180012
0.90	5.0	1.8	22.5	180013
0.90	5.0	1.8	25.0	180014
0.90	5.0	1.8	30.0	180015
0.90	5.0	1.8	37.5	180016
0.90	5.0	1.8	45.0	180017
0.90	5.0	1.8	60.0	180018
0.90	5.0	1.8	70.0	180019
0.90	2.5	1.8	1.0	330004
0.90	2.5	1.8	2.5	330005
0.90	2.5	1.8	5.0	330006
0.90	2.5	1.8	7.5	330007
0.90	2.5	1.8	10.0	330008
0.90	2.5	1.8	12.5	330009
0.90	2.5	1.8	15.0	330010
0.90	2.5	1.8	17.5	330011
0.90	2.5	1.8	20.0	330012
0.90	2.5	1.8	22.5	330013
0.90	2.5	1.8	25.0	330014
0.90	2.5	1.8	30.0	330015
0.90	2.5	1.8	37.5	330016
0.90	2.5	1.8	45.0	330017
0.90	2.5	1.8	60.0	330018
0.90	2.5	1.8	70.0	330019
0.90	7.5	1.8	1.0	460004
0.90	7.5	1.8	2.5	460005
0.90	7.5	1.8	5.0	460006
0.90	7.5	1.8	7.5	460007
0.90	7.5	1.8	10.0	460008
0.90	7.5	1.8	12.5	460009
0.90	7.5	1.8	15.0	460010
0.90	7.5	1.8	17.5	460011
0.90	7.5	1.8	20.0	460012
0.90	7.5	1.8	22.5	460013
0.90	7.5	1.8	25.0	460014
0.90	7.5	1.8	30.0	460015
0.90	7.5	1.8	37.5	460016
0.90	7.5	1.8	45.0	460017
0.90	7.5	1.8	60.0	460018
0.90	7.5	1.8	70.0	460019

M_∞	Re	$\hat{A}$	f_{exc}	MP
1.0	5.0	1.8	1.	220004
1.0	5.0	1.8	2.5	220005
1.0	5.0	1.8	2.5	220006
1.0	5.0	1.8	7.5	220007
1.0	5.0	1.8	10.0	220008
1.0	5.0	1.8	12.5	220009
1.0	5.0	1.8	15.0	220010
1.0	5.0	1.8	17.5	220011
1.0	5.0	1.8	20.0	220012
1.0	5.0	1.8	22.5	220013
1.0	5.0	1.8	25.0	220014
1.0	5.0	1.8	30.0	220015
1.0	5.0	1.8	37.5	220016
1.0	5.0	1.8	45.0	220017
1.0	5.0	1.8	60.0	220018
1.0	5.0	1.8	70.0	220019
1.0	2.5	1.8	1.0	340004
1.0	2.5	1.8	2.5	340005
1.0	2.5	1.8	5.0	340006
1.0	2.5	1.8	7.5	340007
1.0	2.5	1.8	10.0	340008
1.0	2.5	1.8	12.5	340009
1.0	2.5	1.8	15.0	340010
1.0	2.5	1.8	17.5	340011
1.0	2.5	1.8	20.0	340012
1.0	2.5	1.8	22.5	340013
1.0	2.5	1.8	25.0	340014
1.0	2.5	1.8	30.0	340015
1.0	2.5	1.8	37.5	340016
1.0	2.5	1.8	45.0	340017
1.0	2.5	1.8	60.0	340018
1.0	2.5	1.8	70.0	340019
1.0	7.5	1.8	1.0	480004
1.0	7.5	1.8	2.5	480005
1.0	7.5	1.8	5.0	480006
1.0	7.5	1.8	7.5	480007
1.0	7.5	1.8	10.0	480008
1.0	7.5	1.8	12.5	480009
1.0	7.5	1.8	15.0	480010
1.0	7.5	1.8	17.5	480011
1.0	7.5	1.8	20.0	480012
1.0	7.5	1.8	22.5	480013
1.0	7.5	1.8	25.0	480014
1.0	7.5	1.8	30.0	480015
1.0	7.5	1.8	37.5	480016
1.0	7.5	1.8	45.0	480017
1.0	7.5	1.8	60.0	480018
1.0	7.5	1.8	60.0	480019

Table F.4.: List of Measurement Points; M_∞ [-]; Re [10E6]; $\hat{A}$ [mm]; f_{exc} [Hz]; Ψ_{11} model (2017); Table 1 of 2.

M_∞	Re	$\hat{A}$	f_{exc}	MP
1.05	5.0	1.8	1.0	230004
1.05	5.0	1.8	2.5	230005
1.05	5.0	1.8	5.0	230006
1.05	5.0	1.8	7.5	230007
1.05	5.0	1.8	10.0	230008
1.05	5.0	1.8	12.5	230009
1.05	5.0	1.8	15.0	230010
1.05	5.0	1.8	17.5	230011
1.05	5.0	1.8	20.0	230012
1.05	5.0	1.8	22.5	230013
1.05	5.0	1.8	25.0	230014
1.05	5.0	1.8	30.0	230015
1.05	5.0	1.8	37.5	230016
1.05	5.0	1.8	45.0	230017
1.05	5.0	1.8	60.0	230018
1.05	5.0	1.8	70.0	230019
1.05	2.5	1.8	1.0	350005
1.05	2.5	1.8	2.5	350005
1.05	2.5	1.8	5.0	350006
1.05	2.5	1.8	7.5	350007
1.05	2.5	1.8	10.0	350008
1.05	2.5	1.8	12.5	350009
1.05	2.5	1.8	15.0	350010
1.05	2.5	1.8	17.5	350011
1.05	2.5	1.8	20.0	350012
1.05	2.5	1.8	22.5	350013
1.05	2.5	1.8	25.0	350014
1.05	2.5	1.8	30.0	350015
1.05	2.5	1.8	37.5	350016
1.05	2.5	1.8	45.0	350017
1.05	2.5	1.8	60.0	350018
1.05	2.5	1.8	70.0	350019
1.05	7.5	1.8	1.0	490004
1.05	7.5	1.8	2.5	490005
1.05	7.5	1.8	5.0	490006
1.05	7.5	1.8	7.5	490007
1.05	7.5	1.8	10.0	490008
1.05	7.5	1.8	12.5	490009
1.05	7.5	1.8	15.0	490010
1.05	7.5	1.8	17.5	490011
1.05	7.5	1.8	20.0	490012
1.05	7.5	1.8	22.5	490013
1.05	7.5	1.8	25.0	490014
1.05	7.5	1.8	30.0	490015
1.05	7.5	1.8	37.5	490016
1.05	7.5	1.8	45.0	490017
1.05	7.5	1.8	60.0	490018
1.05	7.5	1.8	7.0	490019

M_∞	Re	$\hat{A}$	f_{exc}	MP
1.10	5.0	1.8	1.0	250005
1.10	5.0	1.8	2.5	250005
1.10	5.0	1.8	5.0	250006
1.10	5.0	1.8	7.5	250007
1.10	5.0	1.8	10.0	250008
1.10	5.0	1.8	12.5	250009
1.10	5.0	1.8	15.0	250010
1.10	5.0	1.8	17.5	250011
1.10	5.0	1.8	20.0	250012
1.10	5.0	1.8	22.5	250013
1.10	5.0	1.8	25.0	250014
1.10	5.0	1.8	30.0	250015
1.10	5.0	1.8	37.5	250016
1.10	5.0	1.8	45.0	250017
1.10	5.0	1.8	60.0	250018
1.10	5.0	1.8	70.0	250019
1.10	2.5	1.8	1.0	360004
1.10	2.5	1.8	2.5	360005
1.10	2.5	1.8	5.0	360006
1.10	2.5	1.8	7.5	360007
1.10	2.5	1.8	10.0	360008
1.10	2.5	1.8	12.5	360009
1.10	2.5	1.8	15.0	360010
1.10	2.5	1.8	17.5	360011
1.10	2.5	1.8	20.0	360012
1.10	2.5	1.8	22.5	360013
1.10	2.5	1.8	25.0	360014
1.10	2.5	1.8	30.0	360015
1.10	2.5	1.8	37.5	360016
1.10	2.5	1.8	45.0	360017
1.10	2.5	1.8	60.0	360018
1.10	2.5	1.8	70.0	360019
1.10	7.5	1.8	1.0	500004
1.10	7.5	1.8	2.5	500005
1.10	7.5	1.8	5.0	500006
1.10	7.5	1.8	7.5	500007
1.10	7.5	1.8	10.0	500008
1.10	7.5	1.8	12.5	500009
1.10	7.5	1.8	15.0	500010
1.10	7.5	1.8	17.5	500011
1.10	7.5	1.8	20.0	500012
1.10	7.5	1.8	22.5	500013
1.10	7.5	1.8	25.0	500014
1.10	7.5	1.8	30.0	500015
1.10	7.5	1.8	37.5	500016
1.10	7.5	1.8	45.0	500017
1.10	7.5	1.8	60.0	500018
1.10	7.5	1.8	70.0	500019

M_∞	Re	$\hat{A}$	f_{exc}	MP
1.15	5.0	1.8	1.0	260004
1.15	5.0	1.8	2.5	260005
1.15	5.0	1.8	5.0	260006
1.15	5.0	1.8	7.5	260007
1.15	5.0	1.8	10.0	260008
1.15	5.0	1.8	12.5	260009
1.15	5.0	1.8	15.0	260010
1.15	5.0	1.8	17.5	260011
1.15	5.0	1.8	20.0	260012
1.15	5.0	1.8	22.5	260013
1.15	5.0	1.8	25.0	260014
1.15	5.0	1.8	30.0	260015
1.15	5.0	1.8	37.5	260016
1.15	5.0	1.8	45.0	260017
1.15	5.0	1.8	60.0	260018
1.15	5.0	1.8	70.0	260019
1.15	2.5	1.8	1.0	380004
1.15	2.5	1.8	2.5	380005
1.15	2.5	1.8	5.0	380006
1.15	2.5	1.8	7.5	380007
1.15	2.5	1.8	10.0	380008
1.15	2.5	1.8	12.5	380009
1.15	2.5	1.8	15.0	380010
1.15	2.5	1.8	17.5	380011
1.15	2.5	1.8	20.0	380012
1.15	2.5	1.8	22.5	380013
1.15	2.5	1.8	25.0	380014
1.15	2.5	1.8	30.0	380015
1.15	2.5	1.8	37.5	380016
1.15	2.5	1.8	45.0	380017
1.15	2.5	1.8	60.0	380018
1.15	2.5	1.8	70.0	380019
1.15	7.5	1.8	1.0	510004
1.15	7.5	1.8	2.5	510005
1.15	7.5	1.8	5.0	510006
1.15	7.5	1.8	7.5	510007
1.15	7.5	1.8	10.0	510008
1.15	7.5	1.8	12.5	510009
1.15	7.5	1.8	15.0	510010
1.15	7.5	1.8	17.5	510011
1.15	7.5	1.8	20.0	510012
1.15	7.5	1.8	22.5	510013
1.15	7.5	1.8	25.0	510014
1.15	7.5	1.8	30.0	510015
1.15	7.5	1.8	37.5	510016
1.15	7.5	1.8	45.0	510017
1.15	7.5	1.8	60.0	510018
1.15	7.5	1.8	70.0	510019

M_∞	Re	$\hat{A}$	f_{exc}	MP
1.20	5.0	1.8	1.0	270004
1.20	5.0	1.8	2.5	270005
1.20	5.0	1.8	5.0	270006
1.20	5.0	1.8	7.5	270007
1.20	5.0	1.8	10.0	270008
1.20	5.0	1.8	12.5	270009
1.20	5.0	1.8	15.0	270010
1.20	5.0	1.8	17.5	270011
1.20	5.0	1.8	20.0	270012
1.20	5.0	1.8	22.5	270013
1.20	5.0	1.8	25.0	270014
1.20	5.0	1.8	30.0	270015
1.20	5.0	1.8	37.5	270016
1.20	5.0	1.8	45.0	270017
1.20	5.0	1.8	60.0	270018
1.20	5.0	1.8	70.0	270019
1.20	2.5	1.8	1.0	390004
1.20	2.5	1.8	2.5	390005
1.20	2.5	1.8	5.0	390006
1.20	2.5	1.8	7.5	390007
1.20	2.5	1.8	10.0	390008
1.20	2.5	1.8	12.5	390009
1.20	2.5	1.8	15.0	390010
1.20	2.5	1.8	17.5	390011
1.20	2.5	1.8	20.0	390012
1.20	2.5	1.8	22.5	390013
1.20	2.5	1.8	25.0	390014
1.20	2.5	1.8	30.0	390015
1.20	2.5	1.8	37.5	390016
1.20	2.5	1.8	45.0	390017
1.20	2.5	1.8	60.0	390018
1.20	2.5	1.8	70.0	390019
1.20	7.5	1.8	1.0	520005
1.20	7.5	1.8	2.5	520006
1.20	7.5	1.8	5.0	520007
1.20	7.5	1.8	7.5	520008
1.20	7.5	1.8	10.0	520009
1.20	7.5	1.8	12.5	520010
1.20	7.5	1.8	15.0	520011
1.20	7.5	1.8	17.5	520012
1.20	7.5	1.8	20.0	520013
1.20	7.5	1.8	22.5	520014
1.20	7.5	1.8	25.0	520015
1.20	7.5	1.8	30.0	520016
1.20	7.5	1.8	37.5	520017
1.20	7.5	1.8	45.0	520018
1.20	7.5	1.8	60.0	520019
1.20	7.5	1.8	70.0	520020

Table F.5.: List of Measurement Points; M_∞ [-]; Re [10E6]; $\hat{A}$ [mm]; f_{exc} [Hz]; Ψ_{11} model (2017); Table 2 of 2.

M_∞	Re	$\hat{A}$	f_{exc}	MP
0.70	5.0	1.8	1.0	980004
0.70	5.0	1.8	2.5	980005
0.70	5.0	1.8	5.0	980006
0.70	5.0	1.8	7.5	980007
0.70	5.0	1.8	10.0	980008
0.70	5.0	1.8	12.5	980009
0.70	5.0	1.8	15.0	980010
0.70	5.0	1.8	17.5	980011
0.70	5.0	1.8	20.0	980012
0.70	5.0	1.8	22.5	980013
0.70	5.0	1.8	25.0	980014
0.70	5.0	1.8	30.0	980015
0.70	5.0	1.8	37.5	980016
0.70	5.0	1.8	45.0	980017
0.70	5.0	1.8	60.0	980018
0.70	5.0	1.8	70.0	980019
0.70	2.5	1.8	1.0	820005
0.70	2.5	1.8	2.5	820006
0.70	2.5	1.8	5.0	820007
0.70	2.5	1.8	7.5	820008
0.70	2.5	1.8	10.0	820009
0.70	2.5	1.8	12.5	820010
0.70	2.5	1.8	15.0	820011
0.70	2.5	1.8	17.5	820012
0.70	2.5	1.8	20.0	820013
0.70	2.5	1.8	22.5	820014
0.70	2.5	1.8	25.0	820015
0.70	2.5	1.8	30.0	820016
0.70	2.5	1.8	37.5	820017
0.70	2.5	1.8	45.0	820018
0.70	2.5	1.8	60.0	820019
0.70	2.5	1.8	70.0	820020
0.70	7.5	1.8	1.0	1120004
0.70	7.5	1.8	2.5	1120005
0.70	7.5	1.8	5.0	1120006
0.70	7.5	1.8	7.5	1120007
0.70	7.5	1.8	10.0	1120008
0.70	7.5	1.8	12.5	1120009
0.70	7.5	1.8	15.0	1120010
0.70	7.5	1.8	17.5	1120011
0.70	7.5	1.8	20.0	1120012
0.70	7.5	1.8	22.5	1120013
0.70	7.5	1.8	25.0	1120014
0.70	7.5	1.8	30.0	1120015
0.70	7.5	1.8	37.5	1120016
0.70	7.5	1.8	45.0	1120017
0.70	7.5	1.8	60.0	1120018
0.70	7.5	1.8	70.0	1120019

M_∞	Re	$\hat{A}$	f_{exc}	MP
0.80	5.0	1.8	1.0	990004
0.80	5.0	1.8	2.5	990005
0.80	5.0	1.8	5.0	990006
0.80	5.0	1.8	7.5	990007
0.80	5.0	1.8	10.0	990008
0.80	5.0	1.8	12.5	990009
0.80	5.0	1.8	15.0	990010
0.80	5.0	1.8	17.5	990011
0.80	5.0	1.8	20.0	990012
0.80	5.0	1.8	22.5	990013
0.80	5.0	1.8	25.0	990014
0.80	5.0	1.8	30.0	990015
0.80	5.0	1.8	37.5	990016
0.80	5.0	1.8	45.0	990017
0.80	5.0	1.8	60.0	990018
0.80	5.0	1.8	70.0	990019
0.80	2.5	1.8	1.0	840006
0.80	2.5	1.8	2.5	840007
0.80	2.5	1.8	5.0	840008
0.80	2.5	1.8	7.5	840009
0.80	2.5	1.8	10.0	840010
0.80	2.5	1.8	12.5	840011
0.80	2.5	1.8	15.0	840012
0.80	2.5	1.8	17.5	840013
0.80	2.5	1.8	20.0	840014
0.80	2.5	1.8	22.5	840015
0.80	2.5	1.8	25.0	840016
0.80	2.5	1.8	30.0	840017
0.80	2.5	1.8	37.5	840018
0.80	2.5	1.8	45.0	840019
0.80	2.5	1.8	60.0	840020
0.80	2.5	1.8	70.0	840021
0.80	7.5	1.8	1.0	1140004
0.80	7.5	1.8	2.5	1140005
0.80	7.5	1.8	5.0	1140006
0.80	7.5	1.8	7.5	1140007
0.80	7.5	1.8	10.0	1140008
0.80	7.5	1.8	12.5	1140009
0.80	7.5	1.8	15.0	1140010
0.80	7.5	1.8	17.5	1140011
0.80	7.5	1.8	20.0	1140012
0.80	7.5	1.8	22.5	1140013
0.80	7.5	1.8	25.0	1140014
0.80	7.5	1.8	30.0	1140015
0.80	7.5	1.8	37.5	1140016
0.80	7.5	1.8	45.0	1140017
0.80	7.5	1.8	60.0	1140018
0.80	7.5	1.8	70.0	1140019

M_∞	Re	$\hat{A}$	f_{exc}	MP
0.90	5.0	1.8	1.0	1000004
0.90	5.0	1.8	2.5	1000005
0.90	5.0	1.8	2.5	1000006
0.90	5.0	1.8	7.5	1000007
0.90	5.0	1.8	10.0	1000008
0.90	5.0	1.8	12.5	1000009
0.90	5.0	1.8	15.0	1000010
0.90	5.0	1.8	17.5	1000011
0.90	5.0	1.8	20.0	1000012
0.90	5.0	1.8	22.5	1000013
0.90	5.0	1.8	25.0	1000014
0.90	5.0	1.8	30.0	1000015
0.90	5.0	1.8	37.5	1000016
0.90	5.0	1.8	45.0	1000017
0.90	5.0	1.8	60.0	1000018
0.90	5.0	1.8	70.0	1000020
0.90	2.5	1.8	1.0	860004
0.90	2.5	1.8	2.5	860005
0.90	2.5	1.8	5.0	860006
0.90	2.5	1.8	7.5	860007
0.90	2.5	1.8	10.0	860008
0.90	2.5	1.8	12.5	860009
0.90	2.5	1.8	15.0	860010
0.90	2.5	1.8	17.5	860011
0.90	2.5	1.8	20.0	860012
0.90	2.5	1.8	22.5	860013
0.90	2.5	1.8	25.0	860014
0.90	2.5	1.8	30.0	860015
0.90	2.5	1.8	37.5	860016
0.90	2.5	1.8	45.0	860017
0.90	2.5	1.8	60.0	860018
0.90	2.5	1.8	70.0	860019
0.90	7.5	1.8	1.0	1150004
0.90	7.5	1.8	2.5	1150005
0.90	7.5	1.8	5.0	1150006
0.90	7.5	1.8	7.5	1150007
0.90	7.5	1.8	10.0	1150008
0.90	7.5	1.8	12.5	1150009
0.90	7.5	1.8	15.0	1150010
0.90	7.5	1.8	17.5	1150011
0.90	7.5	1.8	20.0	1150012
0.90	7.5	1.8	22.5	1150013
0.90	7.5	1.8	25.0	1150014
0.90	7.5	1.8	30.0	1150015
0.90	7.5	1.8	37.5	1150016
0.90	7.5	1.8	45.0	1150017
0.90	7.5	1.8	60.0	1150018
0.90	7.5	1.8	70.0	1150019

M_∞	Re	$\hat{A}$	f_{exc}	MP
1.0	5.0	1.8	1.0	1010004
1.0	5.0	1.8	2.5	1030001
1.0	5.0	1.8	5.0	1030002
1.0	5.0	1.8	7.5	1030003
1.0	5.0	1.8	10.0	1030004
1.0	5.0	1.8	12.5	1030005
1.0	5.0	1.8	15.0	1030006
1.0	5.0	1.8	17.5	1030007
1.0	5.0	1.8	20.0	1030008
1.0	5.0	1.8	22.5	1030009
1.0	5.0	1.8	25.0	1030010
1.0	5.0	1.8	30.0	1030011
1.0	5.0	1.8	37.5	1030012
1.0	5.0	1.8	45.0	1030013
1.0	5.0	1.8	60.0	1030014
1.0	5.0	1.8	70.0	1030015
1.0	2.5	1.8	1.0	870004
1.0	2.5	1.8	2.5	870005
1.0	2.5	1.8	5.0	870006
1.0	2.5	1.8	7.5	870007
1.0	2.5	1.8	10.0	870008
1.0	2.5	1.8	12.5	870009
1.0	2.5	1.8	15.0	870010
1.0	2.5	1.8	17.5	870011
1.0	2.5	1.8	20.0	870012
1.0	2.5	1.8	22.5	870013
1.0	2.5	1.8	25.0	870014
1.0	2.5	1.8	30.0	870015
1.0	2.5	1.8	37.5	870016
1.0	2.5	1.8	45.0	870017
1.0	2.5	1.8	60.0	870018
1.0	2.5	1.8	70.0	870019
1.0	7.5	1.8	1.0	1190004
1.0	7.5	1.8	2.5	1190005
1.0	7.5	1.8	5.0	1190006
1.0	7.5	1.8	7.5	1190007
1.0	7.5	1.8	10.0	1190008
1.0	7.5	1.8	12.5	1190009
1.0	7.5	1.8	15.0	1190010
1.0	7.5	1.8	17.5	1190011
1.0	7.5	1.8	20.0	1190012
1.0	7.5	1.8	22.5	1190013
1.0	7.5	1.8	25.0	1190014
1.0	7.5	1.8	30.0	1190015
1.0	7.5	1.8	37.5	1190016
1.0	7.5	1.8	45.0	1190017
1.0	7.5	1.8	60.0	1190018
1.0	7.5	1.8	70.0	1190019

Table F.6.: List of Measurement Points; M_∞ [-]; Re [10E6]; $\hat{A}$ [mm]; f_{exc} [Hz]; Ψ_{21} model (2017); Table 1 of 2.

M_∞	Re	$\hat{A}$	f_{exc}	MP
1.05	5.0	1.8	1.0	1040004
1.05	5.0	1.8	2.5	1040005
1.05	5.0	1.8	5.0	1040006
1.05	5.0	1.8	7.5	1040007
1.05	5.0	1.8	10.0	1040008
1.05	5.0	1.8	12.5	1040009
1.05	5.0	1.8	15.0	1040010
1.05	5.0	1.8	17.5	1040011
1.05	5.0	1.8	20.0	1040012
1.05	5.0	1.8	22.5	1040013
1.05	5.0	1.8	25.0	1040015
1.05	5.0	1.8	30.0	1040016
1.05	5.0	1.8	37.5	1040017
1.05	5.0	1.8	45.0	1040018
1.05	5.0	1.8	60.0	1040019
1.05	5.0	1.8	70.0	1040020
1.05	2.5	1.8	1.0	880004
1.05	2.5	1.8	2.5	880005
1.05	2.5	1.8	5.0	880006
1.05	2.5	1.8	7.5	880007
1.05	2.5	1.8	10.0	880008
1.05	2.5	1.8	12.5	880009
1.05	2.5	1.8	15.0	880010
1.05	2.5	1.8	17.5	880011
1.05	2.5	1.8	20.0	880012
1.05	2.5	1.8	22.5	880013
1.05	2.5	1.8	25.0	880014
1.05	2.5	1.8	30.0	880015
1.05	2.5	1.8	37.5	880016
1.05	2.5	1.8	45.0	880017
1.05	2.5	1.8	60.0	880018
1.05	2.5	1.8	70.0	880019
1.05	7.5	1.8	1.0	1200004
1.05	7.5	1.8	2.5	1200005
1.05	7.5	1.8	5.0	1200006
1.05	7.5	1.8	7.5	1200007
1.05	7.5	1.8	10.0	1200008
1.05	7.5	1.8	12.5	1200009
1.05	7.5	1.8	15.0	1200010
1.05	7.5	1.8	17.5	1200011
1.05	7.5	1.8	20.0	1200012
1.05	7.5	1.8	22.5	1200013
1.05	7.5	1.8	25.0	1200014
1.05	7.5	1.8	30.0	1200015
1.05	7.5	1.8	37.5	1200016
1.05	7.5	1.8	45.0	1200017
1.05	7.5	1.8	60.0	1200018
1.05	7.5	1.8	70.0	1200019

M_∞	Re	$\hat{A}$	f_{exc}	MP
1.10	5.0	1.8	1.0	1060004
1.10	5.0	1.8	2.5	1060005
1.10	5.0	1.8	5.0	1060006
1.10	5.0	1.8	7.5	1060007
1.10	5.0	1.8	10.0	1060008
1.10	5.0	1.8	12.5	1060009
1.10	5.0	1.8	15.0	1060010
1.10	5.0	1.8	17.5	1060011
1.10	5.0	1.8	20.0	1060012
1.10	5.0	1.8	22.5	1060013
1.10	5.0	1.8	25.0	1060014
1.10	5.0	1.8	30.0	1060015
1.10	5.0	1.8	37.5	1060016
1.10	5.0	1.8	45.0	1060017
1.10	5.0	1.8	60.0	1060018
1.10	5.0	1.8	70.0	1060019
1.10	2.5	1.8	1.0	890004
1.10	2.5	1.8	2.5	890005
1.10	2.5	1.8	5.0	890006
1.10	2.5	1.8	7.5	890007
1.10	2.5	1.8	10.0	890008
1.10	2.5	1.8	12.5	890009
1.10	2.5	1.8	15.0	890010
1.10	2.5	1.8	17.5	890011
1.10	2.5	1.8	20.0	890012
1.10	2.5	1.8	22.5	890013
1.10	2.5	1.8	25.0	890014
1.10	2.5	1.8	30.0	890015
1.10	2.5	1.8	37.5	890016
1.10	2.5	1.8	45.0	890017
1.10	2.5	1.8	60.0	890018
1.10	2.5	1.8	70.0	890019
1.10	7.5	1.8	1.0	1210004
1.10	7.5	1.8	2.5	1210005
1.10	7.5	1.8	5.0	1210006
1.10	7.5	1.8	7.5	1210007
1.10	7.5	1.8	10.0	1210008
1.10	7.5	1.8	12.5	1210009
1.10	7.5	1.8	15.0	1210010
1.10	7.5	1.8	17.5	1210011
1.10	7.5	1.8	20.0	1210012
1.10	7.5	1.8	22.5	1210013
1.10	7.5	1.8	25.0	1210014
1.10	7.5	1.8	30.0	1210015
1.10	7.5	1.8	37.5	1210016
1.10	7.5	1.8	45.0	1210017
1.10	7.5	1.8	60.0	1210018
1.10	7.5	1.8	70.0	1210019

M_∞	Re	$\hat{A}$	f_{exc}	MP
1.15	5.0	1.8	1.0	1070004
1.15	5.0	1.8	2.5	1070005
1.15	5.0	1.8	5.0	1070006
1.15	5.0	1.8	7.5	1070007
1.15	5.0	1.8	10.0	1070008
1.15	5.0	1.8	12.5	1070009
1.15	5.0	1.8	15.0	1070010
1.15	5.0	1.8	17.5	1070011
1.15	5.0	1.8	20.0	1070012
1.15	5.0	1.8	22.5	1070013
1.15	5.0	1.8	25.0	1070014
1.15	5.0	1.8	30.0	1070015
1.15	5.0	1.8	37.5	1070016
1.15	5.0	1.8	45.0	1070017
1.15	5.0	1.8	60.0	1070018
1.15	5.0	1.8	70.0	1070019
1.15	2.5	1.8	1.0	900004
1.15	2.5	1.8	2.5	900005
1.15	2.5	1.8	5.0	900006
1.15	2.5	1.8	7.5	900007
1.15	2.5	1.8	10.0	900008
1.15	2.5	1.8	12.5	900009
1.15	2.5	1.8	15.0	900010
1.15	2.5	1.8	17.5	900011
1.15	2.5	1.8	20.0	900012
1.15	2.5	1.8	22.5	900013
1.15	2.5	1.8	25.0	900014
1.15	2.5	1.8	30.0	900015
1.15	2.5	1.8	37.5	900016
1.15	2.5	1.8	45.0	900017
1.15	2.5	1.8	60.0	900018
1.15	2.5	1.8	70.0	900019
1.15	7.5	1.8	1.0	1230004
1.15	7.5	1.8	2.5	1230005
1.15	7.5	1.8	5.0	1230006
1.15	7.5	1.8	7.5	1230007
1.15	7.5	1.8	10.0	1230008
1.15	7.5	1.8	12.5	1230009
1.15	7.5	1.8	15.0	1230010
1.15	7.5	1.8	17.5	1230011
1.15	7.5	1.8	20.0	1230012
1.15	7.5	1.8	22.5	1230013
1.15	7.5	1.8	25.0	1230014
1.15	7.5	1.8	30.0	1230015
1.15	7.5	1.8	37.5	1230016
1.15	7.5	1.8	45.0	1230017
1.15	7.5	1.8	60.0	1230018
1.15	7.5	1.8	70.0	1230019

M_∞	Re	$\hat{A}$	f_{exc}	MP
1.20	5.0	1.8	1.0	1080004
1.20	5.0	1.8	2.5	1080005
1.20	5.0	1.8	5.0	1080006
1.20	5.0	1.8	7.5	1080007
1.20	5.0	1.8	10.0	1080008
1.20	5.0	1.8	12.5	1080009
1.20	5.0	1.8	15.0	1080010
1.20	5.0	1.8	17.5	1080011
1.20	5.0	1.8	20.0	1080012
1.20	5.0	1.8	22.5	1080013
1.20	5.0	1.8	25.0	1080014
1.20	5.0	1.8	30.0	1080015
1.20	5.0	1.8	37.5	1080016
1.20	5.0	1.8	45.0	1080017
1.20	5.0	1.8	60.0	1080018
1.20	5.0	1.8	70.0	1080019
1.20	2.5	1.8	1.0	910004
1.20	2.5	1.8	2.5	910005
1.20	2.5	1.8	5.0	910006
1.20	2.5	1.8	7.5	910007
1.20	2.5	1.8	10.0	910008
1.20	2.5	1.8	12.5	910009
1.20	2.5	1.8	15.0	910010
1.20	2.5	1.8	17.5	910011
1.20	2.5	1.8	20.0	910012
1.20	2.5	1.8	22.5	910013
1.20	2.5	1.8	25.0	910014
1.20	2.5	1.8	30.0	910015
1.20	2.5	1.8	37.5	910016
1.20	2.5	1.8	45.0	910017
1.20	2.5	1.8	60.0	910018
1.20	2.5	1.8	70.0	910019
1.20	7.5	1.8	1.0	1240004
1.20	7.5	1.8	2.5	1240005
1.20	7.5	1.8	5.0	1240006
1.20	7.5	1.8	7.5	1240007
1.20	7.5	1.8	10.0	1240008
1.20	7.5	1.8	12.5	1240009
1.20	7.5	1.8	15.0	1240010
1.20	7.5	1.8	17.5	1240011
1.20	7.5	1.8	20.0	1240012
1.20	7.5	1.8	22.5	1240013
1.20	7.5	1.8	25.0	1240014
1.20	7.5	1.8	30.0	1240015
1.20	7.5	1.8	37.5	1240016
1.20	7.5	1.8	45.0	1240017
1.20	7.5	1.8	60.0	1240018
1.20	7.5	1.8	70.0	1240019

Table F.7.: List of Measurement Points; M_∞ [-]; Re [10E6]; $\hat{A}$ [mm]; f_{exc} [Hz]; Ψ_{21} model (2017); Table 2 of 2.